NREL/TP-442-4822 • UC Category: 261 • DE92001245

Yaw Dynamics of Horizontal Axis Wind Turbines

Final Report

NREL/TP--442-4822

DE92 001245

A.C. Hansen
University of Utah
Salt Lake City, Utah

NREL Technical Monitor: Alan Wright

National Renewable Energy Laboratory
(formerly the Solar Energy Research Institute)
1617 Cole Boulevard
Golden, Colorado 80401-3393
A Division of Midwest Research Institute
Operated for the U.S. Department of Energy
under Contract No. DE-AC02-83CH10093

Prepared under subcontract no: XL-6-05078-2

May 1992

On September 16, 1991, the Solar Energy Research Institute was designated a national laboratory, and its name was changed to the National Renewable Energy Laboratory.

NOTICE

Printed in the United States of America
Available from:
National Technical Information Service
U.S. Department of Commerce
5285 Port Royal Road
Springfield, VA 22161

Price: Microfiche A01
Printed Copy A09

Codes are used for pricing all publications. The code is determined by the number of pages in the publication. Information pertaining to the pricing codes can be found in the current issue of the following publications which are generally available in most libraries: *Energy Research Abstracts (ERA)*; *Government Reports Announcements* and Index (*GRA* and I); *Scientific and Technical Abstract Reports (STAR)*; and publication NTIS-PR-360 available from NTIS at the above address.

Notice

Preface

This Final Report is a summary of work that has been performed at the University of Utah over the past five years. Several graduate students contributed to the research: Xudong Cui, Norman Siedschlag, Robert Schnepp, and Todd Dorius each assisted in the analysis, programming, validating and debugging. Without their help this work would not have been possible. Papers, reports and theses which resulted from their efforts are listed at the end of the list of references.

Work of this type cannot be completed without the efforts and cooperation of many individuals. The SERI technical monitor, contract officials, test personnel and management have all approached this task with the goal of getting a job done in the most straightforward, cost-effective and reasonable manner. And many individuals at the University of Utah have shared that approach and attitude. That spirit is gratefully and warmly acknowledged.

Much of the material of Section 2.0 was originally commissioned by the Wind Turbine Company, Inc. Their permission to include this material in this report is gratefully acknowledged.

Table of Contents

List of Figures

List of Tables

List of Symbols

A = area

a = axial induction factor = $\frac{V_i}{V_z}$

a_f = yaw friction moment

a_v = coefficient to describe mechanical yaw damping system

B = number of rotor blades

C_L = section lift coefficient of blade airfoil

C_D = drag coefficient of blade airfoil

c = blade chord length

D = drag force

EI = blade flap stiffness

$\hat{e}_x$ = unit vector in the x direction

F_n = normal force component on blade element due to aerodynamic lift and drag

F_t = tangential force component on blade element due to lift and drag

g = acceleration due to gravity, 32.174 ft/sec^2

h = step size, in units of time, used to obtain numerical solution

I_b = moment of inertia of blade about its flap axis

I_L = moment of inertia of blade about its lag axis

I_θ = moment of inertia of blade about its pitch axis

I_n, I_s, I_y = moment of inertia of nacelle, rotor shaft and rotor hub about yaw axis

I_{yaw} = total yaw moment of inertia less blade contribution, $I_n + I_s + I_y$

$\bar{I}_1, \bar{I}_2, \bar{I}_3$ = principle moments of inertia of the blade with respect to its mass center

$k_\beta = k$ = blade hinge spring constant

$K1$ = constant used in the Gormont dynamic stall model, equations 3.17 and 3.18

L = lift force

L_s = distance from rotor hub to yaw axis, approximately equivalent to the shaft length

$M_{d\gamma}$ = damping moment on yaw column

M_{edge}=edgewise moment exerted by the blade upon the hub (by both blades for a teetering rotor)

M_{flap} = flapping moment on blade due to aerodynamic forces

M_{hub}=moment exerted by teeter dampers and springs upon the teetering hub

M_{yaw} = yaw moment contribution from aerodynamic forces on blade

M_γ = sum of aerodynamic, friction and damping moments about the yaw axis

m_b = blade mass (one blade)

R = rotor radius

R_h = rotor hub radius

$\overline{R}$ = distance from hinge to blade mass center

$\vec{r}$ = position vector

s = teetered rotor undersling as shown in Figure 3.4

Sign(x) = Signum function (+1 if x>0; -1 if x<0)

$T_s(\psi)$ = tower shadow function

t = time, blade thickness

$\vec{V}$ = velocity vector

V_∞ = free stream wind velocity at hub height

V_i = induced velocity due to air flow over blade

V_n = normal component of relative velocity to blade

V_t = tangential component of relative velocity to blade

$\overline{V}_z$ = average axial wind speed, assumed equal to mean wind speed

W = magnitude of the relative wind velocity with respect to the blade, $\sqrt{V_n^2 + V_t^2}$

X, Y, Z = inertial reference frame (origin at tower top)

X´, Y´, Z´ = yawed reference system (origin at tower top)

$\hat{X}\hat{Y}\hat{Z}$ = spinning reference system (origin at rotor center)

x, y, z = coned reference system (origin at blade hinge)

α = angle of attack

α_b = actual angle of attack used in the Gormont dynamic stall model, equation 3.17

α_{b0} = zero-lift angle of attack

α_m = effective angle of attack used in the Gormont dynamic stall model

β = flapping angle of blade

β_0 = precone angle of blade

ΔV_s = tower shadow velocity deficit fraction

δ = wind direction angle

γ = yaw angle

ψ = blade azimuth angle, defined such that $\psi = 0°$ when blade is down (six o'clock position)

ψ_0 = half-angle of tower shadow region

Ω = blade rotation rate

θ = blade pitch angle, measured from chord line to plane of rotation

ρ = air density, blade material density

τ = tilt angle of the low-speed shaft

T=teeter angle

ϕ = inflow angle of relative velocity vector, $\tan^{-1}\left(\frac{V_n}{V_t}\right)$

ω_h = natural flapping frequency of the hinged blade, $\sqrt{\frac{k_\beta}{I_b}}$

ω_n = ratio of blade natural flapping frequency to blade rotation frequency, $\sqrt{\frac{\omega_h^2}{\Omega^2}}$

Special Symbols

$\dot{(\ )}$ = derivative with respect to time

$(\ )'$ = derivative with respect to azimuth angle ψ

1.0 Introduction

Wind turbines have been found cost-effective and efficient producers of electrical power. The increase in use of wind turbines has been phenomenal in the past several years. But progress and public and private support have been hindered by technical problems. One of the more serious problems has been yaw behavior of free-yaw rotors and yaw loads on controlled-yaw rotors. It has been reported that yaw-related problems are the second-leading cause of failures in the wind farms in California [Lynette, 1988].

1.1 Background and Objectives

Designers of a horizontal axis wind turbine yaw mechanism are faced with a difficult decision. They know that if they elect to use a yaw-controlled rotor then the system will suffer increased initial cost and increased inherent maintenance and reliability problems. On the other hand, if they elect to allow the rotor to freely yaw they know they will have to account for unknown and random, though bounded, yaw rates. They will have a higher-risk design to trade-off against the potential for cost savings and reliability improvement. The risk of a free-yaw system could be minimized if methods were available for analyzing and understanding yaw behavior. But the complexity of yaw behavior has, until recently, discouraged engineers from developing a complete yaw analysis method.

The history of wind energy development is rife with accounts of yaw related problems. The most serious problems are structural failures due to excessive yaw rates or yaw loads. This problem has been highlighted by failures of a number of rigid, three-blade systems in the Altamont and San Gorgonio Pass areas of California. Structural failures have also resulted from upwind operation of a nominal downwind rotor with a flexible blade root. In this situation thrust loads can drive the blades into the tower and cause major damage. Yaw-driven systems have had many instances of excessive yaw loads damaging the yaw drive mechanism. Apparently yaw loads are generally under-predicted by current design methods. Of lesser importance is loss of energy yield due to poor yaw tracking. Many free-yaw rotors consistently operate at small (5°-15°) yaw errors and occasionally operate for extended periods at larger yaw angles. This problem can significantly impair energy yield and customer perception of the quality of the turbine.

With this motivation the following objectives were set for the current work:

> Short term (first year): *Provide a fundamental understanding of free-yaw mechanics and the design concepts most effective at eliminating yaw problems.*
>
> Longer term (five year): *Provide tested design tools and guidelines for use by free-yaw wind system manufacturers.*

The emphasis here is upon developing practical and sufficiently accurate design methods. It was desired that at the end of this research the wind turbine designer would be able to specify with confidence the yaw configuration needed to achieve benign and acceptable yaw behavior. The difficulty and complexity of the problem as well as the need to assist with near term development problems dictated the need for both a short - and long-term goal. The research described in this report has largely achieved both of these goals. A design model named YawDyn is now available for use in free-yaw and fixed-yaw analysis. It has been shown to be accurate in comparisons

with test data and other analyses. However, the model relies upon empirical methods which are not proven for the wide range of rotors and wind conditions which can be conceived.

Yaw dynamics have been investigated by a number of researchers. The most comprehensive work was done by Swift [Swift, 1981]. He developed a model which was used as the starting point for the work reported herein. He used blade-element/momentum aerodynamics and was the first wind turbine analyst to use the skewed wake effects as developed for helicopter analysis [Coleman, Feingold et al., 1945; Gaonkar and Peters, 1986; Pitt and Peters, 1981]. As will be shown later, these effects are crucial to correct estimation of aerodynamic yaw moments. He also considered induction lag, or the time delay between a change in thrust loading of a rotor and the induced velocity field of that rotor. His model uses linear aerodynamics and idealized twist and chord distributions to simplify the aerodynamics analysis.

de Vries [de Vries, 1985] discussed the inability of simple blade-element/momentum theory to adequately predict aerodynamic yaw moments on a rotor. He showed that a simple adjustment to the induced velocity field exhibited the correct qualitative influence on the moments. Swift, mentioned above, however was first to show a quantitative method based in physical principles for performing the adjustment.

Chaiyapinunt and Wilson [Chaiyapinunt and Wilson, 1983] showed that blade stiffness influences yaw motion by affecting the phase angle between an aerodynamic input such as tower shadow and the structural response. They showed that tower shadow will cause a steady yaw tracking error when rotor blades are not infinitely stiff. They also stated that blade element/momentum methods predict very small aerodynamic yaw moments on a rotor unless the rotor has preconing.

Bundas and Dugundji [Bundas and Dugundji, 1981] performed wind tunnel tests and Miller [Miller, 1979] demonstrated theoretically that upwind rotors can be stable in the free-yaw upwind configuration. Such stable upwind operation of nominal downwind rotors has also been observed by the author and others in full-scale systems operating in the natural wind.

Stoddard [Stoddard, 1978; Stoddard, 1988] has developed analytical methods for examining the aerodynamics and stability of rotors. His methods linearize the equations of motion to achieve analytic solutions which are useful for examining dominant effects and trends in yaw behavior.

1.2 Approach

The work and experience just described set the requirements for the current model. It must be capable of the following:

1) The aerodynamic model must include skewed wake effects and not rely solely upon blade-element/momentum methods.

2) Blade root flexibility must be considered in at least the flapping degree of freedom. This flexibility influences the response phase angle which in turn determines whether horizontal or vertical wind input asymmetry will cause a yaw response.

3) Both vertical and horizontal wind shear must be considered. Tower shadow must also be included.

4) Response to time-rates-of-change in wind conditions must be determined. Changes in both wind speed and wind direction must be analyzed.

5) Use of the resulting methods as design tools strongly suggests calculations and outputs in the time domain. Theoretical operations in the frequency domain offer some advantages but are more difficult to understand and less likely to instill confidence in the user.

As the research progressed it was found that this list must be expanded to include the following:

6) Dynamic stall or stall hysteresis has a dramatic effect on yaw loads. Hysteresis in the airfoil characteristics contributes greatly to asymmetry which increases yaw loads.

7) A vertical component of the wind vector approaching the rotor will place a blade at the three o'clock or nine o'clock position in an advancing or retreating flow. This asymmetry will also contribute to yaw loads.

8) Similarly, tilt of the rotor axis will contribute to yaw loads. This results from the advancing and retreating blade loads and the component of the low-speed shaft torque in the yaw direction.

9) Yaw-drive-train stiffness of a controlled yaw system can amplify or attenuate yaw loads depending upon the natural frequencies of the yaw drive and the rotor.

These requirements are imposed by the need to incorporate the essential physical mechanisms of the problem. Another requirement is imposed by the need to achieve practical, understandable and cost-effective solutions: The need for the simplest model possible. The philosophy of the development effort then has been to model each of the effects listed above in the simplest possible manner.

For example, the blade flexibility is modelled using an ideal root hinge/spring with a rigid blade. This permits the essential flap motion but avoids the details of modelling the actual mode shapes. As another example, the skewed wake induced velocity correction is a simple linear adjustment across the rotor disc. This adjustment permits the physical effect to be modelled without the confusion of higher order corrections. For a final example, the horizontal wind shear is modelled as linear shear. This is obviously an oversimplification of wind shear and large scale turbulence effects, but it permits investigation of the importance of wind shear.

Of course, a theoretical model cannot be depended upon until it has been thoroughly tested against turbine operating experience and other models. This is particularly true of models in the form of complex computer codes. It should not be surprising that more time has been devoted to testing the YawDyn code than to creating it. This report will present results from the comparison of prediction with wind-tunnel tests of a 1/20 scale, rigid rotor, Mod-2 and the full-scale SERI Combined Experiment rotor. Such comparisons between actual turbine response and predicted response are the ultimate and necessary test of the physical validity of the model. However, the method of solution and details of the model algorithms are more readily tested through comparison amongst theoretical models. Thus some validation of the method has been accomplished via comparisons with the SERI FLAP code [Wright, Buhl et al., 1987; Wright, Thresher et al., 1991].

The remainder of this report is organized as follows: Section 2 will present a general discussion of the various sources of yaw loads. It is written as a qualitative description and avoids details and equations in the interest of providing an overview. Section 3 presents the governing equations of motion. The equations are derived in Appendices that can be skipped by the reader without loss of continuity. The governing equations are derived in their general form and then simplified to the forms which are available as options in YawDyn. Section 4 briefly discusses the numerical method of solution of the equations and the structure of the computer program. Section 5 presents results of sample calculations and comparisons with test data and other models for purposes of validation. Section 6 discusses the sensitivity of predicted yaw response to a variety of wind and turbine conditions. Section 7 provides conclusions and recommendations for additional research. Appendices also provide a listing and User's Guide to YawDyn as well as the equations of motion mentioned earlier.

2.0 General Introduction to Yaw Loads

2.1 Introduction

This section is an introduction to the causes of wind turbine yaw loads and motions. It is intended to help the reader understand the fundamental mechanisms of yaw dynamics without becoming mired in the details and equations. The section concentrates on a qualitative discussion and is written for the engineer experienced in the analysis, design and terminology of wind turbine loads and dynamic response. Quantitative details are provided in later sections.

The focus of the discussion is the effect of the rotor on the yaw loads. Both rigid and teetering-hub rotors will be discussed. Though other factors may influence yaw, such as aerodynamic loads on the nacelle or a tail vane, or tower-top lateral vibration or tilt, they will not be discussed in this introduction. Emphasis is placed on the important factors influencing yaw. As mentioned, the discussion will be qualitative, with a minimum of equations or numerical results.

The discussion will begin with a description of how the blade root loads influence yaw loads. It will be seen that blade root flapping moments are the dominant cause of yaw loads for many wind turbines. Next a variety of wind conditions which can influence those root flapping moments will be described. Forces acting on the hub can also play a role in determining yaw loads. For a teetering rotor these forces are the dominant cause of yaw because the root flap moments have no load path into the rotor (or low-speed) shaft. After a description of these hub forces, some inertial effects are described which can, in a mildly imbalanced system, be a very important source of undesirable yaw loads. Most of the above discussion will be for rigid hubs. A description will be given of the differences which result when a teetering rotor is used. These differences are very important. The report will conclude with the aforementioned references to where additional information can be found.

2.2 Hub forces and moments of a single blade

Figure 2.1 shows a simplified sketch of a downwind wind turbine with the blades removed. The forces and moments that one of the blades applies to the hub are shown. A coordinate system and two dimensions are also shown for use in the paragraphs that follow. The yaw moment is the moment about the tower longitudinal axis (parallel to the X axis). The sign convention in this report uses the right hand rule to define directions of positive moments and angles. Thus a positive yaw moment is one which would cause a clockwise rotation of the nacelle when viewed from above, looking down. The rotor rotates about the positive Z axis (clockwise when looking downwind).

The hub radius (R_h), for purposes of this discussion, is the point at which the blade root flange is located. If there is no root flange it is the point at which the blade spar attaches to the hub, usually with some rapid change in the flapping stiffness. The yaw axis offset (L_S) is the horizontal distance from the yaw axis to the vertex of the cone of revolution created by the undeflected, rotating blades (the center of the hub).

Concentrate for now on the effect of a single blade. Each of the three forces and the moment shown in Figure 2.1 can cause a yaw moment during some portion of a revolution of the blade. The flap moment (more properly called the out-of-plane bending moment for this discussion) has a component in the yaw direction except when

the blade is vertical. Thus one contribution to the yaw moment will be the flap moment times the sine of the blade azimuth angle ψ (defined such that azimuth is zero when the blade is pointed downward, in the six o'clock position). It is important to note this portion of the yaw moment is independent of the rotor offset from the yaw axis and of the hub radius.

The blade pitching and lead-lag root moments are generally unimportant when considering yaw loads. The blade pitching moment certainly contributes to the total yaw moment. But the magnitude of this moment is usually very small compared with other loads, and it is ignored. The lead-lag (or in-plane) moment will not contribute to the yaw moment if the rotor axis is horizontal. However, if the rotor axis is tilted (many wind turbines use a few degrees of tilt) then the lead-lag moment will contribute. In that case the vertical component of the low-speed shaft torque will be a contributor to the yaw moment.

Each of the three hub forces can be important sources of yaw loads. The out-of-plane (O-P) force can act through the hub radius moment arm to cause a yaw load. This yaw moment depends upon the horizontal component of hub radius as shown in the equation in Figure 2.1. The in-plane (I-P) force has a horizontal component which acts through the moment arm L_S to create a yaw moment. Typically the moment arm for the I-P force is greater than that for the O-P force. Finally, the horizontal component of the tension force acts through the moment arm L_S to add a fourth term to the yaw moment equation. This blade root tension is generally a combination of centrifugal and gravity forces rather than aerodynamic forces. One can easily imagine that if the rotor had only one blade, and no counterbalance mass, the yaw moment caused by the mass imbalance would be extreme. Of course, with two or three blades the yaw moment will be a result of the imbalance in the masses and centers of gravity of the blades. This portion of the moment is directly proportional to L_S. Thus, if the designers wish to minimize the adverse effects of mass imbalance in the rotor, they should minimize L_S.

Recent research has shown that the flap moment term is the dominant source of yaw moments for well-balanced rigid rotor systems. In fact, it has been shown for at least two machines (a Howden 330 and the SERI Combined Experiment) that the yaw moment can be determined to a high degree of accuracy by simply performing vector addition of the contributions from the root flap moment of each of the three blades. This means that for these rotors the flap moment is so dominant that the yaw moment from the three hub forces can be neglected. This is quite remarkable, and in many ways fortunate (at least for the analyst). It means that the distance L_S is not directly a factor in determining the yaw moment. This is counter-intuitive, but of great importance to the designer of the rigid rotor.

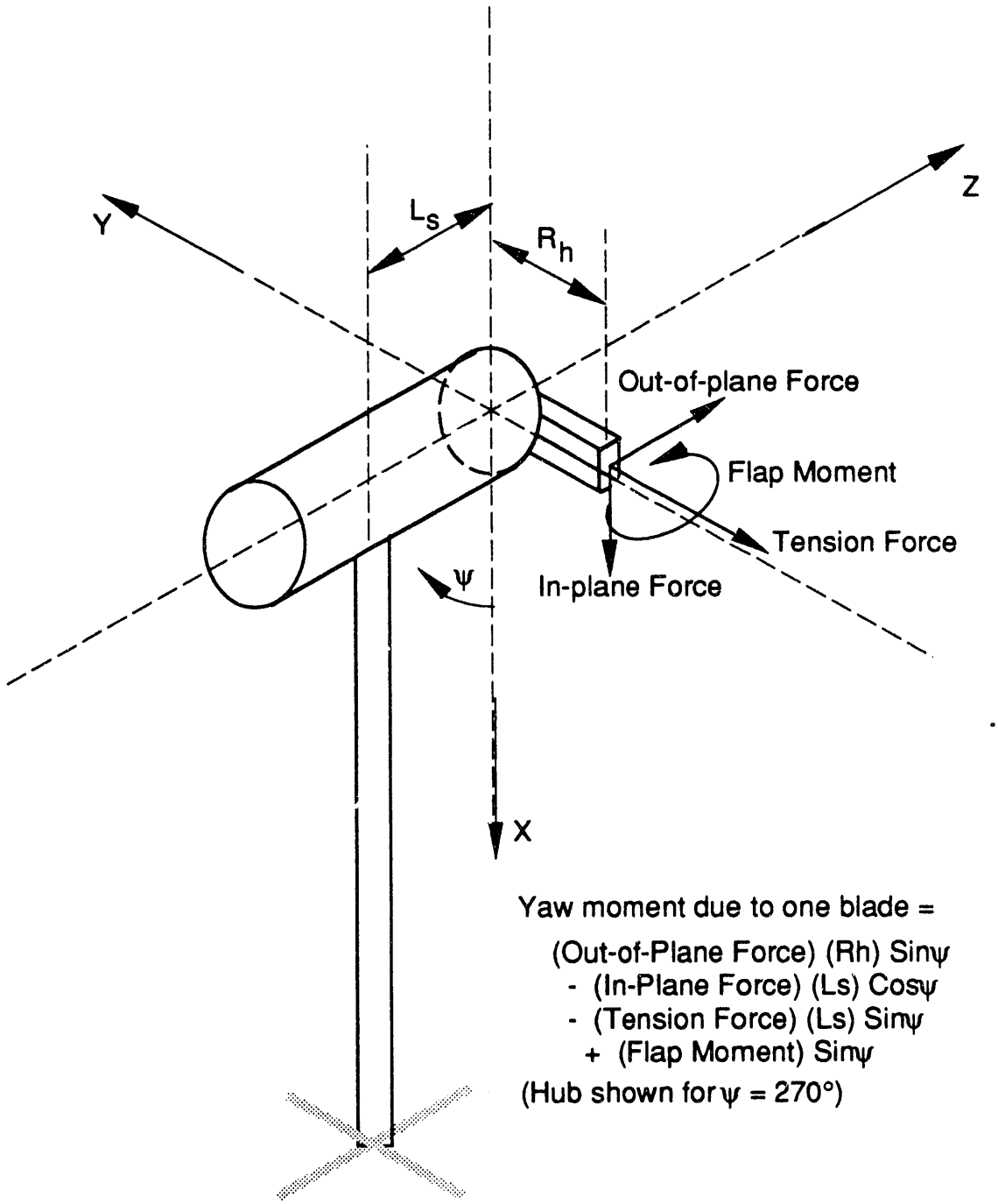

Figure 2.1. Schematic view of the wind turbine showing the forces exerted by one blade upon the hub.

2.3 Hub forces and moments from multiple blades

The system yaw loads are simply due to the contributions from each of the individual blade loads. This is easiest to visualize for a two-bladed rotor but is equally true for any number of blades. Imagine for a moment a perfectly balanced and matched set of blades on a two-bladed rotor. If the rotor axis is perfectly aligned with a perfectly uniform wind, then the loads on each of the blades will be identical and independent of blade azimuth. In this ideal case there will be no yaw moment. Any disturbance, whether aerodynamic or inertial, will upset this balance and cause some yaw load.

When there is a disturbance the yaw loads will depend, generally in some complicated manner, upon differences in the loading on each of the blades. That is, the yaw loads depend upon differences in blade loads (or a vector sum) rather than an algebraic sum of the loads. Quite often the yaw loads result from small differences in large flap moments. On the SERI Combined Experiment rotor it is not uncommon to have mean flap moments of the order of 1000 ft-lbs while the mean yaw moments are of the order of 100 ft-lbs. This complicates the understanding of yaw behavior because relatively small disturbances can create large differences in yaw loads.

Aerodynamic loads on blades of a high tip speed ratio rotor vary primarily as a result of variations in the angle of attack of the blade. Though the magnitude of the relative wind vector does change with changing wind conditions, most rotors operate such that the changes in angle of attack are more important to the loading than are changes in dynamic pressure. Thus to understand difference in aerodynamic loads on the two blades of a simple rotor it is necessary to look at the differences in angle of attack profiles along the two blades. The wide variety of wind disturbances which can cause yaw moments will be detailed in later sections. For now it is more useful to concentrate on the concept that differences in angle of attack on one blade compared with other blades will cause an imbalance of the forces and moments acting on the hub. This imbalance will in turn cause a yaw moment.

The time history of the disturbance will clearly affect the time history of the yaw load. If a disturbance repeats once per revolution of the blade (a frequency of 1p) then the result will be a steady (mean) yaw moment. For example, if every blade sees an increase in aerodynamic loading when it is at 9 o'clock and a decrease when it is at 3 o'clock then the disturbance to the blade will occur at 1p. But the system will see this disturbance as a steady load attempting to yaw the blade at 9 o'clock downwind. It is less clear intuitively but can easily be shown mathematically that the rotor will also see a 2p disturbance. This is the well-known shift of $\pm$1p as one transfers loads from the rotating (blade) reference frame to the stationary (nacelle) reference frame. That is, a 1p disturbance on the blade is seen as a 0p (mean) and 2p disturbance at the yaw axis.

The number of blades on the rotor will determine which of the harmonics of an aerodynamic disturbance will be felt and which will be cancelled as loads are summed at the hub. An n-bladed rotor will experience mean yaw loads and cyclic yaw loads at multiples of np. Thus a two-bladed rotor will have yaw loads at 0p, 2p, 4p,... and a three-bladed rotor will have yaw loads at 0p, 3p, 6p, ... The kp yaw load harmonic will result from (k+1)p and (k-1)p blade loads. If a 3p yaw moment harmonic is observed on the rotor it will have resulted from either 2p or 4p blade loads. The mean yaw moment is always caused by 1p blade loads. If 1p yaw moments are observed then there is a mass or pitch imbalance such that the blades are not all experiencing the same load history.

In the remaining discussion the examples will all use a two-bladed rotor. This is done for ease in visualizing the load summation and for direct applicability to the teetering rotor. However, all principles discussed using the two-bladed rotor examples will apply as well to the three-bladed rotor (with the appropriate changes in frequencies as noted above). The three-bladed rotor requires greater care in computing the vector summation of hub loads. But otherwise all of the discussion and operations are unchanged by the number of blades.

2.4 Stall hysteresis and dynamic stall

Stall hysteresis or dynamic stall has been shown to be very important in the determination of yaw behavior. Stall hysteresis is a dynamic effect which occurs on airfoils if the angle of attack of the airfoil changes more rapidly than the air flow around the blade can adjust. The result is airfoil lift and drag coefficients which depend not only on the instantaneous angle of attack (the usual quasi-steady aerodynamics assumption) but also on the recent angle of attack history. In particular, the lift and drag of the airfoil depend upon the angle of attack and the time rate of change of angle of attack.

Figure 2.2 shows estimated lift coefficients for the SERI Combined Experiment rotor when the rotor is yawed. The conditions for these calculations were: wind speed 30 ft/s, 30° yaw error, no wind shear or tower shadow. These values were generated using the YawDyn computer program, but test data show similar behavior. The top plot shows the characteristic 1p variation in angle of attack as the blade completes one revolution. The middle plot shows the lift coefficient with a large hysteresis loop which is typical of stall hysteresis or dynamic stall. The polar plot shows the C_L variation vs. blade azimuth.

Though the dynamic stall phenomenon has long been known for helicopter rotors, it has been only recently that the existence and importance of dynamic stall has been demonstrated for wind turbines. Fortunately, we now have test data and simple theoretical models to help us understand unsteady aerodynamic effects.

The importance of dynamic stall to the yaw loads can be illustrated qualitatively with a simple comparison. Compare the lift coefficient of Figure 2.2 when the blade azimuth is between 180° and 360° with the C_L when the blade is between 0° and 180°. The average lift of the former is much greater than the latter. This imbalance of the lift from one side of the rotor to the other causes a yaw moment which is much larger than the load that would be seen if the hysteresis were not present in the lift coefficient. Without stall hysteresis the C_L curve of Figure 2.2 would travel up and down along the top half of the loop shown. This shows that if the blade angle of attack varies around the revolution then the presence of stall hysteresis will exaggerate the imbalance of blade forces from one side of the rotor to the other. This enhanced imbalance will result in an increased yaw load over that which would be experienced without stall hysteresis. The reasons for cyclic variations in angle of attack will be discussed in the sections that follow.

2.5 Wind disturbances which cause yaw loads

Cross-wind (or yaw angle): The best known cause of yaw motion or loads is misalignment of the approaching mean wind vector with the rotor axis. With such a cross flow there will typically (though not always) be a yaw moment acting in an attempt to realign the rotor with the wind direction. Though the existence of such a yaw moment is intuitively apparent, it is less clear what the actual mechanism or cause of the moment might be. Figure 2.3 illustrates the situation and the mechanism which causes the yaw moment. With a cross-flow in the positive Y direction a blade which is passing through the twelve o'clock (ψ = 180°) position will be advancing into the crosswind. As shown in the figure, this will result in a decrease in the angle of attack at any given blade section. The blade will experience an increased angle of attack as it retreats from the crosswind when it is at the six o'clock position (ψ = 0°). This situation is identical to that calculated in Figure 2.2. This means the blade experiences

a once-per-revolution (1p) oscillation in angle of attack when the rotor operates at a yaw angle (in the absence of other disturbances).

Figure 2.2 shows that the average C_L is highest for blade positions between 180° and 360°. A blade which is not perfectly rigid will have a phase lag between the time the maximum aerodynamic load is applied and the time of maximum response (which is the time the blade root load is maximum). The amount of phase lag depends upon the stiffness and aerodynamic or mechanical damping of the blade. There is zero lag for an infinitely stiff blade and 90° lag for a very soft blade. This means the maximum root flap moment occurs for a blade angle between 180° and 360°, just after the peak C_L is observed. At the time one blade sees the maximum root moment, the opposite blade sees the minimum moment. This is when the yaw moment due to the difference in root flap moments peaks.

The in-plane (edgewise) forces on the two blades also reach their maximum difference at this same blade angle. The net result is a yaw moment which would be in the negative X direction for the situation of Figure 2.2. If allowed to yaw under the influence of this yaw moment the rotor would tend to align with the wind direction.

Vertical wind or rotor tilt: A vertical wind through the rotor has much the same effect as a horizontal crosswind, with one important difference. Vertical wind causes the blade to be advancing or retreating when it is horizontal. This is the time at which an increased load will feed directly into a yaw moment, so long as the phase lag due to blade structural softness is not large. The concept is illustrated in Figure 2.4. This means that, all else equal on a rigid rotor, a vertical wind will create a higher yaw moment than a horizontal component of crosswind of the same magnitude. Fortunately, vertical winds tend to be much smaller than crosswinds. It would be unusual to have the approaching wind vector tilt 30°, while it is not uncommon at all to have a yaw error of the same magnitude.

Tilt of the rotor shaft has the same effect on the rotor aerodynamics as tilt of the approaching wind vector. Thus shaft tilt can be used to create a yaw moment beyond that mentioned earlier, namely the vertical component of the low-speed shaft torque.

Vertical shear of the approach wind: Vertical shear is the variation in approaching wind speed from the top to the bottom of the rotor. It is usually a result of the rotor being fully immersed in the planetary boundary layer, but vertical shear can also result from upwind obstructions such as other wind turbines or the wake of the tower of the rotor in question. Vertical shear causes a cyclic, 1p, variation in angle of attack. In the typical case the wind at the top of the rotor, and hence the angle of attack and blade load, is higher than when the blade is pointed down. This imbalance of load from the top to the bottom of the rotor will not cause a large yaw moment unless there is a significant phase shift in the blade response (due to structural "softness").

Dynamic stall can increase the importance of vertical wind shear. If the wind speed is high enough that vertical shear causes the rotor to move in and out of stall, then the hysteresis in the C_L curve can result in variations in blade root loads when the blades are horizontal. This is the fundamental requirement to generate an appreciable yaw load.

In summary, for rigid rotors vertical shear is not usually a major source of yaw loads. This is not the case for horizontal shear, the subject of the next section.

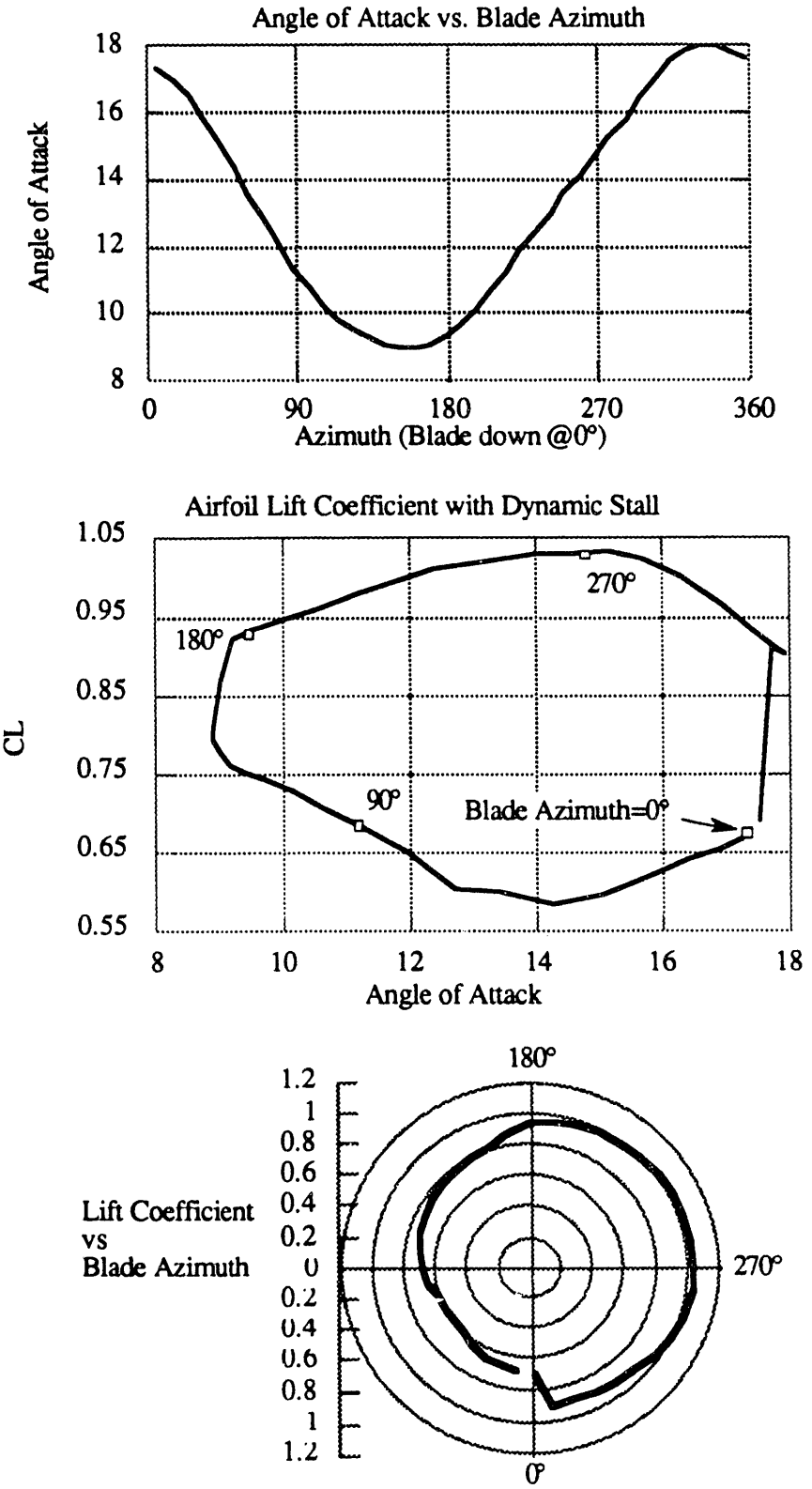

Figure 2.2. Stall hysteresis at the 75% station of the SERI Combined Experiment as calculated by YawDyn. Wind speed 30 ft/s, yaw angle 30°, no wind shear or tower shadow.

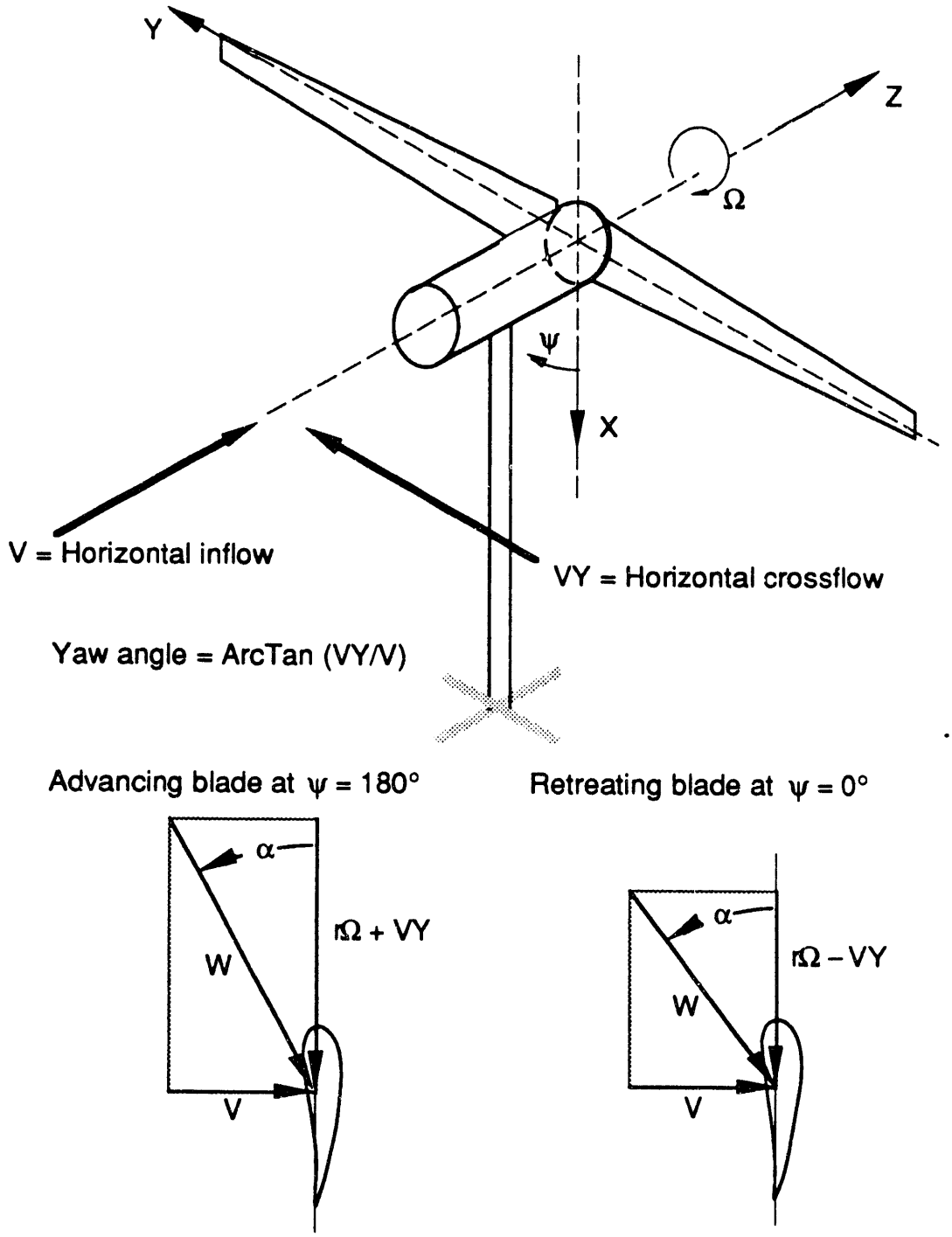

Positive horizontal crossflow (VY) decreases the angle of attack on the blade at 180° azimuth. This decreased aerodynamic load causes little yaw moment unless there is a phase lag in the blade flap response (a soft blade) or stall effects such as stall hysteresis

Figure 2.3. Angle of attack of blades at two azimuth positions when the rotor operates with a yaw error.

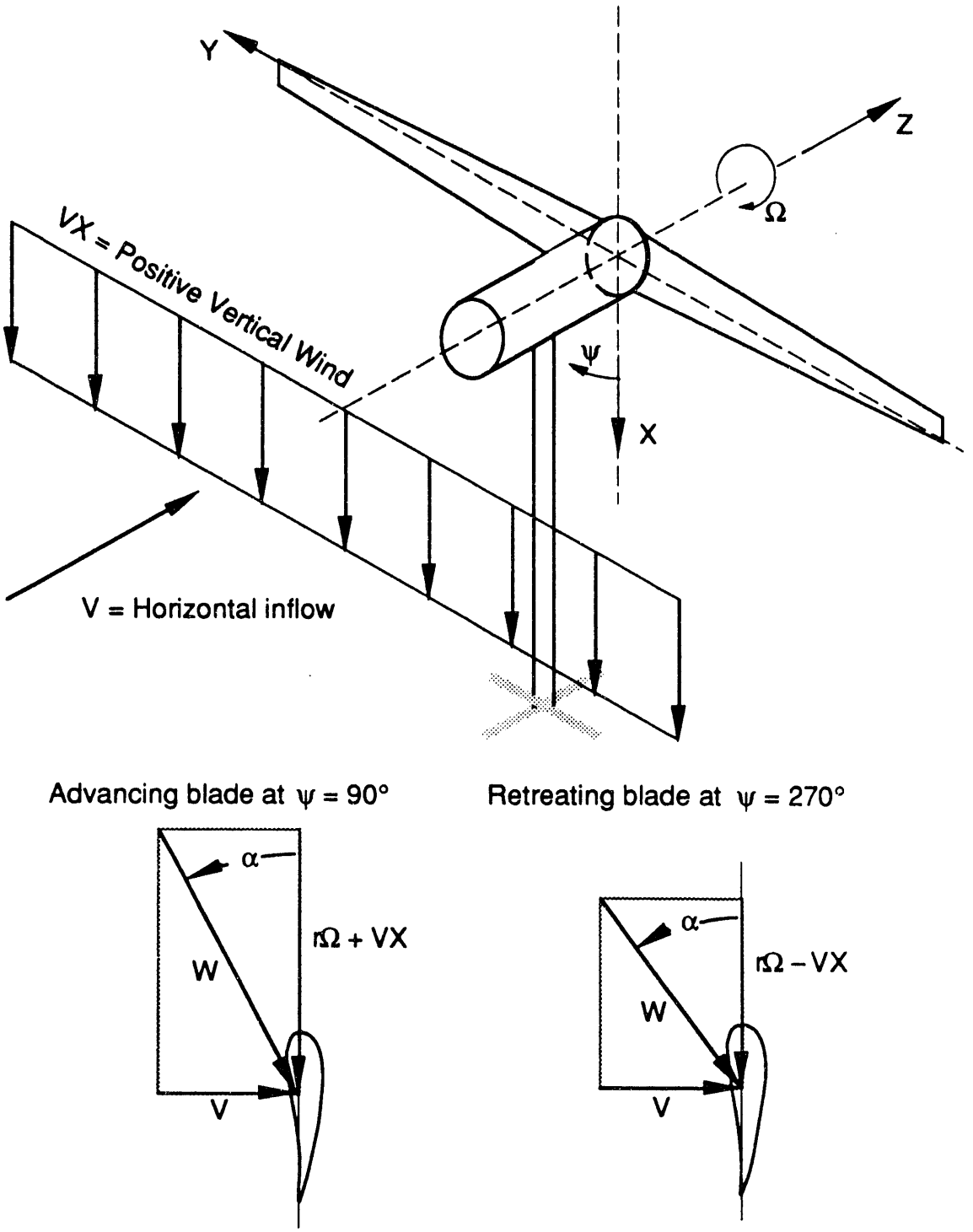

Positive (downward) vertical velocity decreases the angle of attack on the blade at 90° azimuth. This decreased aerodynamic load causes a negative (-X direction) yaw moment

Figure 2.4. Effect of vertical wind component on the angles of attack.

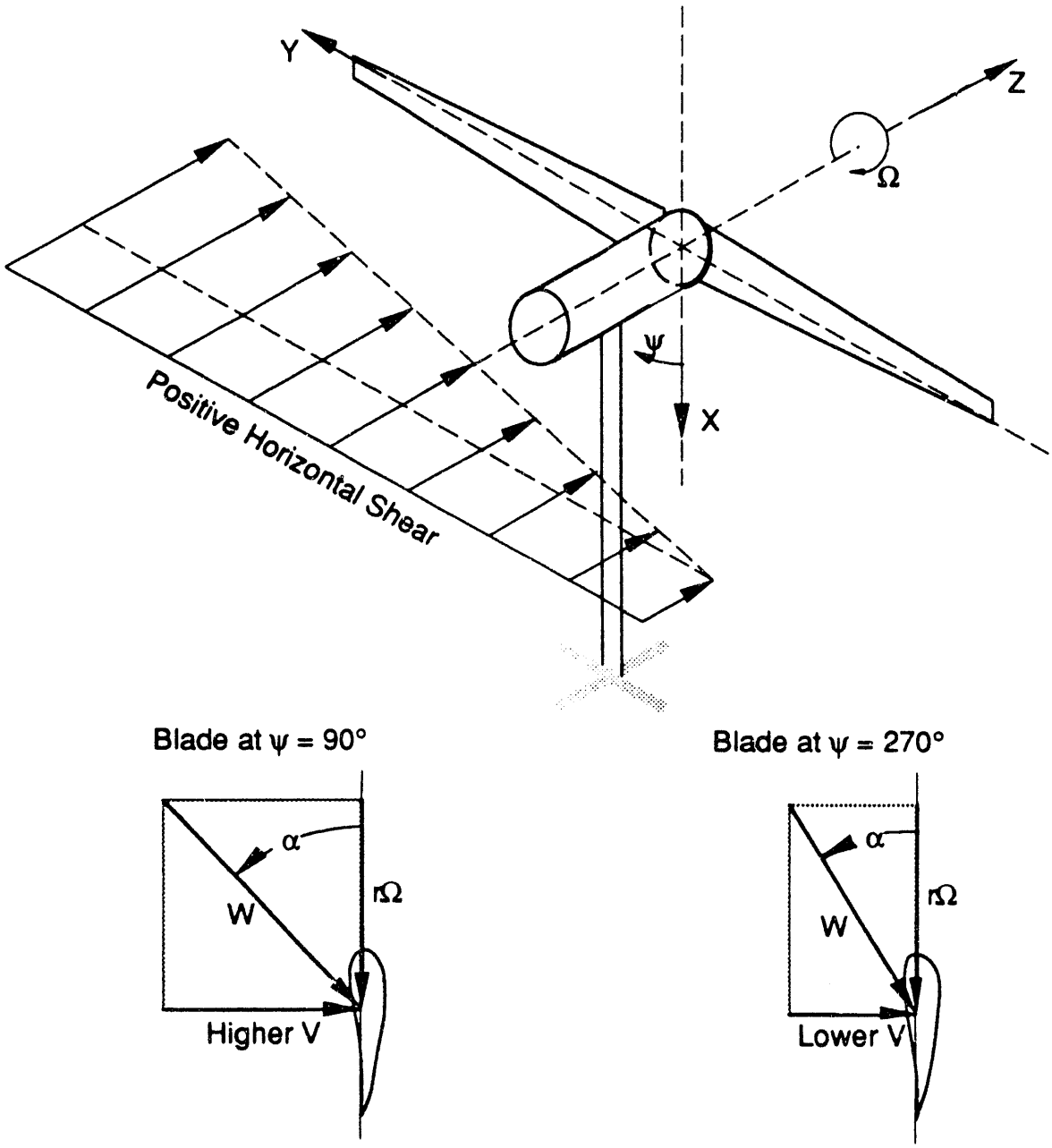

Positive horizontal shear increases the angle of attack on the blade at 90° azimuth. This increased aerodynamic load causes a positive (+X direction) yaw moment

Figure 2.5. Effect of horizontal wind shear on the angles of attack.

Horizontal shear of the approaching wind: Upwind obstructions such as other wind turbines or complex terrain can create strong, persistent variations in wind speed from one side of a rotor disc to the other. This horizontal shear of the wind speed also occurs in short , random periods as a result of turbulence. Horizontal shear has an effect much like vertical shear with one very important difference. Horizontal shear causes a maximum difference in blade flap loads when the blades are horizontal. Thus it acts when the blade is positioned to generate a yaw moment (if the rotor is rigid). This is illustrated in Figure 2.5.

Measurements on a US Windpower rotor and the SERI Combined Experiment have shown that horizontal shear is usually the leading cause of yaw loads for these rigid-rotor machines.

Turbulence: Turbulence is nothing more than a composite of all of the above wind conditions which is varying randomly in time. Thus at any instant the rotor is subjected to wind components in vertical, longitudinal and lateral directions. The wind speeds also vary across the rotor disk in an irregular manner. Turbulence changes the understanding of yaw mechanisms very little. Unfortunately, turbulence does add complexity to the interpretation of test data and the prediction of yaw behavior. These subjects are outside the scope of this introductory discussion and will not be pursued further.

2.6 Other causes of yaw loads

An ideal rotor is subjected to the sources of yaw loads discussed above. A real rotor is also subjected to other sources, and these sources can often dominate the cyclic yaw moment history of a rotor. Mass, center of gravity and pitch differences among the blades of a rotor are the sources of greatest interest.

Mass imbalance: If the blades of a rotor are not perfectly matched then centrifugal forces will cause a 1p yaw moment. This can best be seen by picturing the effect of a mass imbalance as an offset of the c.g. of the rotor from the rotor axis. The centrifugal force at the mass center will be an in-plane force which rotates at the rotor speed. The resulting 1p yaw moment will be directly proportional to the mass offset, the distance L_S, and the square of the rotor speed.

Recent experiments at SERI showed that the mass imbalance was the the largest source of cyclic yaw moments on the Combined Experiment, even though considerable care was taken to add mass to the blades to achieve near balance. One organization in the San Gorgonio area has started offering a rotor balancing service. Apparently the rates of failures of the yaw drives have decreased on those systems which have been carefully mass balanced in the field. The message is clear: Great care should be taken in balancing the rotor in its operating configuration. Cyclic yaw loads are very sensitive to mass imbalance.

Pitch imbalance: If 1p yaw motion or loads are observed on a rotor which is carefully mass balanced, the likely cause is an aerodynamic imbalance. Differences in blade pitch or twist distribution are the common cause of aerodynamic imbalance. If one blade is set at a different pitch angle than the other, then a cyclic yaw load will be generated at the rotor speed. An aerodynamics analysis code such as PROP can be used to estimate the change in flap moment which is caused by an incremental change in pitch. This will be the amplitude of the cyclic yaw moment which results. Typically, blade pitch angles should be set to match within much less than one degree if aerodynamic imbalance is to be avoided.

Cyclic pitch: Another source of yaw loads which results from imperfect construction of the rotor is cyclic pitch. A rotor with pitch controls or a teetering rotor with pitch/flap coupling (delta-three) may have unplanned cyclic variations in blade pitch. If there is some play in the mechanical pitch linkage or torsional flexibility in the pitch control system, then cyclic variations in blade loads can cause variations in blade pitch. On the helicopter, cyclic blade pitch is used to control the direction of flight. The cyclic pitch causes a mean yaw moment (in wind turbine terminology) on the rotor which rotates the tip-path plane and hence the helicopter. The same thing can occur on the wind turbine if gravity or aerodynamic forces can cause changes in pitch angle.

The teetering rotor with pitch/flap coupling may experience cyclic pitch resulting from teeter motion. This may be acceptable or even desirable in normal operation, but it can cause problems when a rotor is starting or stopping and there is little centrifugal stiffening or aerodynamic damping.

2.7 Yaw dynamics of the teetering rotor

The above discussion of yaw behavior has concentrated on the rigid rotor. When a teetering rotor is of interest there is a very important change in the behavior. Unless the teetering rotor strikes the teeter stops (or dampers and/or springs), it has no load path to carry the blade root flap moments into the low-speed shaft or the yaw system. Recall that the root flap loads are the dominant cause of yaw loads of the rigid rotor. Thus, the dominant cause of yaw has been eliminated by the teetering rotor. This means that yaw loads and/or yaw rates will generally be lower for the teetering rotor. Of course, a teeter stop impact can transmit a large bending moment into the shaft and this in turn will cause a large yaw load if the blade is not vertical at the time of impact.

If root flap moments can no longer be important to the yaw behavior, then the rotor forces will become the dominant cause of yaw. Rotor forces fluctuate as a result of changes in angle of attack as discussed at length above. To interpret the effect of a given wind input, evaluate its effect on the angle of attack (and blade force) and determine where in its rotation the blade will be most affected. Thus the basic discussion is still applicable, but one must exercise care in interpreting the relative importance of the different inputs to the rotor. For example, the distance L_S will become more important, because yaw moments will be directly proportional to the hub-yaw axis offset. This is quite different from the situation where flap moments dominate and make L_S relatively unimportant.

The sections that follow in this report quantify this discussion and present a computer model which makes it possible to explore these phenomena in detail for a variety of rotor configurations.

3.0 Theoretical Foundation

3.1 Prediction of Yaw Dynamics

Modeling of yaw dynamics is complicated by the variety of machine and wind characteristics which are important to yaw response. The goal of the current modeling is to develop the simplest model possible while not neglecting significant effects. Previous research indicated the following features must be included in the model:

- Blade root flexibility and flap motion
- Aerodynamic model must include stall effects
- Correction for effects of skewed wake aerodynamics on the induced velocities
- Vertical and horizontal wind shear and tower shadow
- Mechanical yaw damping and friction
- Arbitrarily large yaw angles but small flap angles
- Both free- and fixed-yaw behavior

During the course of this research additional factors were found to be important:

- Dynamic stall
- Vertical component of wind speed
- Stiffness of the yaw restraint of a "fixed" yaw rotor
- Tilt of the low speed shaft

These effects and features are implemented in the current models. The result is a set of equations for yaw and flap motion in the time domain. Simple blade element/momentum aerodynamics are used but corrections are made that account for the interdependence of induced velocities at neighboring blade elements when the wake is skewed with respect to the rotor. Two-dimensional airfoil tables are used to represent the blade lift and drag coefficients and the NASA synthesization method is used to obtain static airfoil characteristics in deep stall [Viterna and Corrigan, 1981]. The Gormont model is used to represent stall hysteresis. The contributions to the yaw moment of all blade flap and lead-lag forces and moments are included in the calculations. Thus the "H" force of helicopter terminology is included (though the lead-lag vibratory degree of freedom is not considered).

Some details of the model are presented in the paragraphs that follow. Appendix A contains a derivation and discussion of the equations of motion which are presented below. The algebraic manipulations required for the derivations were all performed using the Mathematica® symbolic manipulation program [Wolfram, 1991]. Appendix A contains the Mathematica files used in the derivations.

HAWT Representation

A simplified model for a two blade HAWT is shown schematically in Figure 3.1. Only yaw motion, γ, and blade flapping motion, β, have been used in the development of the equations of motion. A teetering degree-of-freedom can be substituted for the flap motion. When teetering is modeled, the blade is completely rigid. Additional degrees of freedom, such as blade pitch and lag motion, are not considered to be as important to yaw response and have been ignored.

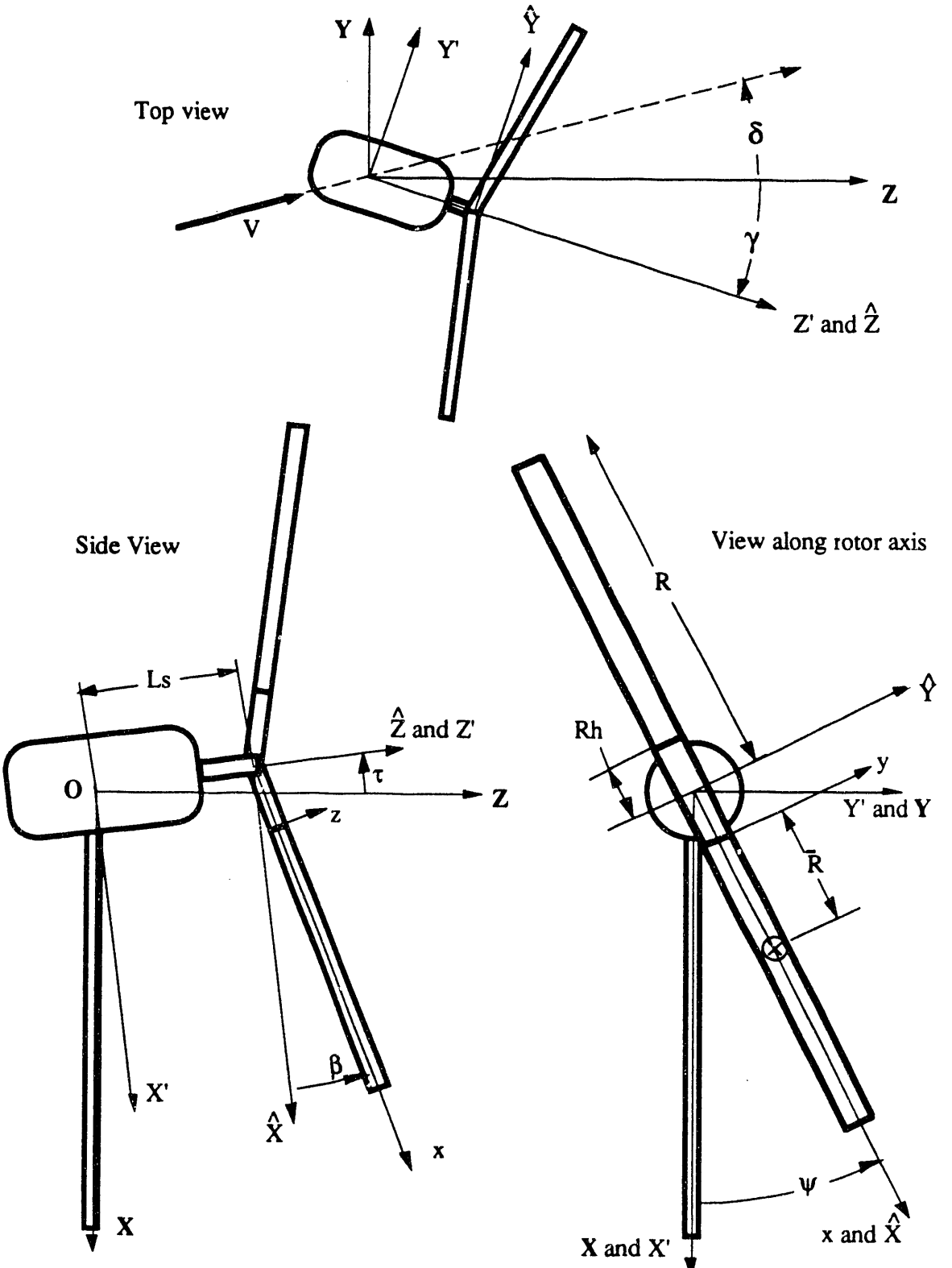

Figure 3.1 Schematic of the rotor showing the primary blade variables. The view on the right is looking into the wind.

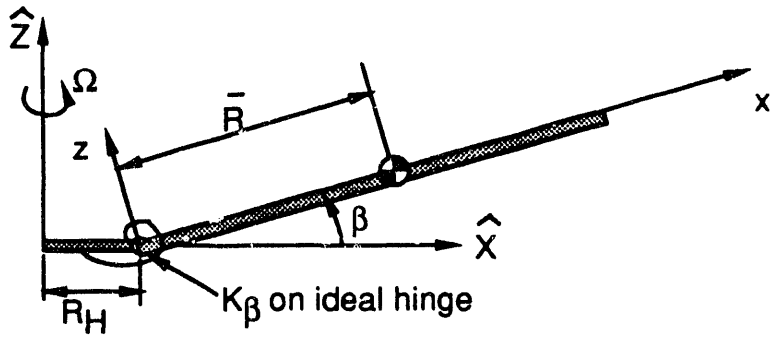

Figure 3.2 Hinged blade with torsional spring

A rigid tower (no top deflection or rotation) is used in the model. This permits the inertial reference frame **XYZ** to be located with its origin (point **O** in Figure 3.1) at the intersection of the yaw column and the rotor shaft. $X'Y'Z'$, $\hat{X}\hat{Y}\hat{Z}$ and xyz designate the nacelle, rotor (hub) and blade reference frames used in developing the equations of motion. The distance from yaw axis to the rotor, the approximate shaft length, is designated by L_s.

The rotor shaft is tilted at angle τ above the horizontal. (All angles in Figure 3.1 are shown in their positive sense.) The flap angle β is measured with respect to the plane perpendicular to the axis of rotation. When the rotor is teetered then the flap angles of the two blades are related by the simple equation:

$$\beta_2 = 2\beta_0 - \beta_1 \tag{3.1}$$

Here β_0 is the precone angle and β_i is the flap angle of blade i.

The rotor rotation rate, Ω, is considered to be constant for each specified operating condition. The blade azimuth position, ψ, is defined with respect to the six o'clock position of the rotor disk. This azimuth angle will be used to describe the positions of all the rotor blades.

The nacelle, rotor shaft and blades are treated as rigid bodies. The blades are connected to the rotor hub by frictionless hinges which permit only out-of-plane flapping motion. Torsional springs with stiffness k_β are attached as shown in Figure 3.2. This models the elastic deflections of each wind turbine blade. Typically the spring stiffness, k_β, is selected to match the flap natural frequency to the first flap bending mode of the actual blade.

The blade flap angle is a function of the instantaneous wind velocity as seen by the blade as it rotates about the shaft. This will cause the i^{th} blade to assume its own motion, described by β_i, independent of each other blade. This gives the model B + 1 degrees of freedom where B is the number of blades. There is one exception to this general statement. If the teetering rotor is modeled then the blades do not flap independently and the model has only one flap degree of freedom and the yaw degree of freedom.

The governing equations were derived from Euler's equation and the more general equations of three-dimensional, rigid body motion. The resulting equation for the flap motion is:

$$\beta'' = -\beta - \frac{k}{I_b\Omega^2}(\beta-\beta_0) + \frac{M_{flap}}{I_b\Omega^2} - \beta\frac{m_b\bar{R}R_h}{I_b} - \frac{m_b g\bar{R}}{I_b\Omega^2}(\tau+\beta\cos\psi)$$
$$-2\gamma'\cos\psi\left[1+\frac{m_b\bar{R}R_h}{I_b}\right]$$
$$+\gamma'^2\left[\frac{m_bL_s\bar{R}}{I_b}+\tau\cos\psi\left(1+\frac{m_b\bar{R}R_h}{I_b}\right)+\beta\left(\cos^2\psi-\frac{m_b\bar{R}R_h}{I_b}\sin^2\psi\right)\right]$$
$$-\gamma''\sin\psi\left[1+\frac{m_b\bar{R}R_h}{I_b}+\frac{m_bL_s\bar{R}}{I_b}\beta\right] \qquad (3.2)$$

The equation for yaw angle is (when the flap degree of freedom is included) is:

$$\gamma''\left[\begin{array}{l} I_{yaw} + Bm_bL_s^2 + m_b\bar{R}L_s\sum_{i=1}^{B}\beta_i\left(1+\cos^2\psi_i\right) \\ -\frac{m_b^2\bar{R}^2R_h}{I_b}\left(L_s\sum_{i=1}^{B}\beta_i\sin^2\psi_i + R_h\sum_{i=1}^{B}\sin^2\psi_i\right) + m_bR_h^2\sum_{i=1}^{B}\sin^2\psi_i \end{array}\right] =$$

$$-\frac{1}{\Omega^2}\sum_{i=1}^{B}M_{edge_i}\left(\tau+\beta_i\cos\psi_i\right) + \frac{m_b\bar{R}R_h}{I_b\Omega^2}\sum_{i=1}^{B}M_{flap_i}\sin\psi_i$$

$$+\frac{1}{\Omega^2}\sum_{i=1}^{B}\left(L_s\beta_i + R_h\right)F_{N_i}\sin\psi_i - \frac{1}{\Omega^2}\sum_{i=1}^{B}\left(L_sF_{T_i}\cos\psi_i + R_h\tau F_{T_i}\right)$$

$$+\left(m_b\bar{R}R_h + \frac{k}{\Omega^2}\right)\left(1+\frac{m_b\bar{R}R_h}{I_b}\right)\sum_{i=1}^{B}\beta_i\sin\psi_i$$

$$+\frac{m_bg\bar{R}}{\Omega^2}\left(1+\frac{m_b\bar{R}R_h}{I_b}\right)\sum_{i=1}^{B}\beta_i\cos\psi_i\sin\psi_i$$

$$-2\gamma'\left[m_bR_h^2\left(1-\frac{m_b\bar{R}^2}{\Omega^2}\right)\sum_{i=1}^{B}\cos\psi_i\sin\psi_i + m_bL_s\bar{R}\sum_{i=1}^{B}\beta_i'\right]$$

$$+\gamma'^2\left[\begin{array}{l} \tau\left(-I_b - m_b\bar{R}R_h + m_bR_h^2 - \frac{m_b^2\bar{R}^2R_h^2}{I_b}\right)\sum_{i=1}^{B}\cos\psi_i\sin\psi_i \\ -m_b\bar{R}R_h\sum_{i=1}^{B}\beta_i\sin\psi_i - I_b\sum_{i=1}^{B}\beta_i\cos^2\psi_i\sin\psi_i \\ -m_b\bar{R}R_h\tau\sum_{i=1}^{B}\cos\psi_i\sin\psi_i + \frac{m_b^2\bar{R}^2R_h^2}{I_b}\sum_{i=1}^{B}\beta_i\sin^3\psi_i \\ -I_b\sum_{i=1}^{B}\beta_i\cos^2\psi_i\sin\psi_i \end{array}\right] \qquad (3.3)$$

For a rigid rotor ($\beta_i' = \beta_i'' = 0$, $\beta_i = \beta_0$), the HAWT model possesses only a single (yaw) degree-of-freedom with the equation of motion becoming:

$$\gamma''\left[I_{yaw} + Bm_b\left(L_s^2 + 2\bar{R}L_s\beta_0\right) + \left(I_b + m_bR_h^2 + 2m_b\bar{R}R_h\right)\sum_{i=1}^{B}\sin^2\psi_i\right]$$

$$+\frac{a_v}{\Omega}\gamma' + \frac{a_f}{\Omega^2}\mathrm{sgn}(\gamma') = \frac{M_{yaw}}{\Omega^2} \qquad (3.4)$$

In this equation M_{yaw} is the net aerodynamic yaw moment acting on the rotor.

Equations 3.2 and 3.3 are the complete set of equations implemented in the program YawDyn for the rigid hub rotor. Equation 3.4 is the governing equation solved when the blade flap DOF is ignored. This equation can be solved more quickly and can be used for comparison with other rigid blade analyses.

Readers who are familiar with annual reports from this project may notice the yaw equation (with flap) differs from that published earlier. There was an error in the earlier derivation using Lagrange's method that was discovered only recently. The previous equation from the earlier reports should be ignored, as should earlier releases of YawDyn implementing that equation. The error affected only those results with coupled free-yaw and flap motion. This was a small fraction of the earlier work published. All results pertaining to fixed yaw and yaw motion without flap are believed to be correct.

3.2 Relation between yaw and flap moments for a rigid rotor

Yaw loads on a wind turbine result from aerodynamic and dynamic forces on the rotor and the nacelle. The current analysis considers only the rotor loads and neglects the nacelle aerodynamic moment. The author considers this acceptable since the nacelle area is small in comparison with the rotor area and the aerodynamic yaw moments will likewise be small unless a tail or other yaw vane has been added to the nacelle. The loads on the rotor can be divided into two categories of interest in yaw behavior: 1) the net horizontal force on the hub, often called the H-force in helicopter analysis and 2) the summation of the blade flap moments, resolved in the yaw direction. Shaft tilt, which provides a component of low-speed shaft torque in the yaw direction, is also considered in the present model.

Consider a three-blade, rigid rotor wind turbine operating in steady-state conditions. In this situation all blades will experience the same flap moments, each lagging the previous by 120 deg. The flap moment for a single blade can be expressed in a Fourier series as follows:

$$M_f = \sum_{n=0}^{\infty} [f_{n_c} \cos(n\psi) + f_{n_s} \sin(n\psi)] \tag{3.5}$$

In this equation the coefficients f_n are constants which represent the sine and cosine components of each harmonic. ψ is the blade azimuth angle, equal to 0 deg when the blade is at the six o'clock position. The yaw moment is the sum of the three flap moments resolved in the yaw direction:

$$M_\gamma(\psi) = \sum_{i=0}^{2} M_f(\psi + i\frac{2}{3}\pi)\sin(\psi + i\frac{2}{3}\pi) \tag{3.6}$$

This yaw moment can also be expressed in terms of a Fourier series:

$$M_\gamma = \sum_{n=0}^{\infty} [\gamma_{n_c} \cos(n\psi) + \gamma_{n_s} \sin(n\psi)] \tag{3.7}$$

When equation (3.5) is substituted in (3.6) and the coefficients of the various sine and cosine harmonics are equated the following equations result.

$$\gamma_{0_c} = \text{mean yaw moment} = \frac{3f_{1_s}}{2} \tag{3.8}$$

$$\gamma_{n_c} = \begin{cases} \frac{3}{2}[f_{(n-1)_s} - f_{(n+1)_s}] & n = 3,6,... \\ 0 & n \neq 3,6,... \end{cases} \tag{3.9}$$

$$\gamma_{n_s} = \begin{cases} \frac{3}{2}[f_{(n-1)_c} - f_{(n+1)_c}] & n = 3,6,... \\ 0 & n \neq 3,6,... \end{cases} \tag{3.10}$$

These results show the following important features for yaw moments resulting from blade flap loads.

1) The mean yaw moment results from the once-per-revolution (1p) sine flap moment only.

2) The only cyclic yaw moments due to balanced rotor loads on a three-blade rotor are moments with a frequency of 3p or integer multiples of 3p. The 3p yaw moments result from 2p and 4p flap moments. This shift of plus or minus 1p from the rotor frame of reference to the fixed (yaw) frame is well known.

Another important source of yaw moments is mass or aerodynamic imbalance of the rotor. If the rotor is not mass balanced then the centrifugal force due to the rotor mass will produce a yaw moment which depends upon the distance from the yaw axis to the hub (L_S), the mass offset ($\bar{r}$), the rotor mass (m), and the rotor angular velocity (Ω):

$$M_\gamma = -L_s m \bar{r} \Omega^2 \sin \psi \tag{3.11}$$

Note this is a 1p yaw moment. A similar 1p yaw moment will result if the blades are not aerodynamically balanced. Thus, if 1p yaw moments are observed during testing, there is probably a mass or aerodynamic (most likely blade pitch) imbalance. Observing the 1p yaw moments can be a very useful diagnostic tool for reducing cyclic yaw moments and/or balancing a rotor after installation. Imbalance is discussed in greater detail by Young, et al [Young, Hansen et al., 1988].

Figure 3.3 shows the result of a simple test to determine the importance of the root flap moments in determining the yaw moment for a rigid rotor. A ten-revolution (approximately 8 second) segment of data was selected from test records from the SERI Combined Experiment rotor. Both blade flap moment and yaw moment measurements were available. The blade flap data were azimuth averaged and then decomposed into a Fourier series to determine the coefficients f_n. Then equations 3.8, 3.9 and 3.10 were used to determine the coefficients γ_n. Next the 1p yaw moment due to mass imbalance was determined from the known offset of the rotor center of gravity using equation (3.11). Finally, the yaw moment was computed from the resulting Fourier series for the flap moment and compared with the directly measured yaw moment.

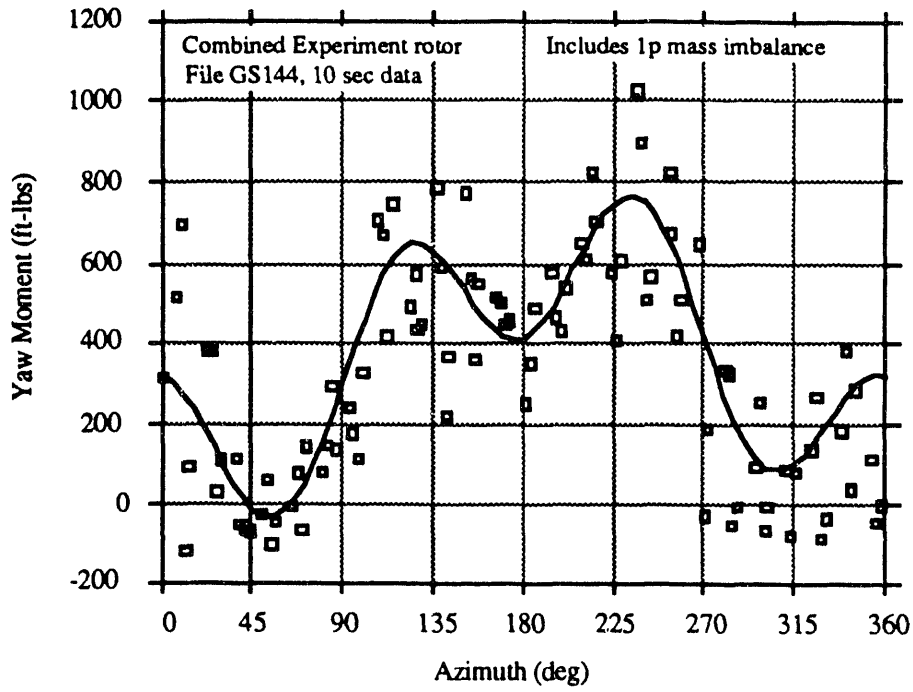

Figure 3.3. Comparison of the measured yaw moment (data points) with the moment calculated using the measured blade flap moment and the 1p rotor mass imbalance.

In Figure 3.3 the data points show the measured yaw moment and the solid line shows the yaw moment computed from the flap moments. It is clear that the reconstructed yaw moment agrees favorably with the actual moment. This implies that the horizontal H-force is unimportant for this rigid rotor and that the nacelle aerodynamic moment is also negligible. It is also interesting to note the 1p harmonic is the largest contributor to the cyclic moment. Thus the mass imbalance is important to the overall yaw load spectrum of this particular rotor.

3.3 Equations of motion of the teetering rotor

The teetering rotor differs sufficiently from the rigid rotor that separate equations of motion are required. The derivation of the equations follows the same basic method presented for the rigid rotor. Details of the derivation are provided in Appendix A. Figure 3.4 shows the geometry and essential parameters of the teetering rotor. The equation governing the teetering motion is given by:

$$\left(1-\frac{m_b s^2}{I_b}\right)T'' = -T - \frac{M_{aero}+M_{hub}}{2I_b\Omega^2} - \frac{m_b g s\cos\psi}{I_b\Omega^2} - 2\gamma'\cos\psi$$
$$-\gamma''\sin\psi\left(1+\frac{m_b L_s s}{I_b}+\frac{m_b s^2}{I_b}\right) \qquad (3.12)$$

The yaw motion of the teetering rotor is governed by the following equation:

$$\gamma''\left[\begin{array}{l} I_{yaw}\left(1-\frac{m_b s^2}{I_b}\right)+2m_b L_s^2+4m_b L_s s \\ -\cos^2\psi\left\{2m_b L_s s\left(2+\frac{m_b L_s s}{I_b}\right)+2m_b s^2\left(1-\frac{m_b s^2}{I_b}\right)\right\} \end{array}\right]=$$

$$-\frac{M_{edge}}{\Omega^2}\left[\left(1-\frac{m_b s^2}{I_b}\right)(\tau+T\cos\psi)\right]-2m_b L_s s T\sin\psi$$

$$-M_{aero}\frac{m_b L_s s}{I_b\Omega^2}\sin\psi+\frac{F_z L_s T}{\Omega^2}\sin\psi\left(1-\frac{m_b s^2}{I_b}\right)$$

$$-\frac{2m_b g s\cos\psi\sin\psi}{\Omega^2}\left(1-\frac{m_b s^2}{I_b}+\frac{m_b L_s s}{I_b}\right)$$

$$+\frac{M_{hub}\sin\psi}{\Omega^2}\left(1-\frac{m_b s^2}{I_b}-\frac{m_b L_s s}{I_b}\right)-4\gamma' m_b L_s s\cos\psi\sin\psi$$

$$+4T' m_b s\cos\psi(L_s-s)\left(1-\frac{m_b s^2}{I_b}\right) \qquad (3.13)$$

In this equation M_{hub} is the net moment exerted on the hub by the teeter springs and dampers, M_{edge} is the net aerodynamic torque on the rotor, T is the teeter angle and s is the undersling as shown in Figure 3.4.

The model contains provisions for simple teeter dampers and springs as shown in schematic form in Figure 3.4. The damper is a linear system which exerts a teeter moment proportional to the teeter rate (and opposing the teeter motion) for all teeter angles greater than the contact angle. The teeter spring is a nonlinear spring such that the teeter moment is a restoring moment given by equation 3.14.

$$M = k_1\varepsilon + k_2\varepsilon^2 \qquad (3.14)$$

Here ε is the deflection of the spring and k_1 and k_2 are constants which are input to the model. The deflection of the spring, ε, is the teeter angle minus a constant angle which is also input to the model (the free-teeter angle). Thus the rotor can teeter without mechanical restraint until the teeter angle exceeds a preselected value.

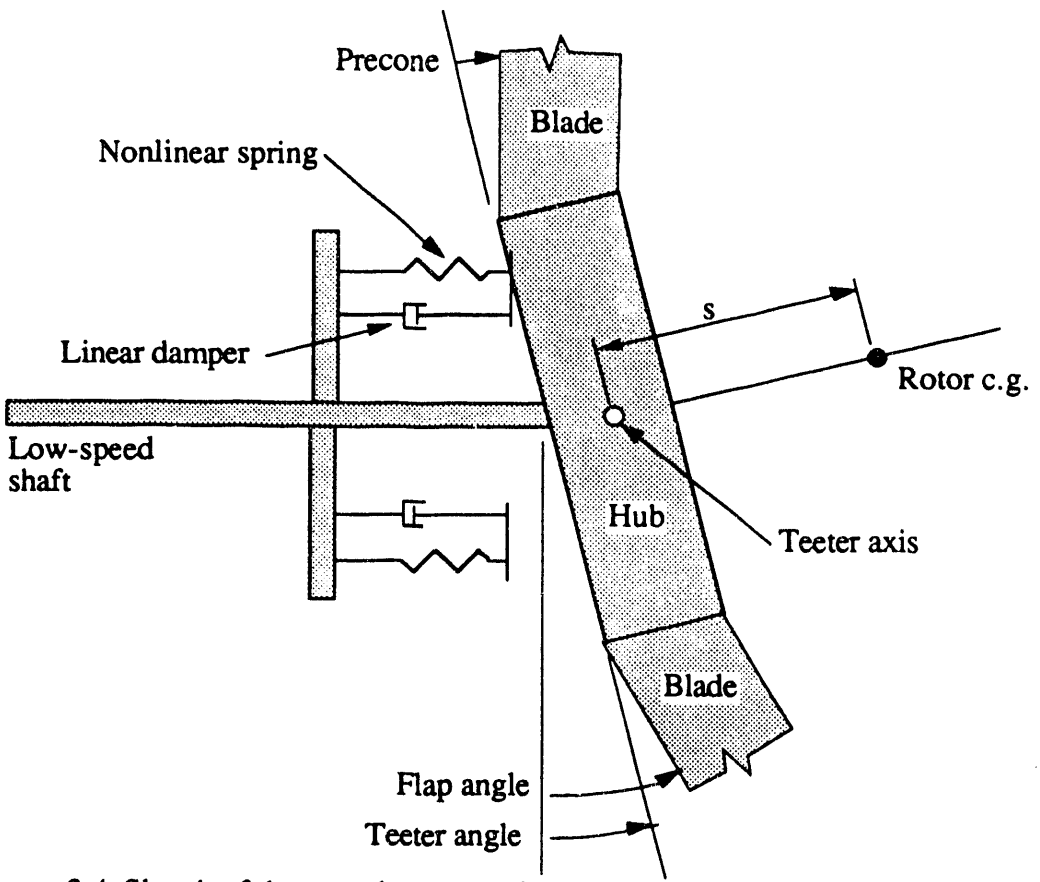

Figure 3.4 Sketch of the teetering rotor, showing key parameters. Free teetering is permitted until the spring and damper are contacted by the hub (in the position shown).

3.4 Subsystem details

Yaw column

The yaw column supports the nacelle and provides a bearing surface about which the nacelle is permitted to yaw. A constant applied moment (i.e., drag from yaw bearings) and a viscous drag moment proportional to the yaw rate are included in the model and provide the following damping moment

$$M_{d\gamma} = -a_v \dot{\gamma} - a_f \text{sign}(\dot{\gamma}) \tag{3.15}$$

where a_v = viscous damping coefficient (ft-lb$_f$-sec/rad)
a_f = moment to overcome bearing friction

The dry friction moment a_f exists only in the case where yaw motion exists. That is, there is no applied moment to the yaw column when the yaw rate is zero. This moment also always resists the motion, hence the signum function. No static friction is included in this model as yaw motions are assumed to be always present in the free-yaw machine even if they are exceedingly small.

A yaw stiffness is also provided in the model for those situations where the nacelle is nominally held fixed in yaw. The stiffness represents the effective torsional stiffness of the connection from the mainframe to ground. Thus it includes the yaw drive, yaw

column and tower stiffness. The yaw moment exerted by this "spring" is simply the yaw deflection (from the initial yaw angle) multiplied by the yaw stiffness.

Rotor Aerodynamics

The blade element/momentum method has been the most useful form of aerodynamics analysis for wind turbine designers. The method offers accuracy, simplicity and ease of intuitive understanding. This is the method selected for the yaw analysis, for the same reasons. The basic method and equations used in this analysis are virtually identical to those detailed by Wilson and Lissaman [Wilson and Lissaman, 1974]. The method includes the static stall model for very high angles of attack developed by Viterna [Viterna and Corrigan, 1981].

However, previous investigators (notably in wind turbine work, [de Vries, 1985]) have shown that simple blade element/momentum methods will predict yaw moments which are less than actual moments and insufficient to cause the yaw stability that is observed on many turbines. Helicopter analysts have noted the same shortcoming in studies of roll and pitch stability in forward flight [Prouty, 1986]. Fortunately, a significant amount of work has been done on this problem by helicopter aerodynamicists. We can apply this work directly to the wind turbine rotor in yaw.

Coleman, et al [Coleman, Feingold et al., 1945] first noted that a skewed wake will perturb the induced velocity field from that which would be expected from blade element theory. They calculated the magnitude of the perturbation and found that induced velocities would be reduced at the upstream edge of the rotor and increased at the downwind edge of the rotor. They also noted a nearly linear variation of induced velocity along the axis aligned with the flight direction (or along a horizontal line through the rotor hub for a yawed wind turbine). Blade element theory is not completely accurate because it assumes independence of all the elements. That is, it assumes that the induced velocity at a particular blade element depends only upon the force on that single element. In fact, the induced velocity field depends upon the distribution of vorticity in the entire wake. This effect becomes important when the wake is no longer symmetric. In a skewed wake the blade elements on the downwind side of the rotor are closer to the wake centerline than are the elements on the upwind side of the rotor. Hence the induced velocities are higher on the downwind side than on the upwind side.

Pitt and Peters [Pitt and Peters, 1981] introduced a method for calculating this effect which is self-consistent in both forward and vertical flight. Gaonkar and Peters [Gaonkar and Peters, 1986] have provided a recent survey of this topic and comparisons with test data that show the method of Pitt and Peters is valid. This is the method that was first applied by Swift [Swift, 1981] to the wind turbine. Swift used an actuator-disc analysis with the skewed wake correction being a linear variation superimposed upon a constant induced velocity.

The method used in the current work is adapted to a blade element analysis and uses the following equation to adjust the axial induction factor, "a".

$$a = a_0\left[1+\frac{15\pi}{32}\sqrt{\frac{1-\cos\gamma}{1+\cos\gamma}}\frac{r}{R}K\sin\psi\right] \tag{3.16}$$

Where a = axial induction factor used to determine actual induced velocity
a_0 = axial induction factor calculated using simple blade element/momentum theory

Note the dependence upon yaw angle, γ, and radial position. When there is zero yaw, no correction is applied. The variation along a horizontal line ($\psi = 90°$) is linear with radius. For small yaw angles the yaw dependence is approximately linearly proportional to γ. The factor K is included only for sensitivity studies in the computer programs. The theory of Pitt and Peters predicts K=1. This is the value used in the final version of YawDyn.

Dynamic Stall

The Combined Experiment rotor has the capability of measuring the angle of attack using a small vane and measuring the lift coefficient using a chordwise distribution of pressure transducers. Figure 3.5 presents such data taken at the 80% span station. The data represents ten revolutions of the rotor, with approximately eight samples measured per revolution (10 Hz sampling frequency). Sequential samples are connected using solid lines to show the hysteresis loop present in the C_L curve. The hysteresis loop progresses clockwise around the figure as time increases. Two-dimensional wind tunnel measurements of steady C_L values are shown for comparison. Notice the C_L decreases below static test values as the angle of attack rapidly decreases from its maximum value during yawed operation.

Attempts to predict yaw loads on the Combined Experiment using YawDyn were unsuccessful when this stall hysteresis was not included in the model. This prompted efforts to incorporate a dynamic stall model in YawDyn. The model selected is the stall hysteresis analysis proposed by Gormont [Gormont, 1973].

Gormont developed a method for treating dynamic stall in helicopter analysis. Sandia National Laboratories has adopted this method for analysis of vertical axis wind turbine dynamic stall [Berg, 1983]. (The complete Gormont model includes dynamic inflow. This portion of the model was not implemented in the present work.) The Gormont model calculates a lift coefficient based upon static two-dimensional wind tunnel values and the time rate of change of angle of attack. A modified blade angle of attack, α_m, is

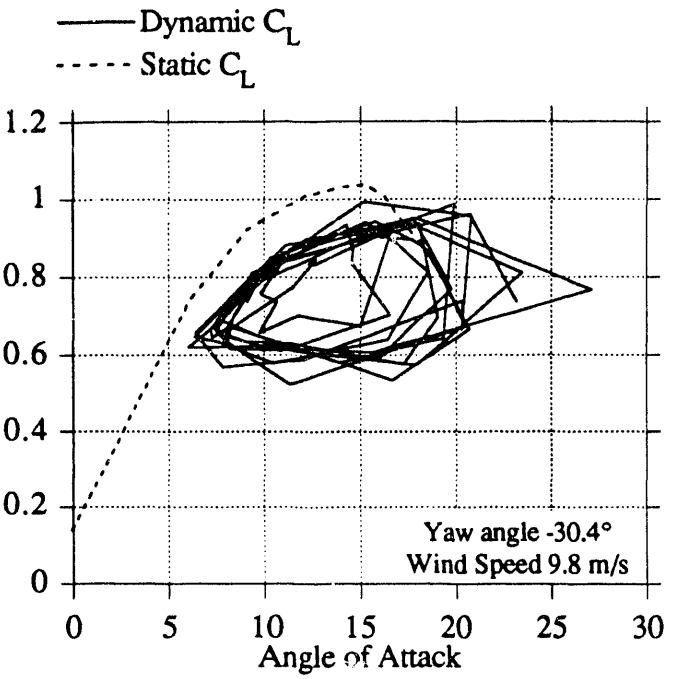

Figure 3.5. Stall hysteresis loop measured at the 80% span on the Combined Experiment rotor.

used which depends upon the actual angle of attack, α_b, and $d\alpha_b/dt$ as follows:

$$\alpha_m = \alpha_b - K_1 \left[1.4 - 6.0(0.06 - \frac{t}{c})\right]\left[\frac{c\,\dot{\alpha}}{2U_r}\right]^{\frac{1}{2}} \mathrm{Sign}(\dot{\alpha}) \tag{3.17}$$

In this equation c is the blade chord, t is the blade thickness, and U_r is the local relative wind speed. K_1 is a constant which assumes either of two values depending upon the sign of $d\alpha_b/dt$ in the following manner.

$$K_1 = \begin{cases} A & \alpha_b \dfrac{d\alpha_b}{dt} > 0 \\ B & \alpha_b \dfrac{d\alpha_b}{dt} < 0 \end{cases} \tag{3.18}$$

The standard Gormont model assigns values of A=1 and B=0.5. Parameter A determines the amount of increase in maximum C_L. B affects the size of the hysteresis loop. The Combined Experiment data of Figure 3.5 demonstrate no increase in maximum C_L. Therefore A=0 was used in most of the calculations which will be presented.

Once α_m is determined the effective C_L is calculated using the following equation:

$$C_L = \frac{\alpha_b - \alpha_{b0}}{\alpha_m - \alpha_{b0}} C_L(\alpha_m) \tag{3.19}$$

Where α_{b0} is the zero-lift angle of attack and $C_L(\alpha_m)$ is the two-dimensional wind tunnel static value of C_L at angle α_m.

To summarize, the induced velocity field is calculated in a three-step process. First the axial induction factor, a_0, is calculated using the blade element/momentum method. Second, the induction factor is adjusted using equation 3.16 to account for the skewed shape of the wake. Third, dynamic stall theory is used to adjust the section lift coefficient and then the blade forces are calculated using the blade element method and the new value of axial induction factor.

Wind Shears

The wind is represented as a velocity varying in magnitude and direction. Temporal variations in the wind vector can be analyzed by reading a wind data file. Spatial variations in the wind speeds are represented by wind shear coefficients which can also vary in time. The wind direction is assumed constant over the rotor disc (i.e. there are no wind direction shears considered in the model). The spatial variations are caused by complex terrain or arrays of turbines upwind of the HAWT (persistent, long-term shear) and also by atmospheric turbulence ("instantaneous" shear). This model treats the shears as linear variations in the wind speed in both the horizontal and vertical directions as shown in Figure 3.6. An option is also available to use power-law wind shear in the vertical direction. A vertical component of wind velocity is also included in the model. This value is a constant across the entire rotor disc (note that a positive vertical wind blows toward the ground with the present coordinate system). The hub height wind input consists of an instantaneous horizontal speed V_∞ and direction δ with respect to the **z** axis. The angle δ can vary independent of the yaw angle γ. The yaw error, or misalignment of the rotor from the wind direction is $\gamma+\delta$. Both γ and δ are shown in the positive direction in Figure 3.6.

Tower Shadow

The downwind HAWT has a region, represented by a sector centered at the blade six o'clock position, through which each rotor blade will encounter the wake of the tower. Within this region, the so-called tower shadow, the wind velocity is altered by turbulence and vorticity. The total effect this has on the aerodynamic loading on the blade is quite complicated. To determine the importance of the tower shadow, it is modeled by assuming the velocity normal to the rotor disc within this region is reduced by a factor that is a function of the blade azimuth angle. Experimental measurements [Hoffman, 1977; Savino and Wagner, 1976] within the near wake region of the tower indicate this velocity deficit has a magnitude which can be 30% to 50% of the undisturbed flow. Values of 5-10% are more typical if the blade is in the far wake.

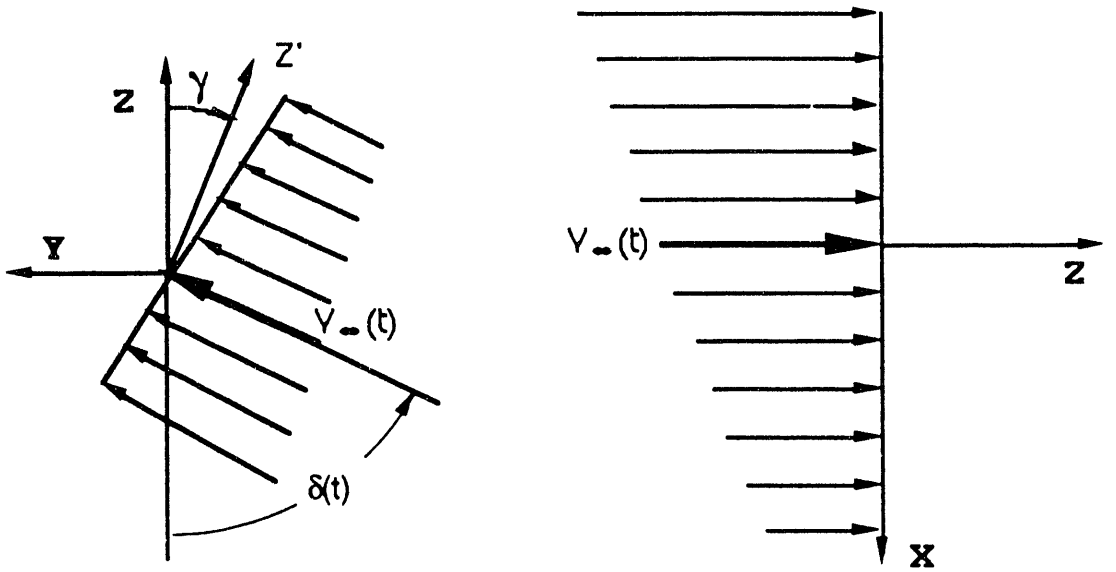

Figure 3.6 Linear wind shear models. Horizontal shear in left sketch, vertical shear in right sketch. (Vertical shear can also be a power-law profile.)

The following expression gives the normal wind speed in terms of the speed which would be present if there were no tower shadow:

$$V_n(x,y,z,\psi) = V_n(x,y,z)\left[1 - T_s(\psi)\right] \tag{3.20}$$

The tower shadow shape function is:

$$T_s(\psi) = \begin{cases} \dfrac{\Delta V_s}{2}\left[1 + \cos\left(\pi \dfrac{\psi}{\psi_0}\right)\right] & \text{if } -\psi_0 \le \psi \le \psi_0 \\ 0 & \text{elsewhere} \end{cases} \tag{3.21}$$

ΔV_s = velocity deficit ratio at the tower shadow centerline

ψ_0 = half-angle of tower shadow sector

In the final version of YawDyn the sector containing the tower shadow has an included angle of $2\psi_0 = 30°$. Notice this "wedge shape" wake is not representative of all tower shadows, and the model always centers the wake at $\psi = 0°$, regardless of the yaw angle. In fact, at large yaw angles, the blade may not enter the wake at all. Nonetheless, the simple model is useful for approximating the importance of the shadow. Future models will implement a more refined model of the tower shadow.

4.0 Numerical Solution

The coupled, nonlinear ordinary differential equations governing yaw and flap motion are far too complex to be solved analytically. Instead, numerical integration is performed for the equations. This approach is less than ideal because it makes completion of sensitivity studies and identification of trends tedious. But it offers the overwhelming advantage that it is possible to consider all of the important nonlinear effects (such as static and dynamic stall) and the details of the turbine (such as blade twist and taper, nonlinear teeter-stop springs, etc.).

4.1 Numerical integration

The primary method of integration is the Modified Adams-Bashforth Predictor-Corrector. This method was selected for speed, stability and accuracy and is commonly used in problems of this type. The ordinary differential equations are first arranged as a series of "n" first order differential equations.

The Adams-Bashforth algorithm requires four sets of starting points $\{x_{k,i}\}$, $\{x_{k,i-1}\}$, $\{x_{k,i-2}\}$,and $\{x_{k,i-3}\}$ at times t_i, t_{i-1}, t_{i-2}, and t_{i-3} where $k = 1, 2, \ldots n$, $t_i = t_{i-1} + h$ and h is the fixed step size. In addition, the function values $\{F_{k,i}\}$, $\{F_{k,i-1}\}$, $\{F_{k,i-2}\}$, and $\{F_{k,i-3}\}$ are required, where $F_{j,i}$ is the jth element of the function vector, evaluated at time t_i and using vector $\{x_{k,i}\}$. Once these starting points are obtained, by a simple predictor-corrector method, perform the following:

Step 1. Find $p_k = x_{k,i} + h/24(55F_{k,i} - 59F_{k,i-1} + 37F_{k,i-2} - 9F_{k,i-3})$

Step 2. Find $c_k = x_{k,i} + h/24(9F^{p}_{k,i+1} + 19F_{k,i} - 5F_{k,i-1} + F_{k,i-2})$

Step 3. Find $x_{k,i+1} = 1/270(251c_k + 19p_k)$

In these equations F is the function on the right-hand side of the first-order differential equations and $F^{p}_{k,i+1}$ is the kth element of F, evaluated by replacing x_{i+1} in the argument by p_k. This solution method requires evaluation of the right-hand side only once per time step. This is the reason the solution is faster than many other methods, such as the Runge-Kutta techniques.

The dynamic stall model requires evaluation of the time-rate-of-change of the blade element angle of attack. Numerical differentiation is inherently "noisy" and the iteration to determine the induced velocities is highly dependent upon the airfoil lift coefficient. Early attempts to implement the Gormont dynamic stall model were unsuccessful because of numerical instabilities in the angle of attack estimation. This problem was solved by smoothing the angle of attack time history before calculating the time derivative. Smoothing was accomplished using a Sine-Butterworth digital low pass filter. The filtered angle of attack is used only for estimating the time derivative.

4.2 Initial conditions and trim solution

The computer program starts with the initial conditions specified by the user and integrates through two complete revolutions of the rotor while wind and yaw conditions remain constant. It then compares the blade motions for the two revolutions. If the root-mean-square difference between the flap angles for the two revolutions are below a

specified tolerance for each blade the "trim" solution has been found. If the trim solution has not been found another revolution is calculated. This process continues until the two most recent revolutions yield the same flap motion (within the tolerance). After the trim solution is found the program allows the simulated time to reset to zero and the integration proceeds with the actual time-varying yaw angle and wind conditions.

The integration requires an initial condition for each of the degrees of freedom of the system. In the general case the flap angle and flap rate for each blade and the yaw angle and yaw rate of the system must be specified by the user of the program. The selection of these initial conditions will have a large influence on the time required to find the trim solution for the rotor. If the flap initial conditions are too different from the conditions that would actually exist on the rotor the program may not be able to converge to a trim solution. This is particularly true for blades which have a low stiffness and are therefore experiencing large deflections. Thus it is important that the user understand the rotor dynamics and have some idea of the blade flap motion that would be expected under the selected operating conditions.

If the blade stiffness is quite high, say greater than 3p, it is often sufficient to use initial conditions for each blade which set the flap angles equal to the precone angle and the flap rates to zero. For "soft" blades it may be necessary to specify different angles and rates for each blade. This can almost always be achieved by a few trial and error runs. The program informs the user of the trim solution initial conditions to help guide the selection of appropriate values. In the most difficult cases it may be necessary to vary operating conditions slowly from a known solution to the desired, difficult condition. For example, if the yaw angle is very large it may be difficult to guess a set of initial conditions which will converge to a trim solution. In that case it may be necessary to run the program in the fixed-yaw mode for a series of progressively increasing yaw angles (starting from low values where the trim is easy) and observe the trend in the trim solution initial conditions. This trend can be used to extrapolate the initial conditions for a new yaw angle.

4.3 Program structure and flow chart

Figure 4.1 shows a summary flow chart of YawDyn. More details are found in the User's Guide in Appendix C.

4.4 Computer requirements

The program was developed with the intent that it would be suitable for tradeoffs and sensitivity studies. This meant it had to run quickly on relatively simple and low-cost computers. Though the computing requirements have grown as more physical phenomena were added to the program, the personal computer capabilities have grown at an even faster rate. Thus the program is still quite suitable for design and tradeoff calculations using hardware available to any small business.

Most of the development of YawDyn has been done using Macintosh II™ computers using Absoft™ MacFortran II. The program will run on these systems with 2 MB of RAM. Other versions of Fortran 77 will run on the Macintosh with 1 MB RAM. Typical run times on a Macintosh IIci system are one to five minutes. The program has also been tested under VAX VMS and IBM PCs (clones) using Lahey F77L™ Fortran and NDP Fortran. System requirements are minimal though the run times are long enough that there is incentive for using a relatively fast personal computer.

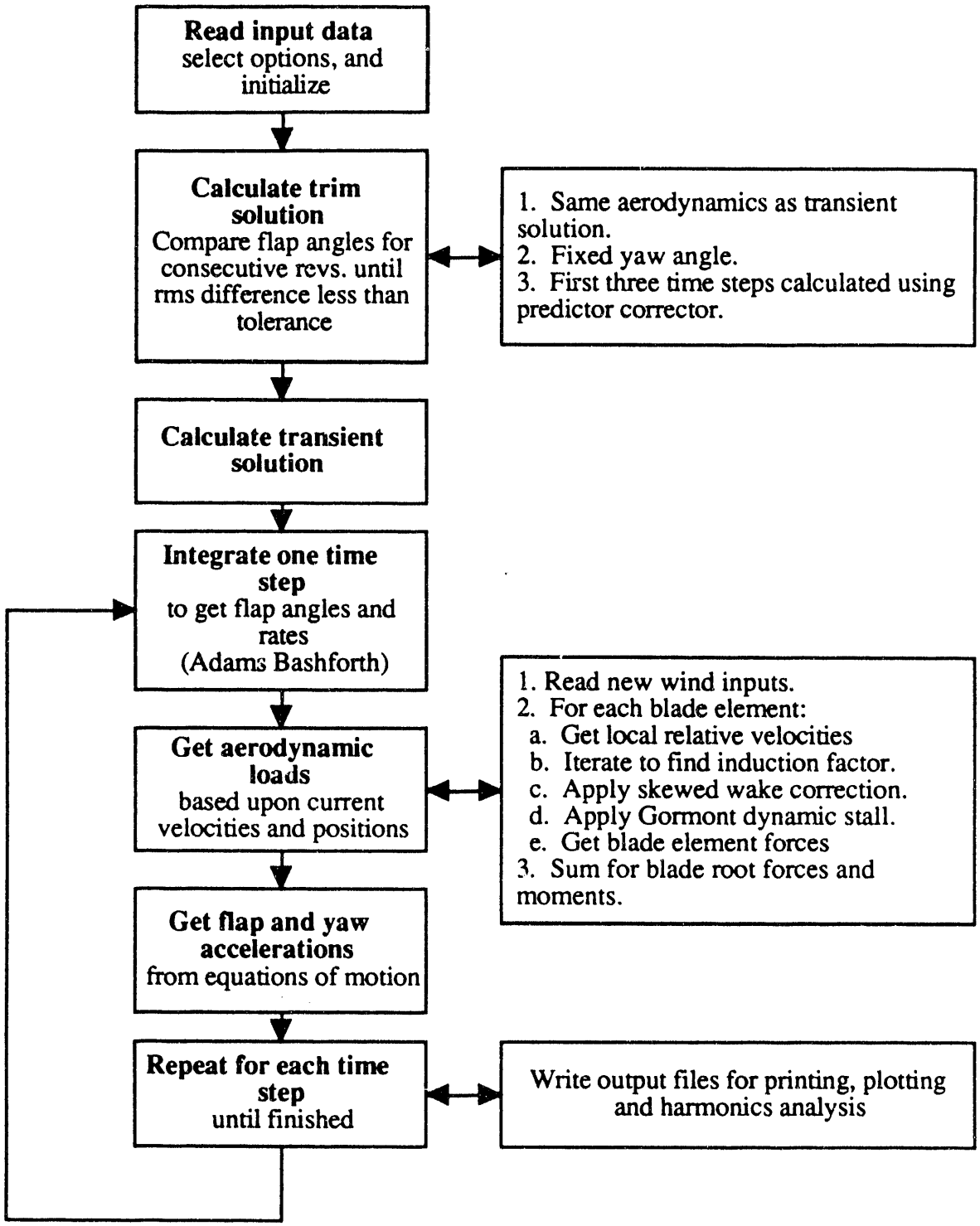

Figure 4.1 Summary flow chart of the YawDyn computer program.

5.0 Validation Studies

5.1 Introduction

One of the most important tasks of the project was validation of the YawDyn model. Several methods were explored to find means of testing the validity of the predictions. The wind energy research field is hampered by a scarcity of complete and reliable test data (particularly for yaw loads and motions). However, two sets of very helpful data were identified and used for testing the computer predictions. Where data could not be found for testing the model, comparisons with predictions of other models were made. This offers the advantage of permitting detailed exploration of the analysis assumptions and options but has the obvious disadvantage that comparisons are made with results which are not proven accurate.

The following sections present comparisons with wind-tunnel measurements, field test data, and predictions of the SERI FLAP code. An attempt has been made to test the limits of the code and find its strengths and weaknesses. Certainly both strengths and weaknesses have been found. Testing and refinement of the computer program will continue, so this section reports a "snapshot" of the status of the method. Hopefully, this will stimulate other researchers to improve the model and provide designers with some indications of the reliability of the predictions and insights which can be obtained from the model.

5.2 Mod-2 Wind Tunnel Test Comparisons

Early in the development of the Mod-2 wind turbine a series of wind-tunnel tests were conducted on a 1/20 scale model [Shipley, 1978]. Two configurations were tested, one with a rigid hub and the other with a teetering hub. The rigid-hub tests provide a good data set for comparison with YawDyn. The rotor was tested at three yaw angles and three wind speeds, each with a vertical shear (but no other non-uniformity) in the approach wind. The pitch angle was adjusted at each wind speed to limit power output. The angle of attack at the tip of the blade typically averaged near 0° in all test cases. Thus the data do not provide insight to deep stall operation of the rotor. Nevertheless, the availability of detailed and controlled test data was very helpful.

Early comparisons with the test data were not encouraging[Hansen and Cui, 1989; Cui, Hansen, et al, 1988]. But investigation of the poor agreement between predictions and measurements lead to the incorporation of skewed wake effects in the model. Then the predictions matched the data quite well, both qualitatively and quantitatively.

Figures 5.1 and 5.2 show comparisons of both mean and cyclic yaw moments. It can be seen that the qualitative trends are in excellent agreement. Note the yaw moment is negative at all wind speeds when the yaw angle is 0°. This means the rotor will not be statically stable directly upwind. The sign of the yaw moment changes with wind speed for negative yaw angles. Thus the stability will depend on the wind speed and the yaw angle. Clearly this rotor would not be satisfactory as a free-yaw, upwind system. It is also interesting to note the cyclic yaw moments are several times larger than the mean moments. This means the yaw loads are fully reversing fatigue cycles on the yaw drive and that peak loads will be much larger than mean loads.

The quantitative agreement is less satisfactory, but still quite encouraging. The mean yaw moments appear to differ by a nearly constant offset. The predicted yaw moment

exceeds the measured value by 3 to 5 ft-lbs (about 20-30% of the largest moment measured). The 2p moments show better agreement at +20° yaw angle than at -20°. The reasons for these discrepancies are not known. This level of accuracy is in large part due to the incorporation of the skewed wake corrections to the basic blade-element/momentum aerodynamics.

Dynamic stall effects were included in the calculations but made little difference in the results. This is because most of the blade never stalled during these tests.

Table 5.1 lists the pertinent conditions for the predictions above. Other machine characteristics are given in Appendix B.

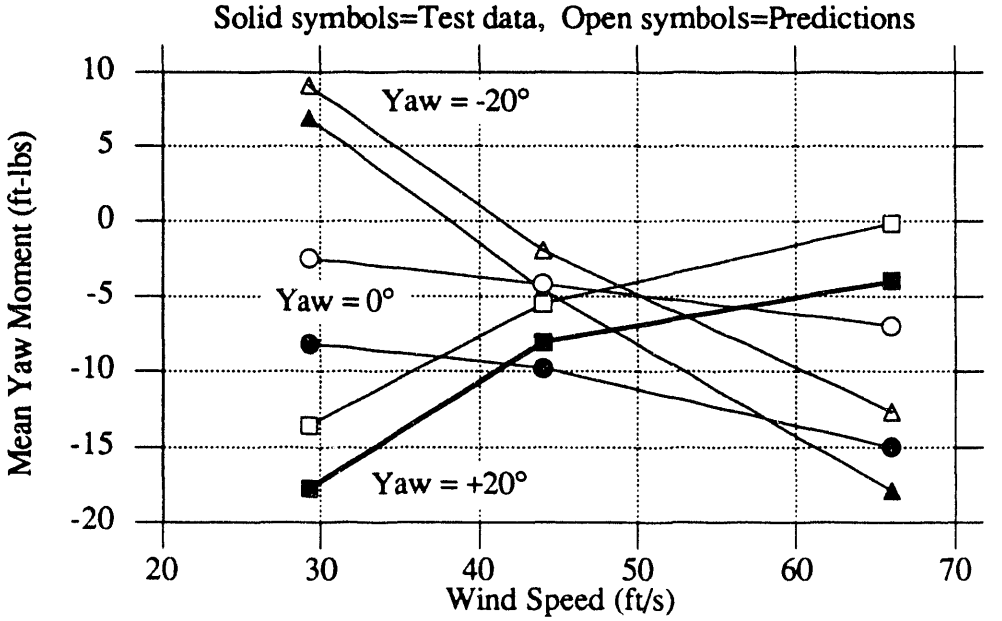

Figure 5.1. Comparison of predicted and measured mean yaw moments for the wind-tunnel model of the rigid-rotor Mod-2.

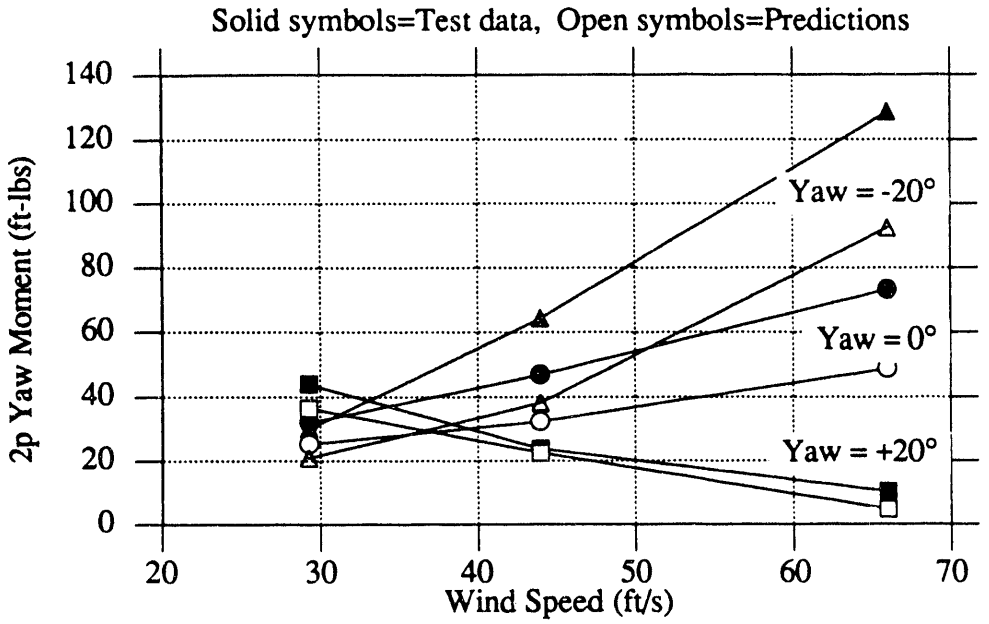

Figure 5.2. Comparison of predicted and measured 2p yaw moments for the wind-tunnel model of the rigid-rotor Mod-2.

Table 5.1 Parameters used in the analysis of the Mod-2 wind-tunnel model.

Parameter	Value
Yaw angle	Fixed
Flap DOF?	Yes
Hub	Rigid
Pitch angles (all blades)	0°@ 29.3 ft/s 9.3° @ 44 ft/s 18° @ 66 ft/s
Dynamic stall	A=0.5, B=0.5 Filter 2 stages at 20p
Number of sectors	200
Convergence tolerance	0.01
Vertical shear	0.14 power law
Horizontal shear	0.0
Vertical wind component	0.0

5.3 SERI Combined Experiment and FLAP Prediction Comparisons

The Combined Experiment rotor operated by SERI[Butterfield, 1989a; Butterfield, 1989b] is perhaps the most thoroughly and carefully instrumented rotor available for understanding aerodynamic and dynamic loads on a wind turbine. It has been the main vehicle for the validation of YawDyn and the SERI FLAP code. In addition to blade, yaw column and low-speed shaft load strain gages, there are numerous pressure taps for airload measurement, angle-of-attack sensors and a vertical-plane array of anemometry upwind of the rotor. This instrumentation has made it possible to explore and document the details of the dynamic loads and dynamic stall occurring on the blades. These tests have clearly demonstrated the existence and importance of dynamic stall in the operation of a wind turbine and were the motivation for including dynamic stall effects in the YawDyn model.

Table 5.2 lists many of the parameters of the YawDyn model which were used in the predictions that follow. Other details of the Combined Experiment rotor are provided in Appendix B. The dynamic stall constants were selected to give good agreement with the data. Note that no dynamic overshoot was included in the dynamic stall but a lower hysteresis loop larger than that suggested by Gormont (B=0.5) was required. One of the weaknesses of the Gormont model is its dependence upon test data for selection of the hysteresis parameters.

Table 5.2 Parameters used in the analysis of the Combined Experiment Rotor.

Parameter	Value
Yaw angle	Fixed
Flap DOF?	Yes
Hub	Rigid
Pitch angles (all blades)	11.3° for data set 901-1 11.2° for data set 901-2 11.5° for data set 901-3
Dynamic stall	A=0.0, B=0.7 Filter 2 stages at 20p
Number of sectors	200
Convergence tolerance	0.01
Vertical shear	Input from data file
Horizontal shear	Input from data file
Vertical wind component	Input from data file

In all of the predictions, measured wind data were input to the calculations from the 'YawDyn.wnd' file. Instantaneous wind speed, wind direction, vertical wind component, and horizontal and vertical wind shear coefficients were used in the calculations. No attempt was made to lag the wind data to allow for the convection time from the vertical plane array to the rotor. Table 5.3 summarizes the conditions for the

three data sets which were used in the validation. Note the test durations are quite short, leading to small standard deviations on all wind characteristics.

Table 5.3 Wind characteristics from the Combined Experiment data sets. Values are Mean ± Standard Deviation.

Characteristic	Data set 901-1	Data set 901-2	Data set 901-3
Test duration (sec)	9.81	5.71	4.03
Wind speed (ft/s)	36.3±1.2	34.9±0.9	52.0±0.9
Wind Direction (deg)	305±3.8	282.4±4.1	283±1.8
Yaw Angle (deg)	315.9±0.1	315.6±0.1	259±0.1
Vertical shear	-0.043±0.18	-0.032±0.17	-0.053±0.068
Horiz. shear	0.045±0.076	-0.027±0.08	0.054±0.076
Vertical wind (ft/s)	-0.092±0.67	-0.54±1.3	-0.18±0.46

Flap Moment Predictions. First examine the blade root flap moments. Since the yaw loads depend almost exclusively on the flap moments for a rigid rotor, it is important to determine the accuracy of the flap load calculations. It is best to begin with a comparison of the YawDyn and FLAP models. This permits isolation of specific phenomena and establishes a baseline for comparison with test data. Figure 5.3 compares the predictions for a simple case where tower shadow and vertical shear are the only excitation of the flap motion. When the models use equivalent tower shadow representations they produce virtually identical results. This demonstrates that YawDyn is capable of predicting flap moments as well as FLAP, with its more sophisticated model of the structural dynamics. It also demonstrates the importance of the tower shadow in determining the amplitude of the 4p response [Hansen and Wright, 1991].

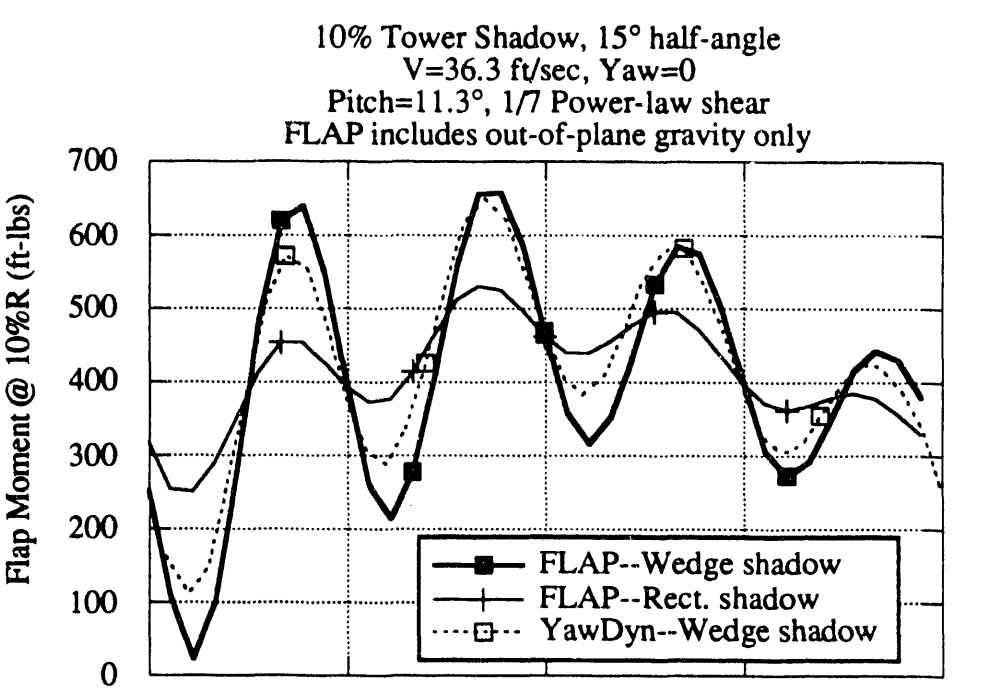

Figure 5.3 Comparison of YawDyn and FLAP predictions for a simple wind shear and tower shadow flow. All tower shadows have the same centerline deficit and the same width at the 75% span station.

Next, look at a comparison of test data and YawDyn and FLAP predictions. Figure 5.4 shows the flap moments from data set 901-3. This represents the best agreement found in any of the comparisons and shows that YawDyn can predict the flap loads with great accuracy. Figure 5.5 compares the same data set with YawDyn predictions when the dynamic stall option is turned off. It can be seen that there is a slight improvement in the agreement between data and predictions when dynamic stall is included. Figures 5.6 and 5.7 show similar comparisons for data set 901-1. Figure 5.6 shows the entire data set and makes it apparent that YawDyn generally predicts the mean flap load and the cyclic content. But there are a number of instances where the measured and predicted loads differ greatly. Figure 5.7 shows the first three seconds of the same data set to concentrate on the cyclic content. Again, the agreement is quite good but not complete.

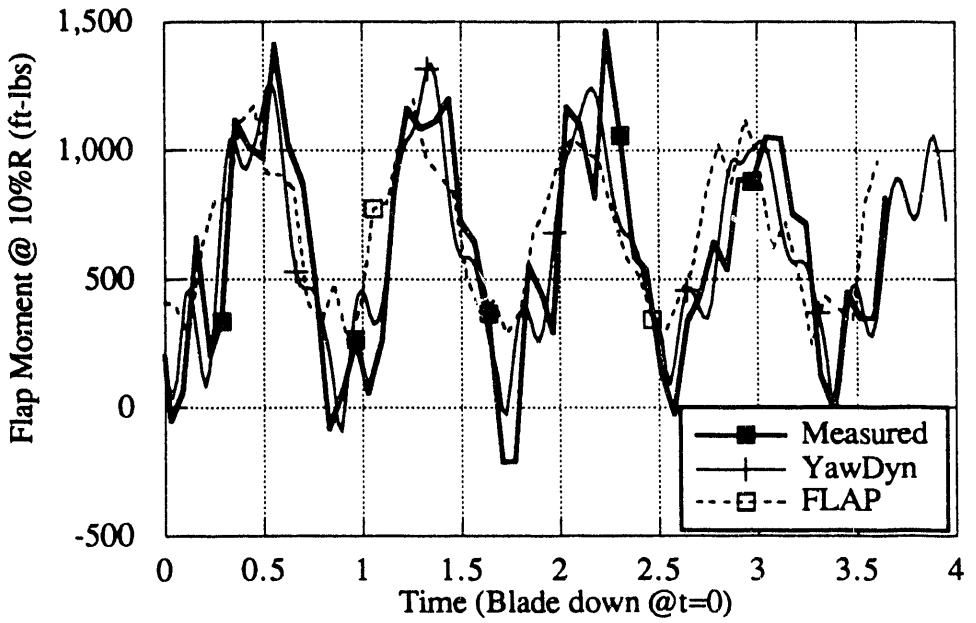

Figure 5.4 Comparison of flap moments for the Combined Experiment data set 901-3.

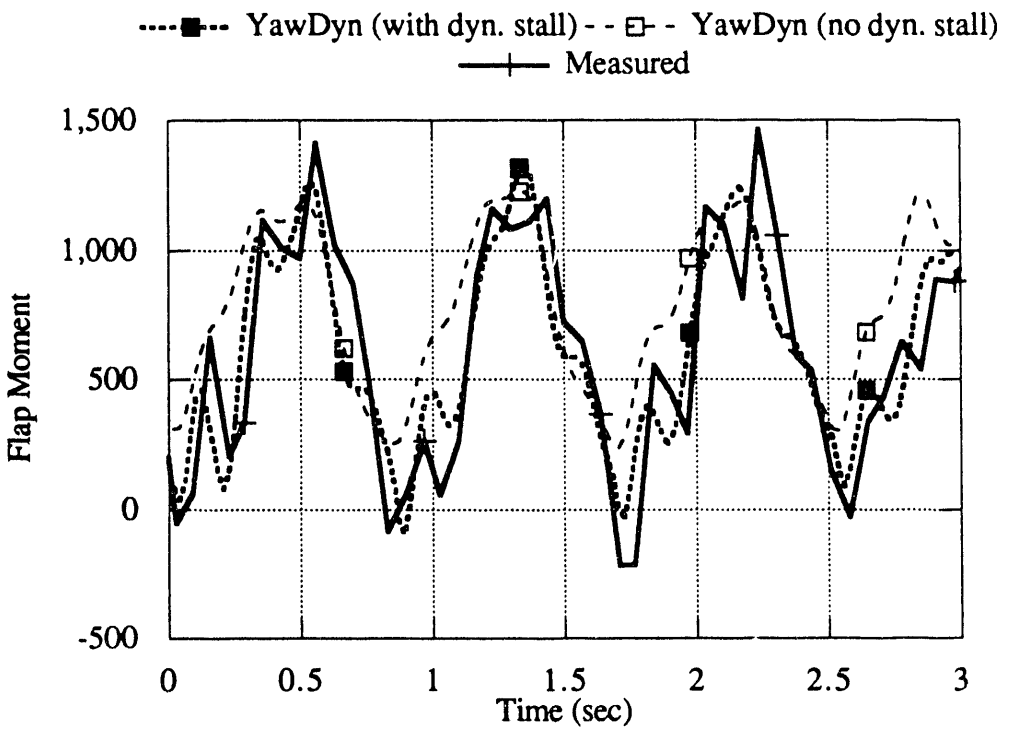

Figure 5.5 Including dynamic stall in the YawDyn predictions makes a slight improvement in the accuracy of the cyclic loads. The data are the same as presented in Figure 5.4.

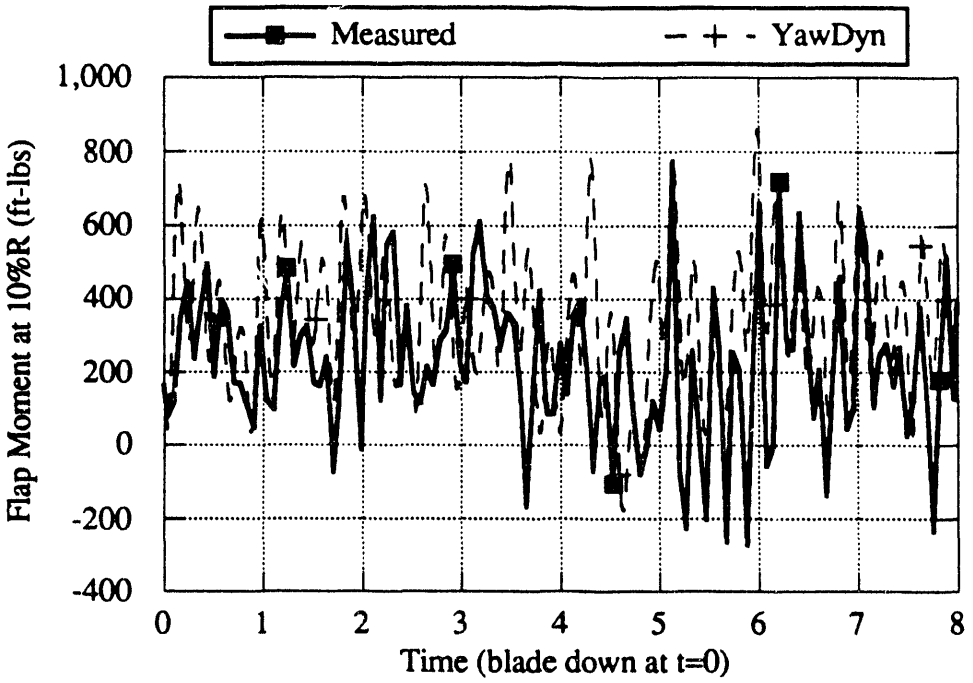

Figure 5.6 Comparison of measured and predicted flap moments for Combined Experiment data set 901-1

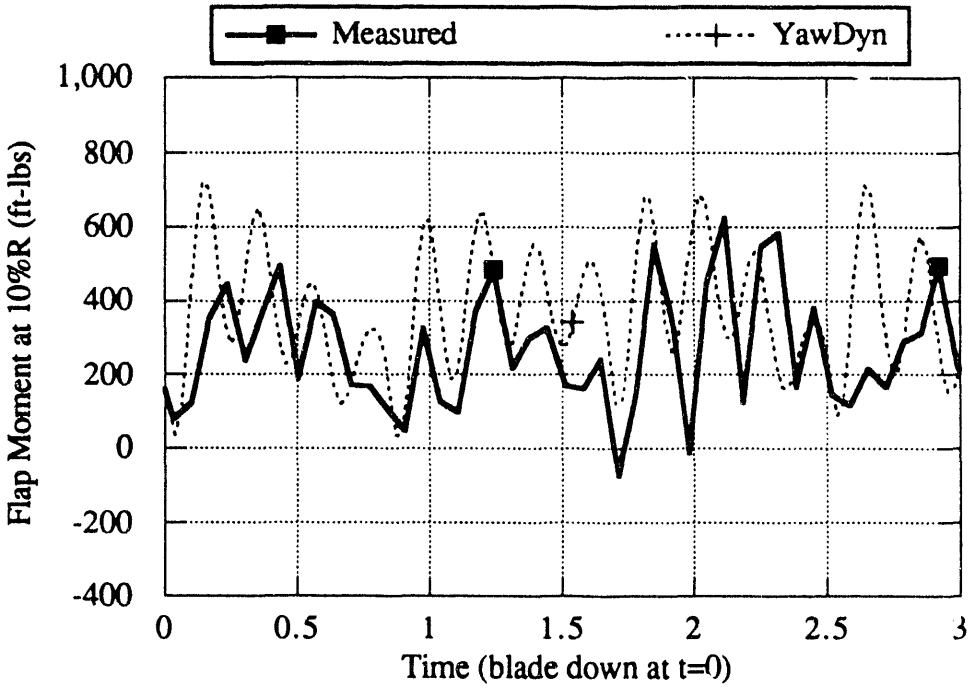

Figure 5.7 An expanded view of Figure 5.6, concentrating on the first three seconds of the test.

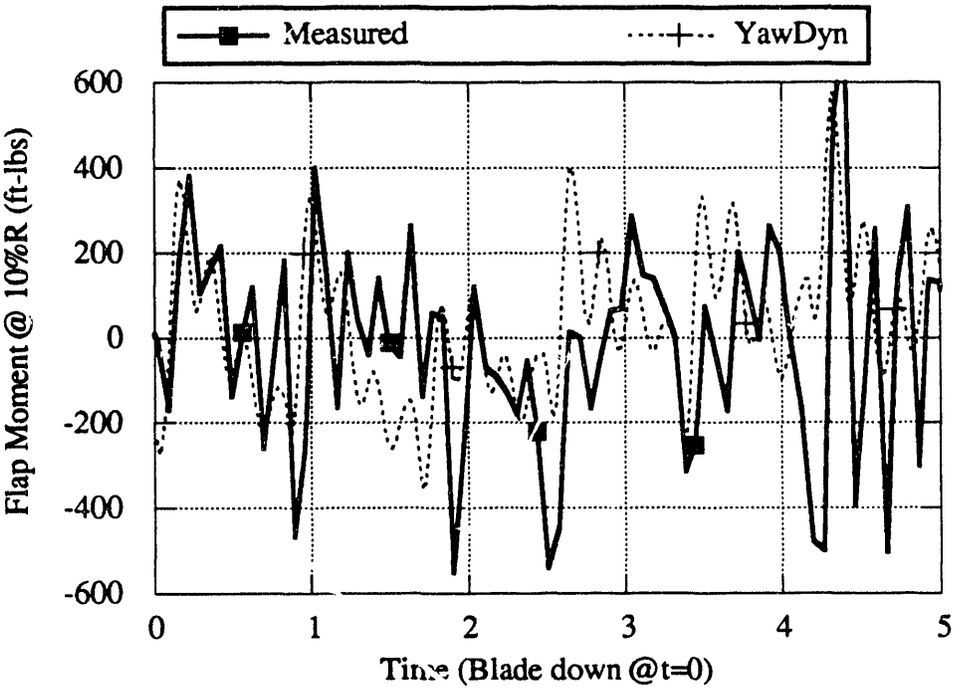

Figure 5.8 Comparison of flap moments from Combined Experiment data set 901-2.

Figure 5.8 shows the final comparison of measured and predicted flap moments. Again the trends are the same. The mean and 1p cyclic moments are matched closely while the 4p cyclic shows greater discrepancies. This is believed to be due to the variability of the strength of the tower shadow in the actual test. In YawDyn the shadow is assumed to be of constant strength, location and width while in fact the tower wake must be meandering and may exhibit some periodic (vortex street) character.

From these three data sets one can conclude that the model is reasonably accurate in representing the flap behavior of the Combined Experiment rotor. It can also be concluded that dynamic stall has a slight effect on the flap moments and that including dynamic stall in the model improves the accuracy of the predictions. From a designer's point of view, it is likely that the model is more accurate than the knowledge of wind characteristics which must be entered into the model when seeking extreme load conditions.

Yaw Moment Predictions. The most important validation for the purposes of this project is of yaw moment predictions. Accurate prediction of yaw moments is necessary for design of yaw control systems. It is also important that the yaw loads be calculated correctly for accurate prediction of free-yaw motions. The same three data sets discussed above were used to examine the adequacy of the yaw load predictions. YawDyn was run with the same inputs as detailed above as well.

Figures 5.9 through 5.12 show comparisons of measured and calculated yaw moments for the three data sets. A 180 ft-lb, 1p cyclic yaw moment was added to all of the predictions to account for the known mass imbalance of the rotor. Since YawDyn cannot directly model the mass imbalance as it can the pitch imbalance, the 1p load was added to the YawDyn outputs. Figures 5.9 and 5.10 show the same data, but Figure

5.10 focuses on the first seconds of the simulation so that the cyclic content of the yaw moment can be more easily seen.

In all cases the mean and 1p yaw moments show the best agreement while the 3p cyclic moment shows less consistent agreement. As in the flap moment comparisons, the cyclic moment is over- and under-estimated at various times in the simulations. Since the 3p load results primarily from 4p flap oscillations, this result is expected and occurs for the same reason as the inconsistencies noted in the 4p flap moments.

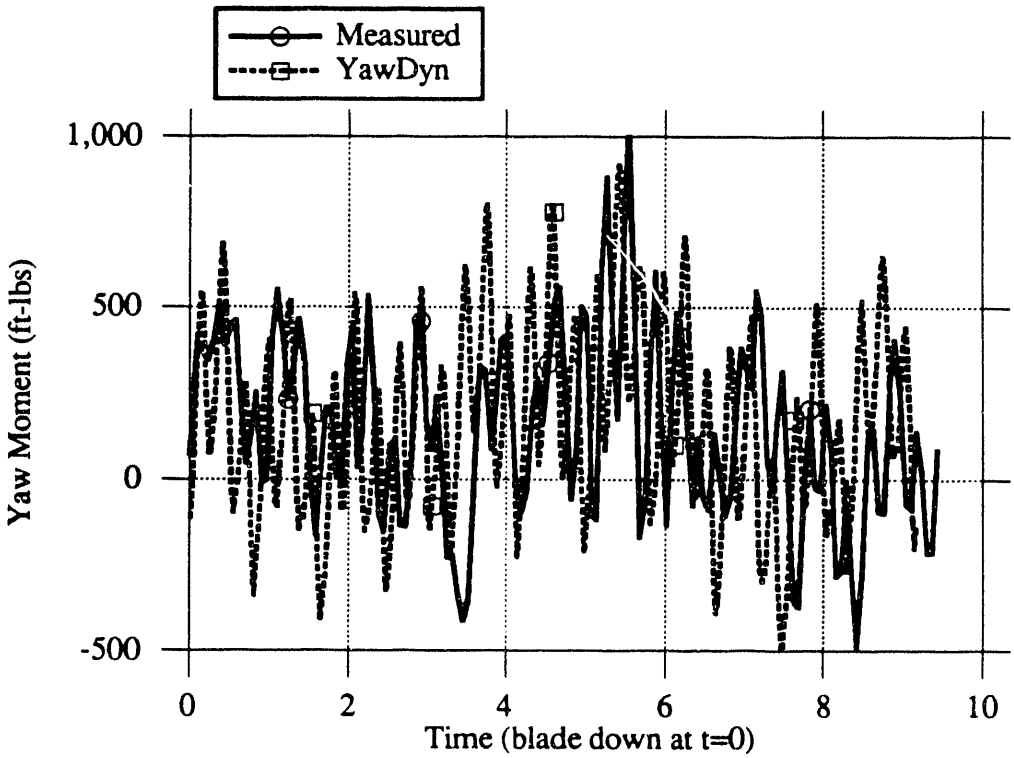

Figure 5.9 Comparison of predicted and measured yaw moments. YawDyn predictions include a 180 ft-lb, 1p moment due to mass imbalance. Combined Experiment data set CE901-1.

It will be shown in Section 6 that the dynamic stall and skewed wake correction have a very significant effect on the yaw moment predictions. Without these factors included in the analysis the agreement between measured and predicted yaw moments is much poorer. For example, Figure 5.13 shows the results from the CE901-3 data set (Figure 5.12) compared with the predictions when dynamic stall is not considered in the model. The curve labeled "YawDyn w/o DS" is the prediction with both Gormont parameters set to zero to entirely remove the stall hysteresis. It is clear that the mean yaw moment is greatly influenced and that the agreement is poorer than when the hysteresis is included. This data set had high wind speed and a large yaw angle resulting in high mean and cyclic angles of attack. Thus it is particularly affected by dynamic stall. But similar influences are seen, though to a lesser extent, in lower winds.

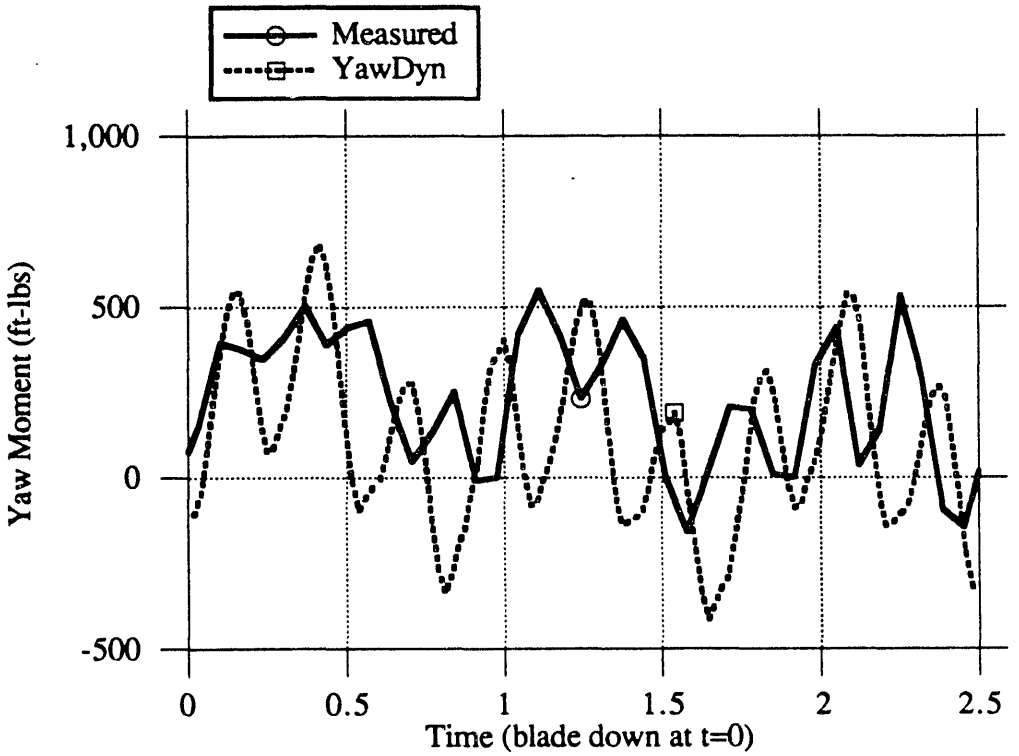

Figure 5.10 Expanded view of Figure 5.9 showing the first three revolutions of the rotor. Combined Experiment data set CE901-1.

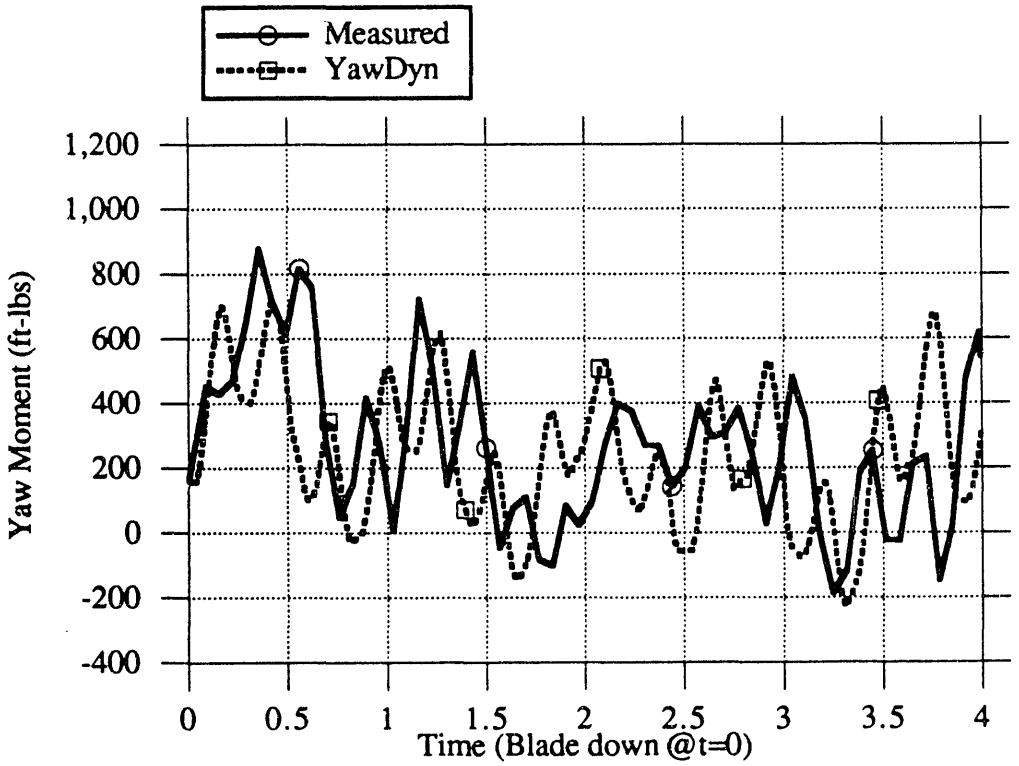

Figure 5.11 Comparison of predicted and measured yaw moments. YawDyn predictions include a 180 ft-lb, 1p moment due to mass imbalance. Combined Experiment data set CE901-2.

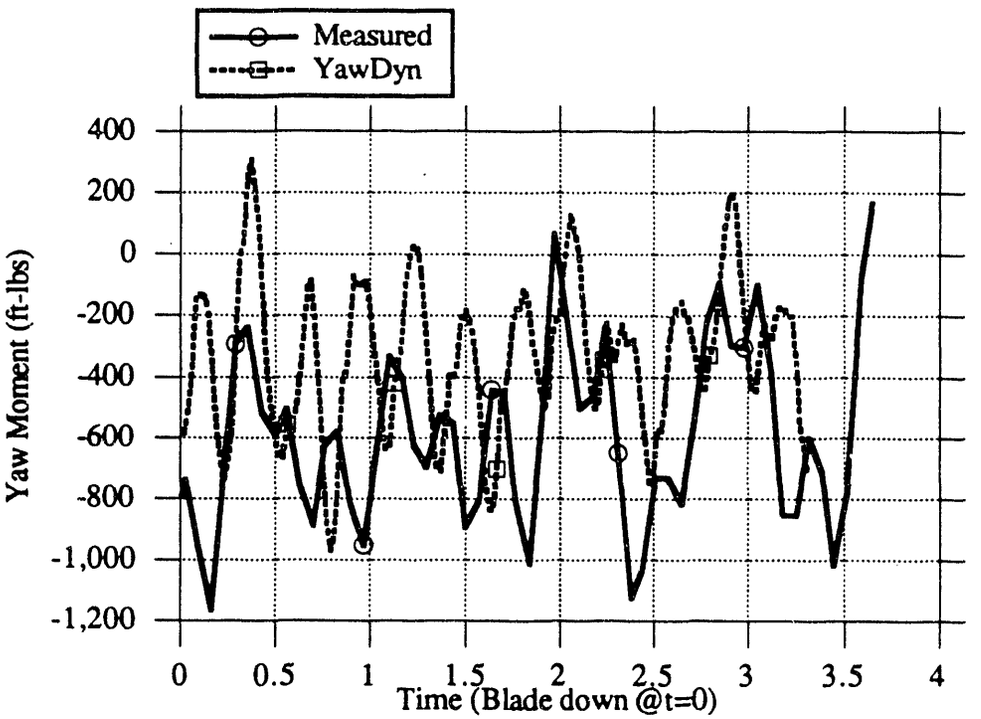

Figure 5.12 Comparison of predicted and measured yaw moments. YawDyn predictions include a 180 ft-lb, 1p moment due to mass imbalance. Combined Experiment data set CE901-3.

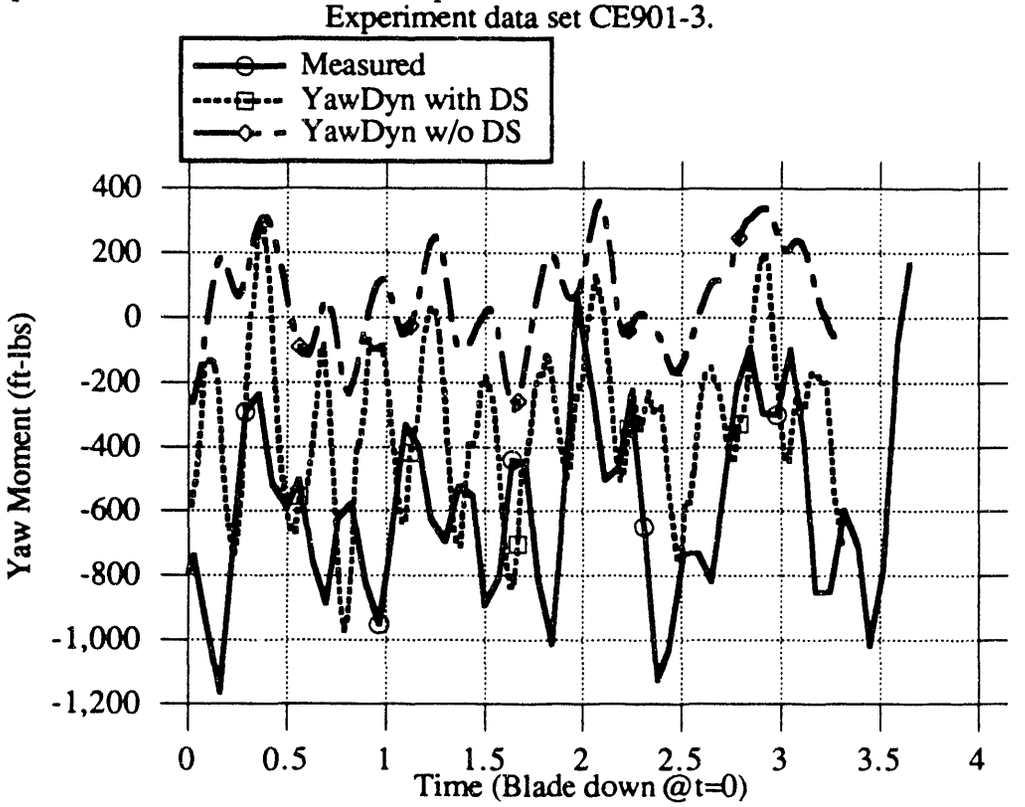

Figure 5.13 Comparison of predicted and measured yaw moments showing the influence of stall hysteresis. YawDyn predictions include a 180 ft-lb, 1p moment due to mass imbalance. Combined Experiment data set CE901-3.

Dynamic Stall Model. A final point regarding the Combined Experiment validation can be made by examining the lift coefficient and angle of attack as measured and predicted. First notice in Figure 5.14 that the angle of attack varies in a cyclic manner, primarily at 1p. The dominant cause of this 1p variation is the advancing and retreating blade while the rotor is yawed. There is also a brief, sharp dip in the angle of attack as the blade passes through the tower shadow. This is observed as a brief (approximately 100-200 ms) episode as the angle reaches the maximum value of each revolution. Both the test data and the predictions display this same character, though it is much less regular in the test data.

Figure 5.15 demonstrates clearly that there is stall hysteresis on this blade. The measurements and predictions both demonstrate the hysteresis, though again the measurements show considerably more variability in the values. As mentioned earlier, this hysteresis results in asymmetry of the lift coefficient from one side of the rotor to the other. This is the cause of the high mean yaw moments observed in the predictions and measurements.

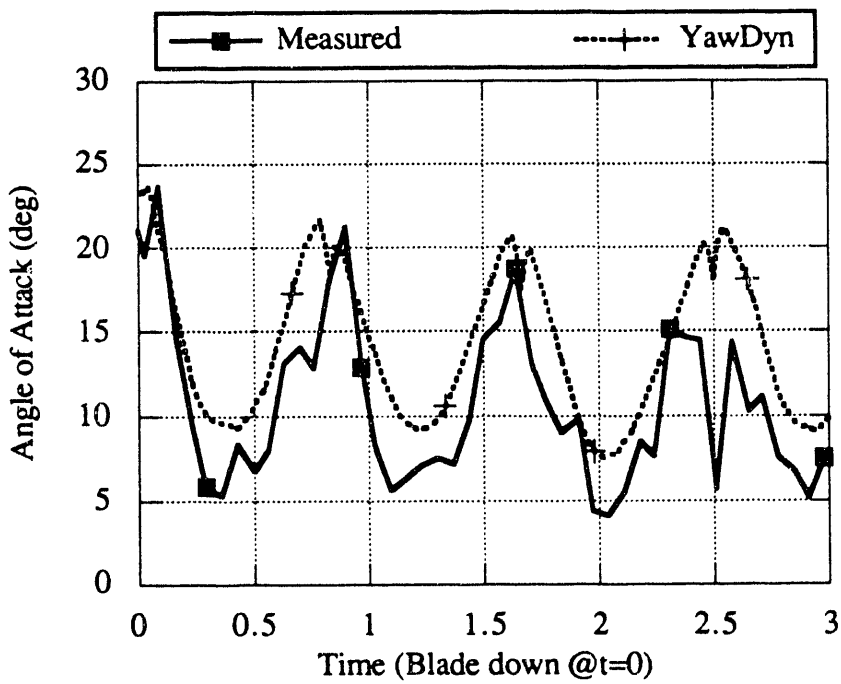

Figure 5.14 Angle of attack time history for data set 901-3. Note the characteristic 1p variation with a sharp dip caused by tower shadow.

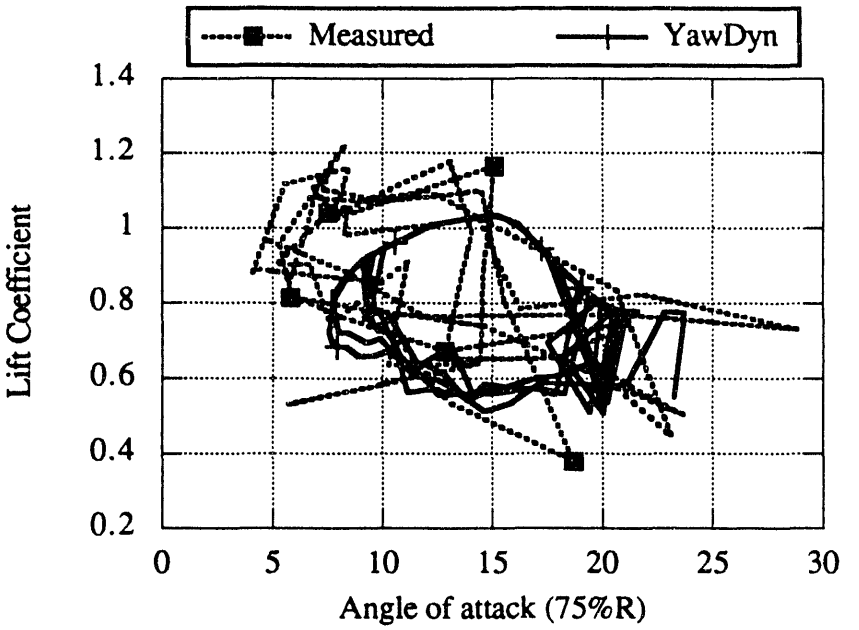

Figure 5.15 Comparison of stall hysteresis as measured at the 80% station and predicted at the 75% station for data set 901-3.

5.4 Free-yaw predictions and measurements from the Combined Experiment rotor

The YawDyn program is capable of predicting yaw motions as well as yaw loads. There is little data available with sufficient resolution of the approach wind (including wind shears and vertical wind) for validation of the calculations. However, one data set was obtained from the SERI Combined Experiment. The rotor was held at a fixed yaw angle, -32° from the wind direction. It was then released (at time=0) to yaw freely for a short period before the yaw brake was once again applied. Measurements of the horizontal wind approaching the rotor were made with a vertical-plane array of vane-type anemometers. The measured wind speed, wind direction, horizontal shear and vertical shear were input to YawDyn as a function of time to simulate the same test conditions. The vertical component of wind was not available and was assumed zero.

The predicted yaw motion is compared with the measured motion in Figure 5.16 below. Both the predictions and measurements show a slight overshoot in the yaw response. The general shapes of the two curves are very similar, with both showing that the rotor does not return to zero yaw angle. The predicted yaw rate (and hence the time required to reach a yaw angle of zero) is faster than the measured value.

The predictions were made assuming a constant yaw friction of 75 ft-lbs and zero mechanical yaw damping. These values were arbitrarily selected since the actual values were not available. Lack of measured values limits the ability to completely assess the accuracy of the prediction method. The mass moment of inertia of the system about the yaw axis was estimated from the weights and locations of major elements. There is an uncertainty of approximately 25% in this value. However, increasing the yaw inertia by 25% is not sufficient to achieve a match between the predicted and measured time to reach zero yaw angle.

This comparison and the results of sensitivity studies lead to the conclusion that the yaw motion predictions are reasonable but of unknown absolute accuracy.

5.5 Teeter Predictions by YawDyn and STRAP

Near the end of the research project, the YawDyn program was modified to permit analysis of the teetering rotor. In this section the program is compared with the STRAP code (the SERI Teetering Rotor Analysis Program, a derivative of the FLAP code). This was done to verify basic operation of the YawDyn teetering option and should not be considered a thorough validation of the program or its underlying assumptions. Considerable work must be done in the future to determine the most useful method for analyzing the teetering rotor.

Table 5.4 lists a number of model inputs for the comparisons that follow. Though at first glance the inputs may appear inconsistent, they were selected to match the location of the rotor center of gravity relative to the teeter axis. To minimize differences in the approaches of YawDyn and STRAP, both were used to analyze an idealized rotor similar to the ESI-80. Since STRAP employs a linear aerodynamics model, both programs were given inputs to create a linear lift curve over the full range of angle of attack (±180°). The drag coefficient was set to zero to eliminate differences in the approach to modeling the drag behavior. This is clearly not realistic but does ensure that differences in the predictions of the code are not due to differences in the airfoil model. The yaw angle was set to zero to eliminate effects due to skewed wake corrections. Dynamic stall, vertical component of wind speed and horizontal shear are not available in STRAP and were therefore not used in YawDyn. Delta-three is not available in the YawDyn model, necessitating use of $\delta_3=0$ in STRAP.

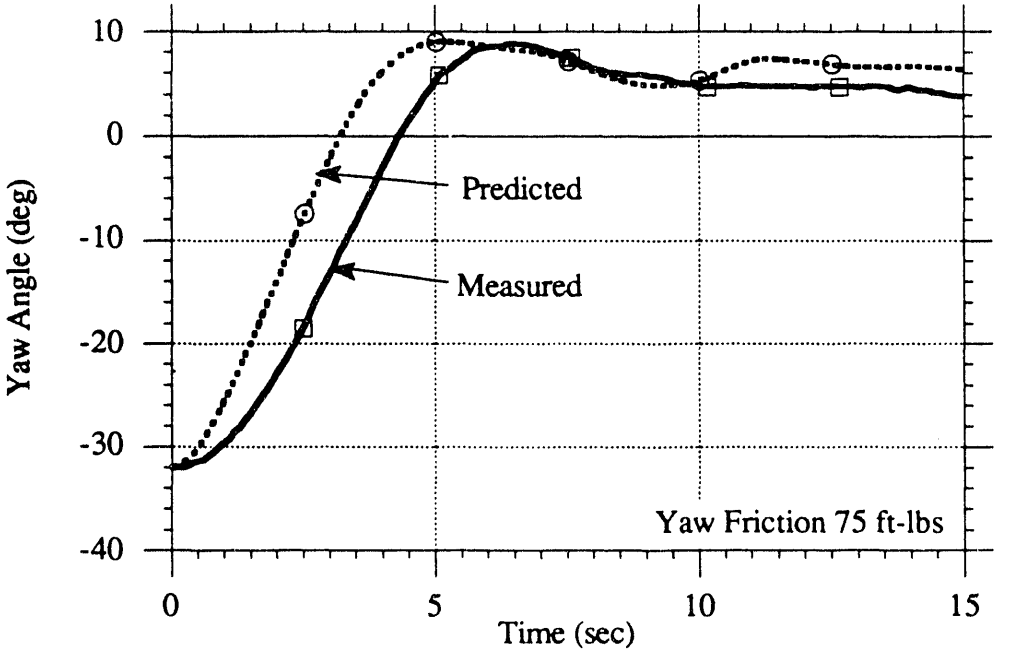

Figure 5.16 Comparison of predicted and measured free-yaw response of the Combined Experiment rotor. At time=0 the rotor was released from rest at a yaw angle of -32°. Data set number GS144.

Table 5.4 Parameters used in the YawDyn and STRAP analyses of the teetering rotor.

Parameter	YawDyn Value	STRAP Value
Yaw angle	0°	0°
Flap DOF?	Rigid teeter	One mode (rigid teeter)
Hub	Teetering, δ_3=0	Teetering, δ_3=0
Pitch angles (all blades)	0°	0°
Dynamic stall	None (A=0.0, B=0.0)	NA
Number of sectors	200	NA
Convergence tolerance	0.01°	2%
Horizontal shear	0.0	0.0
Vertical wind component	0.0	0.0
Tower shadow	None	None
Blade mass (slugs)	55.7	26.71
Hub mass (slugs)	0	55.9
Undersling (feet)	0.28	0.75
Hub distance (feet)	NA	0.24
Lift curve slope	5.2	5.2
Drag coefficient	0.0	0.0

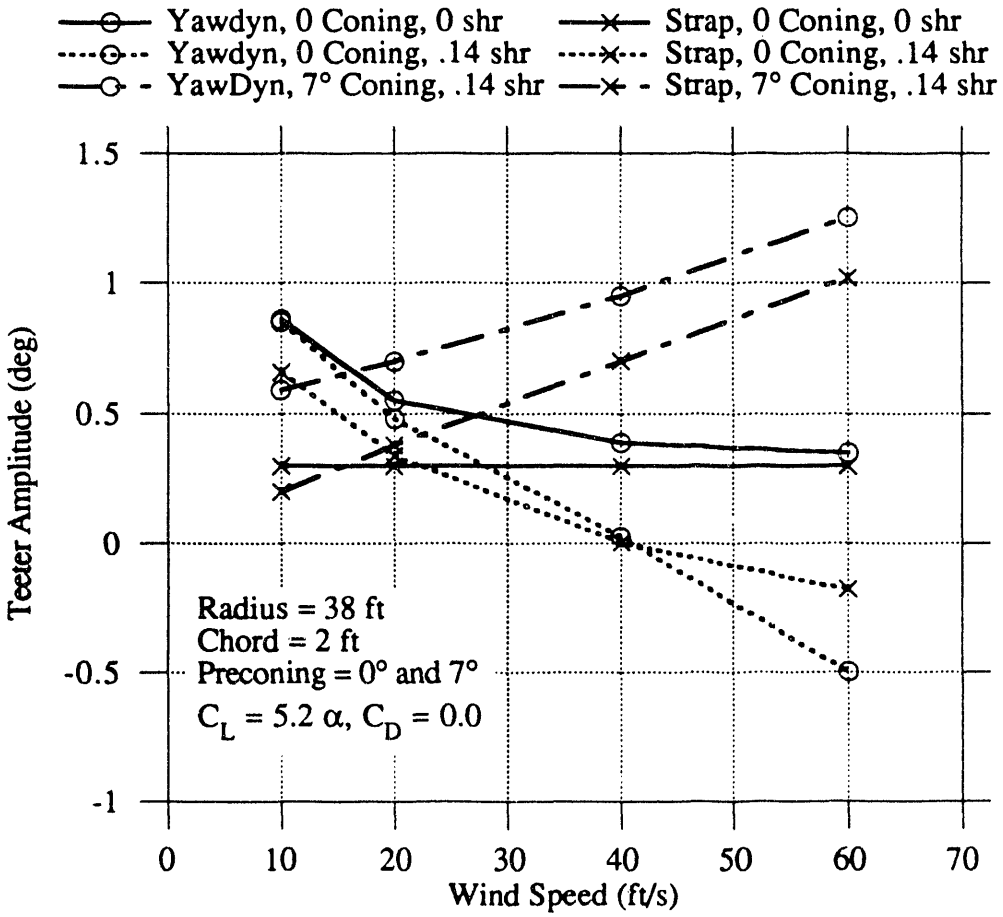

Figure 5.17 Teeter amplitudes predicted by YawDyn and STRAP.

With these restrictions and conditions, the excitation of teeter motion was due to undersling or vertical wind shear. Both were investigated with the results shown in Figure 5.17. In all cases shown the rotor mass offset from the teeter axis caused teetering motion. Four of the curves also show the effect of 1/7 power-law vertical wind shear (.14 shr). The two programs produce the same trend when there is vertical wind shear. With no coning and no shear, STRAP predicts a teeter amplitude independedent of wind speed while YawDyn predicts decreasing teeter amplitude as wind speed increases. This is a result of differences used in the two programs to estimate induced velocities. YawDyn iterates to find a solution to the full, nonlinear equation for the induction factor. STRAP uses small angle assumptions in conjunction with a linear lift curve to develop an approximate, explicit equation for the induced velocity. This leads to significantly reduced computation time, since iteration is not required, but also yields a result which is less accurate. The linearized, analytic solution of Stoddard [Stoddard, 1978; Stoddard, 1988] gives the same result as STRAP in the simple case where undersling is the only teeter forcing function. Since YawDyn is solving the more exact equation, it is expected that it yields a more accurate result. The two programs give the same prediction at the windspeed where they have the same induced velocity.

There is one other potentially important difference between the aerodynamic analyses of YawDyn and STRAP. YawDyn assumes the wake is always in equilibrium (quasi-steady flow). STRAP assumes the wake is frozen. Thus YawDyn includes the effect of the blade flap velocity in the estimation of the induced velocity while STRAP does not. It is unclear from these simple validation tests how much this difference in assumptions may contribute to the differences in the program predictions.

From this simple validation test one can conclude that YawDyn is producing reasonable results and contains no programming errors which give results inconsistent with the underlying equations and assumptions. Much more work is required before the method can be proven to yield results which are accurate in an absolute sense.

6.0 Sensitivity Studies

6.1 Introduction

One of the primary objectives of this research was to determine factors which have the greatest influence on the yaw loads and motions of the horizontal axis wind turbine. To accomplish this objective YawDyn was run for a wide variety of wind, machine and model parameters. Then the changes in predicted mean and cyclic loads were examined to determine which loads were most affected by the various inputs and assumptions. This process was performed continuously throughout the project for a number of rigid-hub rotors. There were far too many conditions and assumptions to present in this report. A number of the findings were presented in annual progress reports and papers. In this report the results of a final series of sensitivity studies will be presented. This series was selected to highlight the most important findings from the past years' work.

All comparisons were done in a manner which was as self-consistent as possible. First a baseline rotor and operating condition was selected. The SERI Combined Experiment rotor was selected for the rigid hub studies and the ESI-80 was selected for the teetering hub cases. The baseline conditions used the model with the most accurate assumptions (e.g. dynamic stall, skewed wake corrections and the flap DOF were included) and typical wind conditions. Then a series of calculations were performed where only one parameter at a time was changed to observe the importance of that parameter.

The magnitude of change for each parameter was subjectively selected to represent a comparable and "significant" change. This rather arbitrary method was employed with the goal of identifying the important parameters in a realistic and practical manner. Other methods which are more quantitative, such as selecting a fixed percentage change in each parameter, were felt to be less useful. For instance, a 50% change in the blade stiffness would be a much more dramatic change (and more difficult to execute in the design) than a 50% change in the vertical wind shear. And many of the parameters have a baseline value of zero, making percent changes meaningless.

It is important to note that the sensitivity results presented in this report are felt to be generally valid and applicable to a variety of wind turbines. It is clear, however, that there will be many exceptions to the general observations noted below. These comparisons are for illustrative purposes only and should not be applied literally to any other wind turbine. The only way to draw conclusions about a particular configuration is to exercise similar sensitivity studies for that turbine.

6.2 Rigid-hub configuration

The SERI Combined Experiment rotor was selected as the configuration for the rigid-hub sensitivity studies. This was done because there is excellent data available for the rotor and airfoil and it is a configuration typical of many others. The general characteristics of the machine are presented in Appendix B. The rotor has some characteristics which are particularly important in the present study. The natural frequency of the blade in the first rotating flap mode is 4.06p. This proximity to a rotor harmonic results in substantial flap response at 4p. The 4p blade flap generates a large 3p yaw moment (see section 3.2). Other rotors will generally not exhibit this large 4p flap response. Also, the blades are untwisted. Thus the stall boundary moves slowly

out along the blade as the wind speed increases rather than abruptly stalling over much of the span as it might if the blade were twisted. This means that other rotors may see more dramatic changes in loads near the stall boundary as wind or rotor conditions are varied.

Prior to conducting the sensitivity studies a number of calculations were performed to establish the basic performance of the system. The rotor was analyzed using YawDyn with all options "on" to provide the most realistic analysis. The wind speed was varied for a zero yaw angle and the yaw angle was varied for a fixed wind speed to see how the global characteristics such as power output and mean loads would change. The results are summarized in the figures below. In these figures the operating conditions are as noted in Table 6.1 except as noted on the figures.

Figure 6.1 shows the variation of mean rotor power and flap moments as a function of yaw angle. The plot uses the Cosine of the yaw angle for the x-axis and shows least-squares curve fits to illustrate that both the power and flap moment vary approximately as the first power of the cosine of the yaw angle. The power and loads are not identical for positive and negative yaw angles because the 1/7 power-law vertical wind shear and tower shadow (with blade flexibility) introduce a slight asymmetry.

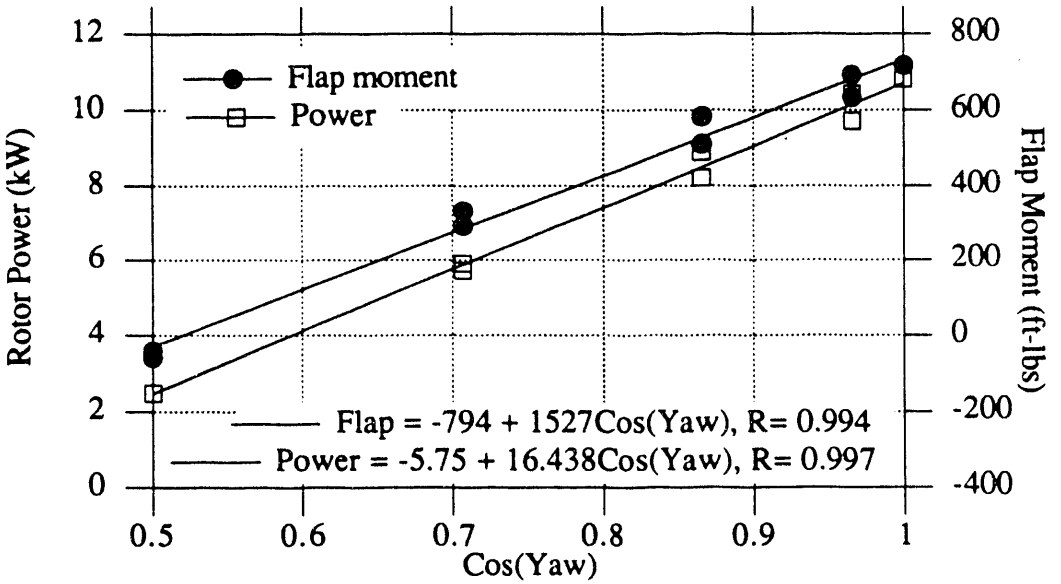

Figure 6.1 Variation of the predicted power output and mean flap moment of the Combined Experiment rotor. Wind speed 37 ft/s, yaw angles from +60° to -60°.

Figure 6.2 shows the variation of mean yaw moment with yaw angle for a wind speed of 37 ft/sec. Note the yaw moment depends nearly linearly upon the yaw angle over a wide range of angles. It is also important to note the yaw moment is not zero at zero yaw angle. This means the rotor will tend to operate in a steady-state at a small (approximately +3°) yaw error. This offset is caused by vertical wind shear and tower shadow and will depend upon the wind speed. The yaw moment is positive when the yaw angle is negative (and vice versa), except at very small angles. Thus the moment acts to reduce the yaw angle. This means the rotor will operate in a statically stable manner in downwind, free-yaw motion.

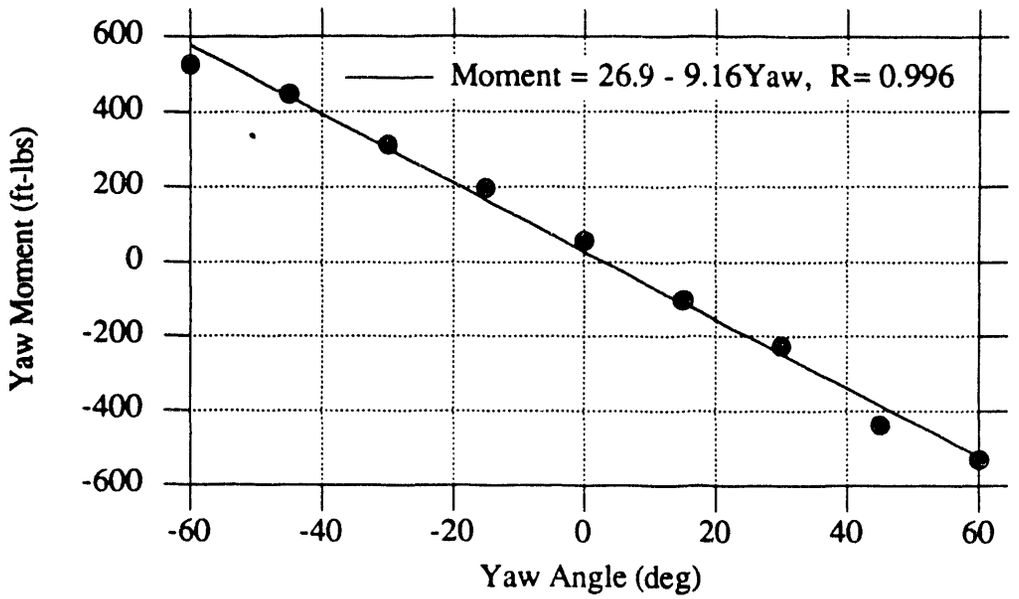

Figure 6.2 Variation of the predicted mean yaw moment of the Combined Experiment rotor. Wind speed 37 ft/s, yaw angles from +60° to -60°.

Figure 6.3 illustrates the variation of the mean loads with changes in wind speed. Figure 6.4 shows the variation in the mean angle of attack at the 75% radius and the mean rotor power for the same conditions.

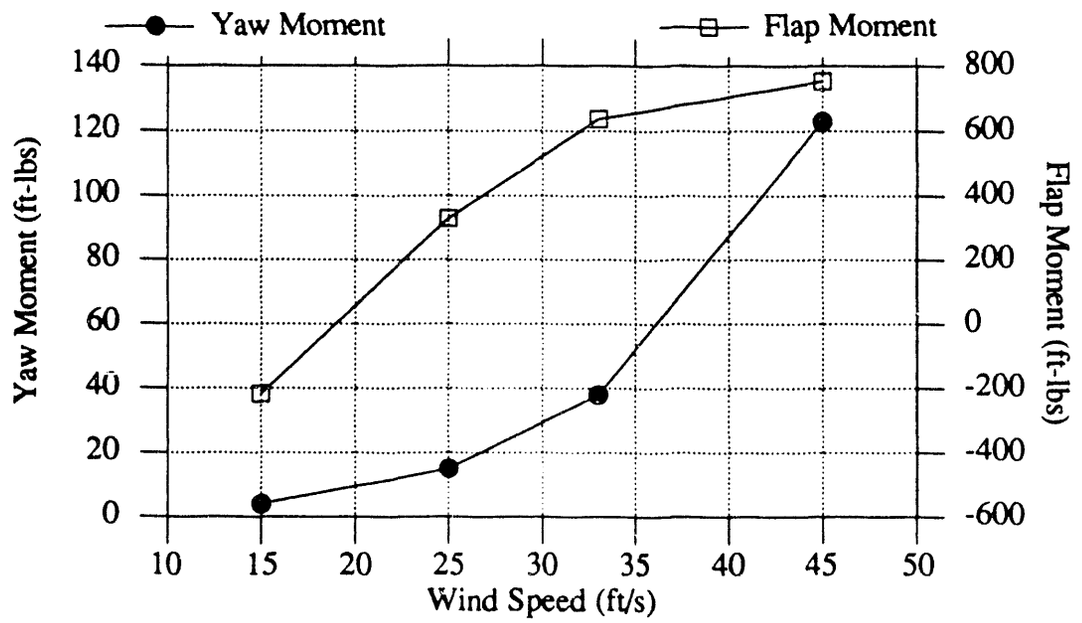

Figure 6.3 Variation of the predicted mean flap and yaw moments of the Combined Experiment rotor with hub-height wind speed. Yaw angle 0°.

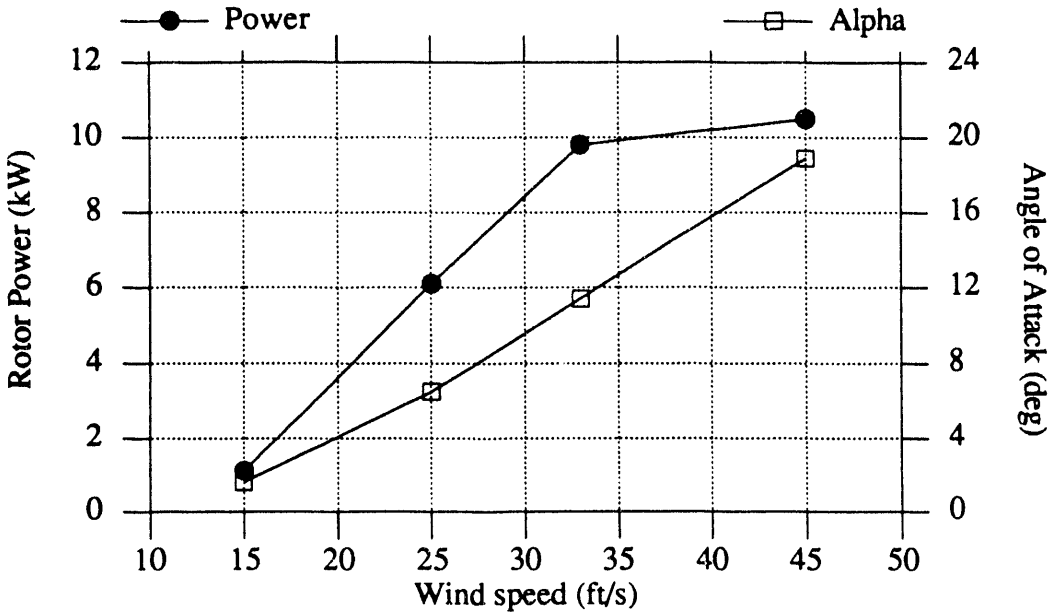

Figure 6.4 Variation of the predicted mean rotor power and angle of attack at the 75% station of the Combined Experiment rotor. Yaw angle 0°.

The results depicted in Figures 6.1 through 6.4 led to selection of a wind speed of 37 ft/sec and a yaw angle of -30° for the sensitivity studies. At these conditions the 75% station is near the stall angle on average and moving in and out of stall as the blade rotates. This makes it possible to observe the effects of stall parameters in the modeling. To assist the reader in understanding the results of the sensitivity studies some figures are provided to depict the state of the rotor while operating in the baseline configuration.

Figure 6.5 shows the variation in angle of attack at the 75% station for the baseline conditions listed in Table 6.1. Note the blade is moving in and out of stall as the yaw angle causes cyclic variation in the angle of attack. For this particular rotor the -30° yaw angle and 10% tower shadow cause a 12° peak-to-peak change in angle of attack. The axial induction factor indicates the blade is moderately loaded at the 75% station.

Table 6.1. Baseline Conditions for the Rigid-Hub Sensitivity Studies

Rotor	SERI Combined Experiment
Pitch angles	Each blade at +5°
Mass balance	Ideal
Wind speed	37. ft/sec
Yaw angle	-30.°
Vertical wind shear	0.14 power law profile
Horizontal wind shear	0.0
Tower shadow	10%
Vertical wind speed	0.0
Dynamic stall parameters	A = 0.0, B = 0.7
Yaw stiffness	"fixed"
Blade flap frequency	4.06 p
Low-speed shaft length	5 ft
Shaft tilt	0°

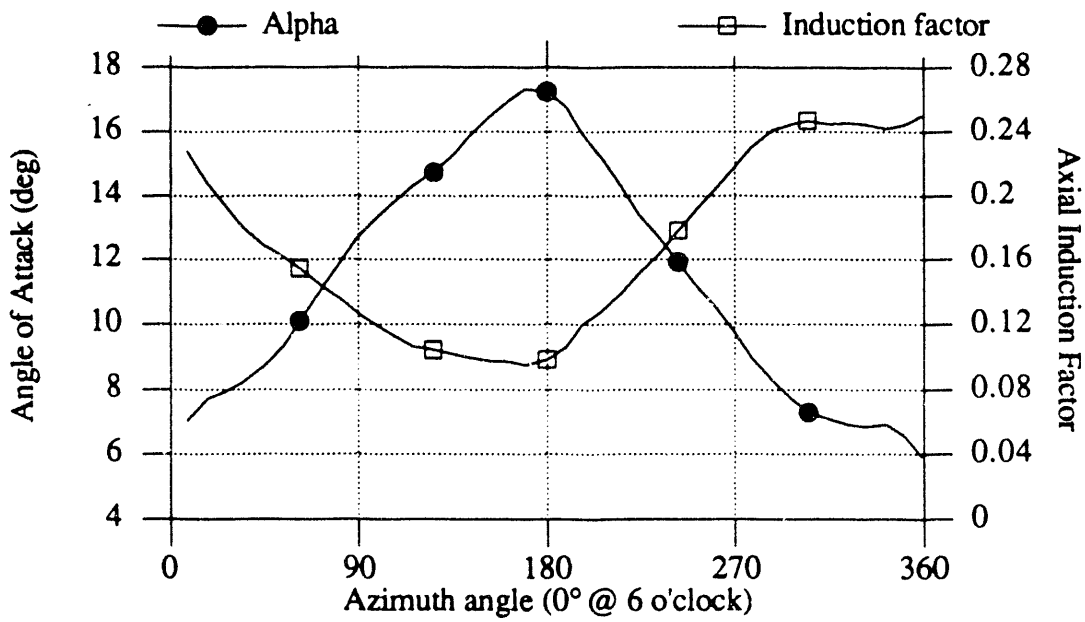

Figure 6.5 Variation of angle of attack and axial induction factor at the 75% station in the baseline configuration.

Figure 6.6 shows the cyclic nature of the root flap and yaw moments. The flap moment contains significant 1p and 4p cyclics caused primarily by the yaw angle and tower shadow. The blade flap natural frequency near 4p results in a large response at 4p. The 4p flap moment causes a significant 3p yaw moment while the mean yaw moment results from the 1p flap moment. Note there is virtually no 1p yaw moment as long as the rotor is mass and pitch balanced.

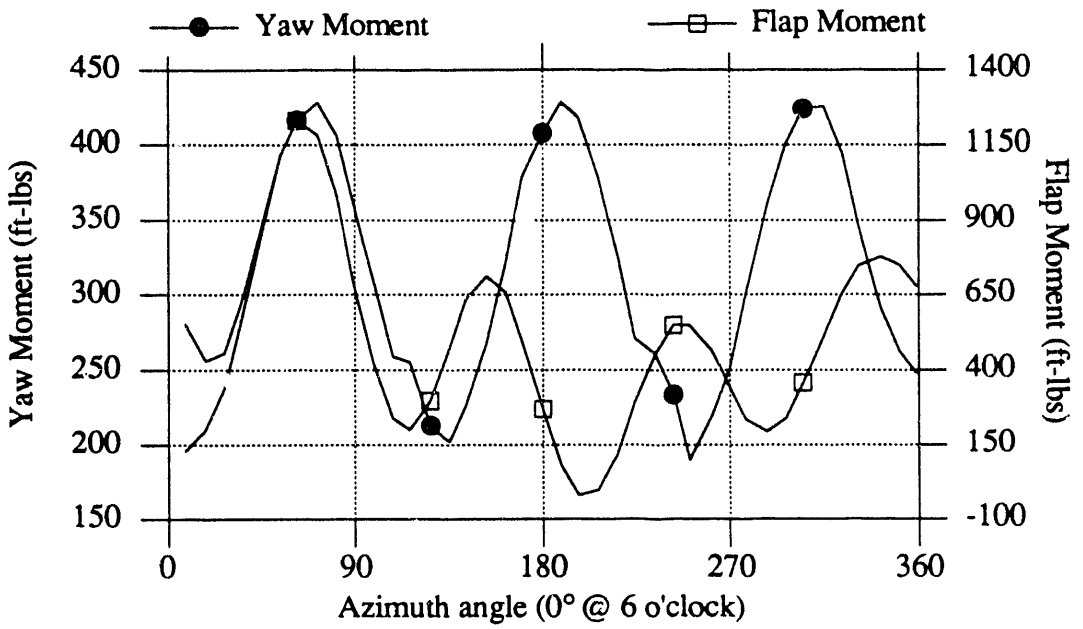

Figure 6.6 Yaw and root flap moments in the baseline configuration.

Figure 6.7 shows the stall hysteresis predicted by YawDyn when the rotor is in the baseline configuration. The upper hysteresis loop constant, A, equals 0.0, and the lower loop constant B equals 0.7 in this figure. Thus there is no dynamic overshoot of the C_L but there is considerable hysteresis as the angle of attack is decreasing. The calculation is shown for azimuth angles between 8° and 359°. The small loop observed in the lower left portion of the figure is caused by the tower shadow.

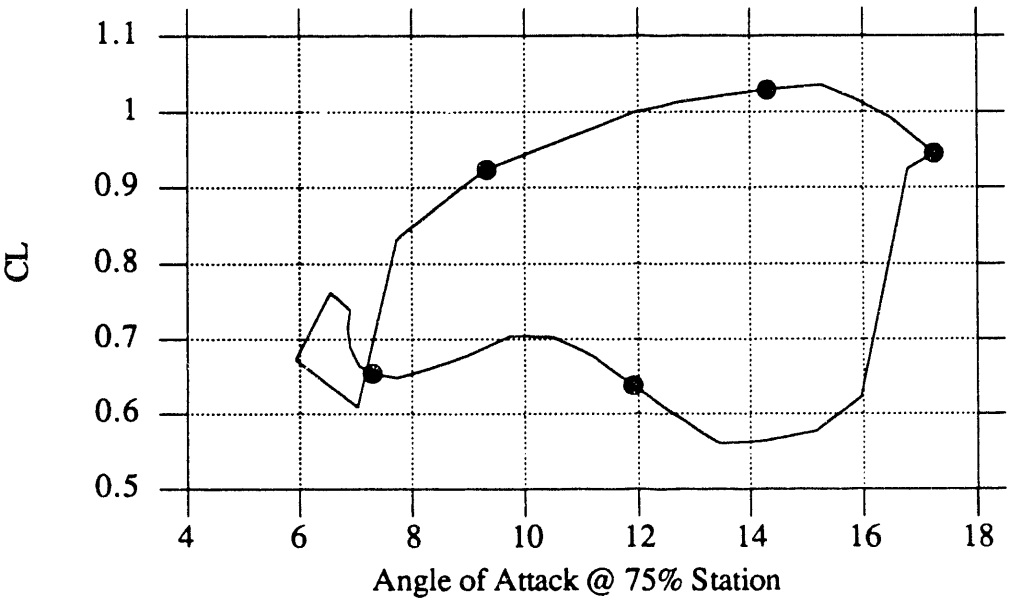

Figure 6.7 Stall hysteresis at the 75% station in the baseline configuration.

Having established the major characteristics of the baseline operation, it is useful to examine the effects of changes in some of the machine, wind and model parameters

which can be selected or adjusted in YawDyn. Rather than present the detailed results for each condition that were presented above for the baseline condition, the key results are summarized in Tables 6.2 and 6.3 below. In all cases the basic waveforms and character of the rotor response remains the same, though there are very large variations in the loads and the relative magnitudes of the various load harmonics. (The only exceptions to this are the cases where the yaw stiffness option is employed in YawDyn. In those cases the waveforms are altered in both harmonic content and amplitude.)

In these tables the first two columns list the parameter under investigation and the new value of the parameter. In each line of the tables the parameter listed is the only change from the baseline configuration. The remaining columns tabulate the loads and the percent change in the load from the baseline result. A quick scan down any given column will show the parameters which have the greatest effect on the given load.

First examine the mean yaw load columns in Table 6.2. The largest changes in mean yaw moment are caused by horizontal wind shear, the neglect of dynamic stall or skewed wake corrections, vertical wind component, and yaw angle. A number of parameters have little influence on the mean yaw moment. Perhaps the most surprising is the "low speed shaft length" (the distance from the hub to the yaw axis). Prior to this research it was common to hear discussion of changes in this moment arm causing changes in a rotor's yaw behavior. But, as noted earlier, the dominant yaw loads from a rigid rotor are caused by differences in flap moments. These moments are essentially independent of the shaft length, hence the mean yaw moment is not greatly influenced by the shaft length.

It is important to note the importance of the dynamic stall and skewed wake corrections in the aerodynamic analysis. The mean yaw moment is over two orders of magnitude too small when classical blade-element/momentum aerodynamics methods are used to estimate the yaw loads.

Next examine the 3p yaw moments. Since these loads result primarily from the 4p flap moments, any factor which influences the 4p flap loads can exert a strong influence on the 3p yaw loads. The dynamic stall and skewed wake corrections and vertical wind component which were so important to mean yaw loads have a lesser influence on the cyclic loads. But tower shadow, blade or yaw axis natural frequency and horizontal wind shear have a striking influence on the cyclic yaw loads.

1p yaw moments are not included in Table 6.2 because the only source of 1p yaw loads is an imbalance in the rotor. Mass or pitch imbalance can cause large 1p yaw loads as indicated in the footnotes to the table. Neither mass nor pitch imbalance cause significant flap loads or mean and 3p yaw loads unless the imbalance is sufficient to excite system natural frequencies by means of nacelle pitch or yaw motion.

Mean flap moments change less than the mean yaw moments for any condition. This emphasizes the fact that the yaw loads result from small differences in the large flap loads. Thus it is reasonable to expect that the yaw loads will be more sensitive to changes in wind or machine characteristics than the flap loads. Elimination of the flap degree of freedom changes the mean flap moment by not allowing the mean coning angle to change in response to airloads. The other parameter which has a strong influence on mean yaw loads is the yaw angle. This is expected as the yaw angle reduces the wind component normal to the rotor.

Cyclic flap moments vary more than the mean flap moments but less than the yaw loads. As noted above the blade and yaw column natural frequencies and the tower shadow and horizontal wind shear have the greatest influence on cyclic flap loads.

Table 6.2 Sensitivity of yaw moments to changes in machine and wind parameters

Condition	New Value	Mean Yaw Moment (ft-lbs)	Percent Change	3p Yaw Moment (ft-lbs)	Percent Change
Baseline	See Table 6.1	312	0	552	0
Machine Configuration					
Low speed shaft length	1 ft	330	6	551	0
Low speed shaft tilt	+4°	343	10	537	-3
Mass balance[1]		313	0	556	0
Pitch balance[2]	Blades @ 4°,5° & 6°	311	0	561	2
Aerodynamics					
Dynamic stall	No dynamic stall	114	-63	447	-19
Skewed wake correction	No skewed wake correct.	207	-34	527	-5
Skewed wake & dynamic stall	No dyn. stall or skew wake	1.6	-99	407	-26
Structural Dynamics					
Blade frequency	4.35p	310	-1	227	-59
Blade frequency	Infinite (no flap DOF)	307	-2	83	-85
Yaw drive stiffness (free yaw)	$1x10^5$ ft-lb/rad	302	-3	48	-91
Yaw drive stiffness (free yaw)	$4x10^5$ ft-lb/rad	294	-6	116	-79
Wind Inputs					
Yaw angle	-15	197	-37	467	-15
Vertical shear	0.4	397	27	454	-18
Horizontal shear	0.2	469	50	754	37
Horizontal shear	0.5	648	108	1091	98
Tower shadow	0.0	306	-2	54	-90
Vertical wind component	3.7 ft/s	430	38	574	4

Notes:

1. Blade imbalance causes a 1p yaw moment of 190 ft-lbs, calculated using equation 3.11. The mass imbalance is assumed to have little effect on other harmonics. Mass imbalance is not modeled directly in YawDyn.
2. Pitch imbalance induces an 78 ft-lb, 1p yaw moment. In the baseline condition there is zero 1p cyclic yaw moment.

Table 6.3 Sensitivity of blade root flap moments to changes in machine and wind parameters.

Condition	New Value	Mean Flap Moment (ft-lbs)	Percent Change	1p Flap Moment (ft-lbs)	Percent Change	4p Flap Moment (ft-lbs	Percent Change
Baseline	See Table 6.1	512	0	274	0	302	0
Machine Configuration							
Low speed shaft length	1 ft	512	0	274	0	302	0
Low speed shaft tilt	+4°	458	-11	262	-4	310	3
Mass balance		512	0	274	0	302	0
Pitch balance	Blades @ 4°,5° & 6°	549	7	297	8	355	18
Aerodynamics							
Dynamic stall	No dynamic stall	584	14	240	-12	283	-6
Skewed wake correction	No skewed wake correct.	511	0	228	-17	329	9
Skewed wake & dynamic stall	No dyn. stall or skewed wake correct.	587	15	227	-17	295	-2
Structural Dynamics							
Blade frequency	4.35p	516	1	273	0	147	-51
Blade frequency	Infinite (no flap DOF)	645	26	275	0	21	-93
Yaw drive stiffness (free yaw)	$1x10^5$ ft-lb/rad	505	-1	261	-5	63	-79
Yaw drive stiffness (free yaw)	$4x10^5$ ft-lb/rad	513	0	271	-1	49	-84
Wind Inputs							
Vertical shear	0.4	449	-12	268	-2	238	-21
Yaw angle	-15	632	23	151	-45	288	-5
Horizontal shear	0.2	498	-3	398	45	415	37
Horizontal shear	0.5	457	-11	563	105	562	86
Tower shadow	0.0	526	3	297	8	110	-64
Vertical wind component	3.7 ft/s	511	0	297	8	328	9

Engineers designing a new rotor or troubleshooting an existing system may find it helpful to conduct sensitivity studies such as these for their system. Only a few hours are required to run enough cases to identify the most critical parameters. This information can then be used to guide selection of more detailed testing or analysis

conditions. Knowledge of the most critical parameters permits focus of resources on the most fruitful (or harmful) areas.

The two cases run to investigate the sensitivity to yaw stiffness deserve additional discussion. These cases were run with the free-yaw option selected (the only time the yaw stiffness is used) and are intended to simulate the stiffness of a yaw drive. They allow interaction of the flap and yaw degrees of freedom. Figure 6.8 shows the time-histories of the yaw and flap moments for the case when the yaw drive equivalent stiffness is 4×10^5 ft-lb/rad. Notice the motions have not yet reached a steady-state condition after four revolutions of the rotor. This is because the trim solution applies only to the flap degree of freedom with the rotor fixed in yaw. The transient solution marks the beginning of the "trimming" process for the combined yaw and flap degrees-of-freedom. The load harmonics given in the tables above are for the fourth revolution of the rotor when the yaw stiffness option is analyzed.

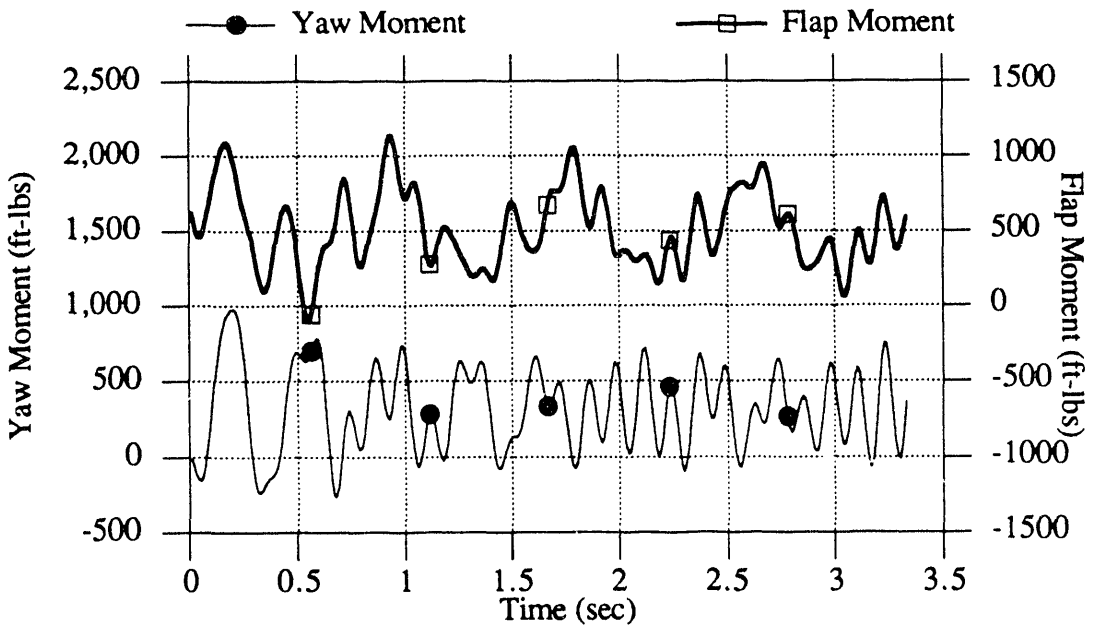

Figure 6.8. Yaw and flap moments with the rotor yawing against an effective stiffness of 4×10^5 ft-lb/rad. All other parameters match the baseline conditions of Table 6.1.

It is clear that selection of the yaw drive stiffness can greatly influence the yaw and flap loads. Obviously, if the stiffness is very high then loads will be the "fixed-yaw" values. If the stiffness places the yaw and flap motions in resonance then considerable amplification will result. A low stiffness can be used to reduce rotor loads if the selection is made with great care.

6.3 Teetering rotor configuration

The ESI-80 rotor was selected for the sensitivity studies with a teetering hub. This rotor was selected because it is one of the few teetering systems commercialized in the U.S. and it is well-known to the principal investigator (who participated in the design of the system). It is also the baseline configuration for the Advanced Wind Turbine design being conducted by R. Lynette and Associates under contract to SERI. The rotor is described in detail in Appendix B.

Baseline conditions for the study are summarized in Table 6.4 below. Table 6.5 summarizes the results of the sensitivity study for the yaw moment. In each case the conditions were as noted in Table 6.4, except for the single condition varied as noted in the "Condition" and "New Value" columns in Table 6.5.

Table 6.4. Baseline Conditions for the Teetered-Hub Sensitivity Studies

Rotor	ESI-80
Pitch angles	Both blades at 0°
Mass balance	Ideal
Wind speed	33.5 ft/sec
Yaw angle	20.°
Vertical wind shear	0.15 power law profile
Horizontal wind shear	0.0
Tower shadow	10%
Vertical wind speed	0.0
Dynamic stall parameters	A = 0.0, B = 0.5
Yaw stiffness	"fixed"
Low-speed shaft length	6.79 ft
Shaft tilt	0°

Characteristics of the rotor behavior are shown for the baseline configuration in Figures 6.8 and 6.9. The rotor teeters at the expected 1p frequency and the angle of attack history is also dominated by 1p fluctuations. However, the angle of attack also contains 2p components due to variations in local wind (including induced velocity) and a pulse at 0° azimuth due to tower shadow. The yaw and flap moments exhibit 2p oscillations with small pulses due to tower shadow. The flap moment also contains some energy at 1p.

Several observations are noteworthy in Table 6.5. First, notice the mean yaw moment is nearly tripled and the 2p moments increase nearly eightfold when the same rotor is not allowed to teeter. This illustrates the relative importance of the flap moments (which are not transmitted to the nacelle of a teetering rotor) and the horizontal force in determining the yaw moments. However, if the teeter stops are contacted (such as in the case with a 40° yaw angle) then the advantage of the teetering rotor is lost and the mean and cyclic yaw moments increase dramatically.

The teetering rotor sensitivity to wind inputs is markedly different from the rigid rotor. Note the increased importance of vertical wind shear and diminished importance of horizontal shear and vertical component of wind. Dynamic stall had little effect on the mean yaw moment in the case examined here. This is quite a contrast to the importance of dynamic stall on a rigid rotor.

The distance from the hub to the yaw axis was of minor significance for rigid rotor yaw loads because of the dominance of the blade flap moments. A teetering rotor depends upon the horizontal rotor force to generate yaw moments. Thus it is not surprising that the yaw load is sensitive to the shaft length. Likewise, the yaw moment is more sensitive to shaft tilt for a teetering rotor than a rigid rotor.

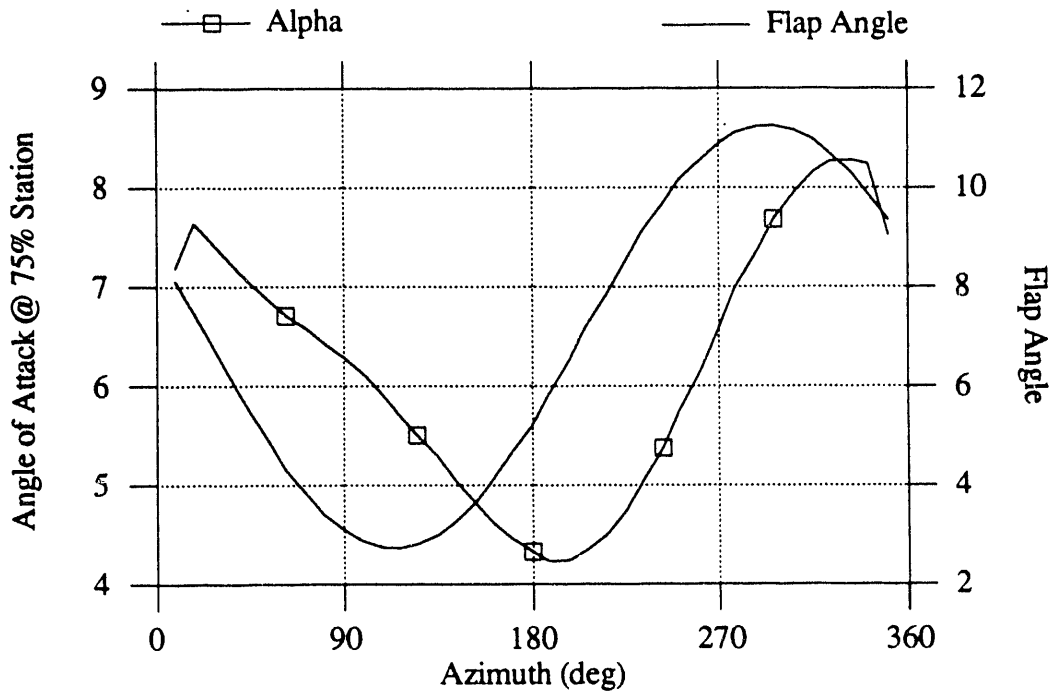

Figure 6.8 Flap angle and angle of attack history for the baseline teetering rotor case. The teeter angle is the difference between the flap angle and the precone angle of 7°.

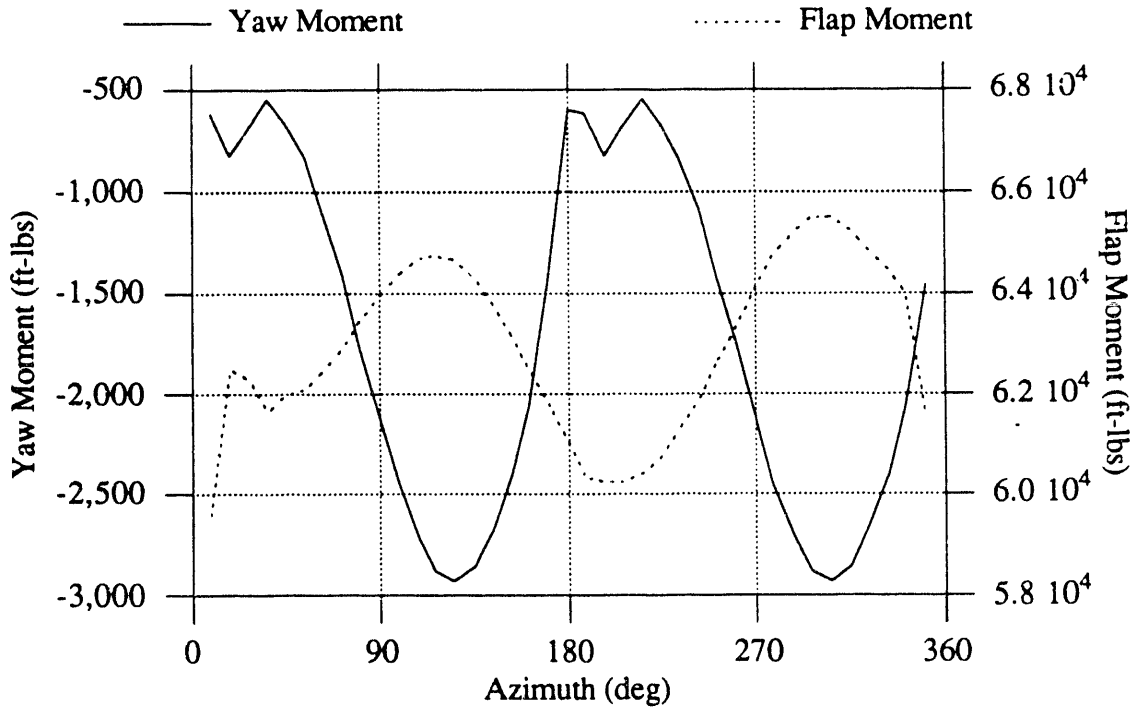

Figure 6.9 Yaw and root aerodynamic flap moment for the baseline teetering rotor case.

Table 6.5 Results of the teetered-hub sensitivity studies for the yaw moment. ESI-80 turbine operated at the conditions of Table 6.4, except as noted.

Condition	New Value	Mean Yaw Moment (ft-lbs)	% Change	2p Yaw Moment (ft-lbs)	% Change
Baseline	–	-1685	0%	1219	0%
Machine Configuration					
Shaft Length	1.79 ft	-591	-65%	632	-48%
Shaft Tilt	+4°	-2786	65%	1623	33%
Shaft Tilt	-4°	-581	-66%	947	-22%
Teeter DOF	None	-4634	175%	9568	685%
Aerodynamics					
Skewed Wake Correction	None	-1459	-13%	946	-22%
Dynamic Stall	None	-1683	0%	1146	-6%
Wind Inputs					
Vertical Shear	0.4	-2499	48%	2750	126%
Horizontal Shear	0.5	-706	-58%	1149	-6%
Horizontal Shear	0.2	-1279	-24%	844	-31%
Tower Shadow	0.0	-1646	-2%	1139	-7%
Vertical Wind	3.7 ft/sec	-1770	5%	1402	15%
Yaw angle	+40°*	-11620	590%	19180	1473%
Yaw angle	+30°	-2022	20%	1664	37%
Yaw angle	0°	-511	-70%	608	-50%
Yaw angle	-20°	614	-136%	886	-27%
Yaw angle	-30°	887	-153%	1218	0%
Yaw angle	-40°	4505	-367%	7160	487%

* Significant teeter stop impacts in this condition

6.4 A Comparison of the Free-Yaw Behavior of Rigid and Teetering Rotors

One final subject is not a sensitivity study per se, but it examines the influence of rotor configuration upon the free-yaw behavior of a turbine. To accomplish this two rotors were analyzed. One is the ESI-80 teetering rotor analyzed earlier. For purposes of comparison a second, imaginary, rotor with a rigid hub was created in YawDyn. This rotor is called the Rigid-80. But all other features of the rotor were selected to match the ESI-80 insofar as possible. The Rigid-80 has three blades, but the radius, coning, solidity, pitch angle, airfoil and planform are identical to the ESI-80. Thus the aerodynamic loading and power output of the rotors are the same in a steady, uniform wind. Different blade stiffnesses were analyzed for the Rigid-80 to determine the influence of flap natural frequency on the free-yaw behavior. The blade and yaw mass moments of inertia were identical for both rotors.

Free-yaw performance was examined by simulating the release of a yaw brake on the rotor when it is initially at a ±20° yaw angle. The yaw motion was then calculated until the rotor reaches an equilibrium location in the steady wind conditions. Varying wind shears were employed to determine their effect on the final equilibrium yaw angle. Figure 6.10 shows a typical set of results for both rotors. Notice that the rotors move to the same equilibrium yaw angle regardless of whether they were released from +20° or -20°. This is expected since the initial angle should affect only the yaw rates and the time to reach equilibrium. The example shown has a rather severe, steady, horizontal

wind shear coefficient of 0.2 as well as vertical shear and tower shadow. Thus the rotors will not align with the wind direction (yaw angle of 0°). It is interesting to note that the rigid rotor shows greater misalignment in this case than its teetering counterpart. Notice also that the Rigid-80 demonstrates a slight "overshoot" in its response while the ESI-80 does not. The rigid rotor also reaches its final equilibrium position much more quickly (even in the case where it yawed over 40°). This is typical of most of the cases examined and indicates the higher yaw moments which are observed on rigid rotors.

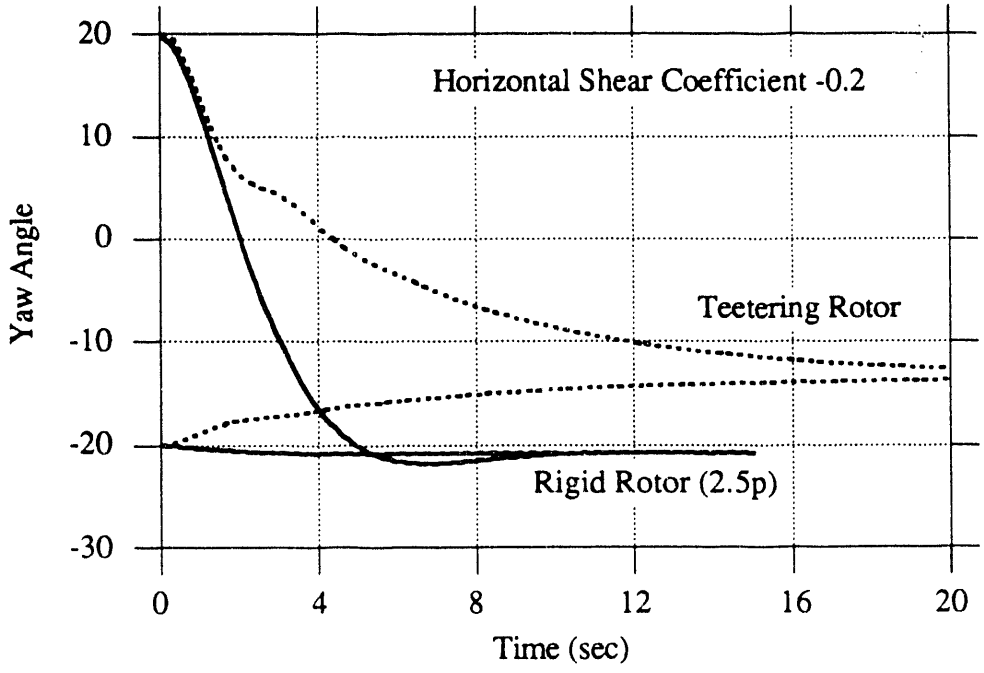

Figure 6.10 Free-yaw time history of the two rotors after release from rest at a ±20° yaw angle. Wind speed, 33.5 ft/s; Vertical wind shear, 0.14 power law; Tower shadow, 10%; Rigid-80 blade stiffness, 2.5p (rotating).

Figure 6.11 shows the influence of blade stiffness and hub articulation on the yaw response when there is no horizontal wind shear. It is clear that the blade stiffness affects the yaw rates and equilibrium position. In a case such as this where only vertical non-uniformities are acting on the rotor, the "softer" rotors show the larger yaw error. When horizontal shears are present the stiff rotors show larger yaw misalignment. This behavior results from the greater phase shift between excitation and response for the softer rotors.

Figure 6.12 shows the results of similar calculations for various blade stiffnesses and horizontal shear coefficients. Notice that the teetering rotor shows the least overall sensitivity to wind shear and the 2.5p rotor shows the greatest variation in equilibrium yaw angle for the same range of horizontal shears. The results for blades with higher natural frequencies (3.5p and 4.5p) are not shown, but were found to be very similar to those for the 2.5p rotor.

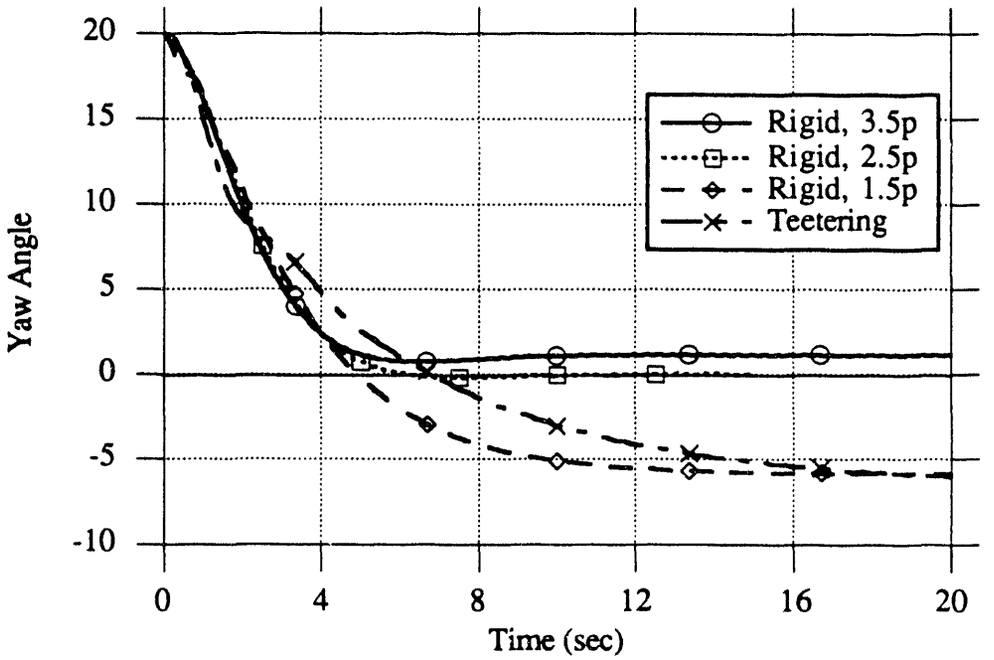

Figure 6.11 Free-yaw time history of four rotors after release from rest at a 20° yaw angle. Wind speed, 33.5 ft/s; Vertical wind shear, 0.14 power law; Tower shadow, 10%.

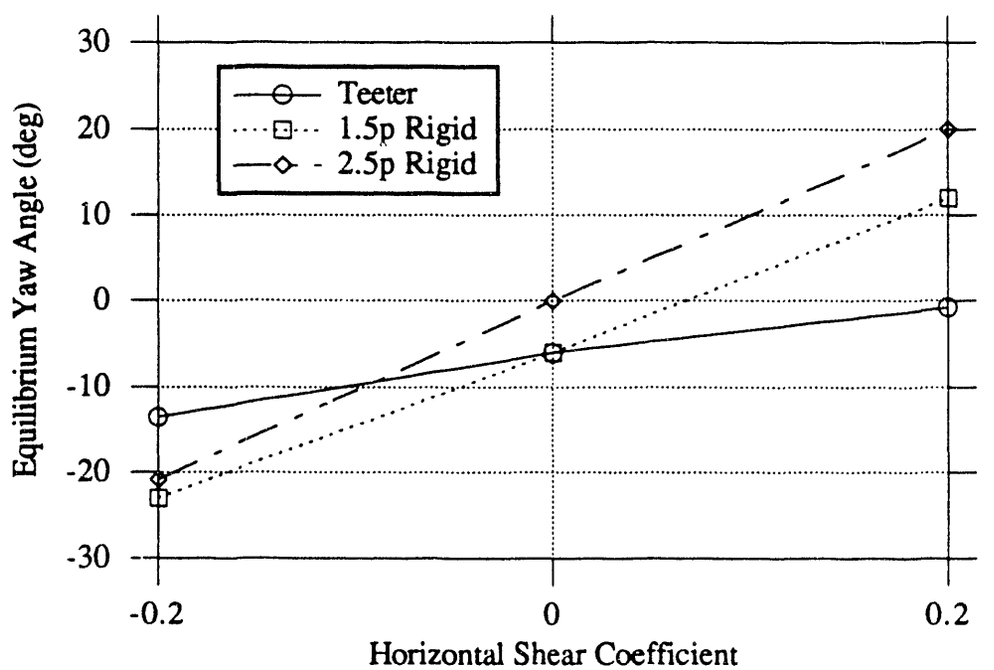

Figure 6.12 Effect of horizontal wind shear on the equilibrium yaw angle. Wind speed, 33.5 ft/s; Vertical wind shear, 0.14 power law; Tower shadow, 10%.

7.0 Conclusions and Recommendations

7.1 The YawDyn Model

The YawDyn model has been developed as a basic design tool and as an aid to understanding the features of a wind turbine which are most important in influencing the system's yaw behavior. The model is applicable to fixed or free yaw motions of rigid-rotor, two- or three-blade turbines and teetering hub turbines. YawDyn calculates yaw loads and motions of a turbine subjected to time-varying wind speeds, wind directions and wind shears. Calculation of blade flap loads and motions is also accomplished by the program. The methods selected to represent each element of the turbine were as simple as possible while retaining the essential physical features.

This research has demonstrated the importance of stall hysteresis and skewed wake corrections in the aerodynamics analysis. Without these two modifications to quasi-steady blade-element/momentum analysis the predicted yaw loads are much lower than those observed on a rigid rotor. In the present model the skewed wake corrections are a quasi-steady implementation of the Pitt and Peters dynamic inflow theory. The importance of the inertial lag of dynamic inflow was not explored.

The model has been tested by comparisons with the FLAP program and with test data from the SERI Combined Experiment rotor and with 1/20-scale wind tunnel tests of a rigid-hub model of the Mod-2 rotor. The comparisons are generally favorable. YawDyn consistently predicts the correct qualitative trends, even when those trends are not obvious. The quantitative accuracy is less consistent. In many cases the mean and cyclic yaw and flap moments are estimated within 20%. But in other cases the loads show larger errors. It is not known how much of the observed error is due to shortcomings in the model and how much is due to incomplete data for the actual input wind and uncertainties in the mass, stiffness and friction values for the machine.

The inadequacy of input wind data and machine characteristics is an inherent problem in all design codes, particularly during the preliminary design phase. The author has concluded, after validation studies on the Combined Experiment rotor, that the YawDyn program is sufficiently accurate for design purposes. Though the calculated loads will not be completely accurate, the errors will generally be less than uncertainties in selection of the design wind inputs. For example, a vertical wind component which is 10% of the mean wind can increase the yaw loads 40% (Table 6.2). The uncertainty in selection of a design vertical wind certainly exceeds 10%. This is a rather bold statement and it certainly cannot be applied to all turbine configurations. But it does hint that attention must be paid to selection of extreme wind conditions and to design of rotors which are inherently insensitive to turbulence and other variations in the wind.

The analysis neglects tower motions, drive-train dynamics and all modes of blade vibration except the first flap mode. Thus, there will be many turbines which are not amenable to thorough analysis by YawDyn. Those turbines with complex system modes of vibration near a resonance with strong excitations cannot be expected to be accurately represented in YawDyn. However, even in this situation the method can still be of some assistance in the role for which it was intended: exploration of the important influences on the yaw loads or free-yaw motion.

7.2 Yaw Loads on a Rigid Rotor

1) Yaw loads result almost entirely from a summation of blade root flap moments on the Combined Experiment rigid rotor. The net lateral, horizontal aerodynamic force on the rotor is negligible by comparison. It is worth noting the yaw moment results from small differences in large (by comparison) flap moments. This makes results sensitive to minor changes in the flap moment distribution. Since the yaw moment is nearly independent of the H-force, it is nearly independent of the distance from the hub to the yaw axis. Thus changing the low speed shaft length cannot be expected to greatly influence the yaw loads of a rigid rotor. One exception to this is the case when the rotor is not mass balanced. Then the cyclic 1p yaw moment will be directly proportional to the yaw axis-hub distance. The yaw inertia may be significantly altered by changes in the distance from the rotor to the yaw axis. Thus increasing this distance may reduce yaw rates of a free-yaw machine.

2) If a rotor is dynamically mass balanced and aerodynamically balanced, then the yaw moments on a three-blade system will be composed of a mean moment, three-per-revolution (3p) cyclic moments, and integer multiples of 3p cyclic moments. The mean yaw moment results from the 1p sine cyclic flap moment. The 3p yaw moments result from the 2p and 4p flap moments. If yaw moments with a large component of 1p cyclic oscillations are observed on a rotor there is strong indication of a mass or blade pitch imbalance that can be eliminated by balancing of the rotor. On one test rotor the cyclic loads due to imbalance were the largest cyclic loads from any cause. Monitoring of yaw moments or accelerations is a sensitive indicator of rotor balance.

3) Corrections for skewed wake effects must be made to the basic blade element/momentum aerodynamics method when the rotor operates at a yaw angle. A quasi-steady version of Pitt and Peters dynamic inflow model gives improved agreement between predicted and measured yaw moments.

4) Dynamic stall hysteresis is important when determining the mean yaw moments on the SERI Combined Experiment rotor. More research is needed to determine the most appropriate dynamic stall model for wind turbine blades. The Gormont model used in this work is able to predict the correct hysteresis loop when two empirical constants are known *a priori*.

5) Horizontal wind shear is much more damaging to yaw drive systems of rigid rotors than vertical wind shear. This can be of great importance in highly turbulent sites or in wind farm arrays. Yaw loads on a well-balanced rotor will be more influenced by horizontal shear than by any other system input with the possible exception of a vertical component of wind speed. "Soft" yaw drives or soft rotors have been suggested as possible means to mitigate the effects of wind shear.

6) Vertical wind components produce much higher loads than comparable horizontal cross-flow components. This has important implications in site selection for very rigid rotors. Though vertical wind components will always be present in atmospheric turbulence, the designer must account for a probability of persistent and strong vertical winds at some sites.

7.3 Yaw Loads on a Teetering Rotor

1) The teetering rotor, by eliminating the load path from the blade flap moments to the rotor shaft, has lower yaw loads. The horizontal forces, which were largely negligible for a rigid rotor, become the dominant source of yaw loads for the teetering rotor. The

net horizontal force is the resultant small difference of relatively large in-plane forces acting on the blades.

2) The yaw moments on a teetering rotor are strongly influenced by the distance from the yaw axis to the rotor, preconing, shaft tilt, and vertical and horizontal wind shears. The teetering rotor yaw moments are more sensitive to yaw error than the rigid rotor, though the magnitudes of the yaw loads remain lower.

7.4 Yaw Motions of Rigid and Teetering Rotors

1) Rigid rotors in free yaw demonstrate many of the characteristics of a damped oscillator. Some rotors are lightly damped and exhibit "overshoot" in their response to step changes in wind direction. Others exhibit heavily damped motion with no overshoot or ringing in the response. The blade flap stiffness and mass moment of inertia appear to be the most important factors in determining the nature of the yaw response.

2) A free-yaw, rigid rotor will experience blade flap moments due to Coriolis or gyroscopic effects. These 1p cyclic moments are proportional to the yaw rate and can easily exceed the aerodynamic moments. It is imperative that the design focus on avoiding high yaw rates. Flap flexibility, nacelle mass (to increase the moment of inertia) and mechanical yaw dampers can be employed to reduce yaw rates.

3) Teetering rotors display more benign response to yaw disturbances than their rigid-hub counterparts. This is due to the lower yaw moments of the teetering configuration. In all cases modeled the teetering rotor exhibited overdamped response to step changes in wind direction.

4) If a rotor is observed operating consistently misaligned with the wind direction, it is likely responding to persistent wind shear or vertical wind. Free-yaw rotors can be expected to misalign with the wind in complex terrain or wind farm arrays. The effect of misalignment on power production will typically be small. Misalignment may reduce loads on the rotor if it is allowed to yaw freely. This is because the equilibrium yaw angle will be determined by seeking the "balance point" in the blade flap loads. For example, if there is vertical shear the rotor will operate at the yaw angle that tends to minimize the 1p variations in angle of attack. Yawing will induce advancing and retreating blade effects which can partially cancel the effects of the wind shear.

5) Following the point of item 4 above, if a yaw-controlled rotor is constrained to align with the wind direction it may experience higher cyclic loads than a free yaw system which is otherwise equal. Of course, if the free-yaw system experiences high yaw rates (because it is too responsive) then any possible advantage will quickly be negated.

7.5 Recommendations for Additional Research

This development is just one step in a long process of fully understanding yaw dynamics and learning to design rotors which take advantage of yaw behavior instead of being punished by it. Many extensions of this modelling technique are possible and needed. The most obvious are addition of other degrees of freedom and improvement of the aerodynamics calculations. It has become clear that the yaw behavior is a result of small differences in the loads on each of the rotor blades. This makes the yaw loads more susceptible to influences which are small in any other context. Rotor (as opposed to individual blade) modes of vibration will certainly be important in some cases.

Future wind turbine codes must be capable of modeling additional structural degrees of freedom. This will be difficult because each new turbine design is likely to have different vibratory modes which are important. Codes written for specific modes, such as YawDyn or the current FLAP program, will not be suitable for all designers even if selected additional degrees of freedom are included. On the other hand, full finite element models are not likely to be widely used because of difficulties in creating and interpreting the model, particularly in the preliminary design stage. Versatile structural dynamics codes such as ADAMS, coupled with sophisticated aerodynamics analysis may be the best solution to this problem. This is the subject of future work at the University of Utah.

The aerodynamics analysis has been found to be of great importance in estimation of yaw loads. YawDyn used simplistic representations of aerodynamic phenomena to determine whether those phenomena may be important. Unfortunately, virtually all the aerodynamic effects introduced did play an important role. This means the model must be improved to more accurately account for each of those effects (stall hysteresis, skewed wake corrections and static stall were all important). It is known that delayed static stall occurs on rotor blades, though this effect is not modelled in YawDyn. The Gormont dynamic stall model depends too heavily upon empiricism to be suitable for design of rotors with new airfoils. Thus it is important that new techniques, perhaps borrowed from the helicopter industry, be employed in the wind turbine codes. Dynamic inflow is not modeled (except in a quasi-steady form). The importance of the skewed wake corrections implies that dynamic inflow corrections will also be significant. Implementing these physical phenomena in codes which will be understood and used by designers is a major challenge to the wind industry.

References

Berg, D. E., 1983, "Recent Improvements to the VDART3 VAWT Code." Wind/Solar Energy Conference, Kansas City, MO.

Bundas, D. and J. Dugundji, 1981, "Some Experiments on Yaw Stability of Wind Turbines with Various Coning Angles." Massachusetts Institute of Technology, NASA CR-168108.

Butterfield, C. P., 1989a, "Aerodynamic Pressure and Flow-Visualization Measurement from a Rotating Wind Turbine Blade." Eighth ASME Wind Energy Symposium, Houston, TX.

Butterfield, C. P., 1989b, "Three-Dimensional Airfoil Performance Measurements on a Rotating Wing." European Wind Energy Conference, Glasgow, Scotland.

Chaiyapinunt, S. and R. E. Wilson, 1983, "Analysis of Wind Turbines in Yaw." Rocky Flats Wind Energy Research Center, RFP-3678.

Coleman, R. P., A. M. Feingold and C. W. Stempin, 1945, "Evaluation of the Induced Velocity Field of an Idealized Helicopter Rotor." NACA, NACA WRL-126.

Cui, X., A. C. Hansen and N. Siedschlag, 1988, "Yaw Dynamics of Horizontal Axis Wind Turbines: First Annual Report." Solar Energy Research Institute, SERI Technical Report, STR-217-3309.

de Vries, O., 1985, "Comment on the Yaw Stability of a Horizontal-Axis Wind Turbine at Small Angles of Yaw." Wind Engineering. Vol. 9, No. 1. pp.

Gaonkar, G. H. and D. A. Peters, 1986, "Effectiveness of Current Dynamic-Inflow Models in Hover and Forward Flight." Journal of American Helicopter Society. Vol. 31, No. 2. pp.

Gormont, R. E., 1973, "A Mathematical Model of Unsteady Aerodynamics and Radial Flow for Application to Helicopter Rotors." U.S. Army Air Mobility Research and Development Laboratory, USAAMRDL Technical Report, 76-67.

Hansen, A. C. and X. Cui, 1989, "Analyses and Observations of Wind Turbine Yaw Dynamics." ASME Journal of Solar Energy Engineering. Vol. 111, No. 4. pp. 367-371.

Hansen, A. C., C. P. Butterfield and X. Cui, 1990, "Yaw Loads and Motions of a Horizontal Axis Wind Turbine." ASME Journal of Solar Energy Engineering. Vol. 112, No. 4. pp. 310-314.

Hansen, A. C. and A. D. Wright, 1991, "A Comparison of Combined Experiment Flap Load Predictions by the FLAP and YawDyn Codes." Tenth ASME Wind Energy Symposium, Houston, TX.

Hoffman, J. A., 1977, "Coupled Dynamics Analysis of Wind Energy Systems." Paragon Pacific, NASA CR-135152.

Lynette, R., 1988, "California Wind Farms Operational Data Collection and Analysis." Solar Energy Research Institute,

Miller, R. H., 1979, "On the Weathervaning of Wind Turbines." AIAA Journal of Energy. Vol. 3, No. 5. pp.

Pitt, D. M. and D. A. Peters, 1981, "Theoretical Predictions of Dynamic Inflow Derivatives." Vertica. Vol. 5, No. 1. pp.

Prouty, R. W., 1986, Helicopter Performance, Stability and Control. Boston, PWS Publishers.

Savino, J. M. and L. H. Wagner, 1976, "Wind Tunnel Measurements of the Tower Shadow on Models of the ERDA/NASA 100 kW Wind Turbine Tower." NASA LeRC, DOE/NASA Report No. 1004-77/1.

Shipley, S. A., 1978, "Wind Tunnel Test, WTS Mod-2, Full Span Control, 1/20th Scale." Boeing Aerospace Co., Unpublished report, Code IDENT No. 81205 D277-10129-1.

Stoddard, F. S., 1978, "Structural Dynamics, Stability and Control of High Aspect Ratio Wind Turbines." Ph.D. Dissertation, University of Massachusetts.

Stoddard, F. S., 1988, "An Analytical Method for Calculating the Aerodynamic Yaw Moment and Evaluating the Yaw Stability of Horizontal Axis Wind Turbines." Seventh ASME Wind Energy Symposium, New Orleans, LA.

Swift, A. H. P., 1981, "The Effects of Yawed Flow on Wind Turbine Rotors." PhD. Dissertation, Washington University.

Viterna, L. A. and R. D. Corrigan, 1981, "Fixed-Pitch Rotor Performance of Large HAWTs." DOE/NASA Workshop on Large HAWTs, Cleveland, OH.

Wilson, R. E. and P. B. S. Lissaman, 1974, "Applied Aerodynamics of Wind Power Machines." Oregon State University, NTIS PB 238594.

Wolfram, S., 1991, Mathematica: a system for doing mathematics by computer. Redwood City, CA, Addison-Wesley Publishing Co.

Wright, A. D., M. L. Buhl and R. W. Thresher, 1987, "FLAP Code Development and Validation." SERI, TR-217-3125.

Wright, A. D., R. W. Thresher and C. P. Butterfield, 1991, "Status of a Teetered Rotor Code Development and Validation Project." Tenth ASME Wind Energy Symposium, Houston, TX.

Young, J., A. C. Hansen and P. B. Anderson, 1988, "Implications of Unmatched Blade Pitch and Twist in 3-bladed Rigid Rotors." Windpower '88, Honolulu, Hawaii.

Bibliography of publications resulting from this research:

Cui, X., 1988, "Yaw Dynamics of Horizontal Axis Wind Turbines." Master of Science Thesis, University of Utah.

Cui, X., A. C. Hansen and N. Siedschlag, 1988, "Yaw Dynamics of Horizontal Axis Wind Turbines: First Annual Report." Solar Energy Research Institute, SERI Technical Report, STR-217-3309.

Dorius, T., 1992, "Yaw Aerodynamics of Horizontal Axis Wind Turbines." Master of Science Thesis, University of Utah.

Hansen, A. C., 1988, "A Method for Analyzing Wind Turbine Dynamic Response Test Data." Journal of Solar Energy Engineering. Vol. 110, No. 4. pp. 335-339.

Hansen, A. C., C. P. Butterfield and X. Cui, 1990, "Yaw Loads and Motions of a Horizontal Axis Wind Turbine." Journal of Solar Energy Engineering. Vol. 112, No. 4. pp. 310-314.

Hansen, A. C. and X. Cui, 1988, "Analyses and Observations of Wind Turbine Yaw Dynamics." Seventh ASME Energy Technology Conference, New Orleans, LA.

Hansen, A. C. and X. Cui, 1989, "Analyses and Observations of Wind Turbine Yaw Dynamics." ASME Journal of Solar Energy Engineering. Vol. 111, No. 4. pp. 367-371.

Hansen, A. C. and X. Cui, 1989, "Recent Progress in the Prediction of Yaw Dynamics." Eighth ASME Wind Energy Symposium, Houston, TX.

Hansen, A. C. and X. Cui, 1989, "Yaw Dynamics of Horizontal Axis Wind Turbines: Second Annual Report." Solar Energy Research Institute, SERI Technical Report, STR-217-3476.

Hansen, A. C. and A. D. Wright, 1991, "A Comparison of Combined Experiment Flap Load Predictions by the FLAP and YawDyn Codes." Tenth ASME Wind Energy Symposium, Houston, TX.

Schnepp, R., 1991, "Wind Turbine Aerodynamic Loads from Blade Bending Moments." Master of Science Thesis, University of Utah.

Siedschlag, N., 1987, "Yaw Dynamics of Horizontal Axis Wind Turbines." Master of Science Thesis, University of Utah.

Appendix A

Derivation of the Equations of Motion

Major Assumptions

It is necessary to make a number of assumptions to keep the model simple enough to satisfy all of the project objectives. The more important assumptions are listed below.

Structural dynamics

- There are a maximum of B+1 degrees of freedom. B is the number of blades. The teetering rotor system has only two degrees of freedom (teeter and yaw).
- Yaw angles can be arbitrarily large.
- Flap angles remain small such that these approximations are valid: $\sin\beta=\beta$, $\cos\beta=1$.
- The blades are completely rigid. All flap motion is confined to rotation about the flap hinge axis. This axis remains in the plane of rotation of the rotor. That is, the pitch and twist angles of the blade are neglected when considering the blade deflections. (Pitch and twist are not neglected in the aerodynamic analysis.)
- Blade lead-lag (in-plane) vibrations are neglected.
- Blade torsional vibrations are neglected.
- The blades are slender such that the mass moments of inertia about the flap "hinge" or the edgewise root are equal and the moment of inertia about the pitch axis is negligible. ($I_b=I_L$, $I_\theta=0$)
- Each blade has identical mass properties and the blades are placed at equally spaced azimuth intervals. However, the pitch angle of each blade can be specified independently.
- The tower is completely rigid and vertical. That is, there is no motion or tilt of the top of the tower.
- The rotor axis intersects the tower (yaw) axis. There is no rotor offset but there may be rotor tilt. The tilt angle is small such that standard small angle assumptions can be applied.
- When the rotor has a teetering hub, the blades are competely rigid and coupled such that the flap rate of blade #1 is the negative of the flap rate of blade #2. The flap angles differ in sign and by an offset (if there is rotor preconing).

Aerodynamics

- Blade element/momentum methods are used to determine "basic" induced velocities.
- The basic induced velocities are corrected for skewed wake effects but not unsteady aerodynamic effects.
- The Viterna flat-plate model is used to estimate static lift and drag coefficients at high angles of attack.
- The Gormont dynamic stall method is applied to find the lift coefficient. Drag coefficients are the static, two-dimensional values.
- A digital filter is used to "smooth" the angle of attack history for estimation of rate of change of angle of attack. The filtered angle of attack is not used in any other calculation.
- The same airfoil data is used for the entire blade. Thus thickness, Reynolds number and changing airfoil section effects are not considered.

The equations were derived using Euler's Equations and the more general, three-dimensional rigid body equations. Though this method requires extensive algebraic manipulation, it also provides other information of value which is not readily available from Lagrange's method. The blade accelerations and blade root reaction forces are determined in the course of the derivation and useful elsewhere.

The commercially-available symbolic manipulation program called Mathematica® was used in all of the derivations. This program makes the extensive algebraic manipulations relatively simple and immune from human error. It also provides a convenient, if somewhat unconventional, method of documenting the derivation. The sections that follow were copied directly from the data files ("notebooks") used in the Mathematica calculations. They are quite simple to read and understand and provide a complete record of the assumptions and manipulations required to generate all of the equations of motion.

Acceleration of the blade center of gravity.

The result of this calculation is used in subsequent derivations of the equations of motion. The text below, in Courier font, is a direct copy of the inputs and outputs of the Mathematica® program. Readers should consult the Mathematica reference book for details of the command syntax. However, most of the Mathematica language is apparent without referring to the Mathematica manuals.

All text enclosed in (* ... *) is a "comment" line for annotation of the Mathematica program. Braces {... , ... , ... } enclose components of a vector (though this is not the exclusive use of braces). All vectors are in Cartesian coordinate systems as identified in the comment sections of the program and the figures of Section 3.0.

```
(* Calculate acceleration of blade cg          *)
(* C. Hansen 6/91, Univ. of Utah               *)
(*                                             *)
(* rbar = the distance from hinge to blade cg *)
(* rh   = hub radius (axis of rot. to hinge)  *)
(* Ls   = distance from hub to yaw axis       *)
(* m    = mass of blade                        *)
(* Ib   = mass mom. inertia about flap hinge  *)
(* psi  = azimuth angle, psi=0 @ 6:00         *)
(* omeg = angular vel. of rotor (rad/sec)     *)
(* g    = yaw angle gamma                      *)
(* b    = flap angle beta                      *)
(* tau = shaft tilt, assumed small & constant *)
(* prime (e.g. g') is deriv. w.r.t. azimuth   *)
(*   e.g.  dg/dt=g'*omeg                       *)
(*                                             *)
(* First load trig and cross product rules    *)
<<:Algebra:Trigonometry.m

<<:LinearAlgebra:Cross.m

(* define a number of vectors in nacelle coord *)
(* in order to get acceleration of hinge       *)
(* nacelle coords. rotate at yaw rate only     *)
w=omeg*{g',0,-g'*tau};

wdot=omeg^2*{g'',0,-g''*tau};

r={rh Cos[psi],rh Sin[psi],0};

v=rh*omeg*{-Sin[psi],Cos[psi],0};

r0={0,0,Ls};

(* acceleration of hub center *)
a0=Cross[ w,Cross[w,r0] ] + Cross[wdot,r0];

(* acceleration of hinge relative to a0 *)
a=-rh omeg^2 * {Cos[psi],Sin[psi],0};
```

```
(* acceleration of hinge *)
ah=a0 + a + 2*Cross[w,v] +
    Cross[w,Cross[w,r]] + Cross[wdot,r]

       2                        2
{-(omeg  rh Cos[psi]) + 2 omeg  rh tau Cos[psi] g' -

          2       2       2       2            2
   Ls omeg  tau g'  - omeg  rh tau  Cos[psi] g'  +

       2
   omeg  rh tau Sin[psi] g'',

        2
  -(omeg  rh Sin[psi]) +

         2
   2 omeg  rh tau Sin[psi] g' -

       2               2
   omeg  rh Sin[psi] g'  -

       2       2            2          2
   omeg  rh tau  Sin[psi] g'  - Ls omeg  g'' -

       2
   omeg  rh tau Cos[psi] g'',

        2                           2   2
  2 omeg  rh Cos[psi] g' - Ls omeg  g'  -

       2                    2       2
   omeg  rh tau Cos[psi] g'  + omeg  rh Sin[psi] g''}

(* Check for recovery of "no tilt" case  *)
check=ah/.tau->0

       2
{-(omeg  rh Cos[psi]),

        2                       2               2
  -(omeg  rh Sin[psi]) - omeg  rh Sin[psi] g'  -

          2            2
   Ls omeg  g'', 2 omeg  rh Cos[psi] g' -

          2   2       2
   Ls omeg  g'  + omeg  rh Sin[psi] g''}

(* now transform to hub coordinates     *)
(* hub coords. rotate with the hub      *)
t={{Cos[psi],Sin[psi],0},{-Sin[psi],Cos[psi],0},
   {0,0,1}};
```

```
MatrixForm[t]

Cos[psi]    Sin[psi]    0

-Sin[psi]   Cos[psi]    0

0           0           1

ahinge=t.ah;

ahinge=Expand[ahinge];

ahinge=TrigReduce[ahinge];

ah=Simplify[ahinge]/omeg^2

                                  2    2
{-(rh - 2 rh tau g' + rh tau  g'  +

                         2                2    2
     Ls tau Cos[psi] g'  + rh Sin[psi]  g'  +

     Ls Sin[psi] g''),

                    2                                  2
  Ls tau Sin[psi] g'  - rh Cos[psi] Sin[psi] g'  -

   rh tau g'' - Ls Cos[psi] g'',

                                 2
  -(-2 rh Cos[psi] g' + Ls g'  +

                        2
     rh tau Cos[psi] g'  - rh Sin[psi] g'')}

(* Now look at coord sys attached to hub    *)
(* and get acceleration of blade cg         *)
(* vectors give cg values relative to hinge *)
w=omeg*t.{g',0,1-g'*tau};

wdot=omeg^2*{g'' Cos[psi]-g' Sin[psi],
      -g'' Sin[psi] - g' Cos[psi],
      -tau*g''};

r={rbar Cos[b],0,rbar Sin[b]};

v=rbar*omeg*b' {-Sin[b],0,Cos[b]};

a=rbar*omeg^2*b''*{-Sin[b],0,Cos[b]}-
  rbar*omeg^2*b'^2*{Cos[b],0,Sin[b]};

cor=2*Cross[w,v];

cent=Cross[w,Cross[w,r]];

tang=Cross[wdot,r];

ag=ah+(a+cor+cent+tang)/omeg^2;
```

```
ag=Expand[ag];

(* drop higher order terms in tau     *)
(* and apply small angle b assumption *)
ag=ag/.{tau^2->0,Cos[b]->1,Sin[b]->b};

ag=ag/.b^2->0;

ag=Simplify[ag];

ag=TrigReduce[ag];

(* Transform to coord sys. parallel to blade *)
t={{1,0,b}
  ,{0,1,0}
  ,{-b,0,1}};

MatrixForm[t]

1   0   b

0   1   0

-b  0   1

ag=t.ag;

(* Apply small flap angle assumptions  *)
ag=Expand[ag]/.{b^2->0,b'^2->0,b*b'->0,b*tau->0};

ag=Simplify[ag];
```

```
ag
{-(rbar + rh - 2 rbar tau g' - 2 rh tau g' -
     2 b rbar Cos[psi] g' - 2 b rh Cos[psi] g' +
                                          2
     2 rbar Sin[psi] b' g' + Ls b g'  +
                        2                 2   2
     Ls tau Cos[psi] g'  + rbar Sin[psi]  g'  +
               2   2
     rh Sin[psi]  g'  + Ls Sin[psi] g'' -
     b rh Sin[psi] g''),
                                                  2
  -(2 rbar Cos[psi] b' g' - Ls tau Sin[psi] g'  +
                              2
     rbar Cos[psi] Sin[psi] g'  +
                             2
     rh Cos[psi] Sin[psi] g'  + rbar tau g'' +
     rh tau g'' + Ls Cos[psi] g'' +
     b rbar Cos[psi] g''),
  b rbar + b rh + 2 rbar Cos[psi] g' +
                            2             2
   2 rh Cos[psi] g' - Ls g'  - b rbar g'  -
                       2                      2
   rbar tau Cos[psi] g'  - rh tau Cos[psi] g'  +
                  2   2                  2   2
   b rbar Sin[psi]  g'  + b rh Sin[psi]  g'  +
   rbar b'' + Ls b Sin[psi] g'' +
   rbar Sin[psi] g'' + rh Sin[psi] g''}
```

Flap Equation of Motion

This Mathematica file derives the flap equation of motion. It employs the result of the previous calculation of the acceleration of the blade c.g.

```
(* Blade moment calculation, uses results from     *)
(* BladeAccelTilt file to obtain flap equation     *)
(* first get angular accel. of blade in flap dir.  *)
(* start in inertial coords and transform to blade *)

<<:LinearAlgebra:Cross.m

<<:Algebra:Trigonometry.m

(* Angular velocity of nacelle coordinates in      *)
(* inertial coordinate system                      *)
w=omeg*{g',0,1-g'*tau};

t1={{Cos[psi],Sin[psi],0},{-Sin[psi],Cos[psi],0},
   {0,0,1}};

MatrixForm[t1]

Cos[psi]   Sin[psi]   0

-Sin[psi]  Cos[psi]   0

0          0          1

t2={{Cos[b],0,Sin[b]},
    {0,1,0},
    {-Sin[b],0,Cos[b]}};

MatrixForm[t2]

Cos[b]   0        Sin[b]

0        1        0

-Sin[b]  0        Cos[b]

w=t2.t1.w;

(* Now in blade coordinates, add flap rate       *)
(* to get angular vel. of blade in blade coords. *)
w=w+{0,-b' omeg,0}

{omeg Cos[b] Cos[psi] g' + omeg Sin[b] (1 - tau g'),

  -(omeg b') - omeg Sin[psi] g',

  -(omeg Cos[psi] Sin[b] g') + omeg Cos[b] (1 - tau g')}

wx=w[[1]];

wy=w[[2]];

wz=w[[3]];
```

```
(* time derivative of wy *)
wydot=-g''*omeg^2*Sin[psi] -
            g'*omeg^2*Cos[psi] -
            b''*omeg^2;

(* enter cg accel from BladeAccel file *)
ag={-(rbar + rh - 2*rbar*tau*Derivative[1][g] -
     2*rh*tau*Derivative[1][g] -
     2*b*rbar*Cos[psi]*Derivative[1][g] -
     2*b*rh*Cos[psi]*Derivative[1][g] +
     2*rbar*Sin[psi]*Derivative[1][b]*Derivative[1][g] +
     Ls*b*Derivative[1][g]^2 +
     Ls*tau*Cos[psi]*Derivative[1][g]^2 +
     rbar*Sin[psi]^2*Derivative[1][g]^2 +
     rh*Sin[psi]^2*Derivative[1][g]^2 +
     Ls*Sin[psi]*Derivative[2][g] -
     b*rh*Sin[psi]*Derivative[2][g]),
  -(2*rbar*Cos[psi]*Derivative[1][b]*Derivative[1][g] -
     Ls*tau*Sin[psi]*Derivative[1][g]^2 +
     rbar*Cos[psi]*Sin[psi]*Derivative[1][g]^2 +
     rh*Cos[psi]*Sin[psi]*Derivative[1][g]^2 +
     rbar*tau*Derivative[2][g] + rh*tau*Derivative[2][g] +
     Ls*Cos[psi]*Derivative[2][g] +
     b*rbar*Cos[psi]*Derivative[2][g]),
  b*rbar + b*rh + 2*rbar*Cos[psi]*Derivative[1][g] +
   2*rh*Cos[psi]*Derivative[1][g] - Ls*Derivative[1][g]^2 -
   b*rbar*Derivative[1][g]^2 -
   rbar*tau*Cos[psi]*Derivative[1][g]^2 -
   rh*tau*Cos[psi]*Derivative[1][g]^2 +
   b*rbar*Sin[psi]^2*Derivative[1][g]^2 +
   b*rh*Sin[psi]^2*Derivative[1][g]^2 +
   rbar*Derivative[2][b] + Ls*b*Sin[psi]*Derivative[2][g] +
   rbar*Sin[psi]*Derivative[2][g] +
   rh*Sin[psi]*Derivative[2][g]};

az=ag[[3]];

(* Coordinate transformation matrix for shaft tilt *)
t3={{1,0,tau},{0,1,0},{-tau,0,1}};

MatrixForm[t3]

1      0      tau

0      1      0

-tau   0      1

(* force of gravity in blade coordinate system *)
(* grav = acceleration due to gravity          *)
fgrav=t2.t1.t3.{m grav,0,0}

{grav m (Cos[b] Cos[psi] - tau Sin[b]),

  -(grav m Sin[psi]), grav m

   (-(tau Cos[b]) - Cos[psi] Sin[b])}
```

```
(* Blade root reaction force (z-component) *)
(* fn is applied aerodynamic normal force  *)
rz=m*omeg^2*az - fn - fgrav[[3]]

-fn - grav m (-(tau Cos[b]) - Cos[psi] Sin[b]) +

        2
  m omeg  (b rbar + b rh + 2 rbar Cos[psi] g' +

                                2             2
     2 rh Cos[psi] g' - Ls g'   - b rbar g'   -

                           2                        2
     rbar tau Cos[psi] g'   - rh tau Cos[psi] g'   +

                    2   2                  2   2
     b rbar Sin[psi]  g'  + b rh Sin[psi]  g'  +

     rbar b'' + Ls b Sin[psi] g'' + rbar Sin[psi] g'' +

     rh Sin[psi] g'')

(* Develop equation of motion using Euler's Eqn. *)
(* k     = flap spring stiffness                 *)
(* b0    = precone angle                         *)
(* mflap = applied aerodynamic flap moment       *)
(* rhs = right hand side of equation             *)
(* lhs = left hand side of equation              *)
(* Iy  = blade mass moment of inertia about c.g. *)
rhs=-mflap + k*(b-b0) + rz*rbar + fn*rbar;

lhs=Iy*(wydot-wx*wz);

soln=Solve[lhs==rhs,b''];

aa=b''/.soln[[1]];

(* Parallel axis theorem for blade inertia *)
aa=aa/.Iy->Ib-m*rbar^2;

num=Numerator[aa];

denom=Expand[Denominator[aa]];

aa=Expand[num/denom];

(* Apply assumption of small b and tau *)
aa=aa/.{Cos[b]->1,Sin[b]->b};

aa=aa/.{b^2->0,tau^2->0,tau*b->0};
```

```
(* This is the final result for b'' *)
Collect[aa,{g',g''}]
```

$$
\begin{aligned}
&-b - \frac{b\,k}{Ib\ omeg^2} + \frac{b0\,k}{Ib\ omeg^2} + \frac{mflap}{Ib\ omeg^2} - \frac{b\,m\,rbar\,rh}{Ib} - \\
&\frac{grav\,m\,rbar\,tau}{Ib\ omeg^2} - \frac{b\,grav\,m\,rbar\,Cos[psi]}{Ib\ omeg^2} + \\
&\left(-2\,Cos[psi] - \frac{2\,m\,rbar\,rh\,Cos[psi]}{Ib}\right) g' + \\
&\left(\frac{Ls\,m\,rbar}{Ib} + \frac{b\,m\,rbar}{Ib}\right)^2 + tau\,Cos[psi] + \\
&\frac{m\,rbar\,rh\,tau\,Cos[psi]}{Ib} + b\,Cos[psi]^2 - \\
&\frac{b\,m\,rbar^2\,Cos[psi]^2}{Ib} - \frac{b\,m\,rbar^2\,Sin[psi]^2}{Ib} - \\
&\left(\frac{b\,m\,rbar\,rh\,Sin[psi]}{Ib}\right)^2 g'^2 + \\
&\left(-Sin[psi] - \frac{Ls\,b\,m\,rbar\,Sin[psi]}{Ib} - \frac{m\,rbar\,rh\,Sin[psi]}{Ib}\right) g''
\end{aligned}
$$

```
(* Check for tilt->0 *)
check=Collect[aa,{g',g''}]/.tau->0
```

$$
\begin{aligned}
&-b - \frac{b\,k}{Ib\ omeg^2} + \frac{b0\,k}{Ib\ omeg^2} + \frac{mflap}{Ib\ omeg^2} - \frac{b\,m\,rbar\,rh}{Ib} - \\
&\frac{b\,grav\,m\,rbar\,Cos[psi]}{Ib\ omeg^2} + \\
&\left(-2\,Cos[psi] - \frac{2\,m\,rbar\,rh\,Cos[psi]}{Ib}\right) g' + \\
&\left(\frac{Ls\,m\,rbar}{Ib} + \frac{b\,m\,rbar}{Ib}^2 + b\,Cos[psi]^2 - \right. \\
&\left.\frac{b\,m\,rbar^2\,Cos[psi]^2}{Ib} - \frac{b\,m\,rbar^2\,Sin[psi]^2}{Ib} - \right. \\
&\left.\frac{b\,m\,rbar\,rh\,Sin[psi]}{Ib}^2\right) g'^2 + \\
&\left(-Sin[psi] - \frac{Ls\,b\,m\,rbar\,Sin[psi]}{Ib} - \frac{m\,rbar\,rh\,Sin[psi]}{Ib}\right) g''
\end{aligned}
$$

Yaw Equation of Motion (Without Flap)

In this section the yaw equation of motion is derived for the case when there is no blade flap motion. The flap rate is zero and the flap angle equals the precone angle. The blade root spring has infinite stiffness and is not used in this derivation.

The result obtained in this section applies to one blade. The complete yaw equation for an arbitrary number of blades is found by summing the equations for single blades (at the appropriate azimuth angles). The resulting equations are presented in Section 3 of this report.

```
(* Yaw equation calculation, case with no flap     *)
(* uses results from BladeAccelTilt file          *)
(* first get angular accel of blade in flap dir   *)
(* start in inertial coords and transform to blade *)
<<:LinearAlgebra:Cross.m

<<:Algebra:Trigonometry.m

(* Coordinate transformation matrices *)
(* t1 = Nacelle to hub                *)
(* t2 = hub to blade                  *)
(* t3 = tower to nacelle (tilt=tau)   *)
t1={{Cos[psi],Sin[psi],0},{-Sin[psi],Cos[psi],0},
   {0,0,1}};

t2={{Cos[b],0,Sin[b]},{0,1,0}
   ,{-Sin[b],0,Cos[b]}};

t3={{1,0,tau},{0,1,0},{-tau,0,1}};

(* yaw rate in tower coordinate system *)
w=omeg*{g',0,0};

(* Add rotor rotation after transformation *)
(* from tower to nacelle coordinates       *)
w=t3.w + {0,0,omeg};

(* Finally, transform to blade coordinates *)
w=t2.t1.w;

(* Add flap rate *)
w=w+{0,-b'*omeg,0};

wx=w[[1]];

wy=w[[2]];

wz=w[[3]];

(* Write time derivatives by inspection *)
wydot=omeg^2*(-g''*Sin[psi] - g'*Cos[psi] - b'');
```

```
wzdot=-omeg^2*(b' g' Cos[psi] Cos[b] +
               Sin[b] g'' Cos[psi] -
               Sin[b] g' Sin[psi] +
               b' Sin[b] - Cos[b]*tau*g'');

(* enter cg accel from BladeAccelTilt file *)
ag={-(rbar + rh - 2*rbar*tau*Derivative[1][g] -
     2*rh*tau*Derivative[1][g] -
     2*b*rbar*Cos[psi]*Derivative[1][g] -
     2*b*rh*Cos[psi]*Derivative[1][g] +
     2*rbar*Sin[psi]*Derivative[1][b]*Derivative[1][g] +
     Ls*b*Derivative[1][g]^2 +
     Ls*tau*Cos[psi]*Derivative[1][g]^2 +
     rbar*Sin[psi]^2*Derivative[1][g]^2 +
     rh*Sin[psi]^2*Derivative[1][g]^2 +
     Ls*Sin[psi]*Derivative[2][g] -
     b*rh*Sin[psi]*Derivative[2][g]),
  -(2*rbar*Cos[psi]*Derivative[1][b]*Derivative[1][g] -
     Ls*tau*Sin[psi]*Derivative[1][g]^2 +
     rbar*Cos[psi]*Sin[psi]*Derivative[1][g]^2 +
     rh*Cos[psi]*Sin[psi]*Derivative[1][g]^2 +
     rbar*tau*Derivative[2][g] + rh*tau*Derivative[2][g] +
     Ls*Cos[psi]*Derivative[2][g] +
     b*rbar*Cos[psi]*Derivative[2][g]),
  b*rbar + b*rh + 2*rbar*Cos[psi]*Derivative[1][g] +
   2*rh*Cos[psi]*Derivative[1][g] - Ls*Derivative[1][g]^2 -
   b*rbar*Derivative[1][g]^2 -
   rbar*tau*Cos[psi]*Derivative[1][g]^2 -
   rh*tau*Cos[psi]*Derivative[1][g]^2 +
   b*rbar*Sin[psi]^2*Derivative[1][g]^2 +
   b*rh*Sin[psi]^2*Derivative[1][g]^2 +
   rbar*Derivative[2][b] + Ls*b*Sin[psi]*Derivative[2][g] +
   rbar*Sin[psi]*Derivative[2][g] +
   rh*Sin[psi]*Derivative[2][g]};

(* Blade weight in blade coordinate system *)
weight=t2.t1.t3.{m grav,0,0};

(* Blade hinge reaction forces from F=ma *)
{rx,ry,rz}=m*omeg^2*ag -
           {0,ft,fn} - weight;

(* Blade hinge moments from Euler's equations  *)
(* The pitch moment is neglected               *)
(* torq = applied aerodynamic torque           *)
(* ft   = applied aerodynamic tangential force *)
mx=0;

my=Iy*(wydot - wx*wz) + mflap - rbar*(rz+fn);

mz=Iy*(wzdot + wx*wy) - torq + rbar*(ry+ft);

(* yaw moment arm to hinge, in tower coords *)
ryaw=Inverse[t3].{rh Cos[psi],rh Sin[psi],Ls};

(* transform from blade to inertial coords *)
trans=Inverse[t3].Inverse[t1].Inverse[t2];
```

```
trans=TrigReduce[trans];

trans=trans/.tau^2->0;

(* change sign of forces to get reaction on hub *)
(* and add moment reaction on hub (transformed) *)
(* Finally, extract the x component             *)
fyaw=-trans.{rx,ry,rz};

myaw={1,0,0}.(Cross[ryaw,fyaw] - trans.{mx,my,mz});

(* Substitute flap inertia about hinge  *)
(* and apply small tau assumption again *)
myaw=myaw/.Iy->Ib-m*rbar^2;

myaw=Expand[myaw]/.{tau^2->0,Cos[b]->1,Sin[b]->b};

myaw=myaw/.{b^2->0, b^3->0,b*tau->0,tau^2->0};

(* This is case with no flap motion *)
myaw=myaw/.{b'->0, b''->0};

soln=Solve[myaw==Iyaw g''*omeg^2, g''];

yawaccel=g''/.soln[[1]];

(* Apply small angle approximations and simplify *)
yawaccel=yawaccel/.{Cos[b]->1,Sin[b]->b};

yawaccel=yawaccel/.{b^2->0, b^3->0,b*tau->0,tau^2->0};

num=Numerator[yawaccel];

denom=Denominator[yawaccel];

denom=Factor[denom];

num=omeg^2*Expand[num/omeg^2];

yawaccel=num/denom;

num=Numerator[yawaccel];

num=Expand[num];

denom=Denominator[yawaccel];

denom=TrigReduce[denom];

(* Drop higher order terms in b and tau  *)
(* Extract portions of the expression to *)
(* expedite simplification               *)
num=num/.{b^2->0,b*tau->0,tau^2->0};

c1=Coefficient[num,g'];

c2=Coefficient[num,g'^2];
```

```
remain=num-c1*g'-c2*g'^2;

fncoef=Coefficient[remain,fn];

ftcoef=Coefficient[remain,ft];

mflapcoef=Coefficient[remain,mflap];

torqcoef=Coefficient[remain,torq];

maero=fncoef*fn + ftcoef*ft +
      mflapcoef*mflap + torqcoef*torq;

remain=Expand[remain-maero];

(* Check to be sure numerator is recovered *)
Expand[num]-Expand[remain+maero+c1*g'+c2*g'^2]

0

(* Now simplify individual terms *)
c1=TrigReduce[c1];

c2tau=Coefficient[c2,tau];

c2tau=TrigReduce[c2tau];

c2remain=Expand[c2-c2tau*tau];

c2remain=TrigReduce[c2remain];

c2=c2remain+Expand[c2tau*tau];

remain=Expand[remain];

remain=remain/.b^2->0;

(* The denominator represents the yaw inertia *)
(* The final yaw equation is of the form:     *)
(*   denom*g'' = num                          *)
denom

         2
Iyaw + Ls  m + 2 Ls b m rbar +

  2 Ls m rbar tau Cos[psi] + Ls m rh tau Cos[psi] +

                       3                2
  Ls m rh tau Cos[psi]  + Ib Sin[psi]  +

                      2       2          2
  2 m rbar rh Sin[psi]  + m rh  Sin[psi]  +

                                2
  Ls m rh tau Cos[psi] Sin[psi]

num=Expand[remain+maero+c1*g'+c2*g'^2];
```

```
Collect[num,{ft,fn,mflap,torq,k,g'}]

          tau      b Cos[psi]
torq (-(-----) - ----------) - Ib b Sin[psi] +
               2           2
         omeg        omeg

  mflap Sin[psi]
  -------------- - Ls m rbar Sin[psi] -
          2
      omeg

  Ls m rh Sin[psi] - b m rbar rh Sin[psi] -

  grav m rh tau Sin[psi]
  ---------------------- +
              2
          omeg

                            2
  grav m rh tau Cos[psi]  Sin[psi]
  -------------------------------- +
                    2
               omeg

                           3
  grav m rh tau Sin[psi]
  ---------------------- +
              2
           omeg

     Ls b Sin[psi]    rh Sin[psi]
  fn (------------- + -----------) +
               2              2
          omeg           omeg

                                          2
       Ls Cos[psi]     rh tau Cos[psi]
  ft (-(-----------) - ---------------- -
               2                2
           omeg             omeg

                     2
     rh tau Sin[psi]
     ---------------) +
               2
           omeg

  (2 Ls m rbar tau Sin[psi] + 2 Ls m rh tau Sin[psi] -

     2 Ib Cos[psi] Sin[psi] -

     4 m rbar rh Cos[psi] Sin[psi] -

           2
     2 m rh  Cos[psi] Sin[psi]) g' +

  (m rbar rh tau Cos[psi] Sin[psi] +
```

```
        2
     m rh  tau Cos[psi] Sin[psi] -

                            3
     m rbar rh tau Cos[psi]  Sin[psi] -

        2              3
     m rh  tau Cos[psi]  Sin[psi] -

                                    3
     m rbar rh tau Cos[psi] Sin[psi]  -

        2                       3    2
     m rh  tau Cos[psi] Sin[psi] ) g'

(* See if no-tilt solution is recovered *)
denom/.tau->0

         2                                    2
Iyaw + Ls  m + 2 Ls b m rbar + Ib Sin[psi]  +

                       2       2         2
  2 m rbar rh Sin[psi]  + m rh  Sin[psi]

Collect[num,{ft,fn,mflap,torq,k,g'}]/.tau->0

  Ls ft Cos[psi]     b torq Cos[psi]
-(--------------) - --------------- - Ib b Sin[psi] +
          2                 2
      omeg              omeg

  mflap Sin[psi]
  -------------- - Ls m rbar Sin[psi] -
          2
      omeg

  Ls m rh Sin[psi] - b m rbar rh Sin[psi] +

      Ls b Sin[psi]    rh Sin[psi]
  fn (------------- + -----------) +
               2              2
           omeg           omeg

  (-2 Ib Cos[psi] Sin[psi] -

     4 m rbar rh Cos[psi] Sin[psi] -

           2
     2 m rh  Cos[psi] Sin[psi]) g'
```

Yaw Equation of Motion (Including Flap DOF)

This section derives the fully coupled yaw equation of motion for the rigid hub, flapping rotor. Terminology and coordinate systems are the same as used in previous Mathematica files. As in the previous derivation, the complete yaw equation of motion is obtained by summing the result of this section over all blades.

```
(* Yaw equation derivation, uses results from      *)
(* BladeMomentTilt file                            *)
(* first get angular accel of blade in flap dir.   *)
(* start in inertial coords and transform to blade *)
<<:LinearAlgebra:Cross.m

<<:Algebra:Trigonometry.m

(* Coordinate transformation matrices *)
(* t1 = Nacelle to hub                *)
(* t2 = hub to blade                  *)
(* t3 = tower to nacelle (tilt=tau)   *)
t1={{Cos[psi],Sin[psi],0},{-Sin[psi],Cos[psi],0},
   {0,0,1}};

t2={{Cos[b],0,Sin[b]},{0,1,0}
   ,{-Sin[b],0,Cos[b]}};

t3={{1,0,tau},{0,1,0},{-tau,0,1}};

(* yaw rate in tower coordinate system *)
w=omeg*{g',0,0};

(* Add rotor rotation after transformation *)
(* from tower to nacelle coordinates       *)
w=t3.w + {0,0,omeg};

(* Finally, transform to blade coordinates *)
w=t2.t1.w;

(* Add flap rate *)
w=w+{0,-b'*omeg,0}

{omeg Cos[b] Cos[psi] g' + Sin[b] (omeg - omeg tau g'),

  -(omeg b') - omeg Sin[psi] g',

  -(omeg Cos[psi] Sin[b] g') + Cos[b] (omeg - omeg tau g')}

wx=w[[1]];

wy=w[[2]];

wz=w[[3]];

wydot=-g'' omeg^2 Sin[psi] -
       g' omeg^2 Cos[psi] -
       b'' omeg^2;
```

```
wzdot=-omeg^2*(b' g' Cos[psi] Cos[b] +
               Sin[b] g'' Cos[psi] -
               Sin[b] g' Sin[psi] +
               b' Sin[b] - Cos[b]*tau*g'');

(* enter cg accel from BladeAccel file *)
ag={-(rbar + rh - 2*rbar*tau*Derivative[1][g] -
     2*rh*tau*Derivative[1][g] -
     2*b*rbar*Cos[psi]*Derivative[1][g] -
     2*b*rh*Cos[psi]*Derivative[1][g] +
     2*rbar*Sin[psi]*Derivative[1][b]*Derivative[1][g] +
     Ls*b*Derivative[1][g]^2 +
     Ls*tau*Cos[psi]*Derivative[1][g]^2 +
     rbar*Sin[psi]^2*Derivative[1][g]^2 +
     rh*Sin[psi]^2*Derivative[1][g]^2 +
     Ls*Sin[psi]*Derivative[2][g] -
     b*rh*Sin[psi]*Derivative[2][g]),
  -(2*rbar*Cos[psi]*Derivative[1][b]*Derivative[1][g] -
     Ls*tau*Sin[psi]*Derivative[1][g]^2 +
     rbar*Cos[psi]*Sin[psi]*Derivative[1][g]^2 +
     rh*Cos[psi]*Sin[psi]*Derivative[1][g]^2 +
     rbar*tau*Derivative[2][g] + rh*tau*Derivative[2][g] +
     Ls*Cos[psi]*Derivative[2][g] +
     b*rbar*Cos[psi]*Derivative[2][g]),
  b*rbar + b*rh + 2*rbar*Cos[psi]*Derivative[1][g] +
   2*rh*Cos[psi]*Derivative[1][g] - Ls*Derivative[1][g]^2 -
   b*rbar*Derivative[1][g]^2 -
   rbar*tau*Cos[psi]*Derivative[1][g]^2 -
   rh*tau*Cos[psi]*Derivative[1][g]^2 +
   b*rbar*Sin[psi]^2*Derivative[1][g]^2 +
   b*rh*Sin[psi]^2*Derivative[1][g]^2 +
   rbar*Derivative[2][b] + Ls*b*Sin[psi]*Derivative[2][g] +
   rbar*Sin[psi]*Derivative[2][g] +
   rh*Sin[psi]*Derivative[2][g]};

(* Blade weight in blade coordinate system *)
weight=t2.t1.t3.{m grav,0,0}

{grav m (Cos[b] Cos[psi] - tau Sin[b]), -(grav m Sin[psi]),

  grav m (-(tau Cos[b]) - Cos[psi] Sin[b])}

(* Blade hinge reaction forces from F=ma *)
{rx,ry,rz}=m*omeg^2*ag -
           {0,ft,fn} - weight;

(* Blade hinge moments from Euler's equations *)
(* The pitch moment is neglected and the flap *)
(* moment is just that transmitted by spring  *)
mx=0;

my=k*(b-b0);

mz=Iy*wzdot + Iy*wx*wy - torq + rbar*(ry+ft);

(* yaw moment arm to hinge, in tower coords *)
ryaw=Inverse[t3].{rh Cos[psi],rh Sin[psi],Ls};
```

```
(* transform from blade to inertial coords *)
trans=Inverse[t3].Inverse[t1].Inverse[t2];

trans=TrigReduce[trans];

trans=trans/.tau^2->0;

(* change sign of force to get reaction on hub *)
(* and add moment reaction on hub (transformed)*)
(* Finally, extract the x component            *)
fyaw=-trans.{rx,ry,rz};

myaw={1,0,0}.(Cross[ryaw,fyaw] - trans.{mx,my,mz});

(* Substitute flap inertia about hinge  *)
(* and apply small tau assumption again *)
myaw=myaw/.Iy->Ib-m*rbar^2;

myaw=Expand[myaw]/.{tau^2->0,Cos[b]->1,Sin[b]->b};

myaw=myaw/.{b^2->0, b^3->0,b*tau->0,tau^2->0};

soln=Solve[myaw==Iyaw g''*omeg^2, g''];

yawaccel=g''/.soln[[1]];

yawaccel=yawaccel/.{Cos[b]->1,Sin[b]->b};

yawaccel=yawaccel/.{b^2->0, b^3->0,b*tau->0,tau^2->0};

num=Numerator[yawaccel];

denom=Denominator[yawaccel];

denom=Factor[denom];

num=omeg^2*Expand[num/omeg^2];

yawaccel=num/denom;

num=Numerator[yawaccel];

num=Collect[num,{g',g''}];

denom=Denominator[yawaccel];

denom=TrigReduce[denom];

(* Drop higher order terms in b or derivatives *)
num=num/.{b*b'->0,b^2->0,b'^2->0,b*b''->0,
          b*tau->0,b'*tau->0,b''*tau->0};

c1=Coefficient[num,g'];

c2=Coefficient[num,g'^2];

remain=num-c1*g'-c2*g'^2;
```

```
fncoef=Coefficient[remain,fn];

ftcoef=Coefficient[remain,ft];

mflapcoef=Coefficient[remain,mflap];

torqcoef=Coefficient[remain,torq];

maero=fncoef*fn + ftcoef*ft +
      mflapcoef*mflap + torqcoef*torq;

remain=Expand[remain-maero];

(* Check to be sure numerator is recovered *)
Expand[num]-Expand[remain+maero+c1*g'+c2*g'^2]

0

(* Now simplify individual terms *)
c1=TrigReduce[c1];

c2tau=Coefficient[c2,tau];

c2tau=TrigReduce[c2tau];

c2remain=Expand[c2-c2tau*tau];

c2remain=TrigReduce[c2remain];

c2=c2remain+Expand[c2tau*tau];

(* Now substitute flap equation to eliminate b'' *)
b''=-b - (b*k)/(Ib*omeg^2) + (b0*k)/(Ib*omeg^2) +
  mflap/(Ib*omeg^2) - (b*m*rbar*rh)/Ib -
  (grav*m*rbar*tau)/(Ib*omeg^2) -
  (b*grav*m*rbar*Cos[psi])/(Ib*omeg^2) +
  (-2*Cos[psi] - (2*m*rbar*rh*Cos[psi])/Ib)*
   Derivative[1][g] + ((Ls*m*rbar)/Ib + (b*m*rbar^2)/Ib +
     tau*Cos[psi] + (m*rbar*rh*tau*Cos[psi])/Ib +
     b*Cos[psi]^2 - (b*m*rbar^2*Cos[psi]^2)/Ib -
     (b*m*rbar^2*Sin[psi]^2)/Ib -
     (b*m*rbar*rh*Sin[psi]^2)/Ib)*Derivative[1][g]^2 +
  (-Sin[psi] - (Ls*b*m*rbar*Sin[psi])/Ib -
     (m*rbar*rh*Sin[psi])/Ib)*Derivative[2][g];

(* make terminology unambiguous *)
Derivative[2][b]=b'';

remain=Expand[remain];

remain=remain/.
     {b*b'->0,b^2->0,b'^2->0};

newnum=Expand[remain+maero+c1*g'+c2*g'^2];

soln=Solve[g''*denom==newnum,g''];

yawaccel=g''/.soln[[1]];
```

```
num=Numerator[yawaccel];

denom=Denominator[yawaccel];

denom=omeg^2*Ib*Expand[denom/(omeg^2*Ib)];

num=omeg^2*Ib*Expand[num/(omeg^2*Ib)];

(* The yaw equation will be of the form: *)
(*      denom*g'' = num                   *)
yawaccel=num/denom;

num=Numerator[yawaccel];

denom=Denominator[yawaccel]

          2
Iyaw + Ls  m + 2 Ls m rbar tau Cos[psi] +

                                                    2
  Ls m rh tau Cos[psi] + 2 Ls b m rbar Cos[psi]   +

                        3                          2
  Ls m rh tau Cos[psi]   + Ls b m rbar Sin[psi]   -

       2     2            2
  Ls b m  rbar  rh Sin[psi]         2         2
  -------------------------- + m rh  Sin[psi]  -
              Ib

   2     2   2          2
  m  rbar  rh  Sin[psi]                                  2
  ---------------------- + Ls m rh tau Cos[psi] Sin[psi]
            Ib
```

```
Collect[num,{ft,fn,mflap,torq,k,g'}]

         tau      b Cos[psi]
torq (-(-----) - ----------) - Ls m rbar Sin[psi] -
              2           2
         omeg        omeg

  Ls m rh Sin[psi] + b m rbar rh Sin[psi] -

                                    2     2   2
  m mflap rbar rh Sin[psi]    b m  rbar  rh  Sin[psi]
  ------------------------ + ---------------------- +
                  2                      Ib
          Ib omeg

  grav m rbar tau Sin[psi]    grav m rh tau Sin[psi]
  ------------------------ - ---------------------- +
                2                        2
           omeg                     omeg

        2     2
  grav m  rbar  rh tau Sin[psi]
  ------------------------------ +
                   2
            Ib omeg

  b grav m rbar Cos[psi] Sin[psi]
  ------------------------------- +
                  2
               omeg

          2     2
  b grav m  rbar  rh Cos[psi] Sin[psi]
  ----------------------------------- +
                       2
                Ib omeg

                            2
  grav m rh tau Cos[psi]  Sin[psi]
  ------------------------------- +
                  2
               omeg

                           3
  grav m rh tau Sin[psi]
  ---------------------- +
                2
             omeg

      Ls b Sin[psi]    rh Sin[psi]
  fn (------------- + -----------) +
                2              2
           omeg           omeg

     b Sin[psi]    b0 Sin[psi]    b m rbar rh Sin[psi]
  k (---------- - ----------- + -------------------- -
            2             2                    2
       omeg          omeg             Ib omeg
```

```
   b0 m rbar rh Sin[psi]
   ---------------------) +
                2
         Ib omeg

                                        2
      Ls Cos[psi]     rh tau Cos[psi]
ft (-(-----------) - ---------------- -
             2                 2
          omeg              omeg

                   2
   rh tau Sin[psi]
   ---------------) +
            2
         omeg

(2 Ls m rbar tau Sin[psi] + 2 Ls m rh tau Sin[psi] -

         2
   2 m rh  Cos[psi] Sin[psi] +

      2     2   2
   2 m  rbar  rh  Cos[psi] Sin[psi]
   ------------------------------- - 2 Ls m rbar b') g' \
                  Ib

          2     2                      2     3
      Ls m  rbar  rh Sin[psi]    b m  rbar  rh Sin[psi]
 + (-(----------------------) - ---------------------- -
                Ib                         Ib

   Ib tau Cos[psi] Sin[psi] -

   m rbar rh tau Cos[psi] Sin[psi] +

      2
   m rh  tau Cos[psi] Sin[psi] -

    2     2   2
   m  rbar  rh  tau Cos[psi] Sin[psi]
   --------------------------------- -
                  Ib

                2
   Ib b Cos[psi]  Sin[psi] -

                     2
   Ls m rbar Cos[psi]  Sin[psi] -

                       2
   b m rbar rh Cos[psi]  Sin[psi] +

      2     3             2
   b m  rbar  rh Cos[psi]  Sin[psi]
   ------------------------------- -
                  Ib
```

```
                          3
     m rbar rh tau Cos[psi]  Sin[psi] -

         2             3                                  3
     m rh  tau Cos[psi]  Sin[psi] - Ls m rbar Sin[psi]  +

                                2     3            3
                           3   b m  rbar  rh Sin[psi]
     b m rbar rh Sin[psi]  + ----------------------- +
                                      Ib

        2     2   2          3
     b m  rbar  rh  Sin[psi]
     ------------------------ -
                Ib

                                       3
     m rbar rh tau Cos[psi] Sin[psi]  -

         2                         3    2
     m rh  tau Cos[psi] Sin[psi] ) g'

(* See if no-tilt solution is recovered *)
denom/.tau->0

          2                              2
Iyaw + Ls  m + 2 Ls b m rbar Cos[psi]  +

                                2     2            2
                         2   Ls b m  rbar  rh Sin[psi]
  Ls b m rbar Sin[psi]  - -------------------------- +
                                      Ib

                       2     2   2          2
      2          2   m  rbar  rh  Sin[psi]
  m rh  Sin[psi]  - ----------------------
                             Ib
```

```
Collect[num,{ft,fn,mflap,torq,k,g'}]/.tau->0

  Ls ft Cos[psi]     b torq Cos[psi]
-(--------------) - --------------- - Ls m rbar Sin[psi] -
          2                 2
       omeg              omeg

  Ls m rh Sin[psi] + b m rbar rh Sin[psi] -

                                      2     2   2
  m mflap rbar rh Sin[psi]    b m  rbar  rh  Sin[psi]
  ------------------------ + ---------------------- +
                  2                      Ib
          Ib omeg

  b grav m rbar Cos[psi] Sin[psi]
  ------------------------------ +
                    2
                omeg

          2     2
  b grav m  rbar  rh Cos[psi] Sin[psi]
  ----------------------------------- +
                       2
                  Ib omeg

      Ls b Sin[psi]    rh Sin[psi]
  fn (------------- + -----------) +
             2               2
          omeg            omeg

     b Sin[psi]    b0 Sin[psi]    b m rbar rh Sin[psi]
  k (---------- - ----------- + -------------------- -
           2             2                  2
        omeg          omeg            Ib omeg

     b0 m rbar rh Sin[psi]
     ---------------------) +
                  2
           Ib omeg

          2
  (-2 m rh  Cos[psi] Sin[psi] +

        2     2   2
     2 m  rbar  rh  Cos[psi] Sin[psi]
     ------------------------------- - 2 Ls m rbar b') g' \
                    Ib

            2     2                     2     3
       Ls m  rbar  rh Sin[psi]    b m  rbar  rh Sin[psi]
   + (-(-----------------------) - ---------------------- -
                  Ib                          Ib

                  2
     Ib b Cos[psi]  Sin[psi] -
```

$$
\begin{aligned}
&\text{Ls m rbar Cos[psi]}^2\ \text{Sin[psi]} - \\
&\text{b m rbar rh Cos[psi]}^2\ \text{Sin[psi]} + \\
&\frac{\text{b m}^2\ \text{rbar}^2\ \text{rh Cos[psi]}^2\ \text{Sin[psi]}^2}{\text{Ib}} - \\
&\text{Ls m rbar Sin[psi]}^3 + \text{b m rbar rh Sin[psi]}^3 + \\
&\left(\frac{\text{b m}^2\ \text{rbar}^3\ \text{rh Sin[psi]}^3}{\text{Ib}} + \frac{\text{b m}^2\ \text{rbar}^2\ \text{rh}^2\ \text{Sin[psi]}^3}{\text{Ib}}\right) g'^2
\end{aligned}
$$

Teetering Rotor Equations

This section derives the yaw and teetering equations of motion for a simple teetering rotor. The blade is completely rigid and connected to the shaft with an idealized teeter hinge, with linear springs and dampers. The center of mass of the rotor is offset from the teeter axis by a length "sl", the undersling. This equation applies only to two bladed rotors and is complete as presented at the end of the derivation. To maintain consistency with previous equations, the blade mass and moment of inertia are for one blade only. This differs from the usual teetering rotor convention and results in equations containing terms such as $2I_b$ instead of the more common I_b.

```
(* Yaw and teetering equation derivations for a     *)
(* teetering rotor with mass offset but no delta-3 *)
(* First get angular accel of blade in flap dir     *)
(* Start in inertial coords and transform to blade *)
<<:LinearAlgebra:Cross.m

<<:Algebra:Trigonometry.m

(* Coordinate transformation matrices *)
(* t1  = Nacelle to shaft              *)
(* t2  = shaft to hub (teetering hub)  *)
(* t3  = tower to nacelle (tilt=tau)   *)
(* tee = teeter angle (assumed small)  *)
t1={{Cos[psi],Sin[psi],0},{-Sin[psi],Cos[psi],0},
   {0,0,1}};

t2={{Cos[tee],0,Sin[tee]},{0,1,0},
   {-Sin[tee],0,Cos[tee]}};

t3={{1,0,tau},{0,1,0},{-tau,0,1}};

(* yaw rate in tower coordinate system *)
w=omeg*{g',0,0};

(* Add rotor rotation after transformation *)
(* from tower to nacelle coordinates       *)
w=t3.w + {0,0,omeg};

(* Transform to shaft coordinates to get ang. vel *)
(* of coord. system including omeg and yaw rate   *)
w=t1.w

{omeg Cos[psi] g', -(omeg Sin[psi] g'), omeg - omeg tau g'}

wxdot=omeg^2*(Cos[psi]*g'' -  Sin[psi]*g');

wydot=omeg^2*(-g''*Sin[psi] - g'*Cos[psi]);

wzdot=-omeg^2*(tau*g'');

wdot={wxdot,wydot,wzdot};

(* Yaw rate and teeter pin (hinge) position *)
(* vector in tower coordinates              *)
wyaw={omeg*g',0,0};
```

```
wyawdot={omeg^2*g'',0,0};

rpin={-Ls*tau,0,Ls};

(* Get acceleration of teeter pin (hinge)    *)
apin=Cross[ wyaw,Cross[wyaw,rpin] ] +
   Cross[ wyawdot,rpin]

              2                   2   2
{0, -(Ls omeg  g''), -(Ls omeg  g' )}

(* Transform teeter pin accel to hub coordinates *)
apin=t2.t1.t3.apin;

(* Get acceleration of cg in hub coordinates    *)
(* Coord sys rotating with omeg and yaw rate    *)
(* sl  = rotor undersling, distance from hinge *)
(*         to rotor c.g.                         *)
vrel={tee'*omeg*sl,0,0};

rrel={0,0,sl};

arel=omeg^2*{sl*tee'',0,-sl*tee'^2};

ag=apin + Cross[w,Cross[w,rrel]] +
          arel +2 Cross[w,vrel] + Cross[wdot,rrel];

ag=Expand[ag/.Sin[psi]^2->1-Cos[psi]^2];

(* Transform w to hub coordinate system *)
w=t2.w;

(* Add teeter rate to get total ang vel of rotor *)
w=w+{0,-tee'*omeg,0}

{omeg Cos[psi] Cos[tee] g' +

   Sin[tee] (omeg - omeg tau g'),

  -(omeg Sin[psi] g') - omeg tee',

  -(omeg Cos[psi] Sin[tee] g') +

   Cos[tee] (omeg - omeg tau g')}

wxdot=omeg^2*(Cos[psi]*Cos[tee]*g'' -
              Sin[psi]*Cos[tee]*g'  -
              Cos[psi]*Sin[tee]*tee'*g'  +
              Cos[tee]*tee'*(1 - tau*g') -
              Sin[tee]*tau*g'');

wydot=omeg^2*(-g''*Sin[psi] -
       g'*Cos[psi] - tee'');
```

```
wzdot=-omeg^2*(tee' g' Cos[psi] Cos[tee] +
               Sin[tee] g'' Cos[psi] -
               Sin[tee] g' Sin[psi] +
               tee' Sin[tee] - Cos[tee]*tau*g'');

wdot={wxdot,wydot,wzdot};

(* Rotor weight in hub coordinate system *)
weight=t2.t1.t3.{m*grav,0,0};

(* Blade hinge reaction forces from F=ma *)
(* fy and fz are net aerodynamic forces  *)
(* acting at the teeter hinge            *)
(* teemaero is net aero teeter moment    *)
{rx,ry,rz} = m*ag - {0,fy,fz} - weight;

(* Mass moment of inertia tensor *)
Itensor={{0,0,0},
         {0,2*Ib,0},
         {0,0,2*Ib}};

(* Rotor moments from angular momentum equations  *)
(* The pitch moment is neglected and the teeter   *)
(* moment is that transmitted by spring & damper  *)
hg=Itensor.w;

(* Evaluate inertial terms in momentum equation   *)
rhs=Itensor.wdot + Cross[w,hg];

(* Applied moment about the y axis *)
lhs = hubmom + teemaero - sl*rx;

solnt=Solve[lhs==rhs[[2]],tee''];

tee''=tee''/.solnt[[1]];

(* Small angle approximations for tee and tau *)
tee''=tee''/.{Sin[tee]->tee,Cos[tee]->1,tau^2->0};

tee''=tee''/.{tee^2->0,tee*tau->0};

denom=Denominator[tee''];

denom=Expand[Factor[denom]/omeg^2]

           2
2 Ib - m sl

num=Expand[Numerator[tee'']/omeg^2];

num=Collect[num,{g',g'',tee}];

(* The teeter equation if of the form          *)
(*      denom * tee'' = num                    *)
tee''=num/denom;

Derivative[2][tee]=tee'';
```

```
(* All g'^2 terms are multiplied by tee or tau  *)
(* and are therefore very small.  Neglect       *)
(* these in the final teeter equation, but      *)
(* retain in the tee'' used in the yaw equation *)
num=num/.g'^2->0
```

$$\frac{\text{hubmom}}{\text{omeg}^2} - 2\,\text{Ib}\,\text{tee} - \frac{\text{teemaero}}{\text{omeg}^2} - \frac{\text{grav m sl Cos[psi]}}{\text{omeg}^2} -$$

```
  4 Ib Cos[psi] g' + (-2 Ib Sin[psi] - Ls m sl Sin[psi] -

        2
     m sl  Sin[psi]) g''
```

```
(* Now derive the yaw equation for the      *)
(* teetering rotor                          *)
(* yaw moment arm to hinge, in tower coords *)
ryaw=Inverse[t3].{0,0,Ls};

(* transform from blade to inertial coords *)
trans=Inverse[t3].Inverse[t1].Inverse[t2];

trans=TrigReduce[trans];

trans=trans/.tau^2->0;

(* change sign of force to get reaction on hub *)
(* and add moment reaction on hub (transformed)*)
(* Finally, extract the x (yaw) component      *)
fyaw=-trans.{rx,ry,rz};

mall=Itensor.wdot+Cross[w,hg];

mx=-mall[[1]] - sl*ry;

(* Only the teeter moment transmitted by the *)
(* spring and damper will contribute to yaw  *)
my=-hubmom;

mz=-mall[[3]] + torq;

myaw={1,0,0}.(Cross[ryaw,fyaw] + trans.{mx,my,mz});

myaw=Expand[myaw]/.{tau^2->0,
                    Sin[tee]->tee,Cos[tee]->1};

myaw=myaw/.{tee^2->0,tee*tau->0,tee^3->0,
            tee*tee'->0,tee'^2->0,tee*tee''->0,
            tee'*tau->0,tee''*tau->0};

(* Get myaw/omeg^2 for use in yaw eqn. *)
myaw=Expand[myaw/omeg^2];

soln=Solve[myaw==Iyaw g'', g''];

yawaccel=g''/.soln[[1]];
```

```
yawaccel=yawaccel/.{tee^2->0, tee^3->0,
                    tee*tau->0,tau^2->0};

num=Numerator[yawaccel];

denom=Denominator[yawaccel];

denom=Expand[denom] omeg^2;

num=Expand[num/omeg^2];

(* Drop higher order terms in tee or derivatives *)
num=num/.{tee*tee'->0,tee^2->0,tee'^2->0,tee*tee''->0,
          tee*tau->0,tee'*tau->0,tee''*tau->0};

denom=Expand[denom/.Sin[psi]^2->1-Cos[psi]^2];

num=Expand[num/2/Ib];

num=Collect[num,{g',torq,fy,fz,hubmom}]
```

$$
\begin{aligned}
&fy\ \left(-\frac{Ls\ Cos[psi]}{omeg^2}+\frac{sl\ Cos[psi]}{omeg^2}+\frac{Ls\ m\ sl^2\ Cos[psi]}{2\ Ib\ omeg^2}-\right.\\
&\qquad \frac{m\ sl^3\ Cos[psi]}{2\ Ib\ omeg^2}\Bigg)+torq\\
&\left(-\frac{tau}{omeg^2}+\frac{m\ sl^2\ tau}{2\ Ib\ omeg^2}-\frac{tee\ Cos[psi]}{omeg^2}+\right.\\
&\qquad \frac{m\ sl^2\ tee\ Cos[psi]}{2\ Ib\ omeg^2}\Bigg)-Ls\ m\ sl\ tee\ Sin[psi]-\\
&\frac{Ls\ m\ sl\ teemaero\ Sin[psi]}{2\ Ib\ omeg^2}-\\
&\frac{grav\ m\ sl\ Cos[psi]\ Sin[psi]}{omeg^2}
\end{aligned}
$$

$$\frac{Ls\ grav\ m^2\ sl^2\ Cos[psi]\ Sin[psi]}{2\ Ib\ omeg^2} +$$

$$\frac{grav\ m^2\ sl^3\ Cos[psi]\ Sin[psi]}{2\ Ib\ omeg^2} +$$

$$hubmom\left(\frac{Sin[psi]}{omeg^2} - \frac{Ls\ m\ sl\ Sin[psi]}{2\ Ib\ omeg^2} - \frac{m\ sl^2\ Sin[psi]}{2\ Ib\ omeg^2}\right) +$$

$$fz\left(\frac{Ls\ tee\ Sin[psi]}{omeg^2} - \frac{Ls\ m\ sl^2\ tee\ Sin[psi]}{2\ Ib\ omeg^2}\right) -$$

$$2\ Ls\ m\ sl\ Cos[psi]\ Sin[psi]\ g' +$$

$$\left(Ls\ m\ sl\ tee\ Sin[psi] - \frac{Ls^2\ m^2\ sl^2\ tee\ Sin[psi]}{2\ Ib}\right) -$$

$$\frac{Ls\ m^2\ sl^3\ tee\ Sin[psi]}{2\ Ib} - 2\ Ib\ tau\ Cos[psi]\ Sin[psi] -$$

$$\frac{Ls^2\ m^2\ sl^2\ tau\ Cos[psi]\ Sin[psi]}{2\ Ib} +$$

$$\frac{m^2\ sl^4\ tau\ Cos[psi]\ Sin[psi]}{2\ Ib} -$$

$$2\ Ib\ tee\ Cos[psi]^2\ Sin[psi] +$$

$$Ls\ m\ sl\ tee\ Cos[psi]^2\ Sin[psi] +$$

$$m^2\ sl^2\ tee\ Cos[psi]^2\ Sin[psi])\ g' +$$

$$2\ Ls\ m\ sl\ Cos[psi]\ tee' - 2\ m\ sl^2\ Cos[psi]\ tee' -$$

```
      2   3                    2   4
  Ls m  sl  Cos[psi] tee'   m  sl  Cos[psi] tee'
  ---------------------- + --------------------
            Ib                      Ib
```

```
denom=denom/2/Ib;

Collect[denom,{Iyaw,Cos[psi]}]
```

```
                                      2
  2                                 m sl
Ls  m + 2 Ls m sl + Iyaw (1 - ----- ) +
                                  2 Ib

                          2  2   2    2   4
                       2   Ls  m  sl    m  sl           2
  (-2 Ls m sl - m sl   - ---------- + ------) Cos[psi]
                           2 Ib       2 Ib
```

Appendix B

Descriptions of the Combined Experiment, Mod-2 (Rigid Hub Wind-Tunnel Model) and ESI-80 Systems

This Appendix contains the wind turbine characteristics used in the YawDyn calculations presented in this report. The data were taken directly from a typical "YawDyn.opt" output file for each machine. The values were obtained from personal communications with SERI personnel.

SERI Combined Experiment Rotor

ROTOR SPEED (RPM) = 72.0

ROTOR RADIUS (FT) = 16.50
HUB RADIUS (FT) = 1.70
HUB HEIGHT (FT) = 55.0
INITIAL PITCH ANGLES (DEG) = 5.0, 5.0, 5.0
BLADE CENTER OF GRAVITY (FT) = 5.44
YAW AXIS-TO-HUB DISTANCE (FT) = 5.0
NUMBER OF BLADES = 3
PRE-CONING ANGLE (DEG) = 3.0
ROTOR TILT ANGLE (DEG) = .00

MASS OF BLADE (SLUG) = 3.340
BLADE FLAP MOMENT OF INERTIA (SLUG*FT^2) = 178.0
NACELLE MOMENT OF INERTIA (SLUG*FT^2) = 1000.0

BLADE STIFFNESS COEF. (LB-FT/RAD) = 155000.
BLADE NATURAL FREQUENCY (HZ) = 4.70
BLADE ROTATING NATURAL FREQUENCY (P#) = 4.06

UNSTEADY STALL PARAMETERS:
STALL ANGLE = 15.2
UPPER HYSTERESIS LOOP CONSTANT = .00
LOWER HYSTERESIS LOOP CONSTANT = .70
AIRFOIL THICKNESS/CHORD = .1500
FILTER CUTOFF FREQUENCY, (PER REV) = 20
NUMBER OF FILTER STAGES = 2

ZERO-LIFT ANGLE OF ATTACK = -1.44

AIRFOIL CHARACTERISTICS:

ANGLE OF ATTACK(DEG)	LIFT COEF.
-.01	.1360
3.08	.4410
6.16	.7390
9.22	.9210
12.22	1.0070
14.24	1.0290
15.24	1.0350
16.24	1.0070
18.20	.8860
20.15	.7840

AIRFOIL CHARACTERISTICS:

ANGLE OF ATTACK(DEG)	DRAG COEF.
-.01	.0121
3.08	.0133
6.16	.0154
9.22	.0373
12.22	.0587
14.24	.0891
15.24	.1151
16.24	.1548

Blade profile in 10% increments from root (5%) to tip (95%):

TWIST ANGLE (DEG)	CHORD (FT)
0.0	1.50
0.0	1.50
0.0	1.50
0.0	1.50
0.0	1.50
0.0	1.50
0.0	1.50
0.0	1.50
0.0	1.50
0.0	1.50

ESI-80 Rotor

ROTOR SPEED (RPM) = 60.0

ROTOR RADIUS (FT) = 40.0
HUB RADIUS (FT) = 3.00
HUB HEIGHT (FT) = 80.0
INITIAL PITCH ANGLES (DEG) = 0.0, 0.0
BLADE CENTER OF GRAVITY (FT) = 16.1
YAW AXIS-TO-HUB DISTANCE (FT) = 6.79

NUMBER OF BLADES = 2
PRE-CONING ANGLE (DEG) = 7.0
ROTOR TILT ANGLE (DEG) = 0.0

MASS OF BLADE (SLUG) = 52.08
BLADE FLAP MOMENT OF INERTIA (SLUG*FT^2) = 7350.0
NACELLE MOMENT OF INERTIA (SLUG*FT^2) = 500.0

FREE TEETER ANGLE (DEG) = 6.00000
FIRST TEETER STIFFNESS COEFF. (FT-LB/RAD) = 2.000000E+06
SECOND TEETER STIFFNESS COEFF. (FT-LB/RAD) = 1.000000E+08
TEETER DAMPING COEF (FT-LB-S) = 20000.0
ROTOR MASS OFFSET (FT) = .180000

UNSTEADY STALL PARAMETERS:
STALL ANGLE = 14.0
UPPER HYSTERESIS LOOP CONSTANT = 0.0
LOWER HYSTERESIS LOOP CONSTANT = .50
AIRFOIL THICKNESS/CHORD = .1500
FILTER CUTOFF FREQUENCY, (PER REV) = 20.0
NUMBER OF FILTER STAGES = 2

ZERO-LIFT ANGLE OF ATTACK = -4.00

AIRFOIL CHARACTERISTICS:

ANGLE OF ATTACK(DEG)	LIFT COEF.
-4.0	-.0436
.0	.4223
4.0	.8786
8.0	1.2557
12.0	1.4846
14.0	1.5217
15.0	1.5172
16.0	1.4957

AIRFOIL CHARACTERISTICS:

ANGLE OF ATTACK(DEG)	DRAG COEF.
-4.0	.0125
.0	.0123
4.0	.0147
8.0	.0201
12.0	.0290
14.0	.0348
15.0	.0380
16.0	.0415
17.0	.0453
18.0	.0494

Blade profile in 10% increments from root (5%) to tip (95%):

TWIST ANGLE (DEG)	CHORD (FT)
1.0	1.00
2.0	2.20
1.9	2.50
1.8	2.90
1.5	2.70
1.2	2.50
.8	2.20
.1	2.00
-.3	1.90
-1.5	1.50

Mod-2, Rigid-Rotor, Wind Tunnel Model

ROTOR SPEED (RPM) = 350.0

ROTOR RADIUS (FT) = 7.5
HUB RADIUS (FT) = .00
HUB HEIGHT (FT) = 10.0
INITIAL PITCH ANGLES (DEG) = .00 & 0 .00
BLADE CENTER OF GRAVITY (FT) = 1.5
YAW AXIS-TO-HUB DISTANCE (FT) = -1.33
NUMBER OF BLADES = 2.0
PRE-CONING ANGLE (DEG) = 0.0
ROTOR TILT ANGLE (DEG) = 0.0

MASS OF BLADE (SLUG) = .3285
BLADE FLAP MOMENT OF INERTIA (SLUG*FT^2) = 2.2
NACELLE MOMENT OF INERTIA (SLUG*FT^2) = 2.0

BLADE STIFFNESS COEF. (LB-FT/RAD) = 22300.0
BLADE NATURAL FREQUENCY (HZ) = 16.0602
BLADE ROTATING NATURAL FREQUENCY (P#) = 2.929

YAW STIFFNESS COEF. (FT-LB/RAD) = 0.0
YAW AXIS FRICTION (FT-LB) = 0.0
YAW AXIS DAMPING (FT-LB-SEC) = 0.0

TOWER SHADOW COEFFICIENT = 0.0

TOLERANCE FOR TRIM SOLUTION
CONVERGENCE TEST = 1.0E-02

UNSTEADY STALL PARAMETERS:
STALL ANGLE = 18.0
UPPER HYSTERESIS LOOP CONSTANT = 0.5
LOWER HYSTERESIS LOOP CONSTANT = 0.5
AIRFOIL THICKNESS/CHORD = 0.15
FILTER CUTOFF FREQUENCY, (PER REV) = 20.0

NUMBER OF FILTER STAGES = 2

ZERO-LIFT ANGLE OF ATTACK = -1.3

AIRFOIL CHARACTERISTICS:

ANGLE OF ATTACK(DEG)	LIFT COEF.
-10.26	-.7184
-4.09	-.2379
.00	.10
2.10	.26
8.27	.73
12.39	1.0570
16.43	1.1750
18.45	1.2165
20.45	1.2173
22.44	1.1938
24.42	1.1506
26.41	1.1164
30.24	.660
35.27	.7470
40.29	.7861
45.29	.8013
50.29	.7790
60.00	.70
70.00	.55
80.00	.37
90.00	.10
100.00	-.17
110.00	-.40
120.00	-.60
130.00	-.80
140.00	-.90
150.00	-.80
160.00	-.60
170.00	-.80
180.00	.00

AIRFOIL CHARACTERISTICS:

ANGLE OF ATTACK(DEG)	DRAG COEF.
-10.26	.0368
-4.09	.0180
.00	.0149
2.10	.0166
8.27	.0310
12.39	.0535
16.43	.0981
18.45	.1218
20.45	.1522
22.44	.2209
24.42	.2209
26.41	.2580
30.24	.5060
35.27	.6350
40.29	.7540
45.29	.8840

50.29	.9850
60.0	1.20
70.0	1.38
80.0	1.50
90.0	1.55
100.0	1.50
110.0	1.40
120.0	1.26
130.0	1.07
140.0	.90
150.0	.60
160.0	.33
170.0	.15
180.0	.0

Blade profile in 10% increments from root (5%) to tip (95%):

TWIST ANGLE (DEG)	CHORD (FT)
.0	.2250
.0	.2250
4.50	.60
3.0	.40
2.50	.39
2.0	.39
.70	.3850
.40	.37
.30	.36
-2.50	.24

USER'S GUIDE

to the Yaw Dynamics Computer Program

YAWDYN

A.C. Hansen
X. Cui

Mechanical Engineering Department
University of Utah
Salt Lake City, UT 84112

User's Guide Date and Version
January, 1992
Version 6

Program date and version
YawDyn 5.4: 1/8/92

Prepared for the Solar Energy Research Institute
under Subcontract No.
XL-6-05078-2

NOTICE

This report was prepared as an account of work sponsored by the Solar Energy Research Institute, a Division of Midwest Research Institute, in support of its Contract No. DE-AC02-83-CH10093 with the United States Department of Energy. Neither the Solar Energy Research Institute, the United States Government, nor the United States Department of Energy, nor any of their employees, nor any of their contractors, subcontractors, or their employees, makes any warranty, express or implied, or assumes any legal liability or responsibility for the accuracy, completeness or usefulness of any information, apparatus, product or process disclosed, or represents that its use would not infringe privately owned rights.

TABLE OF CONTENTS

USER'S GUIDE
to the Yaw Dynamics Computer Program
YAWDYN

User's Guide Date and Version
January, 1992
Version 6

Program date and version
YawDyn 5.4: 1/8/92

Introduction

This report is intended to provide information necessary to prepare inputs for the computer program YawDyn. YawDyn was developed with the support of the Solar Energy Research Institute Wind Research Branch for the analysis of the yaw motions and loads of a horizontal axis wind turbine with a rigid or teetering hub and two or three blades. In this document a detailed description of each of the program inputs and operating instructions will be given. A sample input file and output file are provided for testing the program operation. There is no discussion of the underlying theory or limitations of the models. That discussion is available in annual reports and journal articles [see list of references]. In early reports on this program references were made to three independent programs, YAWDYN, SDOF, and UFLAP. The functions of all three programs are now combined into the single program which is the subject of this document, YawDyn.

This version of the User's Guide is current as of the date and version shown above. It is applicable to versions of the programs with the dates given on the cover page. Since the software development is continuing, and significant changes are continually being made to the programs, the reader should be certain the guide is appropriate to the program version that will be used.

Disk Files Included with YawDyn

Two files contain the source code for the YawDyn program. They are the main body of the program "YAWDYN.FOR" and a single Include file "YAWDYN.INC". The primary data input file is called "YAWDYN.IPT". If desired, a second input file called "YAWDYN.WND" can be read by the program. This file contains time-varying wind data (details are provided below). Up to three output files are created by YawDyn. The "YAWDYN.OPT" file is intended for printing a record of all the input conditions and a sample of the calculated results. File "YAWDYN.PLT" is tabular data intended for plotting results of the simulation with a variety of commercially available graphics packages. Finally, "YHARMON.IPT" is an optional output file intended for use with the program "YHARMON". YHarmon calculates the harmonic content (Fourier series) of the yaw and flap moments which are output by YawDyn.

Nomenclature and Sign Conventions

The analysis is directed toward a wind turbine with the general configuration shown in Figures 1 and 2 or 3. The rotor can have 2 or 3 blades and the hub is rigid or teetering. The blade flap degree of freedom is modeled using an equivalent hinge and spring arrangement as shown in Figure 2 if the hub is rigid (not teetering). The teetering hub

configuration is shown in Figure 3. Effects of undersling and the damping and stiffness characteristics of the teeter stop are included in the teetering model. The model assumes that all blades are identical in all respects *except* that each blade pitch angle is specified independently.

The definitions of yaw angle (γ) and wind direction (δ) are shown in Figure 1. (Note this is an unconventional definition of wind direction.) The yaw angle is the angle the rotor makes with the coordinate system, not with the instantaneous wind vector. Thus the yaw error (or difference between the compass rotor direction and wind direction) is $\gamma + \delta$. However, it is most common to use the program with the wind direction $\delta = 0$. Then the yaw angle and the yaw error are the same. A positive vertical wind shear causes an increase in wind speed with height above ground. A positive horizontal wind shear causes an increase in wind speed with increasing coordinate y. See Figure 4.

The rotor can be downwind of the tower (positive L_S in Figure 1 or FORTRAN variable SL) or it can be upwind (negative L_S). The blade hinge of the rigid hub can be offset an arbitrary distance from the axis of rotation. The location of the hinge defines both the structural hinge axis and the beginning of the aerodynamic surface of the blade. When a teetering rotor is modeled, the hub radius must be zero to place the teeter axis on the rotor axis of rotation.

The rotation of the rotor must be clockwise when viewed looking in the downwind direction. If the rotor to be analyzed actually turns in the counterclockwise direction, the user must be careful interpreting the sign conventions. It is best to consider the position of the blade when it is advancing into the region of increased relative wind speed (due to yaw angle or wind shear) and adjust the signs of the yaw angle and wind shears to be appropriate to this condition.

An example may clarify this potentially confusing topic. In the example, consider a downwind rotor which spins counterclockwise when viewed from a position upwind of the machine. In this case the rotor angular velocity vector (using the right hand rule) is directed from the hub toward the yaw axis and the rotation is opposite that used in the program. Consider also that the wind speed is higher on the left side of the rotor than on the right (when looking downwind). This situation is sketched in the views labeled "actual situation" in Figure 5. It is not possible to run the program with a negative (counterclockwise) rotor rpm, so other signs must be adjusted. With yaw and horizontal wind shear the blade will be advancing into the wind when the blade is vertical upwards (ψ=180°) and the yaw angle is *negative*. If the rotor spin were clockwise the advancing blade would be at ψ=180° when the yaw angle is *positive*, and the horizontal shear is *negative*. Thus the change in the sense of rotation requires a change in the sign of the yaw angle and the horizontal wind shear to achieve the same conditions for the blade. This is depicted in the views labeled "model equivalent" in Figure 5. To summarize, the actual situation in Figure 5 has counterclockwise rotor rotation, a negative yaw angle and positive wind shear. This is modeled with clockwise rotation, positive yaw, and negative horizontal shear. The goal at all times is to keep the orientation of the advancing blade correct.

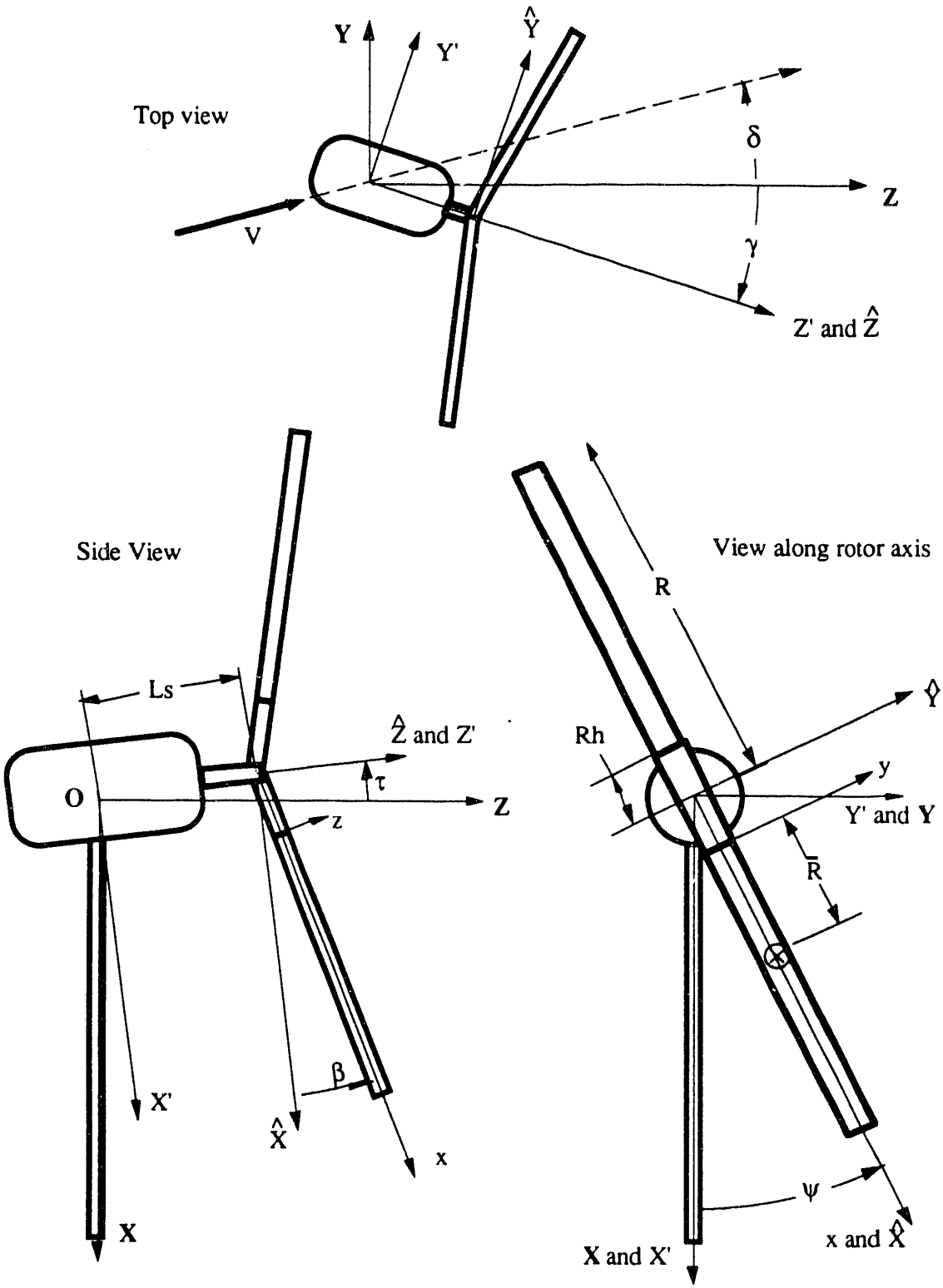

Figure 1. View of the HAWT defining selected terms and coordinates systems. The bold **X,Y,Z** axes are fixed in space while the X',Y',Z' axes are attached to the nacelle and yaw with the machine. The $\hat{X},\hat{Y},\hat{Z}$ system rotates with the shaft of the rotor and the x,y,z system is attached to the blade, with Blade #1 in the direction of the positive x-axis.

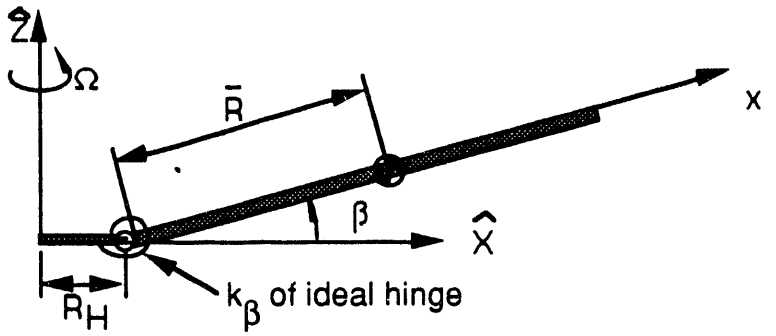

Figure 2. The equivalent hinge-spring model for the blade flap degree of freedom.

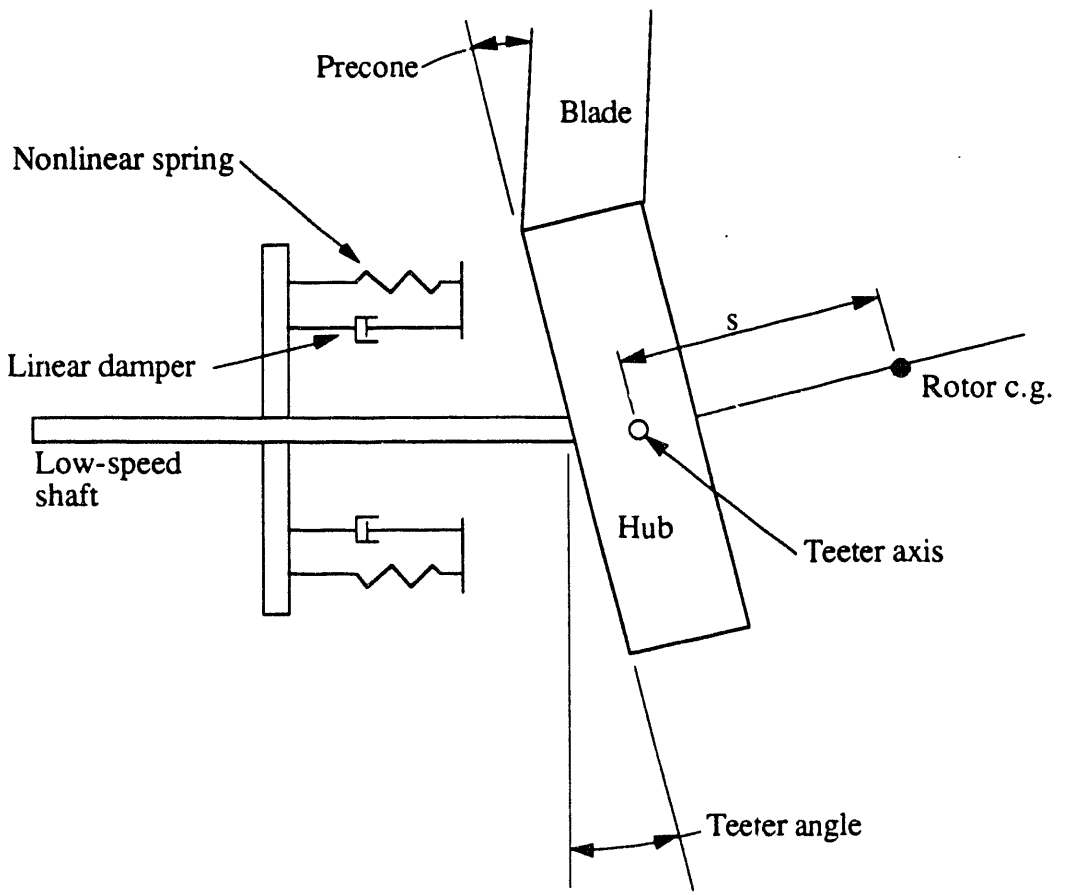

Figure 3. The configuration of the teetering hub model. The spring and damper are only active when the teeter deflection exceeds the angle TEE1.

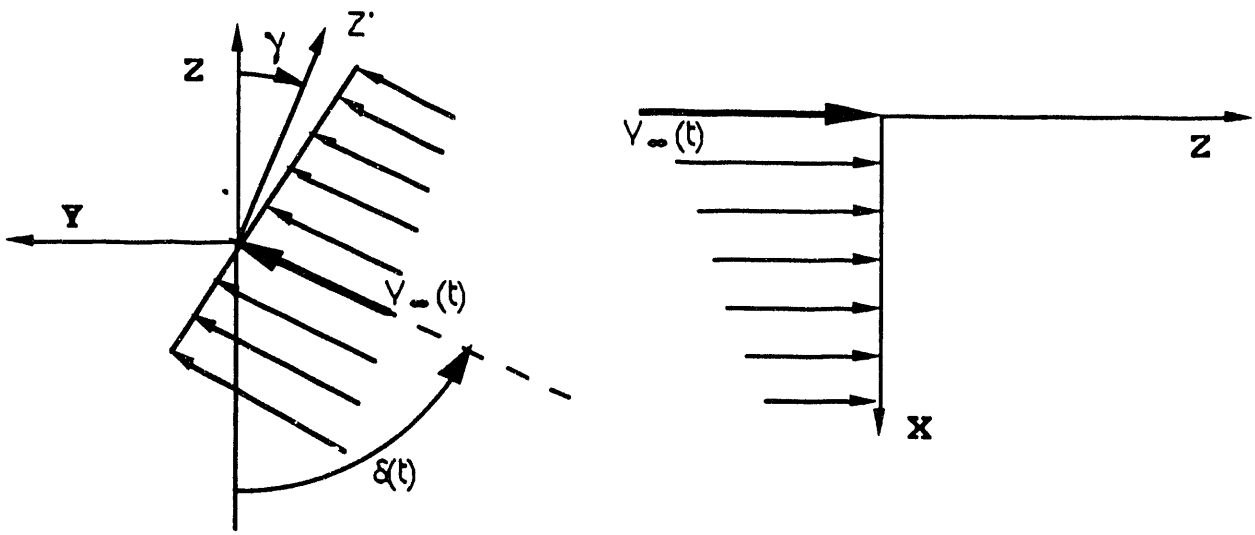

Figure 4. Wind shear models. Horizontal shear in left sketch, Vertical shear in right sketch. Note the wind direction (δ) and yaw angle (γ) are both defined with respect to the **Z** axis.

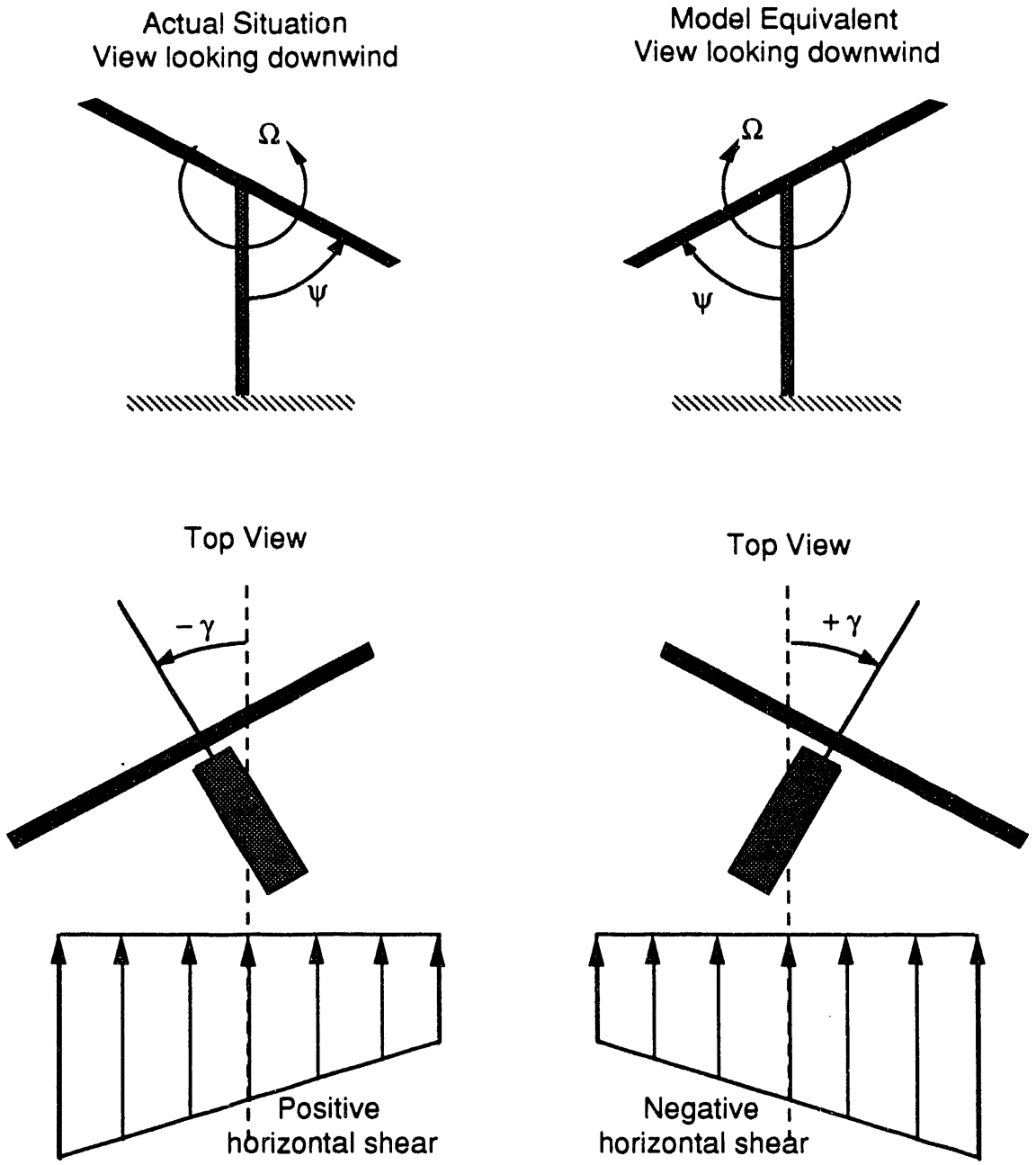

Figure 5. Views of example configuration with horizontal wind shear. Left half shows the actual configuration while the right side shows how that configuration can be modeled in YawDyn.

Input Data File Description

A sample input data file is given in Table 1. A text data file containing each of these items must be available in the directory or folder from which the program is run. The following is a description of each of the input variables. The formatting is list-directed (or free). There are no restrictions on the spacing of the values other than the order of the variables on a line, the order of the lines, and the presence (absence) of a decimal point in a floating point (integer) value. Values on one line should be separated by one or more spaces. Each

line, except the first, can be terminated with a text string to identify that line. Each line must terminate with a return character. Each line must contain all of the variables specified for that line in the table below. Omission of a value, even if it is not used by the program in that particular run, will result in an execution error.

In the description that follows, the units for each parameter are listed for the program as it is used at the University of Utah. However, it is quite simple to change the program to run in SI units. The value of the gravitational constant, GRAV, must be changed in the program source code to GRAV=9.81. Then the units input to the program must all be consistent with the SI system (kg, m, sec, N, deg or rad as listed below, etc.).

The last three values on the second input line control the output of data to the CRT and data files. The volume of data makes it undesirable to print a record of all variables at all times and blade locations during a simulation. Instead, one particular revolution and one blade element are selected for tabulation of the most detailed information. Also, the time steps in the simulation are generally shorter than that needed for data output. The program will decimate the output if desired. The value IPRINT specifies the decimation factor.

Line	Position	Name	Units	Description
1	1	TITLE	--	Any character string (<80 characters) to identify the system being analyzed. This also serves as an aid to identifying the contents of the data file.
2	1	IYAWC	--	A flag to determine whether the simulation is for fixed or free-yaw operation. If IYAWC=0, the system is rigidly fixed, if IYAWC=1, then the system is constrained by the yaw torsional spring. If the spring stiffness (see line 5) is zero then the system is free-yawing.
2	2	MREV	--	Identifies the rotor revolution for which detailed data will be sent to the YawDyn.opt and the YHarmon.ipt files.
2	3	NSEE	--	The blade element number for which detailed data will be sent to the YawDyn.plt and YawDyn.opt files. The value ranges from 1 for the inboard element to 10 for the tip element.
2	4	IPRINT	--	The decimation factor for data output. Typically, printing every 5th to 10th time step will provide output data with adequate resolution.
3	1	FDOF	--	A flag to determine whether the flap degree of freedom is included in the calculations. If FDOF=1, flap motion and its effect on yaw loads are calculated. If FDOF=0, the flap angle is held constant at the precone value and the flap rate is zero. (In the terminology of early reports, program becomes SDOF when FDOF=0 and it becomes the original YawDyn program when FDOF=1.)

3	2	ITETER	--	A flag to determine whether the rotor has a rigid or teetering hub. If ITETER=0 the hub is rigid, if ITETER=1 the hub is teetering. If the hub is teetering then the flap DOF becomes the teeter DOF and the blade is completely rigid. If ITETER=1 then FDOF must be 1 also.
3	3	IWND	--	A flag to identify the source of wind speed and direction data. If IWND=0, then the operating conditions such as wind speed, wind direction, pitch angle and wind shears are read from later lines in this data file. These constant values will be used for all calculations. If you wish to allow the winds or pitch angles to vary with time, then the desired values must be stored as a time series in file YawDyn.Wnd. If IWND=1, then the operating conditions are read from the data file YawDyn.Wnd. This makes it possible to run the program using actual values of operating conditions from test data or artificial time series of wind conditions.
3	4	DELTAT	sec	This is the time interval for the sampled wind data in the file YawDyn.Wnd. The interval must be greater than the time step used in the integration (see variable 'SECTOR' below). During program execution the file is read as simulated time increases. The values of operating conditions at time t_1 are used for simulated time $t_1 < t < t_1$+DELTAT. Thus DELTAT should be kept small to avoid large step changes in the winds. A value of DELTAT must be given, whether YawDyn.Wnd is used or not. But if IOPT=0, the value of DELTAT is ignored, thus any value can be used. See the text in a later section of this document for more details on the YawDyn.Wnd file.
3	5	IHARM	--	A flag which determines whether the output file YHarmon.ipt is created. Enter a value of 1 if you want the file created, 0 if you do not. The Yharmon.ipt file is used by another program, YHARMON.FOR, to calculate the harmonic content of the yaw moment and flap moment during one selected revolution of the rotor (the MREVth revolution).
4	1	YI	slug-ft^2	Mass moment of inertia of the main frame, nacelle and hub about the yaw axis. YI represents the total moment of inertia of all the yawing mass <u>except the blades</u>.
4	2	BM	slugs	The mass of <u>one</u> blade. Even when the rotor has a teetering hub the mass of just one blade should be entered in this location.

4	3	BLINER	slug-ft^2	The blade mass moment of inertia about the flap axis (through the hinge point). If the rotor is teetering then BLINER represents one-half the moment of inertia of the entire rotor (including hub and any concentrated masses) about the teeter axis.
5	1	FS	ft-lb/rad	The torsional spring constant of the equivalent flapping hinge spring at the blade root. This value is named k_β in the reports and literature and in Figure 2 above. When FDOF=0 or when ITETER=1, this value is not used (but it still must be present in the input file).
5	2	YAWSTF	ft-lb/rad	The torsional spring constant of the yaw drive or yaw brake system. This variable can be used to represent an equivalent stiffness of the yaw control system and the tower. The value must always be present in the data file, but is only used when "free yaw" is simulated. If the actual system stiffness is very high, then the system should be run in "fixed yaw".
5a				This line is included only if the system has a teetering rotor. If the hub is rigid, skip to line 6.
5a	1	TEE1	deg	For a teetering rotor only, the teeter angle at which the first contact with the teeter "stop" is made. No mechanical teeter moment is applied at the hub if the absolute value of the teeter angle is less than TEE1. For teeter angles greater than TEE1, a nonlinear spring and a linear damper are active. See Figure 3 for a sketch of the teetering hub configuration.
5a	2	SPRNG1	ft-lb	The first (linear) coefficient in the quadratic equation which describes the teeter spring or "stop". The moment applied by the teeter spring is given as $M = \text{SPRNG1} \cdot \delta + \text{SPRNG2} \cdot \delta^2$ Where δ is the spring deflection in radians and the sign is chosen appropriately for the direction of deflection.
5a	3	SPRNG2	ft-lb	The second coefficient in the equation which describes the teeter spring. SPRNG1 and SPRNG2 determine the shape of the parabolic spring which represents the teeter stop.
5a	4	TDAMP	ft-lb-sec	The coefficient of the linear teeter damping. The damper is active for all teeter angles greater than TEE1. The teeter moment (ft-lbs) due to mechanical damping on the teeter axis is TDAMP multiplied by the teeter rate in radians/sec
5a	5	SLING	ft	The offset of the center of gravity of the rotor from the teeter axis. SLING is positive if the c.g. of the rotor is

				downwind of the teeter axis. Shown as "s" in Figure 3.
6	1	R	ft	The rotor radius.
6	2	RB	ft	The distance along the blade from the hinge axis to the blade center of gravity.
6	3	RH	ft	This value affects the dynamic and aerodynamic analysis. It is the distance from the axis of rotation to the hinge axis (the hub offset). It also represents the distance to the first airfoil section on the blade. The aerodynamic analysis is only performed for blade elements outboard of the hub offset. To maintain the correct flap velocities, RH must be zero for the teetering rotor.
6	4	HH	ft	Hub height of the rotor above the ground.
6	5	B	--	Number of blades, B≥2, except the teetering rotor must have B=2.
6	6	PC	deg	Blade precone angle.
7	1	VB	ft/sec	Horizontal wind speed at the hub (see IWND above for conditions when this value is used by the program).
7	2	VX	ft/s	Vertical component of the wind speed. (The **X**-component, thus a positive value is a wind blowing down toward the ground.) This value is assumed constant in time and uniform over the rotor disc in the present analysis. Normally the average value in flat terrain is zero, but in complex terrain the vertical wind can be very significant.
7	3	RPM	rpm	Rotor rotation speed.
7	4	HSHR	--	A measure of the horizontal wind shear across the rotor disc. The value is typically -1. < HSHR < +1. and represents the wind speed at the 3/4 radius on one side of the rotor, minus the wind at the 3/4 radius on the opposite side of the rotor, divided by the hub wind speed. That is, $$HSHR = \frac{(\text{Wind speed at } y = +\frac{3}{4}R) - (\text{Wind speed at } y = -\frac{3}{4}R)}{\text{Wind Speed at hub } (y=0)}$$ A linear variation of wind speed across the disc is used for shear in the horizontal direction.
7	5	VSHR	--	A measure of the vertical wind shear across the rotor disc. The value can assume two meanings, depending upon the value of ISHR (see next item). If linear shear is requested, then VSHR is defined in a manner identical to HSHR (except, of course, it applies to

				variations in the vertical direction). If power-law shear is requested, the value of VSHR is the exponent in the power law relationship. Typical values would then be 0.1 to 0.2.
7	6	ISHR	--	A flag to indicate the type of vertical wind shear used in the calculations. If ISHR=1, then linear vertical shear is used. If ISHR=2, then power-law vertical shear is used. The horizontal wind shear is always linear shear.
7	7	VELDEF	--	A measure of the strength of the velocity deficit in the wake of the tower (tower shadow). The value is the amplitude of the fractional decrease in hub wind speed at the center of the tower shadow. Typical values are 0.05 to 0.2.
8	1	SL	ft	The distance from the yaw axis to the center of the hub (the vertex of the rotor cone). A positive value is used for a downwind rotor, a negative value for an upwind rotor.
8	2	AV	ft-lb-sec	The linear yaw damping coefficient. The yaw moment (ft-lbs) due to mechanical damping on the yaw axis is AV multiplied by the yaw rate in radians/sec.
8	3	AF	ft-lb	The sliding friction moment. A constant yaw moment due to friction. Note this is not a friction coefficient.
8	4	TILT	deg	The tilt angle of the rotor axis of rotation. The sign convention is <u>not</u> consistent with the coordinate system. That is, positive tilt is a rotation about the negative Y'-axis.
9	1-B	PITCH	deg	The pitch angles of each blade. The values need not be the same for all blades, but a value must be entered for each blade.
10	1	Q(3)	deg	Initial yaw angle for the solution. When a yaw drive stiffness is specified and the program is run for "free yaw", this angle also specifies the undeflected position of the torsion spring.
10	2	Q(4)	deg/sec	Initial yaw rate for the solution.
11	1-2B	QP array	°& °/s	Initial flap angle and flap rate for each blade. (For a teetering rotor, only the values for blade #1 must be input.) The first value is the flap angle for blade #1. The second value is the flap rate for blade #1, and so on. These values are important to the efficient convergence to a rotor trim solution. It is suggested that when a rotor is analyzed for the first time, the flap angles should all equal the precone angle and the flap rates should all be zero. This will result in a slow but

				accurate convergence to a trim solution. When the trim solution is found, the values of flap and flap rate are output to the CRT. These values can be used in subsequent runs of the program to significantly reduce the time required to find the trim solution. When FDOF=0, these values are ignored by the program.
12	1	N	--	Number of rotor revolutions which will be calculated in the solution. This value determines the total run time of the simulation according to the relation Total Time=N*60/RPM.
13	1	SECTOR	--	The rotor disc is divided into 'SECTOR' equally spaced pie-wedge sectors for the integration. The time step is determined from the floating point value SECTOR using the equation $\Delta t=60/(SECTOR*RPM)$. Typically 60-90 sectors are sufficient if the flap degree of freedom is neglected and 150-200 sectors are sufficient if the flap dof is included. As the blade stiffness increases in YawDyn the value of SECTOR must increase as well. If the program will not converge to a trim solution, increase SECTOR. When the program is run in free-yaw the value for SECTOR should be increased if a stiff blade is flapping in the simulation. A value between 600 and 800 may be needed. The maximum value of SECTOR is determined by the 3rd dimension of the FETRIM array in the main program. In the current version of YawDyn the maximum value for SECTOR is 800.
13	2	TOLER	deg	The tolerance used in checking for a trim solution. Typically 0.01-0.02° for a rigid hub and 0.1-0.2° for a teetering hub. If the solution will not converge, try increasing SECTOR or, as a last resort, increasing TOLER.
13	3	RHO	$slug/ft^3$	Ambient air density.
14	1	ALPHAS	deg	This line of input pertains to the dynamic and static stall characteristics of the airfoil. The first parameter is the static stall angle of attack of the airfoil.
14	2	DSTLHI	--	The parameter in the Gormont dynamic stall model which determines the size of the upper hysteresis loop. The nominal value is 0.5. If dynamic stall should not be included in the analysis, this parameter must equal zero.
14	3	DSTLLO	--	The parameter in the Gormont dynamic stall model which determines the size of the lower hysteresis loop. The nominal value is 0.5. If dynamic stall should not be included in the analysis, this parameter must equal zero.

14	4	THICK	--	The thickness/chord ratio of the airfoil. This parameter is used only in the Gormont dynamic stall model. A typical value is 0.15.
15	1	CFILT	p	The use of dynamic stall requires digital filtering (smoothing) of the angle of attack time-history to achieve an accurate estimate of the rate-of-change of angle of attack. This parameter sets the cutoff frequency (-3dB) of the lowpass filter. The value should be as large as is consistent with "smooth" angle of attack behavior (but less than SECTOR/5). A typical value is 30 (30 times the rotor rotation frequency). Low values will result in phase errors in the blade flap and subsequent errors in the yaw moments.
15	2	NFILT	--	The number of stages of the digital filter. Allowed values are 1, 2, or 3. Two stages typically are sufficient.
16	1	NCL	--	The number of points tabulated to specify the lift coefficient curve for the airfoil. The maximum value of NCL is 30.
16	2	NCD	--	The number of points tabulated to specify the drag coefficient curve for the airfoil. The maximum value of NCD is 30.
16	3	ALPHAL	deg	The zero-lift angle-of-attack of the airfoil.
17[1]	1	AL	deg	The angle of attack for the first point in the lift coefficient table.
17	2	CL	--	The lift coefficient corresponding to the angle of attack entered on this line. NCL lines such as this are entered to completely specify the lift coefficient vs. angle of attack curve. Flat-plate values of CL and CD are calculated by the program when the angle of attack is outside the range supplied in this table. Care must be taken to verify the complete CL-Alpha curve w
--[2]	1	AD	deg	The angle of attack for the first point in the drag coefficient table.
--	2	CD	--	The drag coefficient corresponding to the angle of attack entered on this line. NCD lines such as this are entered to completely specify the drag coefficient vs. angle of attack curve.

[1]Line numbers 17 through 16+NCL
[2]Line numbers 17+NCL through 16+NCL+NCD

--[1]	1	TWIST	deg	The blade is described in terms of 10 equally spaced elements. The last ten lines of the input data file provide the twist and chord distribution for the ten elements. The first value of TWIST is the twist angle at the inner-most element (r/R=0.05). The last line of the input file contains the twist and chord of the blade tip element (r/R=0.95).
--	2	CHORD	ft	The blade chord of the first (inner) blade element.

Integration of the equations of motion is accomplished using an explicit, forward stepping technique called the Adams-Bashforth method. There is no internal self-testing to determine if the step size (determined by the variable SECTOR) is small enough to give accurate results. Hence, the user must verify that SECTOR is large enough. The simplest way to do this is to run the same data set with increasing numbers of sectors until the results no longer change. Of course there is incentive to keep SECTOR as small as possible because the total run time of the simulation is proportional to the number of time steps. Generally, as the stiffness of the blade hinge increases the size of the time step must decrease to maintain accuracy.

When a free-yaw rotor with blade flapping is modeled, the system typically has a "stiff" set of equations. That is, there is a large difference between the high flap frequency and the low yaw motion frequency. YawDyn will be more stable when a large value of SECTOR (perhaps 800) is used for these free-yaw cases. This is particularly the case when the blade is quite stiff (say, for example 3 or 4p). These very stiff systems will tend to show numerical instability when the yaw motion is very slow. For example, when a rotor is released from rest with a yaw error, the solution will proceed smoothly as the rotor yaws to align with the wind. But after the rotor is aligned and the yaw rate becomes small, then numerical problems may appear. This should not be a problem as that phase of rotor operation can easily be handled by running a fixed-yaw simulation.

[2] Line numbers 17+NCL+NCD through 26+NCL+NCD (the last ten lines of the file)

The YawDyn.Wnd Data File

If the parameter IWND in line 3 of the YawDyn.ipt file is equal to 1, the program will look for a tabular time series of operating conditions in file YawDyn.Wnd. (If IWND=0, then the file YawDyn.Wnd need not be present.) In the current version of the program the values of wind speed at the hub (VB), wind direction (DELTA), horizontal wind shear (HSHR), and vertical wind shear (VSHR) are entered in tabular form as a function of time (TDATA). Read statements which access this file are found in two locations in the program. The first is in the main program, and the second is in subroutine GETWND. Both statements are of the form `READ(11,*) TDATA,VB,DELTA,HSHR,VSHR`. If desired, the list of variables read in can be shortened or extended to meet particular requirements. All that is required is to change these two READ statements. One parameter which might be added is blade pitch. If that is done one additional change may be required. Since the program retains pitch angles for each blade independently, the YawDyn.Wnd file must contain pitch data for each blade [i.e. `READ(11,*) TDATA, VB, ..., (PITCH(I),I=1,NB)`]. However, if all pitch angles are the same, one value may be read and program lines must be added to equate the pitch of each blade to the data value. That is,

```
READ(11,*) TDATA, VB, ..., PITCH0
PITCH(1) = PITCH0
PITCH(2) = PITCH0
etc.
```

It can be seen from the READ statement that the tabular values can be separated by spaces in the YawDyn.Wnd file, all values read in for a particular time TDATA must be on one line, and each line must end with a return character.

Table 1.
Sample Input Data File for the SERI Combined Experiment Wind Turbine

```
Combined Experiment Baseline
  0     1     8      5                  Free yaw=1, Print: Rev#, Element#, Interval
  1     0     0     .0672      1        FDOF,ITETER,IWND,DELTAT,IHARMonics file?
 1000.        3.34     178.             YawInertia, Blade mass, Blade flap inertia
 1.55E+5       4.0E5                   Flap Stiffness=1.55E+5, Yaw Stiffness
 16.5     5.44    1.7    55.   3.   3. Radius,RBar,RHinge,HubH,#Blades,PreCone
 37.0   0.0   72. 0.0   0.14   2 0.1   VB,VX,RPM,HSHR,VSHR,2=PWR LAW, VELDEF
 5.        0.0      0.0       0.0      SL, AVdamping, AFriction, TILTangle
 5.0       5.0      5.0                PITCH ANGLES
-30.0      0.0                         INITIAL YAW, YAW RATE (DEG,DEG/S)
 3.25   -1.7   3.08   1.5   3.20 1.4   INITIAL (FLAP, FLAP RATE) (DEG,DEG/S)
  1                                    Number of rotor revolutions
 200.     0.01     .0020               SECTOR, TOLERance, RHO=air density
15.24     0.0      0.7          0.15   STALL ANGLE, HI LOOP, LO LOOP,t/Chord
20.0      2                  Filter cutoff freq (p), #filter stages (<=3)
 10        8      -1.44       NLIFT, NDRAG, ALPHAL=zero lift angle
      -.01         .136       AL, CL FOR Re=1E6, Rough
      3.08         .441
      6.16         .739
      9.22         .921
      12.22       1.007
      14.24       1.029
      15.24       1.035
      16.24       1.007
      18.2         .886
      20.15        .784
      -.01         .0121      AD, CD (ANGLE OF ATTACK AND CD TABLE)
      3.08         .0133
      6.16         .0154
      9.22         .0373
      12.22        .0587
      14.24        .0891
      15.24        .1151
      16.24        .1548
      0.0         1.5         TWIST, Chord (10 SETS)
      0.0         1.5
      0.0         1.5
      0.0         1.5
      0.0         1.5
      0.0         1.5
      0.0         1.5
      0.0         1.5
      0.0         1.5
      0.0         1.5
```

USER OPERATION AT RUN TIME

No user input is required after the program is run. The CRT will display information on the status of the calculations and a few statements about the run conditions so that the calculations can be interrupted if the desired conditions are not being run. The lines below are typical of what will be seen as the program executes. The Courier font is used for information that will be sent to the CRT. Annotations are shown in the Helvetica font.

The search for the trim solution will continue until all "RMS ERROR" values are less than the "TOLER" value from the input file. If 30 trim revolutions are run before the solution converges to a trim condition the calculation will be aborted. If this occurs, use of different initial conditions, a larger value of SECTOR, or a larger tolerance on the trim criteria should be tried.

```
 Combined Experiment Baseline
    FIXED-YAW ANALYSIS
   BLADE ROTATING NATURAL FREQUENCY (P#) = 4.06092   <<Misc. calculated values

RUNNING  200 POINTS
WITH  200.000 POINTS PER REVOLUTION
TOTAL TIME DURATION SIMULATED (SEC) =  .833333

 NDELAY (PHASE SHIFT TIME STEPS) =  4
SEEKING TRIM SOLUTION FOR FLAP DOF                  <<Blade 1 status during
                    AZ=  45.0  FLAP=  3.4           search for trim solution
                    AZ=  90.0  FLAP=  3.2
...etc....                                          <<This printout shortened
                                                    for brevity

 TRIM REVOLUTION  2
    BLADE #1  FLAP=   3.23     FLAP RATE=   -1.47    RMS ERROR=    .021
    BLADE #2  FLAP=   3.09     FLAP RATE=    1.50    RMS ERROR=    .001
    BLADE #3  FLAP=   3.19     FLAP RATE=    1.45    RMS ERROR=    .014
                    AZ=  45.0  FLAP=  3.3
                    AZ=  90.0  FLAP=  3.3
...etc....

 TRIM REVOLUTION  3
    BLADE #1  FLAP=   3.24     FLAP RATE=   -1.68    RMS ERROR=    .009
    BLADE #2  FLAP=   3.09     FLAP RATE=    1.51    RMS ERROR=    .001
    BLADE #3  FLAP=   3.20     FLAP RATE=    1.43    RMS ERROR=    .003

INITIAL VALUES FOR TRANSIENT SOLUTION:              <<Values found from
BLADE      FLAP    FLAP RATE                        the trim solution
   1      3.25     -1.68                            (degrees and deg/sec)
   2      3.08      1.51
   3      3.19      1.43

STARTING TRANSIENT SOLUTION...
 T=    .02    AZ=   9.0    YAW= -30.0    YR=     .0    FLAP=  3.2  FR= -2.5
 T=    .04    AZ=  18.0    YAW= -30.0    YR=     .0    FLAP=  3.2  FR= -1.0

 etc.....
```

The output file YawDyn.opt is intended for printing a summary of the simulation conditions and some representative results. More detailed results are provided in the YawDyn.Plt file. In all files and displays the blade flap angle is the angle, β, which the blade makes with the plane of rotation. If a teetering rotor is being modeled, the teeter angle is the flap angle minus the precone angle.

The output file YawDyn.Plt is useful for plotting predictions as a function of time. The columns in the table are separated by tabs to allow the file to be read by many graphics software packages written for desktop computers. The first line of the file gives column headings, also separated by tabs. If your graphics package will not permit reading of the column headings in this way, delete the first (and only) line of text.

Sample YawDyn.Opt file from Program YawDyn
Using input file given in Table 1.

FILE YAWDYN.OPT:

```
Combined Experiment Baseline
 ANALYSIS OF A RIGID ROTOR

 INITIAL WIND SPEED AT HUB (FT/SEC) = 37.0000
 INITIAL WIND DIRECTION DELTA (DEG) = .000000
 VERTICAL COMPONENT OF WIND SPEED (FT/SEC) = .000000
 ROTOR SPEED (RPM) = 72.0000
 AIR DENSITY (SLUG/FT^3) = 2.000000E-03

 ROTOR RADIUS (FT) = 16.5000
 HUB RADIUS (FT) = 1.70000
 HUB HEIGHT (FT) = 55.0000
 INITIAL PITCH ANGLES (DEG) = 5.00000 5.00000 5.00000
 BLADE CENTER OF GRAVITY (FT) = 5.44000
 YAW AXIS-TO-HUB DISTANCE (FT) = 5.00000
 NUMBER OF BLADES = 3.00000
 PRE-CONING ANGLE (DEG) = 3.00000
 ROTOR TILT ANGLE (DEG) = .000000

 MASS OF BLADE (SLUG) = 3.34000
 BLADE FLAP MOMENT OF INERTIA (SLUG*FT^2) =     178.0
 NACELLE MOMENT OF INERTIA (SLUG*FT^2) =     1000.0

 BLADE STIFFNESS COEF. (LB-FT/RAD) = 155000.
 BLADE NATURAL FREQUENCY (HZ) = 4.69652
 BLADE ROTATING NATURAL FREQUENCY (P#) = 4.06092

 YAW STIFFNESS COEF. (FT-LB/RAD) = 400000.
 YAW AXIS FRICTION (FT-LB) =  .000000
 YAW AXIS DAMPING (FT-LB-SEC) =  .000000

 LINEAR HORIZONTAL WIND SHEAR
   INITIAL SHEAR COEFFICIENT =  .000000
 POWER LAW VERTICAL WIND SHEAR
   INITIAL POWER LAW EXPONENT =  .140000
 TOWER SHADOW COEFFICIENT =  .100000


 INITIAL FLAP ANGLE (BLADE 1) (DEG) =  3.25000
 INITIAL FLAP RATE (BLADE 1) (DEG/S) =  -1.70000
 INITIAL YAW ANGLE (DEG)  =  -30.0000
 INITIAL YAW RATE (DEG/S) =  .000000
 FIXED YAW OPERATION
 FLAP DEGREE OF FREEDOM WAS CONSIDERED
 PRINT INTERVAL (TO PLOT FILE) =  5

 TOLERANCE FOR TRIM SOLUTION
    CONVERGENCE TEST = 1.000000E-02

 UNSTEADY STALL PARAMETERS:
    STALL ANGLE = 15.2400
    UPPER HYSTERESIS LOOP CONSTANT = .000000
    LOWER HYSTERESIS LOOP CONSTANT = .700000
    AIRFOIL THICKNESS/CHORD = .150000
    FILTER CUTOFF FREQUENCY, (PER REV)  = 20.0000
    NUMBER OF FILTER STAGES = 2
```

ZERO-LIFT ANGLE OF ATTACK = -1.44000

AIRFOIL CHARACTERISTICS:

ANGLE OF ATTACK(DEG)	LIFT COEF.
-.0100	.1360
3.0800	.4410
6.1600	.7390
9.2200	.9210
12.2200	1.0070
14.2400	1.0290
15.2400	1.0350
16.2400	1.0070
18.2000	.8860
20.1500	.7840

AIRFOIL CHARACTERISTICS:

ANGLE OF ATTACK(DEG)	DRAG COEF.
-.0100	.0121
3.0800	.0133
6.1600	.0154
9.2200	.0373
12.2200	.0587
14.2400	.0891
15.2400	.1151
16.2400	.1548

TWIST ANGLE (DEG)	CHORD (FT)
.0000	1.5000
.0000	1.5000
.0000	1.5000
.0000	1.5000
.0000	1.5000
.0000	1.5000
.0000	1.5000
.0000	1.5000
.0000	1.5000
.0000	1.5000

FLAP MOMENT IS THE BLADE DEFLECTION TIMES THE SPRING STIFFNESS.
YAW MOMENT IS APPLIED AERODYNAMIC MOMENT

DATA FOR CYCLE NUMBER 1, BLADE ELEMENT 8

PSI DEG	YAW DEG	YAWMOMENT FT-LB	FLAPMOMENT FT-LB	ALPHA DEG	CL	CD	A
1.8	-30.0	-.2134E+03	0.6550E+03	5.99	.647	.015	.250
3.6	-30.0	-.1933E+03	0.6317E+03	6.16	.618	.015	.247
5.4	-30.0	-.1714E+03	0.6068E+03	6.42	.603	.017	.241
7.2	-30.0	-.1477E+03	0.5793E+03	6.73	.602	.019	.235
9.0	-30.0	-.1231E+03	0.5512E+03	7.03	.608	.022	.228
10.8	-30.0	-.9738E+02	0.5227E+03	7.31	.631	.024	.222
12.6	-30.0	-.7220E+02	0.4950E+03	7.52	.673	.025	.217
14.4	-30.0	-.5145E+02	0.4702E+03	7.65	.750	.026	.214
16.2	-30.0	-.4003E+02	0.4485E+03	7.69	.830	.026	.211
18.0	-30.0	-.2092E+01	0.4352E+03	7.73	.832	.027	.208
19.8	-30.0	0.3718E+02	0.4288E+03	7.78	.835	.027	.205

(center portion of table deleted for brevity)

340.2	-30.0	0.1387E+01	0.7720E+03	6.89	.730	.021	.243
342.0	-30.0	-.5126E+02	0.7724E+03	6.90	.738	.021	.242
343.8	-30.0	-.9991E+02	0.7705E+03	6.92	.746	.021	.241
345.6	-30.0	-.1442E+03	0.7668E+03	6.93	.756	.021	.240
347.4	-30.0	-.1809E+03	0.7616E+03	6.88	.768	.021	.240
349.2	-30.0	-.2096E+03	0.7551E+03	6.74	.774	.020	.242
351.0	-30.0	-.2297E+03	0.7466E+03	6.55	.762	.018	.244
352.8	-30.0	-.2429E+03	0.7370E+03	6.34	.750	.017	.248
354.6	-30.0	-.2522E+03	0.7249E+03	6.13	.736	.015	.251
356.4	-30.0	-.2530E+03	0.7111E+03	5.97	.721	.015	.253
358.2	-30.0	-.2472E+03	0.6949E+03	5.90	.713	.015	.253

References

Cui, X. Hansen, A.C. and Siedschlag, N., 1988, "Yaw Dynamics of Horizontal Axis Wind Turbines: First Annual Report". SERI Technical Report SERI/STR-217-3309.

Hansen, A.C. and Cui, X., 1989, "Yaw Dynamics of Horizontal Axis Wind Turbines: Second Annual Report". SERI Technical Report SERI/STR-217-3476.

Hansen, A.C. and Cui, X, "Analyses and Observations of Wind Turbine Yaw Dynamics". ASME Journal of Solar Energy Engineering, Vol 111, November, 1989. Also presented at the ASME Energy Technology Conference, New Orleans, LA, January, 1988.

```
C     **********************YawDyn****************************
C
C     VERSION 5.4, 1/8/92
C
C     YAWDYN CALCULATES YAW ANGLE, YAW RATE, YAW MOMENT
C     FLAP ANGLE, FLAP RATE AND FLAP MOMENT FOR EACH BLADE OF
C     A 2 OR 3-BLADED HAWT.  OPTIONS ARE AVAILABLE FOR OPERATING
C     IN FIXED YAW OR WITHOUT FLAP DEGREE OF FREEDOM. A TEETERING
C     ROTOR OPTION IS ALSO AVAILABLE.  WHEN THE TEETERING ROTOR
C     IS ANALYZED, THE MODEL HAS ONLY TWO DEGREES OF FREEDOM--
C     THE TEETER ANGLE AND THE YAW ANGLE.  THAT IS, THE BLADE
C     STIFFNESS AND FREQUENCY ARE NO LONGER CONSIDERED.  BUT
C     PROVISIONS ARE INCLUDED FOR SPRING AND DAMPER TEETER STOPS.
C
C     WHEN TEETERING MOTION IS CALCULATED, THE TERMS FLAP AND TEETER
C     ARE EQUIVALENT FOR THE NUMBER 1 BLADE (EXCEPT THAT THE
C     FLAP ANGLE AND THE TEETER ANGLE DIFFER BY THE CONSTANT PRECONE)
C
C     FILE YAWDYN.INC MUST BE PRESENT WHEN THIS PROGRAM IS COMPILED
C
C     FILE YAWDYN.IPT CONTAINS THE HAWT DATA AND INITIAL
C          CONDITIONS.
C     FILE YAWDYN.OPT IS AN OUTPUT SUMMARY (ECHO OF INPUT DATA
C          AND DETAILS OF CALCULATIONS DURING ONE REVOLUTION).
C     FILE YAWDYN.PLT IS AN OUTPUT TABLE FOR THE ENTIRE RUN.
C     FILE YAWDYN.WND CONTAINS ACTUAL OPERATING PARAMETER DATA
C          SUCH AS WIND VECTOR, SEE SUBROUTINE GETWND FOR DETAILS
C     ALL I/O UNITS ARE FEET,SLUGS,SECONDS,POUNDS FORCE AND DEGREES.
C     UNITS CAN BE CHANGED TO SI EQUIVALENTS BY CHANGING VALUE OF
C          THE CONSTANT NAMED 'GRAV' AND USING CONSISTENT UNITS
C
C     FILE YHARMON.IPT CAN BE CREATED CONTAINING YAW AND FLAP MOMENT
C       RESULTS FOR ONE SELECTED REVOLUTION OF THE ROTOR.
C       THIS FILE IS USED BY PROGRAM YHARMON.FOR TO CALCULATE
C       HARMONIC CONTENT OF THE YAW AND FLAP LOADS.
C
C     WRITTEN BY XUDONG CUI AND CRAIG HANSEN,
C     UNIVERSITY OF UTAH, MECHANICAL ENGINEERING DEPARTMENT
C
C     REVISION RECORD (AFTER 5/90):
C       5/24/90 CHANGE ALL VELOCITIES TO NONDIMENSIONAL FORM
C               V/(REVS*R), Q(2)/REVS AND Q(4)/REVS
C       6/9/90  SKEWED WAKE INFLOW MODEL MODIFIED.
C       8/5/90  REMOVED PITCH AND ROLL MOMENTS FROM THE INFLOW MODEL
C        8/24/90 REMOVED BLADE PITCH AND EDGE MOMENTS OF INERTIA
C                RE-ARRANGED INPUT FILE (VERSION 3.3)
C       10/10/90 RETURNED TO USING INCLUDE FILE FOR COMMON STMTS (3.4)
C        2/28/91 REMOVED MANY AERO SUBROUTINES TO YAWSUBS.F
C        3/01/91 V3.5, CHANGED RUNGE-KUTTA (RK) TO SECOND ORDER PRED.-CORRECTOR
C                (PREDCOR) TO SIMPLIFY THE PROGRAM.  NO CHANGE IN RESULTS.
C        3/16/91 INCORPORATED ALL ASPECTS OF THE 'YAWTEETER' CODE
C                AND YAWDYN V3.5 INTO A SINGLE PROGRAM WITH THE
C                NEW TEETER INPUT DATA REQUIRED WHEN TEETER USED (4.0).
C        6/14/91 NEW YAW DOF EQN. IMPLEMENTED (PREVIOUS VERSIONS HAD ERROR
C                WHICH AFFECTED COUPLED FREE YAW/FLAP VERSION ONLY)
C                ALSO FIXED BUG IN CALL F2(..,PSIA) (THE MISSING A) (5.0)
C        6/26/91 INCORPORATED SHAFT TILT INTO CORRECTED EQNS OF MOTION.
C                INCORPORATED FULL FREE-YAW TEETER EQUATIONS AND
C                MOVED INTERACTIVE INPUT TO YAWDYN.IPT FILE. (5.2)
C        8/30/91 FIXED BUG IN YAW MOMENT OUTPUT (RIGID ROTOR WITH FLAP ONLY)
C                CHANGED FM TO FMYM IN YAWM CALCULATION (SUB. AERO)
C                MINOR COSMETIC CHANGES AND RECOMBINATION WITH ALL
```

```
C                SUBROUTINES TO CREATE THE FINAL FORM OF YAWDYN. (5.3)
C         1/08/92 CHANGED FLAP MOMENT WHICH IS OUTPUT FOR TEETER ROTOR (5.4)
C
C       ******************************************************
C
C       PARTIAL LIST OF VARIABLES:
C
C       AD      = ANGLE OF ATTACK ARRAY IN DRAG COEFF. TABLE
C       AF      = DRY FRICTION YAW MOMENT
C       AL      = ANGLE OF ATTACK ARRAY IN LIFT COEFF. TABLE
C       ALP     = ARRAY OF LOW-PASS SINE BUTTERWORTH FILTER COEFFICIENTS
C       ALPHAL  = ZERO LIFT ANGLE OF ATTACK (DEG)
C       ALPHAS  = STALL ANGLE OF ATTACK (DEG)
C       AV      = VISCOUS YAW DAMPING COEFFICIENT (FT-LBS-SECS/RADIAN)
C       AVGINFL= AVERAGE INDUCE VELOCITY DUE TO MOMENTUM EQUATION
C       B       = NUMBER OF BLADES
C       BLINER  = BLADE FLAP MOMENT OF INERTIA ABOUT HINGE AXIS
C       BLP     = ARRAY OF LOW-PASS SINE BUTTERWORTH FILTER COEFFICIENTS
C       BM      = BLADE MASS
C       C       = BLADE CHORD LENGTH ARRAY (AT TEN BLADE STATIONS)
C       CD      = BLADE AERODYNAMIC DRAG COEFFICIENTS
C       CDMAX   = FLAT PLATE DRAG COEFFICIENT (FUNCTION OF ASPECT RATIO)
C       CFILT   = ANGLE-OF-ATTACK FILTER CUTOFF FREQUENCY (PER REV)
C       CL      = BLADE AERODYNAMIC LIFT COEFFICIENTS
C       CLP     = ARRAY OF LOW-PASS SINE BUTTERWORTH FILTER COEFFICIENTS
C       DEG     = DEGREE/RADIAN CONVERSION CONSTANT, 57.29...
C       DELTA   = WIND DIRECTION, YAW ERROR=DELTA+YAW ANGLE
C       DELTAT  = TIME STEP OR INTERVAL IN WIND DATA FILE YAWDYN.WND
C       DSTLLO  = CONSTANT USED IN DYNAMIC STALL CALCULATION
C                 FOR THE LOWER HYSTERESIS LOOP
C       DSTLHI  = CONSTANT USED IN DYNAMIC STALL CALCULATION
C                 FOR THE UPPER HYSTERESIS LOOP
C       FALPHA  = FILTERED ANGLE OF ATTACK (FILTERED ALPHA)
C       FCUT    = FILTER CUTOFF FREQUENCY (HZ)
C       FDOF    = FLAG TO DETERMINE IF FLAP DOF INCLUDED (0=NO,1=YES)
C       FETRIM  = ARRAY CONTAINING BLADE FLAP HISTORY FOR TRIM SOLUTION
C                 INDEX1->REVOLUTION, INDEX2->BLADE #, INDEX3->AZIMUTH
C       FMYM    = FLAP MOMENT USED IN THE YAW MOMENT CALCULATION
C       FS      = BLADE HINGE TORSIONAL SPRING STIFFNESS (FT-LB/RAD)
C       GRAV    = ACCELERATION OF GRAVITY  =  32.174 IN ENGLISH UNITS
C       HFORCE  = HORIZONTAL FORCE ON HUB (NET), NORMAL TO ROTOR AXIS
C       HH      = HUB HEIGHT
C
C       HSHR    = HORIZONTAL WIND SHEAR=[V(+3/4R)-V(-3/4R)]/V(HUB)
C       HUBMOM  = MOMENT APPLIED TO HUB BY THE TEETER SPRING AND DAMPER
C       IHARM   = FLAG TO DETERMINE CREATION OF YHARMON.IPT FILE (1=YES)
C       ISHR    = VERTICAL SHEAR FLAG, 1=LINEAR SHEAR, 2=POWER LAW SHEAR
C       ITETER  = TEETER FLAG, 0=RIGID ROTOR, 1=TEETER ROTOR
C       IWND    = WIND DATA FILE OPTION FLAG, READ YAWDYN.WND IF IWND=1
C       IYAWC   = YAW CONTROL FLAG, 0=FIXED YAW, 1=FREE YAW
C       MFLAP   = FLAP MOMENT
C       MYAW    = YAW MOMENT
C       N       = NUMBER OF DATA POINTS (TIME STEPS) TO BE COMPUTED
C       NDRAG   = NUMBER OF DRAG COEFFICIENTS IN AIRFOIL TABLE
C       NFILT   = NUMBER OF 2nd ORDER BUTTERWORTH STAGES
C       NLIFT   = NUMBER OF LIFT COEFFICIENTS IN AIRFOIL TABLE
C       NSEE    = NUMBER OF THE BLADE ELEMENT SUMMARIZED IN YAWDYN.OPT
C                 (1=ROOT, 10=TIP ELEMENT)
C       OLDA    = ARRAY CONTAINING VALUES OF INDUCTION FACTOR 'A' FOR
C                 EACH BLADE AND BLADE ELEMENT FOR THE PREVIOUS TIME STEP
C       OLALFA  = ARRAY CONTAINING VALUES OF ANGLE OF ATTACK FOR
C                 EACH BLADE AND BLADE ELEMENT FOR THE LAST 2 TIME STEPS
C       OLFALF  = ARRAY CONTAINING VALUES OF FILTERED ANGLE OF ATTACK FOR
C                 EACH BLADE AND BLADE ELEMENT FOR THE PREVIOUS TIME STEP
```

```
C       PC      = PRECONING ANGLE
C       PI      = 3.14159...
C       PIBY2   = PI/2
C       PITCH   = PITCH ANGLE ARRAY (ONE VALUE FOR EACH BLADE)
C       PITNOW  = PITCH OF BLADE IN CURRENT CALCULATION
C       POWER   = ROTOR OUTPUT POWER (KW)
C       Q       = INSTANTANEOUS VALUES OF ITH BLADE DEGREES-OF-FREEDOM:
C                 FLAP ANGLE, FLAP RATES, YAW ANGLE AND YAW RATE
C       R       = ROTOR RADIUS
C       RB      = DISTANCE FROM BLADE HINGE TO BLADE CENTER OF MASS
C       REVS    = ROTOR SPEED IN RADIANS/SEC
C       RH      = BLADE HINGE OFFSET
C       RHO     = AIR DENSITY
C       RPM     = ROTOR ROTATIONAL SPEED (IN REVOLUTIONS/MINUTE)
C       SECTOR  = NUMBER OF SECTORS (STEPS) IN ONE REV OF ROTOR
C       SL      = DISTANCE FROM YAW AXIS TO ROTOR HUB
C       SLING   = UNDERSLING OF THE TEETERING ROTOR (FT)
C       SPRNG1  = SPRING CONSTANT OF FIRST TEETER STOP (FT-LB/RAD)
C                 THE SPRING EXERTS A TEETER MOMENT ON THE HUB
C                 MOMENT = SPRNG1*(DEFLECTION)+SPRNG2*DEFLECTION**2
C       SPRNG2  = SECOND SPRING CONSTANT OF TEETER STOP (FT-LB/RAD**2)
C       STLGAM  = CONSTANT USED IN GORMONT DYNAMIC STALL MODEL
C       SUMERR  = ARRAY CONTAINING RMS ERROR IN TRIM SOLUTION (ERROR
C                 FROM ONE REVOLUTION TO THE NEXT) FOR EACH BLADE
C       TDAMP   = LINEAR TEETER DAMPER COEFFICIENT.  THE DAMPER
C                 EXERTS A TEETER MOMENT ON THE HUB =TDAMP*TEETER RATE
C       TEE1    = TEETER ANGLE AT WHICH THE TEETER STOP IS ENCOUNTERED
C       TEEMOM  = NET AERODYNAMIC TEETER MOMENT APPLIED TO THE ROTOR
C       TILT    = SHAFT TILT ABOVE THE HORIZONTAL (INPUT IN DEG)
C       TITLE   = ANY TITLE TO DESCRIBE THE DATA FILE (<80 CHARACTERS)
C       TOLER   = TOLERANCE FOR TRIM CONVERGENCE TEST (DEG)
C       TWIST   = BLADE TWIST ANGLE ARRAY (AT EACH OF TEN BLADE STATIONS)
C       TWOPI   = 2*PI
C       V       = MEAN FREE STREAM WIND SPEED AT HUB HEIGHT
C       VELDEF  = TOWER SHADOW VELOCITY DEFICIT FRACTION
C       VSHR    = VERTICAL WIND SHEAR (POWER LAW EXPONENT OR LINEAR COEFF.)
C       YI      = YAW MOMENT INERTIA OF ALL YAWING MASS EXCEPT THE BLADES
C       YAWMPR  = YAW MOMENT THAT IS PRINTED TO OUTPUT FILES
C       YAWSTF  = STIFFNESS OF TORSION SPRING ON THE YAW AXIS (FT-LB/RAD)
C
C       ********************************
C       MAIN  PROGRAM
C       ********************************
C
      INCLUDE 'YAWDYN.INC'
      COMMON/TEETER/ TEE1, SPRNG1, SPRNG2, TDAMP, SLING,
     &               TEEMOM, HUBMOM, ITETER
C
      DIMENSION QP(8),F(8,4),QP2(8)
      DIMENSION FETRIM(2,3,800), SUMERR(3)
C
C     ASCII CHARACTER 9 IS TAB FOR TABULAR OUTPUT
C     ALSO, DEFINE OTHER COMMONLY USED CONSTANTS
C
      CHARACTER*1  TAB
      TAB    = CHAR(9)
      PI     = 4.*ATAN(1.)
      PIBY2  = PI/2.
      TWOPI  = 2.*PI
      DEG    = 180./PI
      GRAV   = 32.174
      TIME   = 0.0
C
      DO 2 I=1,10
```

```
        DO 4 J=1,3
           IFLAG(I,J) = 0
 4      CONTINUE
 2    CONTINUE
C
C     INITIALIZE INFLOW FOR SKEWED WAKE MODEL
C
      AVGINFL = 0.
C
C     OPEN INPUT AND OUTPUT FILES
C
      OPEN (UNIT=10, FILE= 'YAWDYN.IPT',STATUS='OLD',IOSTAT=IERR)
      IF(IERR.NE.0)  THEN
            WRITE(*,*) 'ERROR OPENING YAWDYN.IPT'
            WRITE(*,*) 'IOSTAT=',IERR
            PAUSE 'ENTER CR TO CONTINUE'
            STOP
      ENDIF
C
      OPEN (UNIT=100, FILE='YAWDYN.OPT',IOSTAT=IERR)
      IF(IERR.NE.0)  THEN
            WRITE(*,*) 'ERROR OPENING YAWDYN.OPT'
            WRITE(*,*) 'IOSTAT=',IERR
            PAUSE 'ENTER CR TO CONTINUE'
            STOP
      ENDIF
C
      OPEN (UNIT=12, FILE= 'YAWDYN.PLT',IOSTAT=IERR)
      IF(IERR.NE.0)  THEN
            WRITE(*,*) 'ERROR OPENING YAWDYN.PLT'
            WRITE(*,*) 'IOSTAT=',IERR
            PAUSE 'ENTER CR TO CONTINUE'
            STOP
      ENDIF
C
C     READ AND ECHO INPUT DATA **********
C
      CALL INOUT(SECTOR,N,IWND,DELTAT,TDATA,IHARM,TOLER,QP)
C
C
C     CHECK THAT TEETERING ROTOR HAS ZERO HUB RADIUS
C
      IF( ( ITETER .EQ. 1 ) .AND. ( ABS(RH) .GT. 1.0E-2 ) ) THEN
          WRITE(*,*) ' TEETERING ROTOR MUST HAVE ZERO HUB RADIUS'
          WRITE(*,*) ' CHECK INPUT DATA FILE '
          PAUSE 'ENTER CR TO CONTINUE'
          STOP
      ENDIF
C
      IF( IHARM .EQ. 1 ) THEN
         OPEN (UNIT=14, FILE= 'YHARMON.IPT',IOSTAT=IERR)
         IF(IERR.NE.0)  THEN
               WRITE(*,*) 'ERROR OPENING YHARMON.IPT'
               WRITE(*,*) 'IOSTAT=',IERR
               PAUSE 'ENTER CR TO CONTINUE'
               STOP
         ENDIF
         WRITE(14,2400) IFIX(SECTOR)
      ENDIF
C
C     WRITE VARIABLE IDENTIFICATIONS TO FIRST LINE OF PLOT FILE
C
      IF ( ITETER .EQ. 1) THEN
          WRITE(12,*) 'Time (sec)',TAB,'Wind Speed (ft/s)',TAB,
```

```
     &    'Wind Dir',TAB,'Yaw Angle',TAB,'Yaw Moment',
     &    TAB,'Flap Angle',TAB,'Aero Flap Moment',TAB,
     &    'Teeter Moment',TAB,'Hub Moment',TAB,'Power',TAB,
     &    'Alpha',TAB,'CL',TAB,'CD',TAB,'AAA'
        ELSE
          WRITE(12,*) 'Time (sec)',TAB,'Wind Speed (ft/s)',TAB,
     &    'Wind Dir',TAB,'Yaw Angle',TAB,'Yaw Moment',
     &    TAB,'Flap Angle',TAB,'Flap Moment',TAB,
     &    'Power',TAB,'Alpha',TAB,'CL',TAB,'CD',TAB,'AAA'
       ENDIF
C
C      SET UP THE INITIAL VALUES
C
       NB      = B
       NSECT   = SECTOR
       PC      = PC/DEG
       H       = TWOPI/SECTOR
       FY4     = 0.0
       Q(1)    = Q(1)/DEG
       Q(2)    = Q(2)/DEG/REVS
       Q(3)    = Q(3)/DEG
       Q(4)    = Q(4)/DEG/REVS
       YSAVE   = Q(3)
       YRSAVE  = Q(4)
       IYSAVE  = IYAWC
C
C      AZIMUTH RANGE FOR PRINTING RESULTS TO FILE YAWDYN.OPT
C
       PRNAZ1 = (MREV-1)*TWOPI
       PRNAZ2 = PRNAZ1 + TWOPI
C
C      CALCULATE THE FILTER COEFFICIENTS (FOR ANGLE OF ATTACK FILTER)
C
       CALL LPDES(SECTOR)
C
C      ****************************************
C      START SECTION TO FIND THE TRIM SOLUTION
C      ****************************************
C
C      TEMPORARILY SET FIXED YAW FOR TRIM SOLUTION
C
       IYAWC  = 0
       Q(4)   = 0.0
       PSI    = 0.0
       ERRMAX = 100.
C
C      CALCULATE INITIAL CONDITIONS FOR TRIM SOLUTION
C
       QP(7) = Q(3)
       QP(8) = Q(4)
C
       IF ( FDOF .EQ. 0 ) THEN
C           WITHOUT FLAP DOF
            DO 125  IBLADE=1,NB
               JK = 2*IBLADE-1
               QP(JK) = PC
               QP(JK+1)  = 0.0
               PSIA   = FLOAT(IBLADE-1)*TWOPI/B
               PITNOW = PITCH(IBLADE)
               CALL INITIAL(PSIA)
 125        CONTINUE
C
       ELSE
C           WITH FLAP DOF USE INITIAL FLAP AND FLAP RATE FROM INPUT FILE
```

```
            DO 550 IBLADE=1,NB
               JK = 2*IBLADE-1
               QP(JK)   = QP(JK)/DEG
               QP(JK+1) = QP(JK+1)/DEG/REVS
               PSIA     = FLOAT(IBLADE-1)*TWOPI/B
               PITNOW   = PITCH(IBLADE)
               CALL INITIAL(PSIA)
 550        CONTINUE

      ENDIF
C
      IF (FDOF .EQ. 1) THEN
         WRITE(*,*) 'SEEKING TRIM SOLUTION FOR FLAP DOF'
      ELSE
         WRITE(*,*) 'CALCULATING INITIAL REVOLUTION (NO FLAP)'
      ENDIF
C
C     USE PREDICTOR-CORRECTOR CALCULATIONS TO INITIALIZE THE SOLUTION
C
C     FIRST P-C PASS
C
      CALL FK(PSI,QP,QP2,YAWM,AMFP,HFORCE,POWER,ALF,CLL,CDD,AAA)
      DO 440 I=1,8
          F(I,1) = QP2(I)
 440  CONTINUE
      CALL PREDCOR(PSI,QP)
            DO 400 IBLADE = 1,NB
              FETRIM(1,IBLADE,1) = QP(2*IBLADE - 1)
 400        CONTINUE
C
C     SECOND P-C PASS
C
      CALL FK(PSI,QP,QP2,YAWM,AMFP,HFORCE,POWER,ALF,CLL,CDD,AAA)
      DO 450 I=1,8
          F(I,2) = QP2(I)
 450  CONTINUE
      CALL PREDCOR(PSI,QP)
            DO 420 IBLADE = 1,NB
              FETRIM(1,IBLADE,2) = QP(2*IBLADE - 1)
 420        CONTINUE
C
C     THIRD P-C PASS
C
      CALL FK(PSI,QP,QP2,YAWM,AMFP,HFORCE,POWER,ALF,CLL,CDD,AAA)
      DO 460 I=1,8
          F(I,3) = QP2(I)
 460  CONTINUE
      CALL PREDCOR(PSI,QP)
            DO 430 IBLADE = 1,NB
              FETRIM(1,IBLADE,3) = QP(2*IBLADE - 1)
 430        CONTINUE
C
      CALL FK(PSI,QP,QP2,YAWM,AMFP,HFORCE,POWER,ALF,CLL,CDD,AAA)
      DO 470 I=1,8
          F(I,4) = QP2(I)
 470  CONTINUE
C
C     SWITCH TO A-B PREDICTOR-CORRECTOR CALCULATION IN DO LOOP
C     THE INDEX ITER COUNTS THE NUMBER OF ROTOR REVS, JAZ COUNTS
C          AZIMUTH POSITION IN THE SEARCH FOR A TRIM SOLUTION
C
      DO 100 ITER=1,30
        IF( ITER .EQ. 1 ) THEN
            ISTART = 4
```

```
          ELSE
            ISTART = 1
         ENDIF
C
         DO 110 JAZ=ISTART,NSECT

            CALL AB(PSI,QP,F,YAWM,AMFP,HFORCE,
     &                  POWER,ALF,CLL,CDD,AAA)
C
C           PRINT EVERY 25TH TIME STEP DURING TRIM SEARCH
            IF(JAZ/25 .EQ. FLOAT(JAZ)/FLOAT(25) )
     &          WRITE(*,2100) AMOD(PSI,TWOPI) * DEG, QP(1)*DEG
            IF(ITER .LE. 2) THEN
               DO 500 IBLADE = 1,NB
                 FETRIM(ITER,IBLADE,JAZ) = QP(2*IBLADE - 1)
 500           CONTINUE
            ELSE
               DO 510 IBLADE = 1,NB
                  FETRIM(1,IBLADE,JAZ) = FETRIM(2,IBLADE,JAZ)
                  FETRIM(2,IBLADE,JAZ) = QP(2*IBLADE - 1)
 510           CONTINUE
            ENDIF
 110     CONTINUE
C
        IF( FDOF .EQ. 0) GO TO 200
        IF( ITER .GT. 1) THEN
C
             DO 160 IBLADE = 1,NB
                SUMERR(IBLADE) = 0.
 160         CONTINUE
C
             DO 120 JAZ=1,NSECT
                DO 130 IBLADE = 1,NB
                  SUMERR(IBLADE) = SUMERR(IBLADE) +
     &               ( FETRIM(2,IBLADE,JAZ) - FETRIM(1,IBLADE,JAZ) )**2
 130            CONTINUE
 120         CONTINUE
C
             ERRMAX = 0.
             DO 150 IBLADE = 1,NB
                SUMERR(IBLADE) = SQRT( SUMERR(IBLADE)/SECTOR ) * LEG
                IF(SUMERR(IBLADE) .GT. ERRMAX) ERRMAX = SUMERR(IBLADE)
 150         CONTINUE
             WRITE(*,2200) ITER,
     &       (K,FETRIM(2,K,1)*DEG,QP(2*K)*DEG*REVS, SUMERR(K), K=1,NB)
        ENDIF
C
C       IF MAXIMUM RMS ERROR LESS THAN 'TOLER' DEG ACCEPT TRIM SOL'N
C
        IF( ERRMAX .LE. TOLER ) GO TO 200
C
 100  CONTINUE
      PAUSE 'EXCEEDED 30 REVS WHILE SEEKING TRIM, CR TO CONTINUE'
      STOP
C
C     ************************************************
C     START INTEGRATION FOR TRANSIENT SOLUTION
C     ************************************************
C
  200 WRITE(*,*) '  '
      WRITE(*,*) 'INITIAL VALUES FOR TRANSIENT SOLUTION:'
      WRITE(*,*) 'BLADE     FLAP   FLAP RATE'
      DO 210 K = 1,NB
          JK = 2*K-1
```

```
          WRITE(*,2800) K, QP(JK)*DEG, QP(JK+1)*DEG*REVS
  210 CONTINUE
      WRITE(*,*) '  '
      WRITE(*,*) 'STARTING TRANSIENT SOLUTION...'
C
      PSI   = 0.
      QP(7) = YSAVE
      QP(8) = YRSAVE
      IYAWC = IYSAVE
C
C     LOOP THROUGH A-B PREDICTOR-CORRECTOR, ONCE FOR EACH TIME STEP
C
      DO 300 I=1,N
        IF( IWND .EQ. 1 ) CALL GETWND(TIME,DELTAT,TDATA)
        CALL AB(PSI,QP,F,YAWM,AMFP,HFORCE,POWER,ALF,CLL,CDD,AAA)
            TIME = TIME + H/REVS
            AZIM = AMOD(PSI,TWOPI) * DEG
            YE = QP(7) * DEG
            YR = QP(8) * DEG * REVS
            FE = QP(1) * DEG
            FR = QP(2) * DEG * REVS
            IF( IYAWC .EQ. 0 ) THEN
C               FOR FIXED YAW, YAW MOMENT=AERO MOMENT
                YAWMPR = YAWM
              ELSE
C               FOR FREE YAW, YAW MOMENT= SPRING STIFF*DEFLECTION
                YAWMPR = YAWSTF*( Q(3) - YSAVE )
            ENDIF
C
            IF( PSI .LE. PRNAZ2 .AND. PSI .GE. PRNAZ1 ) THEN
                WRITE(100,2600) AZIM,YE,YAWMPR,AMFP,ALF,CLL,CDD,AAA
                IF( IHARM .EQ. 1 ) WRITE (14,2500)  AZIM,YAWMPR,AMFP
            ENDIF
C
            IF(I/IPRINT .EQ. FLOAT(I)/FLOAT(IPRINT) ) THEN
               WRITE(*,2000) TIME,AZIM,YE,YR,FE,FR
               IF ( ITETER .EQ. 1 ) THEN
                 WRITE(12,2700) TIME, TAB, V*REVS*R, TAB, DELTA*DEG,
     &           TAB, YE,TAB, YAWMPR,TAB, FE,TAB, AMFP,TAB,TEEMOM,TAB,
     &           HUBMOM,TAB,POWER,TAB, ALF,TAB, CLL,TAB, CDD,TAB, AAA

               ELSE

                 WRITE(12,2710) TIME, TAB, V*REVS*R, TAB, DELTA*DEG,
     &              TAB, YE,TAB, YAWMPR,TAB, FE,TAB, AMFP,TAB,
     &              POWER,TAB, ALF,TAB, CLL,TAB, CDD,TAB, AAA
               ENDIF
            ENDIF
  300   CONTINUE
C
C
 2000 FORMAT(1X,'T= ',F5.2,'   AZ= ',F5.1,'   YAW= ',F5.1,
     &          '   YR= ',F5.1,'   FLAP= ',F4.1, '  FR=', F5.1)
 2100 FORMAT(20X,'AZ= ',F5.1,'  FLAP= ',F4.1)
 2200 FORMAT (1X,'TRIM REVOLUTION ',I2, 3(/
     &       3X,'BLADE #',I1,'  FLAP= ', F6.2,
     &       '     FLAP RATE= ',F7.2,'    RMS ERROR= ',F7.3) )
 2400 FORMAT (I5)
 2500 FORMAT ( 3E15.6 )
 2600 FORMAT ( 1X,F6.1,2X,F6.1, 2(3X,E10.4),2X,F7.2,3(2X,F6.3) )
 2700 FORMAT ( ' ',G10.4, 13(A1,E10.4) )
 2710 FORMAT ( ' ',G10.4, 11(A1,E10.4) )
 2800 FORMAT ( 3X,I1,4X,F5.2,3X,F6.2 )
C
```

```
      IF( IWND .EQ. 1 ) CLOSE(11)
      CLOSE(12)
      IF( IHARM .EQ. 1 ) CLOSE(14)
      CLOSE(100)
C
      PAUSE 'FINISHED, ENTER CR TO CONTINUE'
C
      STOP
      END
C
C     ****************************************
C     SUBROUTINES
C     ****************************************
C
C     ****************************************
C     F2 COMPUTES THE FLAP ACCELERATION FUNCTION
C     FOR THE HAWT BLADE AT AZIMUTH ANGLE PSI
C     ****************************************
C
      SUBROUTINE F2(FM,F21,PSI)
C
      INCLUDE 'YAWDYN.INC'
      COMMON/TEETER/ TEE1, SPRNG1, SPRNG2, TDAMP, SLING,
     &               TEEMOM, HUBMOM, ITETER
C
      CPSI = COS(PSI)
      SPSI = SIN(PSI)
C
C     BRANCH FOR TEETERING OR RIGID HUB
C
      IF ( ITETER .EQ. 0 ) GO TO 100
C
C     TEETERING CASE ONLY
C     SELECT TEETER SPRING AND DAMPING, 'TEETER'=TEETER ANGLE IN RADS
C     TEE1 = TEETER ANGLE AT FIRST CONTACT OF TEETER SPRING
C
      TEETER = Q(1) - PC
      IF ( ABS( TEETER ) .LT. TEE1 ) THEN
            SPRING = 0.
            DAMP   = 0.
        ELSE IF ( TEETER .GT. TEE1 ) THEN
            DEFLEC = TEETER - TEE1
            SPRING = SPRNG1*DEFLEC + SPRNG2*DEFLEC*DEFLEC
            DAMP   = TDAMP
          ELSE
            DEFLEC = TEE1 + TEETER
            SPRING = SPRNG1*DEFLEC - SPRNG2*DEFLEC*DEFLEC
            DAMP   = TDAMP
      ENDIF
C
      HUBMOM = SPRING + DAMP * Q(2) * REVS
C
C     TILT IS INCLUDED IN THESE EQUATIONS
C     THE TEETER INERTIA IS TWICE THE BLADE FLAP INERTIA
C
      E1   = 2. * BLINER * REVS * REVS
      F21 = -TEETER - HUBMOM/E1  -
     &          ( TEEMOM + 2.*SLING*BM*GRAV*CPSI )/E1 -
     &          2. * Q(4) * CPSI -
     &          FY4*SPSI*( 1. + BM/BLINER*SLING*(SL + SLING) )
      F21 = F21/(1. - BM*SLING*SLING/BLINER)
      RETURN
C
  100 CONTINUE
```

```
C
C     RIGID HUB CASE, USING THE YAW ACCELERATION (FY4) FROM
C     THE PREVIOUS TIME STEP
C
      A1 = 1. + BM*RB*RH/BLINER
      A2 = BLINER*REVS*REVS
      A3 = BM*RB*SL/BLINER
      E1 = ( -1. + (A1*SPSI*SPSI) )*Q(1) - A3 - TILT*A1*CPSI
      E2 = 2. * A1 * CPSI
      E3 = A1*Q(1) + FS/A2 * ( Q(1)-PC )
      E4 = BM*GRAV*RB*( Q(1)*CPSI + TILT )/A2
      E5 = A1 + A3*Q(1)
C
      F21 = FM/A2 - ( E1*Q(4) + E2 )*Q(4) - E3 - E4 - E5*SPSI*FY4
C
      RETURN
      END
C
C     ********************************************************
C     AERO CALCULATES YAW MOMENT, H FORCE, POWER, FLAP MOMENT
C     ********************************************************

      SUBROUTINE AERO(YAWM,YAERO,HFORCE,POWER,AMFP,PSI,
     &                PK,PK2,ALF,CLL,CDD,AAA)
C
      INCLUDE 'YAWDYN.INC'
      COMMON/TEETER/ TEE1, SPRNG1, SPRNG2, TDAMP, SLING,
     &               TEEMOM, HUBMOM, ITETER
C
      DIMENSION PK(8), PK2(8)
C
      Q(3)    = PK(7)
      Q(4)    = PK(8)
      YAWM    = 0.
      YAERO   = 0.
      HFORCE  = 0.
      POWER   = 0.
      FY      = 0.
      FZ      = 0.
C
      AVGINFL1 = 0.
C
      DO 10 IBLADE = NB,1,-1
         J = IBLADE*2 - 1
         K = J + 1
         Q(1) = PK(J)
         Q(2) = PK(K)
         PSIA = PSI + FLOAT(IBLADE-1)*TWOPI/B
         SPSIA  = SIN(PSIA)
         CPSIA  = COS(PSIA)
         PITNOW = PITCH(IBLADE)
C
         CALL BLDFM(FN,FT,FM,ZM,AVEL,PSIA,ALF,CLL,CDD,AAA)
C
         AVGINFL1 = AVGINFL1 + AVEL
         HFORCE   = HFORCE + FT*CPSIA
         POWER    = POWER + (FT*RH + ZM)
C
C        THE FLAP MOMENT TRANSMITTED BY THE SPRING CONTRIBUTES
C        TO THE RIGID ROTOR YAW MOMENT
C
         IF( (FDOF .EQ. 1) .AND. (ITETER .EQ. 0) ) THEN
              FMYM = FS * ( Q(1) - PC )
            ELSEIF ( (FDOF .EQ. 0) .AND. (ITETER .EQ. 0) ) THEN
```

```
            FMYM = FM - (BLINER*REVS*REVS*PC + GRAV*BM*PC*RB*CPSIA)
         ENDIF
C
         IF ( ITETER .EQ. 1 ) THEN
            FMYM = FM - (BLINER*REVS*REVS + GRAV*BM*RB*CPSIA) * Q(1)
         ENDIF
C
C        THE ROTOR TEETER MOMENT IS (BLADE 1 FM) - (BLADE 2 FM)
C          VARIABLE TEEMOM = - AERODYNAMIC TEETER MOMENT
C
         IF ( IBLADE .EQ. 2 ) THEN
            TEEMOM = FM
            ZMTOT  = ZM
            FY     = -FT
            FZ     = FN
         ENDIF
C
         IF ( IBLADE .EQ. 1 ) THEN
           TEEMOM = TEEMOM - FM
           ZMTOT  = ZMTOT + ZM
           FY     = FY + FT
           FZ     = FZ + FN
C
C        FLAP MOMENT OUTPUT FOR TEETER ROTOR IS THE AERODYNAMIC MOMENT
           IF ( ITETER .EQ. 1) THEN
               AMFP = FM
           ELSE
               AMFP = FMYM
           ENDIF
         ENDIF
       IF ( ITETER .EQ. 1 ) GO TO 10
C
C        RIGID HUB ANALYSIS ONLY
C
         IF ( FDOF .EQ. 1 ) THEN
C
C            GET FLAP ACCELERATION
             PK2(J) = PK(K)
             CALL F2(FM,F21,PSIA)
             PK2(K) = F21
          ELSE
C
C            FLAP ACCELERATION = 0
             PK(J)  = PC
             PK(K)  = 0.
             PK2(J) = 0.
             PK2(K) = 0.
         ENDIF
C
C        ACCUMULATE YAW MOMENT TERMS (SUM FOR ALL BLADES)
C          YAWM = TOTAL YAW MOMENT APPLIED BY ROTOR
C          YAERO= AERODYNAMICS TERMS USED IN YAW DOF EQN
C
         DYAW1 = -ZM * (Q(1)*CPSIA + TILT)
         DYAW2 = (RH + SL*Q(1))*FN*SPSIA - FT*(SL*CPSIA + TILT*RH)
         YAWM  = YAWM + DYAW1 + DYAW2 + FMYM*SPSIA
         YAERO = YAERO + DYAW1 + DYAW2 - FM*SPSIA*BM*RB*RH/BLINER
C
C
  10   CONTINUE
C
C      LOOK AT TEETER ACCELERATION IF APPROPRIATE
       IF ( ITETER .EQ. 0 ) GO TO 20
C
```

```
C        GET THE TEETER ACCELERATION FROM THE NET MOMENT
C        AND THE APPROPRIATE AERODYNAMIC YAW MOMENT
C
         Q(1) = PK(1)
         Q(2) = PK(2)
         PK2(1) = PK(2)
C
         TEETER = Q(1) - PC
         CPSI   = COS(PSI)
         YAERO  = -FY*(SL - SLING)*CPSI + F2*SL*TEETER*SIN(PSI)
     &            - ZMTOT*( TILT + TEETER*CPSI )
C
         CALL F2(FM,F21,PSI)
         PK2(2) = F21
C
C        YAW MOMENT RESULTS FROM THE HORIZONTAL FORCE,
C           TORQUE, AND THE TEETER STOP MOMENT (HUBMOM)
C           (USED FOR FIXED YAW ONLY)
C
         YAWM = YAERO + HUBMOM * SIN(PSI)
C
C     POWER OUTPUT IN KILOWATTS
C
 20  POWER   = POWER * REVS * .001356
     AVGINFL = AVGINFL1/3.
C
     RETURN
     END
C
C     ***********************************************
C     BLDFM CALCULATES THE FORCES AND MOMENTS FOR
C     THE BLADE AT AZIMUTH ANGLE PSI.
C     ***********************************************
C
     SUBROUTINE BLDFM(FN,FT,FM,ZM,AVEL,PSI,ALF,CLL,CDD,AAA)
C
     INCLUDE 'YAWDYN.INC'
C
     FN   = 0.
     FT   = 0.
     YM   = 0.
     ZM   = 0.
     AVEL = 0.
C
C     AVEL IS THE INDUCED VELOCITY IN NORMAL
C     DIRECTION BY USING MOMENTUM EQUATION.
C
C     VELD CALCULATE THE VELOCITIES RELATIVE TO THE ROTOR DISK
C
     CALL VELD(SDEL,CDEL,ANGFLW,NTEST)
C
     DO 10 J = 1,10
        X = (J*.1 - .05)*R - RH
        IF( X .LE. 0. ) GO TO 10
        CALL VEL(VY,VZ,X,PSI)
        CALL VIND(A,J,X,PSI,VY,VZ,VN,VT)
        VNORM = VN/(1. - A)
        AVEL  = AVEL + VNORM*A*COS(Q(1))*TWOPI*X*(0.1*R)
C
        IF( NTEST .EQ. 1 ) THEN
            CALL VNMOD(VN,X,A,AXY,PSI,SDEL,CDEL,ANGFLW)
        ELSE
            AXY=A
        ENDIF
```

```
C
        PHI    = ATAN2(VN,VT)
        ALPHA = PHI - TWIST(J) - PITNOW/DEG
        ALPHA = AMOD(ALPHA,TWOPI)
        W2     = VN*VN + VT*VT
C
        CALL FILTER(ALPHA,FALPHA,J,ALPHA1,ALPHA2,ALPHA3)
        CALL STALL(FALPHA,W2,J,ALPHA,ALPHAM)
C
        CALL CDSUB(ALPHA,CDA)
        CALL CLSUB(ALPHAM,CLA)
        CLA = (ALPHA-ALPHAL)*CLA/(ALPHAM-ALPHAL)
C
C       SAVE VALUES AT APPROPRIATE STATION
C
        IF ( J .EQ. NSEE )  THEN
           ALF = ALPHA*DEG
           CLL = CLA
           CDD = CDA
           AAA = AXY
        ENDIF
C
C       UPDATE OLD-ALPHA IN REVERSED ORDER
C
        IF ( NDELAY .GE. 1 ) THEN
           DO 20 K=NDELAY,1,-1
              OLFALF(J,IBLADE,K+1) = OLFALF(J,IBLADE,K)
20         CONTINUE
        ENDIF
        OLFALF(J,IBLADE,1) = FALPHA
C
        OLDA(J,IBLADE) = A
C
        OLALFA(J,IBLADE,2) = OLALFA(J,IBLADE,1)
        OLALFA(J,IBLADE,1) = ALPHA
        FF1(J,IBLADE,2) = FF1(J,IBLADE,1)
        FF1(J,IBLADE,1) = ALPHA1
        FF2(J,IBLADE,2) = FF2(J,IBLADE,1)
        FF2(J,IBLADE,1) = ALPHA2
        FF3(J,IBLADE,2) = FF3(J,IBLADE,1)
        FF3(J,IBLADE,1) = ALPHA3
C
        W2RC = W2*0.1*R*C(J)
C
        DFN  = CLA*COS(PHI) + CDA*SIN(PHI)
        DFT  = CLA*SIN(PHI) - CDA*COS(PHI)
        DMY  = -X*DFN
        DMZ  =  X*DFT
C
        FN = FN + DFN*W2RC
        FT = FT + DFT*W2RC
        YM = YM + DMY*W2RC
        ZM = ZM + DMZ*W2RC
C
   10 CONTINUE
C
      AVEL = AVEL/(PI*R**2)
C
C     FN, FT, FM, AND ZM ARE IN DIMENSIONAL FORM
C
      VREF = R * REVS
      CONT = 0.5 * RHO * VREF * VREF
      FN   =  FN * CONT
      FT   =  FT * CONT
```

```
      FM    = -YM * CONT
      ZM    =  ZM * CONT
C
      RETURN
      END
C
C     ****************************************************
C     FK EVALUATES THE FIRST DERIVATIVES OF THE COMPONENTS
C     OF VECTOR PK AND RETURNS THE VALUES IN VECTOR PK2.
C
C     SUBROUTINES F2 AND F4 ARE USED TO EVALUATE
C     THE DERIVATIVES OF THE VELOCITY COMPONENTS OF QP.
C     ****************************************************
C
      SUBROUTINE FK(PSI,PK,PK2,YAWM,AMFP,HFORCE,POWER,ALF,CLL,CDD,AAA)
C
      INCLUDE 'YAWDYN.INC'
C
      DIMENSION PK(8),PK2(8)
      Q(3) = PK(7)
      Q(4) = PK(8)
C
      CALL F4(PSI,PK,PK2,YAWM,AMFP,HFORCE,POWER,ALF,CLL,CDD,AAA)
      PK2(7) = PK(8)
      PK2(8) = FY4
C
      RETURN
      END
C
C     ************************************************************
C     F4 COMPUTES THE YAW ACCELERATION FUNCTION AND YAW MOMENT
C     ************************************************************
C
      SUBROUTINE F4(PSI,PK,PK2,
     &              YAWM,AMFP,HFORCE,POWER,ALF,CLL,CDD,AAA)
C
      INCLUDE 'YAWDYN.INC'
      COMMON/TEETER/ TEE1, SPRNG1, SPRNG2, TDAMP, SLING,
     &               TEEMOM, HUBMOM, ITETER
C
      DIMENSION PK(8), PK2(8), CY(11)
C
C     INITIALIZE
C
      Q(3) = PK(7)
      Q(4) = PK(8)
C
      CALL AERO(YAWM,YAERO,HFORCE,POWER,AMFP,
     &          PSI,PK,PK2,ALF,CLL,CDD,AAA)
C
      IF( IYAWC .NE. 1 ) THEN
          FY4 = 0.
          RETURN
      ENDIF
C
C     CHECK FOR USE OF FLAP DOF AND TEETER MOTION
C
      IF ( FDOF .EQ. 0 )  GO TO 20
      IF ( ITETER .EQ. 1 ) GO TO 15
C
C     SUM TERMS IN YAW EQUATION OF MOTION FOR RIGID HUB
C     WITH FLAP
      DO 5 I=1,11
         CY(I) = 0.0
```

```
    5  CONTINUE
C
       DO 10 IBLADE = 1,NB
         J     = 2*IBLADE - 1
         K     = J + 1
         Q(1)  = PK(J)
         Q(2)  = PK(K)
         PSIA  = PSI + FLOAT(IBLADE-1)*TWOPI/B
         SPSIA = SIN(PSIA)
         CPSIA = COS(PSIA)
         CY(1) = CY(1) + SPSIA * SPSIA
         CY(2) = CY(2) + Q(1)
         CY(4) = CY(4) + Q(1)*SPSIA
         CY(5) = CY(5) + Q(1)*CPSIA*CPSIA
         CY(6) = CY(6) + Q(1)*SPSIA*SPSIA
         CY(7) = CY(7) + Q(1)*CPSIA*SPSIA
         CY(8) = CY(8) + Q(2)
         CY(9) = CY(9) + SPSIA*CPSIA
         CY(10)= CY(10) + Q(1)*CPSIA*CPSIA*SPSIA
         CY(11)= CY(11) + Q(1)*SPSIA*SPSIA*SPSIA
C
   10  CONTINUE
C
       COEF1 = 1. + BM*RB*RH/BLINER
       E0 = YAERO/(REVS*REVS)
       E1 = YI + B*BM*SL*SL + ( BM*RH*RH - (BM*RB*RH)**2/BLINER )*CY(1)
      &         + RH*SL*CY(6) + BM*SL*RB*( CY(2) + CY(5) )
       E2 = BM*RB*RH*COEF1*CY(4)
       E3 = BM*GRAV*RB/REVS/REVS*COEF1*CY(7)
       E4 = FS/REVS/REVS*COEF1*CY(4)
       E5 = SL*RB*CY(8) + RH*RH*( 1. - BM*RB*RB/BLINER )*CY(9)
       E6 = BLINER*COEF1*CY(10) - BM*RB*RH*COEF1*CY(11) +
      &        TILT*CY(9) * ( BLINER + BM*RB*RH +
      &        BM*RH*RH*( -1. + BM*RB*RB/BLINER ) )
       E7 = YAWSTF * ( Q(3) - YSAVE )/(REVS*REVS)
C
       IF( ABS(Q(4)) .LE. 1.E-08 ) THEN
             SGN = 0.
         ELSE
             SGN = SIGN(1.,Q(4))*AF/(REVS*REVS)
       END IF
C
       YM1 = E0 - SGN - AV*Q(4)/REVS + E2 + E3 + E4
      &          - 2.*Q(4)*BM*E5 - Q(4)*Q(4)*E6 - E7
       FY4 = YM1/E1
C
       RETURN
C
C      THIS SECTION FOR USE WITH TEETERING ROTOR ONLY
C
   15  CPSI = COS(PSI)
       SPSI   SIN(PSI)
       TEETER = PK(1) - PC
       E1 = BLINER*REVS*REVS
       E2 = 1. - BM*SLING*SLING/BLINER
       E3 = YI*E2 + 2.*BM*SL*SL + 4.*BM*SL*SLING -
      &        2.*CPSI*CPSI*BM*( SL*SLING*(2. + BM*SL*SLING/BLINER)
      &       + SLING*SLING*E2 )
       E4 = YAERO*E2/REVS/REVS
       E5 = 2.*BM*SL*SLING*TEETER*SPSI
       E6 = BM*SL*SLING*TEEMOM*SPSI/E1
       E7 = 2.*BM*GRAV*SLING*CPSI*SPSI/REVS/REVS
      &        * ( E2 + BM*SLING*SL/BLINER )
       E8 = HUBMOM*SPSI*( E2 - BM*SL*SLING/BLINER )/REVS/REVS
```

```
      E9 = 4.*BM*SL*SLING*CPSI*SPSI
      E10 = 4.*CPSI*BM*SLING*E2 * ( SL - SLING )
      E11 = YAWSTF * ( Q(3) - YSAVE )/(REVS*REVS)
C
      IF( ABS(Q(4)) .LE. 1.E-08 ) THEN
           SGN = 0.
        ELSE
           SGN = SIGN(1.,Q(4))*AF/(REVS*REVS)
      END IF
C
      FY4 = E4 - E5 - E6 - E7 + E8 - E9*Q(4) + E10*PK(2) - E11 - SGN
      FY4 = FY4/E3
C
      RETURN
C
C     THIS SECTION FOR USE WHEN FLAP DOF NOT CONSIDERED
C
   20 CONTINUE
      IF (NB .EQ. 2) THEN
           S2 = 2.*SIN(PSI)**2
        ELSE
           S2 = B/2.
      ENDIF
C
      E0 = YAWM/(REVS*REVS)
      E1 = YI + B*BM*SL*SL + ( BLINER + BM*RH*(RH+2.*RB) )*S2
     &     + 2.*BM*RB*SL*B*PC
      E7 = YAWSTF * ( Q(3) - YSAVE )/(REVS*REVS)
C
      IF( ABS(Q(4)) .LE. 1.E-08 ) THEN
          SGN = 0.
      ELSE
          SGN = SIGN(1.,Q(4))*AF/(REVS*REVS)
      ENDIF
C
      C1  = E0 - SGN - AV*Q(4)/REVS - E7
      FY4 = C1/E1
C
      RETURN
      END
C
C
C     ************************************************************
C     AB SOLVES THE FIRST ORDER EQUATION USING ADAMS-BASHFORTH
C     PREDICTOR-CORRECTOR SCHEME.
C     ************************************************************
C
C     THE MATRIX F CONTAINS THE PREVIOUS FOUR SETS OF DERIVATIVE
C     FUNCTIONS EVALUATED BY SUBROUTINE FK.  THE DEGREES-OF-FREEDOM
C     CONTAINED IN VECTOR QP ARE ADVANCED
C     ONE STEP SIZE, H, AND THE MATRIX F IS SHIFTED TO STORE
C     THE NEW SET OF DERIVATIVE FUNCTION VALUES DURING EACH RUN OF AB.
C
C     VARIABLES:
C       CK   = CORRECTOR TERM (LOCAL TO THIS SUBROUTINE)
C       PK   = PREDICTOR TERM (PASSED TO FK FOR EVALUATION OF FUNCTION F)
C       QP   = SOLUTION VECTOR (BETA1,BETA1',BETA2,BETA2',
C              BETA3,BETA3',GAMMA,GAMMA')
C       F    = RHS OF 8 GOVERNING EQUATIONS, EVALUATED AT LAST FOUR
C              TIME STEPS (THE LAST FOUR VALUES OF PK2)
C       PK2  = PK PRIME
C              MOST RECENT VALUE OF F, THAT IS, THE DERIVATIVE OF PK
C              BETA1',BETA1'',BETA2',BETA2'',BETA3',BETA3'',GAMMA',GAMMA''
C
```

```
      SUBROUTINE AB(PSI,QP,F,YAWM,AMFP,HFORCE,POWER,ALF,CLL,CDD,AAA)
C
      INCLUDE 'YAWDYN.INC'
      COMMON/TEETER/ TEE1, SPRNG1, SPRNG2, TDAMP, SLING,
     &               TEEMOM, HUBMOM, ITETER
C
      DIMENSION QP(8),F(8,4),PK(8),CK(8),PK2(8)
C
      IF ( FDOF .EQ. 0 ) THEN
         DO 5 K=1,NB
            KK = 2*K - 1
            QP(KK)   = PC
            QP(KK+1) = 0.0
            PK(KK)   = PC
            PK(KK+1) = 0.0
    5    CONTINUE
      ENDIF
C
      IF ( FDOF .EQ. 1 ) THEN
          DO 10 I = 1,2*(NB - ITETER)
              PK(I) = QP(I) + ( 55.*F(I,4)-59.*F(I,3)+37.*F(I,2)
     &                  -9.*F(I,1) ) * H/24.
   10     CONTINUE
          IF( ITETER .EQ. 1 ) THEN
C            FORCE BLADE 2 TO FOLLOW BLADE 1 FOR TEETERING
             PK(3) = 2.*PC - PK(1)
             PK(4) = -PK(2)
          ENDIF
      ENDIF
C
      DO 20 I = 7,8
            PK(I) = QP(I) + ( 55.*F(I,4)-59.*F(I,3)+37.*F(I,2)
     &               -9.*F(I,1) ) * H/24.
   20 CONTINUE
C
      PSI = PSI + H
      CALL FK(PSI,PK,PK2,YAWM,AMFP,HFORCE,POWER,ALF,CLL,CDD,AAA)
C
      IF ( FDOF .EQ. 1 ) THEN
         DO 30 I = 1,2*(NB - ITETER)
            CK(I)=QP(I) + ( 9.*PK2(I) + 19.*F(I,4) - 5.*F(I,3)
     &                  + F(I,2) ) * H/24.
            QP(I)   = ( 251.*CK(I) + 19.*PK(I) )/270.
            F(I,1) = F(I,2)
            F(I,2) = F(I,3)
            F(I,3) = F(I,4)
            F(I,4) = PK2(I)
   30    CONTINUE
C
C        FORCE COORDINATION OF TWO BLADES IF TEETERING ROTOR
C
         IF ( ITETER .EQ. 1) THEN
             QP(3) = 2.* PC - QP(1)
             QP(4) = -QP(2)
         ENDIF
      ENDIF
C
      DO 40 I = 7,8
            CK(I) = QP(I) + ( 9.*PK2(I) + 19.*F(I,4) - 5.*F(I,3)
     &                     + F(I,2) ) * H/24.
            QP(I)   = ( 251.*CK(I) + 19.*PK(I) )/270.
            F(I,1) = F(I,2)
            F(I,2) = F(I,3)
            F(I,3) = F(I,4)
```

```
            F(I,4) = PK2(I)
   40   CONTINUE
C
        RETURN
        END
C
C       ***************************************************************
C       PREDCOR SOLVES THE EQUATION USING PREDICTOR-CORRECTOR METHOD
C       ***************************************************************
C
C       THE NEW VALUES ARE RETURNED IN QP. SUBROUTINE
C       FK IS USED TO EVALUATE THE DERIVATIVE FUNCTIONS.
C
        SUBROUTINE PREDCOR(PSI,QP)
C
        INCLUDE 'YAWDYN.INC'
        COMMON/TEETER/ TEE1, SPRNG1, SPRNG2, TDAMP, SLING,
       &               TEEMOM, HUBMOM, ITETER
C
        DIMENSION QP(8),PK(8),QK(8),TK(8)
C
        IF ( FDOF .EQ. 0 ) THEN
           DO 30 K = 1,NB
              KK = 2*K - 1
              QP(KK)   = PC
              QP(KK+1) = 0.0
   30      CONTINUE
        ENDIF
C
C       PREDICTOR CALCULATION
C
        CALL FK(PSI,QP,TK,YAWM,AMFP,HFORCE,POWER,ALF,CLL,CDD,AAA)
        DO 10 I = 1,2*(NB - ITETER)
            PK(I) = QP(I) + TK(I) * H
   10   CONTINUE
        IF ( ITETER .EQ. 1 ) THEN
            PK(3) = 2.*PC - PK(1)
            PK(4) = -PK(2)
        ENDIF
        DO 15 I = 7,8
            PK(I) = QP(I) + TK(I) * H
   15   CONTINUE
C
C       CORRECTOR TERM
C
        PSI = PSI + H
        CALL FK(PSI,PK,QK,YAWM,AMFP,HFORCE,POWER,ALF,CLL,CDD,AAA)
        DO 20 I = 1,2*(NB - ITETER)
            QP(I) = QP(I) + ( QK(I) + TK(I) ) * H/2.
   20   CONTINUE
        DO 25 I = 7,8
            QP(I) = QP(I) + ( QK(I) + TK(I) ) * H/2.
   25   CONTINUE
C
C       FORCE TEETER MOTION FOR BLADE 2 IF TEETERING ROTOR
C
        IF ( ITETER .EQ. 1 ) THEN
            QP(3) = 2. * PC - QP(1)
            QP(4) = -QP(2)
        ENDIF
        RETURN
        END
C       SUBROUTINES USED IN YAWDYN
C          ACH 6/5/91
```

```
C
C     ****************************************************
C     SUBROUTINE INOUT IS USED TO READ INPUT DATA AND ECHO
C     THE DATA TO THE OUTPUT FILE
C     ****************************************************
C
      SUBROUTINE INOUT(SECTOR,N,IWND,DELTAT,TDATA,IHARM,TOLER,QP)
C
      INCLUDE 'YAWDYN.INC'
      COMMON/TEETER/ TEE1, SPRNG1, SPRNG2, TDAMP, SLING,
     &               TEEMOM, HUBMOM, ITETER
C
      CHARACTER*80 TITLE
      DIMENSION QP(8)
C
      READ(10,2100) TITLE
C
C     READ RUN-TIME CONTROL PARAMETERS
C
      READ(10,*)  IYAWC, MREV, NSEE, IPRINT
C
C     CHECK TO SEE WHETHER FLAP DOF WILL BE INCLUDED (FDOF=1)
C       AND WHETHER WIND INPUT DATA FILE WILL BE USED (IWND=1)
C
      READ(10,*) FDOF, ITETER, IWND, DELTAT, IHARM
      IF( .NOT.(FDOF .EQ. 0 .OR. FDOF .EQ. 1) ) THEN
          PAUSE 'ERROR IN FDOF VALUE FROM FILE YAWDYN.IPT'
          STOP
      ENDIF
      IF( .NOT.(ITETER .EQ. 0 .OR. ITETER .EQ. 1) ) THEN
          PAUSE 'ERROR IN ITETER VALUE FROM FILE YAWDYN.IPT'
          STOP
      ENDIF
      IF( ITETER .EQ. 1 .AND. FDOF .EQ. 0 ) THEN
          PAUSE 'TEETER, BUT NOT FLAP DOF REQUESTED, CHECK YAWDYN.IPT'
          STOP
      ENDIF
      IF( .NOT.(IWND .EQ. 0 .OR. IWND .EQ. 1) ) THEN
          PAUSE 'ERROR IN IWND VALUE FROM FILE YAWDYN.IPT'
          STOP
      ENDIF
      IF( .NOT.(IHARM .EQ. 0 .OR. IHARM .EQ. 1) ) THEN
          PAUSE 'ERROR IN IHARM VALUE FROM FILE YAWDYN.IPT'
          STOP
      ENDIF
C
C     READ THE REMAINDER OF THE INPUT FILE
C
      READ(10,*) YI, BM, BLINER
      READ(10,*) FS, YAWSTF
C
      IF (ITETER .EQ. 1) THEN
         READ(10,*) TEE1, SPRNG1, SPRNG2, TDAMP, SLING
         TEE1 = TEE1/DEG
      ENDIF
C
      READ(10,*) R, RB, RH, HH, B, PC
      NB = B
      READ(10,*) V, VX, RPM, HSHR, VSHR, ISHR, VELDEF
      IF( .NOT.(ISHR .EQ. 1 .OR. ISHR .EQ. 2) ) THEN
          PAUSE 'ERROR IN ISHR VALUE FROM FILE YAWDYN.IPT'
          STOP
      ENDIF
C
```

```
      IF( IWND .EQ. 1) THEN
         OPEN (UNIT=11, FILE= 'YAWDYN.WND',STATUS='OLD',IOSTAT=IERR)
         IF(IERR.NE.0)  THEN
            WRITE(*,*) 'ERROR OPENING YAWDYN.WND'
            WRITE(*,*) 'IOSTAT=',IERR
            STOP
         ENDIF
      ENDIF
C
      REVS = RPM*PI/30.
      IF( (ITETER .EQ. 1) .AND. (NB .NE. 2) ) THEN
           WRITE(*,*) ' YOU MUST HAVE TWO BLADES FOR TEETERING ROTOR'
           PAUSE 'ENTER CARRIAGE RETURN TO CONTINUE'
           STOP
      ENDIF
C
C     READ WIND DATA TO INITIALIZE (IF THAT OPTION SELECTED)
C
      DELTA=0.
      IF( IWND .EQ. 1 ) READ(11,*) TDATA,V,DELTA,VX,HSHR,VSHR
      DELTA=DELTA/DEG
C
C     NON-DIMENSIONALIZE WIND SPEEDS USING TIP SPEED
C
      VREF = R*REVS
      VX   = VX/VREF
      V    = V/VREF
C
      READ(10,*) SL,AV,AF,TILT
      TILT = TILT/DEG
      READ(10,*) (PITCH(I),I=1,NB)
      READ(10,*) Q(3),Q(4)
      READ(10,*) ( QP(I),QP(I+1), I=1,2*(NB-ITETER)-1,2 )
      IF ( ITETER .EQ. 1 ) THEN
         QP(3) = 2.*PC - QP(1)
         QP(4) = -QP(2)
      ENDIF
      Q(1) = QP(1)
      Q(2) = QP(2)
      READ(10,*) N
      READ(10,*) SECTOR,TOLER,RHO
      N = N * SECTOR
C
      WRITE(*,2100) TITLE
      IF ( IYAWC .EQ. 0 ) THEN
         WRITE(*,*) '  FIXED-YAW ANALYSIS'
      ELSE
         WRITE(*,*) '  FREE-YAW ANALYSIS'
      ENDIF
C
      WRITE(100,2100) TITLE
      IF ( ITETER .EQ. 0 ) THEN
           WRITE(100,*) '  ANALYSIS OF A RIGID ROTOR'
        ELSE
           WRITE(100,*) '  ANALYSIS OF A TEETERING ROTOR'
      ENDIF
      WRITE(100,*) ' '
      WRITE(100,*) '  INITIAL WIND SPEED AT HUB (FT/SEC) =', V*REVS*R
      WRITE(100,*) '  INITIAL WIND DIRECTION DELTA (DEG) =', DELTA*DEG
      WRITE(100,*) '  VERTICAL COMPONENT OF WIND SPEED (FT/SEC) =',
     &                      VX*R*REVS
      WRITE(100,*) '  ROTOR SPEED (RPM) =', RPM
      WRITE(100,*) '  AIR DENSITY (SLUG/FT^3) =', RHO
      WRITE(100,*) ' '
```

```
      WRITE(100,*) '  ROTOR RADIUS (FT) =', R
      WRITE(100,*) '  HUB RADIUS (FT) =', RH
      WRITE(100,*) '  HUB HEIGHT (FT) =', HH
      WRITE(100,*) '  INITIAL PITCH ANGLES (DEG) =', (PITCH(I),I=1,NB)
      WRITE(100,*) '  BLADE CENTER OF GRAVITY (FT) =', RB
      WRITE(100,*) '  YAW AXIS-TO-HUB DISTANCE (FT) =',SL
      WRITE(100,*) '  NUMBER OF BLADES =', B
      WRITE(100,*) '  PRE-CONING ANGLE (DEG) =', PC
      WRITE(100,*) '  ROTOR TILT ANGLE (DEG) =', TILT*DEG
      WRITE(100,*) ' '
      WRITE(100,*) '  MASS OF BLADE (SLUG) =', BM
      WRITE(100,2200) BLINER
      WRITE(100,2300) YI
      WRITE(100,*) ' '
      IF( ITETER .EQ. 1) THEN
         WRITE(100,*) '  FREE TEETER ANGLE (DEG) =',  TEE1*DEG
         WRITE(100,*) '  FIRST TEETER STIFFNESS COEFF. (FT-LB/RAD) =',
     &                  SPRNG1
         WRITE(100,*) '  SECOND TEETER STIFFNESS COEFF. (FT-LB/RAD) =',
     &                  SPRNG2
         WRITE(100,*) '  TEETER DAMPING COEF (FT-LB-S) =', TDAMP
         WRITE(100,*) '  ROTOR MASS OFFSET (FT) =', SLING
      ENDIF
      IF( ITETER .EQ. 0 ) THEN
         WRITE(100,*) '  BLADE STIFFNESS COEF. (LB-FT/RAD) =', FS
         FREQ = SQRT(FS/BLINER)/TWOPI
         WRITE(100,*) '  BLADE NATURAL FREQUENCY (HZ) =',FREQ
         P = SQRT( 1. + RH*RB*BM/BLINER + FS/BLINER/REVS/REVS )
         WRITE(100,*) '  BLADE ROTATING NATURAL FREQUENCY (P#) =',P
         WRITE(*,*)   '  BLADE ROTATING NATURAL FREQUENCY (P#) =',P
      ENDIF
      WRITE(100,*) ' '
      WRITE(100,*) '  YAW STIFFNESS COEF. (FT-LB/RAD) =', YAWSTF
      WRITE(100,*) '  YAW AXIS FRICTION (FT-LB) = ',AF
      WRITE(100,*) '  YAW AXIS DAMPING (FT-LB-SEC) = ',AV
      WRITE(100,*) ' '
      WRITE(100,*) '  LINEAR HORIZONTAL WIND SHEAR'
      WRITE(100,*) '    INITIAL SHEAR COEFFICIENT = ',  HSHR
      IF (ISHR .EQ. 1)  THEN
         WRITE(100,*) '  LINEAR VERTICAL WIND SHEAR'
         WRITE(100,*) '    INITIAL SHEAR COEFFICIENT = ',  VSHR
      ELSE
         WRITE(100,*) '  POWER LAW VERTICAL WIND SHEAR '
         WRITE(100,*) '    INITIAL POWER LAW EXPONENT = ',  VSHR
      ENDIF
      WRITE(100,*) '  TOWER SHADOW COEFFICIENT = ',VELDEF
      WRITE(100,*) ' '
      IF(IWND .EQ. 1) THEN
         WRITE(100,*) '  OPERATING PARAMETERS READ FROM YAWDYN.WND FILE'
         WRITE(100,*) '  TIME INTERVAL FOR WIND INPUT DATA =', DELTAT
      ENDIF
      WRITE(100,*) ' '
C
      IF( FDOF .EQ. 1 ) THEN
         WRITE(100,*) '  INITIAL FLAP ANGLE (BLADE 1) (DEG) = ',  Q(1)
         WRITE(100,*) '  INITIAL FLAP RATE (BLADE 1) (DEG/S) = ', Q(2)
      ELSE
         WRITE(100,*) '  INITIAL FLAP ANGLE (BLADE 1) (DEG) = ',  PC
         WRITE(100,*) '  INITIAL FLAP RATE (BLADE 1) (DEG/S) = 0.0'
      ENDIF
      WRITE(100,*) '  INITIAL YAW ANGLE (DEG)  = ',  Q(3)
      WRITE(100,*) '  INITIAL YAW RATE (DEG/S) = ', Q(4)
      IF(IYAWC .EQ. 0) THEN
           WRITE(100,*) '  FIXED YAW OPERATION'
```

```
        ELSE
           WRITE(100,*) '  FREE YAW OPERATION'
        ENDIF
C
        IF(FDOF .EQ. 0) THEN
           WRITE(100,*) '  FLAP DEGREE OF FREEDOM NOT CONSIDERED'
        ELSE
           WRITE(100,*) '  FLAP DEGREE OF FREEDOM WAS CONSIDERED'
        ENDIF
        WRITE(100,*) '  PRINT INTERVAL (TO PLOT FILE) = ',IPRINT
        WRITE(100,*) ' '
        WRITE(100,*) '  TOLERANCE FOR TRIM SOLUTION'
        WRITE(100,*) '     CONVERGENCE TEST =', TOLER
        WRITE(100,*) ' '
C
C       READ SECTION CL AND CD AND OTHER AIRFOIL CHARACTERISTICS
C
        READ(10,*) ALPHAS, DSTLHI, DSTLLO, THICK
        READ(10,*) CFILT, NFILT
        ALPHAS = ALPHAS/DEG
        WRITE(100,*) '  UNSTEADY STALL PARAMETERS: '
        WRITE(100,*) '     STALL ANGLE =', ALPHAS*DEG
        WRITE(100,*) '     UPPER HYSTERESIS LOOP CONSTANT =', DSTLHI
        WRITE(100,*) '     LOWER HYSTERESIS LOOP CONSTANT =', DSTLLO
        WRITE(100,*) '     AIRFOIL THICKNESS/CHORD =',THICK
        WRITE(100,*) '     FILTER CUTOFF FREQUENCY, (PER REV)  =', CFILT
        WRITE(100,*) '     NUMBER OF FILTER STAGES =', NFILT
C
C       CONSTANT USED IN GORMONT DYNAMIC STALL MODEL
C
        STLGAM = 1.4 - 6.*(.06 - THICK)
C
        READ(10,*) NLIFT,NDRAG,ALPHAL
        ALPHAL = ALPHAL/DEG
        WRITE(100,*) ' '
        WRITE(100,*) '  ZERO-LIFT ANGLE OF ATTACK =', ALPHAL*DEG
C
        WRITE (100,2400)
C
        DO 40 I=1,NLIFT
              READ(10,*) AL(I),CL(I)
              WRITE(100,2500) AL(I),CL(I)
              AL(I)=AL(I)/DEG
  40    CONTINUE
C
        WRITE(100,*) ' '
        WRITE(100,2600)
        DO 50 I=1,NDRAG
              READ(10,*) AD(I),CD(I)
              WRITE(100,2500) AD(I),CD(I)
              AD(I)=AD(I)/DEG
50      CONTINUE
        WRITE(100,*) ' '
C
C       READ TWIST ANGLE AND CHORD VALUES, CONVERT TWIST TO RADIANS
C
        WRITE(100,2700)
        CHORD = 0.0
        DO 60 I=1,10
              READ(10,*) TWIST(I),C(I)
              WRITE(100,2800) TWIST(I),C(I)
              TWIST(I) = TWIST(I)/DEG
              CHORD = CHORD + C(I)
  60    CONTINUE
```

```
C
C     ASPECT RATIO (AR) AND CDMAX FOR USE IN VITERNA AIRFOIL DATA
C
      AR = R/CHORD*10.
      CDMAX = 1.11 + 0.018*AR
C
C     FINISHED READING INPUT DATA
C
      CLOSE(10)
C
      WRITE(100,*) ' '
      IF ( (FDOF .EQ. 1) .AND. (ITETER .EQ. 0) ) THEN
         WRITE(100,*) '  FLAP MOMENT IS THE BLADE DEFLECTION',
     &               ' TIMES THE SPRING STIFFNESS'
        ELSEIF ( (FDOF .EQ. 1) .AND. (ITETER .EQ. 1) ) THEN
         WRITE(100,*) '  FLAP MOMENT IS THE APPLIED AERODYNAMIC',
     &              ' MOMENT'
        ELSE
         WRITE(100,*) '  FLAP MOMENT IS THE APPLIED AERODYNAMIC,',
     &              ' GRAVITY AND CENTRIFUGAL MOMENT'
      ENDIF
C
      IF ( IYAWC .EQ. 1 ) THEN
         WRITE(100,*) '  YAW MOMENT IS YAW DEFLECTION*YAW STIFFNESS'
        ELSE
         WRITE(100,*) '  YAW MOMENT IS APPLIED AERODYNAMIC MOMENT'
      ENDIF
C
      WRITE(100,2900) MREV,NSEE
      WRITE(100,*) ' '
C
      WRITE(*,*) ' '
      WRITE(*,*) 'RUNNING ',N,' POINTS'
      WRITE(*,*) 'WITH ',SECTOR,' POINTS PER REVOLUTION'
      TOFF = TWOPI*N/SECTOR/REVS
      WRITE(*,*) 'TOTAL TIME DURATION SIMULATED (SEC) = ',TOFF
      WRITE(*,*) ' '
C
 2100 FORMAT (A)
 2200 FORMAT ('  BLADE FLAP MOMENT OF INERTIA (SLUG*FT^2) =',F10.1)
 2300 FORMAT ('  NACELLE MOMENT OF INERTIA (SLUG*FT^2) =',F10.1)
 2400 FORMAT (/,'  AIRFOIL CHARACTERISTICS:',/,'  ANGLE OF ATTACK(DEG)
     &       LIFT COEF.          ')
 2500 FORMAT (4X, F10.4, 8X, F10.4 )
 2600 FORMAT (/,'  AIRFOIL CHARACTERISTICS:',/,'  ANGLE OF ATTACK(DEG)
     &      DRAG COEF.          ')
 2700 FORMAT (/'  TWIST ANGLE    CHORD  '/'      (DEG)        (FT)'/)
 2800 FORMAT (1X, F10.4, 4X,  F7.4 )
 2900 FORMAT (/'   DATA FOR CYCLE NUMBER',I3,', BLADE ELEMENT ',I2,
     &       //'   PSI     YAW       YAWMOMENT',3X,
     & 'FLAPMOMENT    ALPHA      CL      CD        A'/
     & '    DEG     DEG        FT-LB         FT-LB         DEG')
C
      RETURN
      END
C
C     ************************************************************
C     SUBROUTINE INITIAL
C     CALCULATES INITIAL VALUES OF ANGLE OF ATTACK FOR ONE BLADE
C     TO INITIALIZE THE FILTER 'MEMORY'
C     ************************************************************
C
      SUBROUTINE INITIAL(PSI)
C
```

```
      INCLUDE 'YAWDYN.INC'
C
C     ASSUME AVGINFL=0 AT THE BEGINING OF TRIM SOLUTION
C
      CALL VELD(SDEL,CDEL,ANGFLW,NTEST)
C
      DO 100 J=1,10
            X = ( 0.1*J - .05 )*R - RH
            IF( X .LE. 0. ) GO TO 100
            OLDA(J,IBLADE) = 0.1
            CALL VEL(VY,VZ,X,PSI)
            CALL VIND(A,J,X,PSI,VY,VZ,VN,VT)
            IF( NTEST .EQ. 1 ) THEN
                CALL VNMOD(VN,X,A,AXY,PSI,SDEL,CDEL,ANGFLW)
            ELSE
                AXY=A
            ENDIF
C
            ALPHA = ATAN2(VN,VT) - TWIST(J) - PITNOW/DEG
            ALPHA = AMOD(ALPHA,TWOPI)
            DO 200 K=1,2
                 OLALFA(J,IBLADE,K) = ALPHA
                 FF1(J,IBLADE,K) = ALPHA
                 FF2(J,IBLADE,K) = ALPHA
                 FF3(J,IBLADE,K) = ALPHA
 200        CONTINUE
            OLDA(J,IBLADE) = A
           DO 250 K=1,NDELAY+1
                 OLFALF(J,IBLADE,K) = ALPHA
 250        CONTINUE
 100  CONTINUE
C
      RETURN
      END
C
C     ****************
C     SUBROUTINE GETWND
C     ****************
C
C     THIS SUBROUTINE IS USED TO READ WIND DATA (OR OTHER
C     INDEPENDENT OPERATING PARAMETERS SUCH AS PITCH) FROM THE
C     DATA FILE YAWDYN.WND.  THIS OPTION IS EXERCISED WHEN IWND=1
C     IN THE YAWDYN.IPT DATA FILE.
C     THIS OPTION SHOULD BE EXERCISED WHEN SIMULATING ACTUAL
C     TIME SERIES DATA FROM FIELD EXPERIMENTS.
C     AC HANSEN, 10/88
C
C     THE READ STATEMENT IN THIS ROUTINE AND IN THE INITIALIZING
C     SECTION OF THE MAIN PROGRAM CAN BE CHANGED TO READ IN ANY
C     OR ALL OF THE FOLLOWING: V, DELTA, HSHR, VSHR, PITCH(I)
C        IF DELTA IS USED IT MUST BE IN (or converted to) RADIANS
C        IF PITCH IS USED IT MUST BE IN UNITS OF DEGREES
C
C     TIME   = CURRENT TIME IN SIMULATION
C     DELTAT = TIME STEP AT WHICH THE WIND DATA IS SAMPLED
C              THIS TIME STEP MUST EXCEED THE INTEGRATION STEP IN YAWDYN
C              BUT IT SHOULD NOT EXCEED THE TIME FOR A FEW ROTOR REVS.
C     TDATA  = TIME AT WHICH MOST RECENT DATA SCAN WAS SAMPLED
C
C     THE VALUES OF WIND FOR T = TDATA ARE ASSIGNED WHEN
C             TDATA <= TIME < TDATA + DELTAT
C
      SUBROUTINE GETWND(TIME,DELTAT,TDATA)
C
```

```
      INCLUDE 'YAWDYN.INC'
C
C     READ NEW VALUES IF TIME EXCEEDS OLD TDATA+DELTAT
C          OTHERWISE RETURN WITH OLD VALUES
C     ERROR TRAP FOR TIME VALUES OUTSIDE RANGE TDATA TO TDATA+2*DELTAT
C
      IF( TIME .LT. TDATA ) GO TO 100
C
      IF( TIME .GE. TDATA+DELTAT) THEN
          IF( TIME .GT. TDATA+2.*DELTAT ) GO TO 100
          READ(11,*) TDATA, V, DELTA, VX, HSHR, VSHR
          DELTA = DELTA/DEG
          V = V/REVS/R
          VX = VX/REVS/R
      ENDIF
C
      RETURN
C
 100  WRITE(*,*) ' ERROR TRAP IN GETWND SUBROUTINE'
      WRITE(*,*) ' CHECK DELTAT IN FILES YAWDYN.WND AND YAWDYN.IPT'
      WRITE(*,*) ' ALSO, CHECK TIME STEP IN THE PROGRAM < DELTAT'
      PAUSE '       ENTER CR TO CONTINUE'
      STOP
      END
C
C     ************************************************
C     VIND CALCULATES THE AXIAL INDUCTION FACTOR FOR EACH
C     ANNULAR SEGMENT AND SPECIFIED AZIMUTH ANGLE PSI.
C     ************************************************
C
      SUBROUTINE VIND(A,J,X,PSI,VY,VZ,VN,VT)
C
      INCLUDE 'YAWDYN.INC'
C
      SOLID  = B*C(J)/(PI*X)
      AI     = OLDA(J,IBLADE) - 0.1
      DAI1   = 0.1
      STEP   = 0.5
      ICOUNT = 0
C
      SQ1  = SIN( Q(1) )
      CQ1  = COS( Q(1) )
      SQ3  = SIN( Q(3) )
      CQ3  = COS( Q(3) )
      SPSI = SIN(PSI)
      CPSI = COS(PSI)
C
      VT = (X*CQ1 + RH)/R - VY*(CQ3*CPSI + TILT*SQ3*SPSI)
     &     - VZ*(SQ3*CPSI - TILT*CQ3*SPSI)
     &     - ( (X*SQ1+SL)*CPSI+TILT*(X*CQ1+RH) )*Q(4)/R + VX*SPSI
C
      VNORM = VZ*( CQ3*CQ1 - SPSI*SQ3*SQ1 - TILT*CQ3*CPSI )
     &        - VY*( SPSI*CQ3*SQ1 + CQ1*SQ3 - TILT*SQ3*CPSI )
     &        - VX*( SQ1*CPSI + TILT*CQ1) - X*Q(2)/R
     &        - ( X + RH*CQ1 + SL*SQ1 )*Q(4)*SPSI/R
C
10    ICOUNT = ICOUNT + 1
      VN     = VNORM * (1. - AI)
      CALL AXIND(VN,VT,VY,VZ,A2,J,SOLID,ALPHA,CLA,CDA)
      DAI    = A2 - AI
C
C     TEST FOR CONVERGENCE, STOP AFTER 100 ITERATIONS
C
      IF(ICOUNT .GT. 100) THEN
```

```
            WRITE(*,*) 'EXCESSIVE ITERATIONS TO FIND INDUCTION FACTOR'
            WRITE(*,*) 'ELEMENT= ',J,'     PSI= ',PSI*DEG
            WRITE(*,*) 'VN= ',VN,'     VT= ',VT
            WRITE(*,*) 'ALPHA= ',ALPHA*DEG,'     CL= ',CLA,'   CD= ',CDA
            WRITE(*,*) 'AI= ',AI,'      DAI= ',DAI
            WRITE(*,*) 'Q(I)= ',(Q(I),I=1,4)
            PAUSE 'ENTER CR TO CONTINUE'
            STOP
         ENDIF
C
         IF(ABS(DAI) .LE. 0.005) GO TO 14
         IF( IFIX(SIGN(1.,DAI)) .NE. IFIX(SIGN(1.,DAI1)))
        &       STEP = 0.5 * STEP
         AI    = AI + STEP * DAI
         DAI1 = DAI
         GO TO 10
C
   14    A = AI
C
         RETURN
         END
C
C        ***************************************************
C        AXIND CALCULATES A NEW AXIAL INDUCTION FACTOR FROM
C        GIVEN VALUES OF VELOCITIES AND GEOMETRY.  THIS ROUTINE
C        IS CALLED BY VIND AS PART OF THE ITERATION PROCESS
C        ***************************************************
C
         SUBROUTINE AXIND(VN,VT,VY,VZ,A2,J,SOLID,ALPHA,CLA,CDA)
C
         INCLUDE 'YAWDYN.INC'
C
C        GET AIRFOIL CL AND CD
C
         PITNOW = PITCH(IBLADE)
         PHI = ATAN2(VN,VT)
C
         ALPHA = PHI - TWIST(J) - PITNOW*DEG
         ALPHA = AMOD(ALPHA,TWOPI)
C
         CALL CLSUB(ALPHA,CLA)
         CALL CDSUB(ALPHA,CDA)
         W2 = VN*VN + VT*VT
C
C        CALCULATE NEW VALUE OF A ( BOTH W2 AND VZP ARE DIMENSIONLESS )
C
         VZP = -VX*SIN(TILT) + ( VZ*COS(Q(3))-VY*SIN(Q(3)) )*COS(TILT)
         CH  = W2*SOLID*(CLA*COS(PHI) + CDA*SIN(PHI))/(2.*(VZP*VZP))
         IF( CH .LT. 0.96 ) THEN
              A2 = ( 1. - SQRT(1.-CH) )/2.
           ELSE
              A2 = 0.143 + SQRT( .0203 - .6427*(.889-CH) )
         ENDIF
C
         RETURN
         END
C
C        ***********************************************
C        THIS SUBROUTINE USES DYNAMIC STALL MODEL
C        ***********************************************
C
         SUBROUTINE STALL(FALPHA,W2,J,ALPHA,ALPHAM)
C
         INCLUDE 'YAWDYN.INC'
```

```
C
C     USING PREVIOUS ANGLE OF ATTACK TO CALCULATE ALDOT
C     TO COMPENSATE THE DELAY DUE TO FILTER
C
      IF ( NDELAY .EQ. 0 ) THEN
           ALDOT = ( FALPHA - OLFALF(J,IBLADE,1) )*REVS/H
      ELSE
           NDELAY1 = NDELAY +1
           ALDOT = ( OLFALF(J,IBLADE,NDELAY)
     &             - OLFALF(J,IBLADE,NDELAY1) ) * REVS/H
      ENDIF
C
      IF( ALPHA .GE. ALPHAS ) IFLAG(J,IBLADE) = 1
      IF( ALPHA .LT. ALPHAS .AND. ABS(ALDOT) .LE. 1.E-6 )
     &    IFLAG(J,IBLADE) = 0

      IF( IFLAG(J,IBLADE) .EQ. 1 ) THEN
C
C        USING DYNAMIC STALL MODEL
C
         UR = SQRT(W2) * REVS*R
         ST = C(J) * ALDOT/(2.*UR)
         ST = SQRT(ABS(ST)) * SIGN(1., ALDOT)
C
         IF( ALDOT*ALPHA .GT. 0.) THEN
             XK = DSTLHI
           ELSE
             XK = DSTLLO
         ENDIF
C
C         USE UNFILTERED ANGLE OF ATTACK
C
          ALPHAM = ALPHA - XK*STLGAM*ST
      ELSE
C
C         NOT USING DYNAMIC STALL
          ALPHAM = ALPHA
      ENDIF
C
      RETURN
      END
C
C
C     ************************************************************
C     LOWPASS BUTTERWORTH DIGITAL FILTER DESIGN SUBROUTINE
C     SOURCE FILENAME              LPDES
C     ************************************************************
C     THE SUBROUTINE WILL RETURN THE COEFFICIENTS TO A CASCADE
C     REALIZATION OF A MULTIPLE SECTION LOWPASS FILTER. THE
C     Kth SECTION HAS THE FOLLOWING TRANFER FUNCTION:
C
C            A(K)*( 1 + 2*Z**-1 + Z**-2 )
C     H(Z) = ------------------------------
C            1 + B(K)*Z**-1 + C(K)*Z**-2
C
C     THUS, IF F(M) AND G(M) ARE THE INPUT AND OUTPUT OF THE
C     Kth SECTION, THE FOLLOWING DIFFERENCE EQUATION IS SATISFIED:
C
C     G(M) = A(K)*( F(M)+2*F(M-1)+F(M-2) ) - B(K)*G(M-1) - C(K)*G(M-2)
C
C     REFERENCE: DIGITAL SIGNAL ANALYSIS, SAMUEL D. STEARNS,
C     HAYDEN BOOK COMPANY, INC. ROCHELLE PARK
C     NEW JERSEY, APPENDIX C
C
```

```
      SUBROUTINE LPDES(SECTOR)
C
      INCLUDE 'YAWDYN.INC'
      COMPLEX CJ, Z, Z1, Z2, Z3, Z4
C
      SAMT = TWOPI/SECTOR/REVS
      FCUT = CFILT*REVS/TWOPI
C
      Q1   = FCUT * PI * SAMT
      WCP  = SIN(Q1)/COS(Q1)
      WCP2 = WCP * WCP
C
      DO 10 K = 1,NFILT
         CS = COS( FLOAT(2*(K+NFILT)-1)*PI/FLOAT(4*NFILT) )
         X  = 1./(1. + WCP2 - 2. * WCP * CS)
         ALP(K) = WCP2 * X
         BLP(K) = 2. * (WCP2 - 1) * X
         CLP(K) = (1. + WCP2 + 2.*WCP*CS) * X
10    CONTINUE
C
C     CALCULATE THE PHASE DELAY AT 1P FREQUENCY
C
      CJ    = CMPLX(0.,1.)
      FW    = REVS * SAMT
      PHASE = 0.

      DO 20 I=1,NFILT
         Z1 = CEXP(-CJ*FW)
         Z2 = CEXP(-2.*CJ*FW)
         Z3 = ALP(I)*( 1. + 2.*Z1 + Z2 )
         Z4 = 1. + BLP(I)*Z1 + CLP(I)*Z2
         Z  = Z3/Z4
         PHASE = PHASE + ATAN2( AIMAG(Z),REAL(Z) )
20    CONTINUE
C
C     CALCULATE NUMBER OF TIME STEPS CORRESPONDING TO PHASE SHIFT
C
      NDELAY = ANINT( -PHASE*SECTOR/TWOPI )
      WRITE(*,*) ' NDELAY (PHASE SHIFT TIME STEPS) = ', NDELAY
C
      RETURN
      END
C
C     ************************************************
C     FILTER CALCULATES ALPHA AFTER THE FILTER
C     AND UPDATES THE OLD VALUES
C     THE FILTER IS A LOW-PASS SINE BUTTERWORTH TYPE
C     ************************************************
C
      SUBROUTINE FILTER(ALPHA,FALPHA,J,ALPHA1,ALPHA2,ALPHA3)
C
      INCLUDE 'YAWDYN.INC'
C
C     IF NFILT=0, DO NOT FILTER
C
      IF ( NFILT .EQ. 0) THEN
         FALPHA = ALPHA
         RETURN
      ENDIF
C
C     GO THROUGH UP TO THREE STAGES OF THE FILTER
C
C     FIRST STAGE
C
```

```
      ALPHA1 = ALP(1)*( ALPHA + 2.*OLALFA(J,IBLADE,1)
     &                        +    OLALFA(J,IBLADE,2) )
     &       - BLP(1)*FF1(J,IBLADE,1) - CLP(1)*FF1(J,IBLADE,2)
      IF( NFILT .EQ. 1 ) THEN
          FALPHA = ALPHA1
          RETURN
      ENDIF
C
C     SECOND STAGE
C
      ALPHA2 = ALP(2)*( ALPHA1 + 2.*FF1(J,IBLADE,1)
     &                        +    FF1(J,IBLADE,2) )
     &       - BLP(2)*FF2(J,IBLADE,1) - CLP(2)*FF2(J,IBLADE,2)
      IF( NFILT .EQ. 2 ) THEN
          FALPHA = ALPHA2
          RETURN
      ENDIF
C
C     THIRD STAGE
C
      ALPHA3 = ALP(3)*( ALPHA2 + 2.*FF2(J,IBLADE,1)
     &                        +    FF2(J,IBLADE,2) )
     &       - BLP(3)*FF3(J,IBLADE,1) - CLP(3)*FF3(J,IBLADE,2)
C
C
      FALPHA = ALPHA3
C
      RETURN
      END
C
C     ***************************************************
C     VEL COMPUTES THE NONDIMENSIONAL VELOCITY COMPONENTS
C     IN THE INERTIAL FRAME OF REFERENCE
C     ***************************************************
C
      SUBROUTINE VEL(VY,VZ,XB,PSI)
C
      INCLUDE 'YAWDYN.INC'
C
      CPSI = COS(PSI)
      SPSI = SIN(PSI)
      CDELTA = COS(DELTA)
      SDELTA = SIN(DELTA)
      SQ1  = SIN( Q(1) )
      SQ3  = SIN( Q(3) )
      CQ1  = COS( Q(1) )
      CQ3  = COS( Q(3) )
C
      X = XB*CPSI*CQ1 + RH*CPSI
      Y = XB*(SPSI*CQ1*CQ3-SQ1*SQ3) + RH*SPSI*CQ3 - SL*SQ3
      Z = XB*(SPSI*CQ1*SQ3+SQ1*CQ3) + RH*SPSI*SQ3 + SL*CQ3
C
C     CHOOSE LINEAR WIND SHEAR OR POWER WIND SHEAR
C
      IF ( ISHR .EQ. 1 )  THEN
          V1 = V*( 1.+HSHR*( Y*CDELTA - Z*SDELTA )/(1.5*R)
     &           - VSHR*X/(1.5*R)  )
        ELSE
          V1 = V* HSHR*( Y*CDELTA - Z*SDELTA )/(1.5*R)
     &           + V * (1.-X/HH)**(VSHR)
      ENDIF
C
      VY = V1*SDELTA
      VZ = V1*CDELTA
```

```
C
C     TOWER SHADOW EFFECT
C
      TS = 0.
      PSIDEG = DEG*AMOD( PSI, TWOPI )
C
      IF( PSIDEG .LT. 15.  .OR.  PSIDEG .GT. 345. )
     &        TS = VELDEF*( 1. + COS(12.*PSI) )/2.
C
      VZ = VZ * (1. - TS)
C
      RETURN
      END
C
C     ****************************************
C     VELD CALCULATE THE VELOCITIES RELATIVE
C     TO THE ROTOR DISK
C     ****************************************
C
      SUBROUTINE VELD(SDEL,CDEL,ANGFLW,NTEST)
C
      INCLUDE 'YAWDYN.INC'
C
C     VELOCITIES AT ROTOR HUB IN XYZ COOR.
C
      VY1 = V*SIN(DELTA)
      VZ1 = V*COS(DELTA)
C
      CTILT = COS(TILT)
      STILT = SIN(TILT)
      CQ3   = COS(Q(3))
      SQ3   = SIN(Q(3))
      VYZ1  = VZ1*CQ3 - VY1*SQ3
C
C     VELOCITIES IN ROTOR DISK COOR.
C
      VEL1 = VX*CTILT + VYZ1*STILT
      VEL2 = VY1*CQ3 + VZ1*SQ3 + SL*Q(4)*CTILT/R
      VEL3 = -VX*STILT + VYZ1*CTILT
C
      VEL = SQRT( VEL1**2 + VEL2**2 )
C
      IF ( VEL .GE. 1.0E-6 ) THEN
           NTEST  = 1
           SDEL   = VEL2/VEL
           CDEL   = VEL1/VEL
           ANGFLW = ATAN2( ABS(VEL3-AVGINFL), VEL )
        ELSE
           NTEST = 0
      ENDIF
C
      RETURN
      END
C
C     ****************************************
C     VNMOD APPLIES THE SKEWED WAKE CORRECTION
C     TO THE NORMAL VELOCITY COMPONENT.
C     ****************************************
C
      SUBROUTINE VNMOD(VN,XB,A,AXY,PSI,SDEL,CDEL,ANGFLW)
C
      INCLUDE 'YAWDYN.INC'
C
      SANG = SIN(ANGFLW)
```

```
      BB    = 0.7363 * SQRT( ( 1. - SANG )/(1. + SANG) )
C
      AXY = A * ( 1. + 2.*XB/R*COS(Q(1)) *
     &            BB*( SDEL*SIN(PSI) + CDEL*COS(PSI) ) )
C
      VN    = VN * (1. - AXY)/(1. - A)
C
      RETURN
      END
C
C     ***********************************************
C     SUBROUTINE CLSUB RETURNS VALUES OF LIFT COEFF.
C     ***********************************************
C
      SUBROUTINE CLSUB(ALPHA,CLA)
C
C     THIS SUBROUTINE COMPUTES THE LIFT COEFFICIENTS
C     FROM A TABLE OF AIRFOIL DATA OR, FOR HIGH ANGLES OF ATTACK,
C     FROM THE METHOD OF VITERNA.
C
C     VARIABLES:
C        CLA   = RETURNED VALUE OF LIFT COEFF
C        ALPHA = ANGLE OF ATTACK (RADIANS)
C
C     USES SUBPROGRAMS GETCL, GETCD, LOCATE, FPL, FPD
C
      CLA=GETCL(ALPHA)
         IF( CLA .LT. -900. ) CLA=FPL(ALPHA)
C
      RETURN
      END
C
C     ***********************************************
C     SUBROUTINE CDSUB RETURNS VALUES OF DRAG COEFF.
C     ***********************************************
C
      SUBROUTINE CDSUB(ALPHA,CDA)
C
C     THIS SUBROUTINE COMPUTES THE DRAG COEFFICIENTS
C     FROM A TABLE OF AIRFOIL DATA OR, FOR HIGH ANGLES OF ATTACK,
C     FROM THE METHOD OF VITERNA.
C
C     VARIABLES:
C        CDA   = RETURNED VALUE OF DRAG COEFF
C        ALPHA = ANGLE OF ATTACK (RADIANS)
C
C     USES SUBPROGRAMS GETCL, GETCD, LOCATE, FPL, FPD
C
      CDA=GETCD(ALPHA)
         IF( CDA .LT. -900. ) CDA=FPD(ALPHA)
C
      RETURN
      END
C
C     *****************************************************
C     FUNCTION GETCL IS INTERPOLATION ROUTINE FOR AIRFOIL CL
C     *****************************************************
C
      FUNCTION GETCL(ANG)
C
      INCLUDE 'YAWDYN.INC'
C
      GETCL = -999.
      IF( ANG .LT. AL(1) .OR. ANG .GT. AL(NLIFT) ) RETURN
```

```
C
      CALL LOCATE(AL,NLIFT,ANG,N)
C
      P = ( ANG-AL(N) )/( AL(N+1)-AL(N) )
      GETCL = CL(N) + P*( CL(N+1)-CL(N) )
      RETURN
      END
C
C     ****************************************************
C     FUNCTION GETCD IS INTERPOLATION ROUTINE FOR AIRFOIL CD
C     ****************************************************
C
      FUNCTION GETCD(ANG)
C
      INCLUDE 'YAWDYN.INC'
C
      GETCD = -999.
      IF( ANG .LT. AD(1) .OR. ANG .GT. AD(NDRAG) ) RETURN
C
      CALL LOCATE(AD,NDRAG,ANG,N)
      P = ( ANG-AD(N) )/( AD(N+1)-AD(N) )
      GETCD = CD(N) + P*( CD(N+1)-CD(N) )
      RETURN
      END
C
C     ************************************************
C     SUBROUTINE LOCATE FINDS POSITION IN AIRFOIL TABLE
C     ************************************************
C     SEE 'NUMERICAL RECIPES' BY PRESS, ET AL, PAGE 89.
C     SIMPLIFIED TO WORK ONLY WITH MONOTONICALLY INCREASING
C     VALUES OF XX IN THE TABLE. ACH 10/88.
C
C     VARIABLES:
C       XX    = ARRAY (ANGLES OF ATTACK IN TABLE)
C       N     = NUMBER OF ENTRIES IN THE TABLE
C       X     = GIVEN VALUE OF ANGLE OF ATTACK
C       J     = INDEX POSITION OF X IN TABLE
C     J IS SUCH THAT X IS BETWEEN XX(J) AND XX(J+1)
C
      SUBROUTINE LOCATE(XX,N,X,J)
      DIMENSION XX(N)
      JL = 0
      JU = N+1
   10 IF( (JU-JL) .GT. 1 ) THEN
          JM = (JU+JL)/2
          IF( X .GT. XX(JM) ) THEN
               JL = JM
            ELSE
               JU = JM
          ENDIF
          GO TO 10
      ENDIF
      J = JL
      RETURN
      END
C
C     ********************************************
C     FUNCTION FPL CALCULATES PLATE LIFT COEFFICIENT
C     USING THE VITERNA METHOD
C     ********************************************
      FUNCTION  FPL(ANG)
C
      INCLUDE 'YAWDYN.INC'
C
```

```
      A1   = CDMAX/2.
      SSI = SIN( AL(NLIFT) )
      SCO = COS( AL(NLIFT) )
      A2   = ( CL(NLIFT) - CDMAX*SSI*SCO )*SSI/SCO/SCO
C
C     FIND PROPER QUADRANT AND ASSIGN CL
C     THE ASSIGNMENTS ARE AS FOLLOWS:
C       AL(NLIFT) < ANG <.PI/2       : VITERNA METHOD
C       PI/2 < ANG < PI-AL(NLIFT)    : -VITERNA
C       ANG NEAR +/- PI              : LINEAR INTERPOLATION
C       -AL(NLIFT) < ANG < AL(1)     : LINEAR INTERPOLATION
C       -PI/2 < ANG < -AL(NLIFT)     : -VITERNA
C       -PI+AL(NLIFT) < ANG < -PI/2 : VITERNA
C
      IF( ANG .GT. AL(NLIFT) .AND. ANG .LE. PIBY2 ) THEN
            SANG = SIN(ANG)
            COSANG = COS(ANG)
            FPL = 2.*A1*SANG*COSANG + A2*COSANG*COSANG/SANG
        ELSEIF( ANG .GT. PIBY2 .AND.  ANG .LE. PI-AL(NLIFT) ) THEN
            ANG = PI-ANG
            SANG = SIN(ANG)
            COSANG = COS(ANG)
            FPL = 2.*A1*SANG*COSANG + A2*COSANG*COSANG/SANG
            FPL = -FPL
        ELSEIF(ANG .GT. PI-AL(NLIFT) .AND. ANG .LE. PI) THEN
            ANG = ANG-PI
            FPL = -CL(NLIFT)+(ANG+AL(NLIFT))/(AL(NLIFT)+AL(1))
     &             *(CL(NLIFT)-CL(1))
        ELSEIF( ANG .GT. -AL(NLIFT) .AND. ANG .LE. AL(1) ) THEN
            FPL = -CL(NLIFT)+(ANG+AL(NLIFT))/(AL(1)+AL(NLIFT))
     &             *(CL(NLIFT)+CL(1))
        ELSEIF( ANG .LE. -AL(NLIFT) .AND. ANG .GE. -PIBY2 )  THEN
            ANG = -ANG
            SANG = SIN(ANG)
            COSANG = COS(ANG)
            FPL = 2.*A1*SANG*COSANG + A2*COSANG*COSANG/SANG
            FPL = -FPL
        ELSEIF( ANG .LT. -PIBY2 .AND. ANG .GE. -PI+AL(NLIFT) )  THEN
            ANG = PI+ANG
            SANG = SIN(ANG)
            COSANG = COS(ANG)
            FPL = 2.*A1*SANG*COSANG + A2*COSANG*COSANG/SANG
        ELSEIF(ANG .LT. -PI+AL(NLIFT) .AND. ANG .GE. -PI) THEN
            ANG = ANG+PI
            FPL = CL(1)+(ANG-AL(1))*(CL(NLIFT)-CL(1))/(AL(NLIFT)-AL(1))
      ENDIF
C
      RETURN
      END
C
C
C     ************************************************
C     FUNCTION FPD CALCULATES DRAG COEFFICIENT FOR HIGH
C     ANGLE OF ATTACK USING THE VITERNA METHOD.
C     ************************************************
C
      FUNCTION FPD(ANG)
C
      INCLUDE 'YAWDYN.INC'
C
      SSI = SIN( AD(NDRAG) )**2
      SCO = COS( AD(NDRAG) )
      B22 = ( CD(NDRAG)-CDMAX*SSI )/SCO
C
```

```
C     FIND PROPER QUADRANT AND ASSIGN CD
C
      IF( ANG .GT. AD(NDRAG) .AND. ANG .LE. PIBY2 ) THEN
            FPD = CDMAX*SIN(ANG)**2+B22*COS(ANG)
        ELSEIF( ANG .GT. PIBY2 .AND.  ANG .LE. PI ) THEN
            ANG = PI-ANG
            FPD = CDMAX*SIN(ANG)**2+B22*COS(ANG)
        ELSEIF( ANG .GT. -AD(NDRAG) .AND. ANG .LE. AD(1) ) THEN
            FPD = CD(1)+(-ANG+AD(1))*(CD(NDRAG)-CD(1))/(AD(NDRAG)+AD(1))
        ELSEIF( ANG .LE. -AD(NDRAG) .AND. ANG .GE. -PIBY2 )  THEN
            ANG = -ANG
            FPD = CDMAX*SIN(ANG)**2+B22*COS(ANG)
        ELSEIF( ANG .LT. -PIBY2 .AND.  ANG .GE. -PI ) THEN
            ANG = -PI-ANG
            FPD = CDMAX*SIN(ANG)**2+B22*COS(ANG)
      ENDIF
C
      RETURN
      END
C
C     ************** END OF FILE ***************
```

Listing of the YawDyn.Inc include file

```
C      INCLUDE FILE FOR YAWDYN PROGRAM
C      6/14/91 ACH
C
       COMMON/MACH/ AF, AV, B, NB, BLINER, BM, C(10), FS, FY4, HH, PC,
      &       PITCH(3), PITNOW, R, RB, REVS, RH, SL, TWIST(10), YI,
      &       YAWSTF, YSAVE, Q(4), AVGINFL
C
       COMMON/WIND/ DELTA, HSHR, RHO, TILT, V, VELDEF, VSHR, VX
C
       COMMON/CONST/ DEG, GRAV, PI, PIBY2, TWOPI,
      &       FDOF, IPRINT, ISHR, IYAWC, MREV, NSEE
C
       COMMON/AIRFOL/ NLIFT,NDRAG,AL(30),AD(30),CL(30),CD(30),CDMAX
C
       COMMON/UNSTDY/ ALPHAL, ALPHAS, H, IBLADE, DSTLLO,DSTLHI,STLGAM,
      &       FF1(10,3,2), FF2(10,3,2), FF3(10,3,2), IFLAG(10,3),
      &       OLDA(10,3), OLALFA(10,3,2), OLFALF(10,3,100)
C
       COMMON/LPFILT/ CFILT, NFILT, NDELAY, ALP(10), BLP(10), CLP(10)
C
       INTEGER FDOF
```

Document Control Page	1. NREL Report No. NREL/TP-442-4822	2. NTIS Accession No. DE92001245	3. Recipient's Accession No.

4. Title and Subtitle

Yaw Dynamics of Horizontal Axis Wind Turbines--Final Report

5. Publication Date
April 1992

6.

7. Author(s)
A.C. Hansen

8. Performing Organization Rept. No.

9. Performing Organization Name and Address

University of Utah
Mechanical Engineering Dept.
Salt Lake City, Utah 84112

10. Project/Task/Work Unit No.
WE21.8202

11. Contract (C) or Grant (G) No.

(C) XL-6-05078-2

(G)

12. Sponsoring Organization Name and Address

National Renewable Energy Laboratory
1617 Cole Blvd.
Golden, CO 80401

13. Type of Report & Period Covered
Subcontract Report

14.

15. Supplementary Notes
NREL Technical Monitor: Alan Wright (303) 231-7651

16. Abstract (Limit: 200 words)

Designers of a horizontal axis wind turbine yaw mechanism are faced with a difficult decision. They know that if they elect to use a yaw-controlled rotor then the system will suffer increased initial cost and increased inherent maintenance and reliability problems. On the other hand, if they elect to allow the rotor to freely yaw they know they will have to account for unknown and random, though bounded, yaw rates. They will have a higher-risk design to trade-off against the potential for cost savings and reliability improvement. The risk of a yaw-free system could be minimized if methods were available for analyzing and understanding yaw behavior. The complexity of yaw behavior has, until recently, discouraged engineers from developing a complete yaw analysis method. The objectives of this work are to (1) provide a fundemantal understanding of free-yaw mechanics and the design concepts most effective at eliminating yaw problems, and (2) provide tested design tools and guidelines for use by free-yaw wind systems manufacturers. The emphasis here is on developing practical and sufficiently accurate design methods.

17. Document Analysis
a. Descriptors
wind energy, yaw dynamics, structures

b. Identifiers/Open-Ended Terms

c. UC Categories
231

18. Availability Statement
National Technical Information Service
U.S. Department of Commerce
5285 Port Royal Road
Springfield, VA 22161

19. No. of Pages
186

20. Price
A09

Form No. 0069E (6-30-87)

END

DATE FILMED

7/2/92

NREL/TP-253-4422 • UC Category: 233 • DE92001246

High-Flux Solar Photon Processes: Opportunities for Applications

NREL/TP--253-4422

DE92 001246

J.I. Steinfeld, S.L. Coy, H. Herzog,
J.A. Shorter, M. Schlamp, J.W. Tester,
W.A. Peters
Massachusetts Institute of Technology
Cambridge, Massachusetts

NREL Technical Monitor: Meir Carasso

National Renewable Energy Laboratory
(formerly the Solar Energy Research Institute)
1617 Cole Boulevard
Golden, Colorado 80401-3393
A Division of Midwest Research Institute
Operated for the U.S. Department of Energy
under Contract No. DE-AC02-83CH10093

Prepared under subcontract no: XM-0-10135-1

June 1992

On September 16, 1991 the Solar Energy Institute was designated a national laboratory, and its name was changed to the National Renewable Energy Laboratory.

Printed in the United States of America
Available from:
National Technical Information Service
U.S. Department of Commerce
5285 Port Royal Road
Springfield, VA 22161

Price: Microfiche A01
Printed Copy A05

Codes are used for pricing all publications. The code is determined by the number of pages in the publication. Information pertaining to the pricing codes can be found in the current issue of the following publications which are generally available in most libraries: *Energy Research Abstracts (ERA)*; *Government Reports Announcements* and Index (*GRA* and I); *Scientific and Technical Abstract Reports (STAR)*; and publication NTIS-PR-360 available from NTIS at the above address.

PREFACE

This report is the outcome of a study carried out at the Massachusetts Institute of Technology under subcontract XM-0-10135-1 from the National Renewable Energy Laboratory (formerly the Solar Energy Research Institute), Golden, Colorado, between October 1, 1990, and March 31, 1991. Dr. Meir Carasso was the contract monitor. The study was performed by an interdisciplinary team centered in the MIT Energy Laboratory, as described in the body of the report. The authors would like to thank the numerous experts, listed in Section 2 of the report, for contributing their time and expertise. In particular, we acknowledge the contributions of Dr. John Haggerty to the areas of materials processing and ceramics, Prof. Roland Winston of the University of Chicago for arranging a visit to his facility, Mr. Zheng Chen of the MIT Energy Laboratory for literature searches and preparation of figures, Ms. Bonnie Santos and Ms. Mary Elliff of the MIT Energy Laboratory and Mr. Paul Stewart of the Chemistry Department for secretarial support, Ms. Hea Kyung Chung for preparing the final typed version of the project report, Ms. Barbara Johnson for help with figures, and other MIT Energy Laboratory personnel for assistance with contract administration and preparation of this report.

EXECUTIVE SUMMARY

The overall goal of this study was to identify new high-flux solar photon (HFSP) processes which show promise of being feasible and in the national interest. Electric power generation and hazardous waste destruction were excluded from this study at sponsor request.

Our specific objectives were:

- to survey pertinent information bases;
- to construct and assemble in prescribed electronic form a bibliography of relevant literature;
- to prepare an initial list of potentially promising HFSP applications;
- to define a set of criteria for evaluating potential HFSP applications;
- to carry out more detailed evaluations of some of the more promising applications;
- to provide recommendations on HFSP process applications indicating special promise;
- to discuss the status of current relevant research; and
- to recommend research needed to advance basic understanding of HFSP applications and to further their potential for practicality.

Our approach was to carry out the project with a core team of researchers providing expertise over a broad array of foundational topics, viz., chemical physics, optics, spectroscopy, photochemistry, high-temperature reactions, industrial chemistry, and chemical process engineering. Because of the wide range of scientific and engineering disciplines relevant to the study goals and the relatively short time available for the study, members of the core team carried out intense, round-table discussions with invited experts in a diverse sphere of pertinent disciplines, e.g., pure and applied optics, solar energy, furnace design, combustion, materials science and engineering, etc. Core team members conferred with experts at the Solar Energy Research Institute (SERI) (now known as the National Renewable Energy Laboratory, NREL) and the University of Chicago, and with participants in related studies being conducted by the National Academy of Sciences and SRI International, Inc. PC-compatible software was used to carry out an in-depth survey of post-1985 literature and to assemble in electronic form a bibliographic data base of important publications. Our approach emphasized the importance of delineating critical scientific and engineering foundations for identifying, evaluating, and discriminating among potentially promising options for HFSP applications. For example, limitations on solar photon intensity and wavelength and temporal variations in solar insolation impact process capacity, duty cycle, and controllability. Competition from alternative sources of intense photon fluxes was also considered in some detail. Formal economic and engineering cost estimates were outside our charter, but the study noted the importance of considering both conventional and externalized factors (e.g., environmental impacts, national security, global competitiveness, quality of fossil or other energy displaced) in determining overall costs of HFSP and competing options.

Our overall conclusion is that there is promise for new applications of concentrated solar photons, especially in certain aspects of materials processing and premium materials synthesis. Evaluation of the full potential of these and other possible applications (see below), including opportunities for commercialization, requires further research and testing.

Our specific recommendations are:

- **NREL should establish, at their Golden, Colorado, solar furnace site, a user research facility including a support program for extramural participation**. Drawing on previous models of DOE-funded user facilities, this NREL

operation would be a national resource to provide world class scientific and engineering foundations for proposed and yet-to-be identified applications of concentrated solar photons in research, materials and systems testing, and commercial processing. This extramural support program would be an incentive to user participation and would catalyze further innovations in solar photon applications. A wide variety of concentrators could be part of this facility to accommodate low-, medium-, high-, and ultrahigh flux requirements and multiple users. A corollary of this recommendation is that construction of large-scale demonstration facilities should await further research and evaluation at smaller scale. NREL can achieve maximum leverage in a season of limited resources, by avoiding large hardware programs, and by emphasizing the acquisition of sound scientific and engineering foundations to advance commercialization of HFSP.

- **Synthesis, processing, and testing of selected materials are among the most promising areas with potential for applications at larger scale**. In particular, further research and evaluation should be performed on:

  - synthesis of premium value products, e.g., certain fine ceramic powders and specialized carbon forms;
  - thin-film deposition of metals or inorganic compounds;
  - surface treatment of metals and alloys; and
  - materials testing for high severity environments, e.g., solar reactors, aerothermal protection and propulsion systems for space exploration and defense applications.

- **A research emphasis on high-temperature, high-intensity, photochemistry is highly recommended**. Such research could lead to significant new applications of concentrated solar energy.

- **Applications are also possible in more specialized situations because of pressing environmental considerations or unavailability of alternative energy sources**. Examples include recyling chemical process wastes to useful intermediates or starting materials; heat sources for Stirling engines for shaft power and pumped water storage in remote locations.

- **Drawing on the evaluation criteria developed in this and other studies, NREL should adopt and frequently update methodologies for systematic, continuing evaluation of candidate HFSP applications**. Such evaluations should take account of technical feasibility, economic tractability, competing solar and non-solar options, potential domestic and international markets, and less-traditional factors such as environmental impacts, reduced energy importation, and stewardship of national and global resources.

- **Detailed economic and technical analyses of a small number of preferred and more far-reaching candidate applications should be performed**. The process modeling and analysis tools described in Section 4 of this report may be used for such analyses.

- **High priority should be given to involving industry in identifying, refining, and developing new and improved applications for concentrated solar photons**. New opportunities for collaboration with NREL, e.g., hands-on testing

of new ideas at the proposed user facility, while protecting intellectual property rights, should be communicated to industry.

- **There is need to bring about increased awareness among the general public, industry, state and local governments, and the scientific and engineering research community, of the growing opportunities to participate in, and obtain external funding for, research and technology development in the field of concentrated solar energy**. We believe this will help enrich the intellectual base for new ideas and applications by reinvolving "old-timers" who had perhaps abandoned hope for significant support in this domain, and by attracting newcomers who will bring fresh perspectives to the field.

TABLE OF CONTENTS

LIST OF FIGURES

LIST OF TABLES

SECTION 1

INTRODUCTION

1.1 Background

The sun is the ultimate source of nearly all the energy we use on earth. Fossil oil and coal combustion, biomass, hydropower, wind power, tidal energy, human and animal muscular exertion -- all derive from the radiation reaching the earth from the solar reactor 93 million miles out in space. Only the relatively small amounts of geothermal, nuclear fission, and fusion energy released during the past several decades does not have a solar origin.

As we have come to recognize the many undesirable environmental, political, and economic consequences of intense utilization of secondary energy sources, particularly fossil fuel combustion, attempts to use effectively the primary energy source, solar radiation, have gained increasing impetus. One of the major limitations of solar energy use is that solar energy, while ubiquitous, is a widely dispersed and intermittent resource. The solar radiation flux reaching the earth's surface is approximately 1 kW/m^2, or about 0.95 Btu $sec^{-1}m^{-2}$. This value is an upper bound average, of course, which decreases substantially under overcast or nocturnal conditions. Many applications, such as propulsion engines, electricity generation, and thermal processing of chemical feedstocks and materials, require or function more efficiently at higher energy densities. Some sort of concentration of the available energy is therefore necessary for such applications. Fossil fuel combustion is itself a form of concentration, with energy harvested over millions of years of growth and decay being released in the few seconds required to oxidize the fuel in a furnace. It is only recently, however, that we have come to recognize the formidable, negative consequences associated with intensive use of fossil fuels, including resource depletion, global climate change, other environmental degradations such as acid rain, the human cost of coal and oil extraction, and the political and military conflicts arising from competition for control of these resources.

An alternative approach might be to use the solar energy available in "real time" by spatially concentrating the dispersed solar flux. Concentrated fluxes of solar energy could find beneficial applications in several areas of modern science and technology. While the full range of possibilities remains to be established, there is potential for significant impacts on several nationally important problems, such as hazardous waste management, synthesis and processing of high-technology materials, water decontamination, and development of new technologies for international export. Recent advances in solar concentrator technology at the National Renewable Energy Laboratory, (NREL) formerly known as the Solar Energy Research Institute, (SERI) (Carasso and Lewandowski 1990), and at the University of Chicago (Gleckman et al. 1989; Welford and Winston 1989; Winston 1991) have demonstrated the potential of very high flux density solar furnaces, capable of furnishing peak photon intensities of up to 50,000 times the natural solar insolation at the earth's surface.

With this capability in mind, NREL commissioned three separate detailed assessments of opportunities for applying concentrated solar photons to practical and scientific problems. The goals of these assessments are to suggest innovative, high-flux solar photon processes that show promise of being feasible and in the national interest; to identify potential technical impediments to promising applications; and to recommend research to help overcome those barriers. The present report is the result of one such study conducted by the MIT Energy Laboratory.

1.2 Objectives and Approach

The primary goal of this study was to identify new high-flux solar photon processes which show promise of being feasible and in the national interest. Additional goals were to identify barriers to effective use of concentrated solar photons and to identify research that could enhance the likelihood of realizing useful applications of this energy source. Our recommendations and conclusions, with supporting documentation, form the body of this report.

We specifically excluded detailed consideration of photovoltaic and solar thermal electricity generation and detoxification of hazardous waste, because those areas are addressed by other ongoing programs and studies. Particular emphasis was given to innovative photochemical technologies.

To accomplish these objectives, the project team undertook the following tasks:

- We surveyed the current state of knowledge in modern photochemistry to identify major U.S. centers of research excellence in disciplines directly relevant to utilization of concentrated solar energy. This was accomplished by interviewing a number of experts in the fields of solar energy, lasers, and photochemical processing, and carrying out a detailed literature search using electronic bibliographic software. The preliminary results of the screened search were provided to SERI on electronic media at the beginning of December, 1990, and a final version was delivered in early February 1991 (see appendix B).

- We sought to identify current and potential beneficial applications of high-flux solar photons for fundamental and practical problems. Particular emphasis was placed on science and technology that could affect pressing national issues such as manufacture of advanced materials and development of innovative chemical processing or other technologies with high export potential. An initial list of innovative processes was generated (appendix C), and a set of evaluation and decision criteria for screening and assessment of specific applications was formulated (Section 4).

- For each process identified as having high or moderate potential, we sought to identify technical barriers to the applications of high-flux solar photons specified above, and to recommend research priorities for overcoming these barriers. Discussions of specific applications, and the conclusions of our study, are presented in Sections 5 and 6 of this report.

The methodology we employed is described in Section 2. Following a review of the basic parameters characteristic of concentrated solar energy, and the identification of evaluation and decision criteria for assessment of specific applications, specific processes and applications showing potential promise are discussed. Finally, we present a set of recommendations for research and development in the utilization of concentrated solar energy.

SECTION 2

METHODOLOGY

To fulfil the study objectives, it was necessary to assemble and review critically a broad body of scientific and engineering information on optics, photochemistry, solar concentrators, photon-matter interactions, materials science and engineering, and chemical processing. Our approach was therefore to assemble a core study team representing broad expertise in several critical study areas, and to buttress that team by promoting succinct but intensive interactions with invited experts on a wide range of topics viewed to be particularly relevant to identifying novel applications for concentrated solar photons.

2.1. Project Core Team

The core team provided expertise in photochemistry, spectroscopy, optics, laser science and engineering, and in various aspects of chemical process science and engineering including high-temperature reactions and chemical engineering practice. The core team members, their areas of technical expertise, and their role in this project were:

Prof. Jeffrey I. Steinfeld: Professor of Chemistry, MIT, Project Principal Investigator. Areas of expertise include spectroscopy; chemical physics; molecular energy transfer; photochemistry; laser applications to chemistry.

Dr. William A. Peters: Principal Research Engineer and Associate Director, MIT Energy Laboratory. Project Principal Investigator. Areas of expertise include applied kinetics; fuels technology; industrial chemistry; thermal chemical reactions of condensed phase and fluid-solids media; environmental health effects of anthropogenic pollutants.

Prof. Jefferson W. Tester: Professor of Chemical Engineering, MIT, Director, MIT Energy Laboratory, Project Principal Investigator. Areas of expertise include geothermal energy; processing of wastes in supercritical water; chemical process engineering; applications of high-intensity lasers in hard rock drilling.

Mr. Howard Herzog: Research Engineer, MIT Energy Laboratory. Areas of expertise include energy conservation and end use management; process design and simulation; chemical process engineering; technologies for management of greenhouse gases.

Dr. Stephen Coy: Project Consultant. Areas of expertise include spectroscopy; laser science and engineering; pure and applied optics.

Mr. Michael Schlamp: Undergraduate student, Department of Chemistry, MIT. Project task was assembly, editing and updating of computerized bibliographic data base using Pro-Cite Software requested by SERI for use in this study.

Mr. Jeffrey Shorter: Graduate Student, Department of Chemistry, MIT. Project task was assembly and review of literature on potential applications of concentrated solar photons in the synthesis or processing of materials.

2.2. Invited Experts

To obtain up-to-date information on specialized topics, meetings of about one to two hours duration were held with experts invited from within and outside MIT. Prior to the scheduled date of the meeting, invited guests were sent written materials summarizing the

capabilities of the SERI Solar Furnace in Golden, Colorado, and the goals of the current study. After a brief oral presentation on the SERI Solar Furnace by Prof. Steinfeld, each meeting generally took the form of an open-ended round-table discussion in which guests and core team members exchanged comments on the potential applicability of solar furnaces to research or commercial problems in their areas of expertise. In these brainstorming sessions, potential opportunities as well as possible limitations and problem areas in equipment design, scale-up, or operation were discussed. Detailed notes were taken and later rewritten and typed up for the project files and for use in the project final report. These gatherings (Solar Seminars) functioned as a seminar in the neoclassical sense, and proved to be one of the most valuable sources of information for the project core team.

The invited guests and their affiliations and areas of technical expertise were:

Seminar 1: **Prof. Michael S. Feld, and Drs. Ramachandra R. Dasari, Irving Itzkan, G. Sargent Janes, and Richard Rava**, Harrison Spectroscopy Laboratory, MIT: pure and applied spectroscopy; laser science and engineering; optical devices and instrumentation; and practical applications of lasers.

Seminar 2: **Dr. John S. Haggerty**, MIT Materials Processing Center: laser synthesis of ceramics and other specialized materials; materials science and engineering; high-temperature processing; materials properties at high temperatures; and solar energy technology.

Seminar 3: **Prof. Hoyt C. Hottel**, Dept. of Chemical Engineering, MIT, and **Prof. Jack B. Howard**, Dept. of Chemical Engineering, MIT: solar energy; solar furnace design and scale-up; radiative heat transfer; combustion; fuels and energy technology; flame synthesis of carbon forms including diamondlike carbons and "buckminsterfullerene" C_{60} and C_{70} cluster structures; flame chemistry; coal and biomass pyrolysis; high-temperature reactions of solid fuels; and soot and polycyclic hydrocarbons formation in high-temperature processes.

Seminar 4: **Prof. Roy G. Gordon**, Dept. of Chemistry, Harvard University: solar energy including scientific research and commercial applications; Prof. Peter Langhoff, Department of Chemistry, Indiana University, Visiting Professor, Harvard University; solar photochemistry; and solar thermal engines.

Seminar 5: **Profs. Thomas F. Deutsch and Irene Kochevar**, Wellman Laboratories, Massachusetts General Hospital and Harvard Medical School: photomedicine, photobiology, and applications of lasers in medicine.

Seminar 6: **Prof. Adel F. Sarofim**, Department of Chemical Engineering, MIT: radiative heat transfer; solar energy; applied chemical kinetics; high temperature fluid-solid reactions; synergisms between thermal, photochemical, and catalytic processing; hazardous substances management; and formation and control of pollutant emissions.

Seminar 7: **Prof. Mark S. Wrighton**, Provost of MIT and Ciba-Geigy Professor of Chemistry: inorganic photochemistry; catalysis; photoelectrochemistry; surface chemistry; and molecular electronics.

Seminar 8: **Prof. Roland Winston**, Dept. of Physics, University of Chicago: design, operation, and application of solar concentrators providing ultrahigh solar flux densities. (Prof. Winston was an invited speaker in the Spring 1991 Modern Optics and Spectroscopy Seminar series.)

2.3 Interactions with NREL and with Other Studies

To facilitate further timely assimilation, communication and updating of study findings, the core team interacted with the SERI technical project officer, Dr. Meir Carasso. Three core team members visited SERI shortly after the startup of the project to consult with SERI scientists, engineers, and technical managers interested in solar concentrators and their applications (including Drs. J. Anderson, D. Blake, M. Carasso, J. Connolly, B. Gupta, S. Hauser, A. Lewandowski, T. Milne, L. Murphy, M. Nimlos, A. Nozik, R. Pitts, and M. Seibert), to provide an oral presentation on the scope and methodology of the then just starting project, and to view the SERI solar concentrator and related hardware and instrumentation facilities first hand. Approximately four weeks later, two core team members attended a workshop at SERI headquarters set up to brief members of a National Academy of Sciences study panel the Committee on Potential Applications of Concentrated Solar Photons. Similar to the current study, this panel was examining opportunities for promising applications of solar furnaces. Unlike the current study, hazardous waste detoxification was specifically included in their charter. Our core team members participated in several of the topical sessions at this workshop, including Introductory Plenary; Materials Processing and Synthesis; Plenary on European Perspectives; Solar Pumping of Lasers; Photochemical Synthesis; Advanced Research; and the Wrap-up Plenary With Reports From Individual Session Rapporteurs. Our team members spoke one-on-one with several experts in the field and met with members of a second and also independent study team from SRI International, Inc. Based on those interactions and a follow-on telephone conversation and letter, is was agreed that the SRI and MIT teams would carry out their studies independently with each team giving special, but by no means exclusive, attention to areas deemed to be particularly appropriate for them in light of their own technical expertise and access to other experts.

Two core team members also visited the laboratory of Prof. Roland Winston in the Dept. of Physics at the University of Chicago to view, first hand, Prof. Winston's specialized solar concentrators that provide, within selected dielectric media, solar flux densities exceeding 8 kW/cm^2.

2.4 Bibliographic Data Bases

The methodology employed in the construction of the bibliographic data bases can be clearly divided into two processes: (1) searching for/collecting of citations and (2) cleaning/sorting of citations. The searching and collecting involved the initial interactions with various outside information sources whereas the sorting and cleaning was carried out entirely within the Pro-Cite bibliographic management software program.

Although many citations arose independently in the course of the everyday work of the members of the project team, the majority of them were retrieved from the computerized Science Citation Index (SCI) available in the MIT Science Library. The search focused on material published between January 1987 and June 1990, although a fair degree of material from 1985 and 1986 was also reviewed. With the use of both chemical intuition and trial and error, a working set of criteria emerged, which, when used to search the SCI, yielded a great many pertinent citations. Each set of criteria produced a separate Pro-Cite data base - thus 14 existing data bases correspond to 14 distinct searches, with 2 data bases arising from sources other than the SCI (primarily an earlier Pro-Cite data base received from Dr. D. M. Blake at SERI). It should be made clear that the SCI limited itself to title searches only, and while it is conceivable that some relevant citations "fell through" our extremely broad net of criteria due to the phrasing of their titles, this was the only practical alternative and did in fact yield a rich variety of pertinent material.

The citations that were retained (some 6000 in all) were downloaded onto floppy disks and transferred directly into the Pro-Cite data base for review and sorting.

At this point, the gathered citations were scanned individually and critical decisions were made concerning their relevance for the next phase of review. In all, approximately 60% (or 3600) of those citations downloaded from the SCI were particularly relevant and examined in more detail. The remainder were immediately deleted. Some records that were retained were copied and moved to ensure that each citation appeared in all the Pro-Cite data bases to which it was relevant, and in only those to which it was relevant. Indeed, while most citations appear in the final collection of data bases only a single time, some of the more interdisciplinary material may appear two or even three times.

Appendix B contains a detailed description of the criteria used to construct each data base as well as a guide for efficient internal searching within Pro-Cite.

SECTION 3.
CHARACTERISTICS OF CONCENTRATED SOLAR ENERGY AND COMPETING TECHNOLOGIES

3.1 The Sun Itself

The sun is a main sequence star with approximately another 5 billion years of life before it becomes a red dwarf and expands radially outward to a point somewhere in the asteroid belt beyond Mars, evaporating the inner planets (Smoluchowski 1983). On this time scale, the only viable energy sources are renewable ones. Such resources should be developed as soon as possible, because many of the nonrenewable resources are much more valuable as chemical feedstocks than as fuels for combustion, and will be necessary during the long (or short) history of humanity.

The radiative energy density ρ at the surface of the sun may be calculated by the Stefan-Boltzmann law for a black-body (Richtmyer et al. 1955). The Stefan-Boltzmann law is

$$\rho = \sigma T^4$$

where $\sigma = 7.56 \times 10^{-15}$ erg/(cm^3 - deg).

In order to convert this energy density to a directional flux (e.g., kW/cm^2), ρ must be multiplied by one-quarter the speed of light. A factor of 1/2 is introduced to select energy propagating away from the sun from that propagating toward the sun, and the second factor of 1/2 is introduced in calculating the flux through an imaginary surface by averaging the velocity normal to the surface. The flux is then

$$F = A T^4$$

where $A = 5.666 \times 10^{-15}$ (kW/cm^2) / (deg^4).

Black body-fluxes for various temperatures are illustrated in Neugebauer and Becklin (1973). They are quite smooth, with each higher temperature exceeding the radiation from lower temperatures at all wavelengths. Absorption bands in the solar atmosphere modify the spectral distribution from that of a black-body and reduce the effective temperature when viewed from outside the earth's atmosphere. The actual temperature of the photosphere varies from about 6600 K to 4300 K over its 500- km depth. The effective temperature of the photosphere is estimated to be 5800 K giving 6.4 kW/cm^2 (Noyes 1976). Gleckman et al. (1989) give the flux at the sun's surface as 6.3 kW/cm^2, which corresponds to an effective black-body temperature of 5775 K.

The actual AM0 spectrum (air mass zero outside the earth's atmosphere) is reported by Thekaekara (1974) and shows more structure than the black-body curve, especially in the visible and ultraviolet (UV). The integrated solar flux above the atmosphere is known as the solar constant, and is given by Thekaekara as .1352 W/cm^2. Using the square law to calculate the flux at the solar surface from the solar constant gives 6.03 kW/cm^2, so that about 4% of the energy is absorbed in the sun's own atmosphere. Buhl et al. (1984) reported the effective solar irradiance at different air masses and zenith angles using two different computer codes for modeling radiative transport. They report total fluxes for AM1 (solar radiance through clear air at sea level) in the vicinity of 0.1 W/cm^2 for midday levels, decreasing to 0.07 W/cm^2 at zenith angles of 45 degrees. Thus concentrated solar

radiation of 10,000 suns corresponds to a total flux of 1 kW/cm^2, with the spectral distribution shown in Fig. 1.

The useful solar flux in any particular location is further reduced by clouds, haze, and smog, so that clear-sky locations and batch-processing applications are favored. Fig. 2 shows a sequence of solar flux records for Cambridge, Massachusetts, illustrating the types of intermittency that occur in a non-ideal location. Superimposed on the normal diurnal variation are fluctuations from passing clouds or other obstructions. On two out of the five days, the available solar flux is reduced to nearly zero by overcast conditions. Even on a bright but hazy day [trace (f)], direct sunlight reaching the photoreceptor (equivalently, a primary concentrator) is degraded by up to a factor of 3.

3.2. Concentration of Solar Energy

3.2.1 Theoretical and Practical Limits in Solar Furnace Design

In this section we consider both theoretical and practical limits to flux levels that can be achieved with a solar source, with emphasis on estimating practical working fluxes. Non-imaging concentrators are sometimes seen as the answer to all requirements for collection and concentration of solar radiation, necessarily providing a dramatic increase in available solar fluxes. In fact, non-imaging concentrators, even though they may attain very high fluxes exactly at the concentrator exit, become comparable to imaging systems when the focus is at significant working distances from the concentrator. This limitation may be especially important to material processing applications. We examine the specific requirements of concentrators: high concentration in air, high concentration in dielectric materials, and good collection efficiency.

3.2.1.1 Maximum Concentrations in Air

The thermodynamic limit, or, equivalently, the limit from geometric optics, for concentration in a material with index of refraction n=1.0, is (Bassett et al. 1989)

$$C_{max} = \sin^2 \Theta' / \sin^2 \Theta$$

where Θ' is the maximum angle from the normal of radiation striking the target and Θ is the maximum angle from the normal to the collector aperture of incoming radiation. The highest concentrations are achievable for hemispherical illumination of the target, corresponding to $\Theta' = 90^0$. The important number in determining the peak concentration is the f number: the ratio of the object distance to the final aperture diameter for a non-imaging concentrator, or to the collection diameter for imaging systems. Practically achievable lens systems are limited to f numbers of 0.5 to 1.0, providing maximum concentrations about a factor of 4 lower.

Hemispherical illumination of the target corresponds to a target placement in the exit plane of the concentrator. With any optical system, the closer the object, the higher the possible magnification. It is this ability to concentrate very close to the concentrator itself, and to illuminate from all directions of a hemisphere, that accounts for the greater peak concentrations achievable with non-imaging optics. It is also this requirement that limits the usefulness of the fluxes achieved because ablation of the target may destroy the

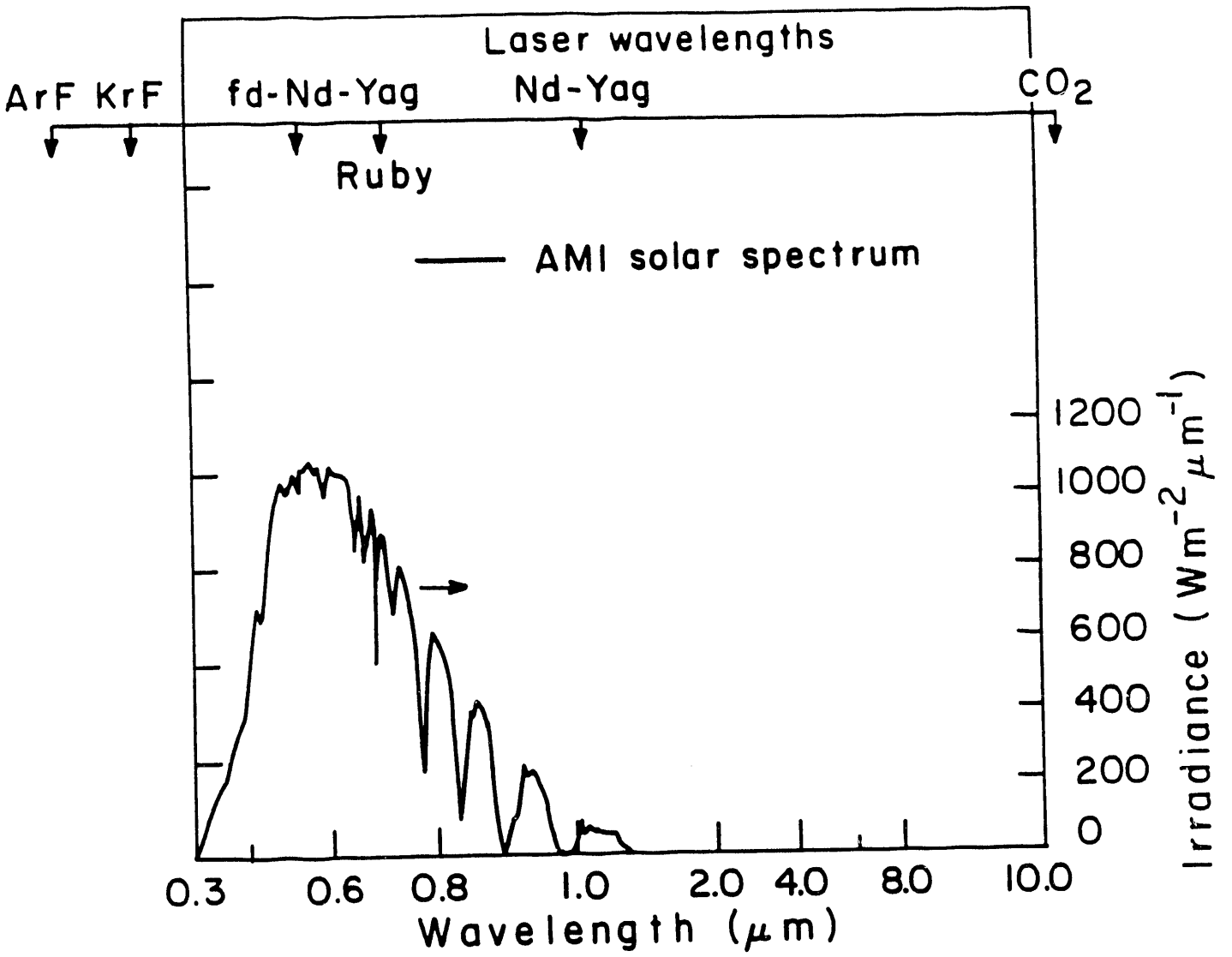

Figure 1. Standard AM1 solar spectrum and wavelengths of various lasers.

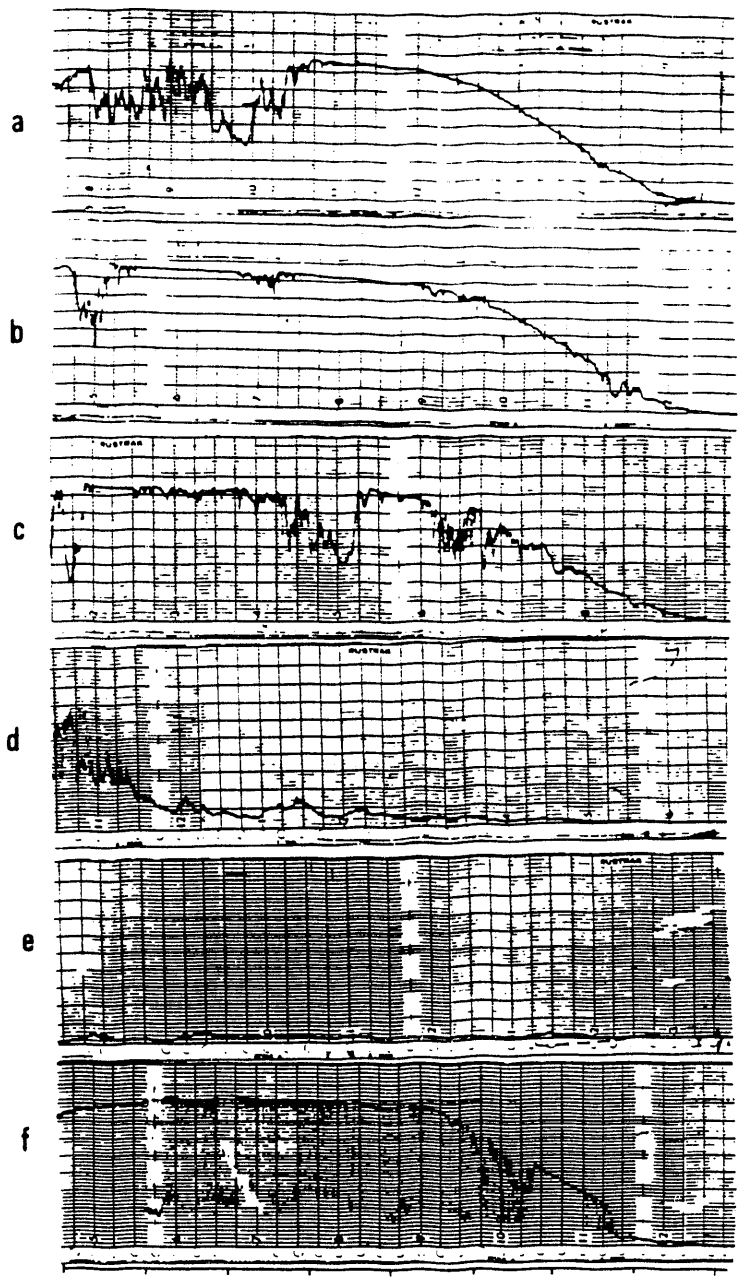

Figure 2. Variation of solar flux intensity. These traces record the short-circuit current from a silicon solar cell mounted on the roof of an MIT building in Cambridge, Massachusetts, at a fixed south-facing position approximately 45° from horizontal, between 8:30 a.m. and 5:00 p.m. Traces a - e were recorded in a consecutive five-day period in early February, 1991. Variations caused by solar aspect and passing clouds are readily apparent, as is the essentially complete unavailability of the solar source on two overcast days, d and e. Trace f, recorded on an earlier day, shows the effect of haze or high, thin clouds. Although the average brightness is high, the receiver sees high-frequency fluctuations with a modulation depth of more than 70%. These traces were provided by Mobil Solar Energy Corp. of Billerica, Massachusetts.

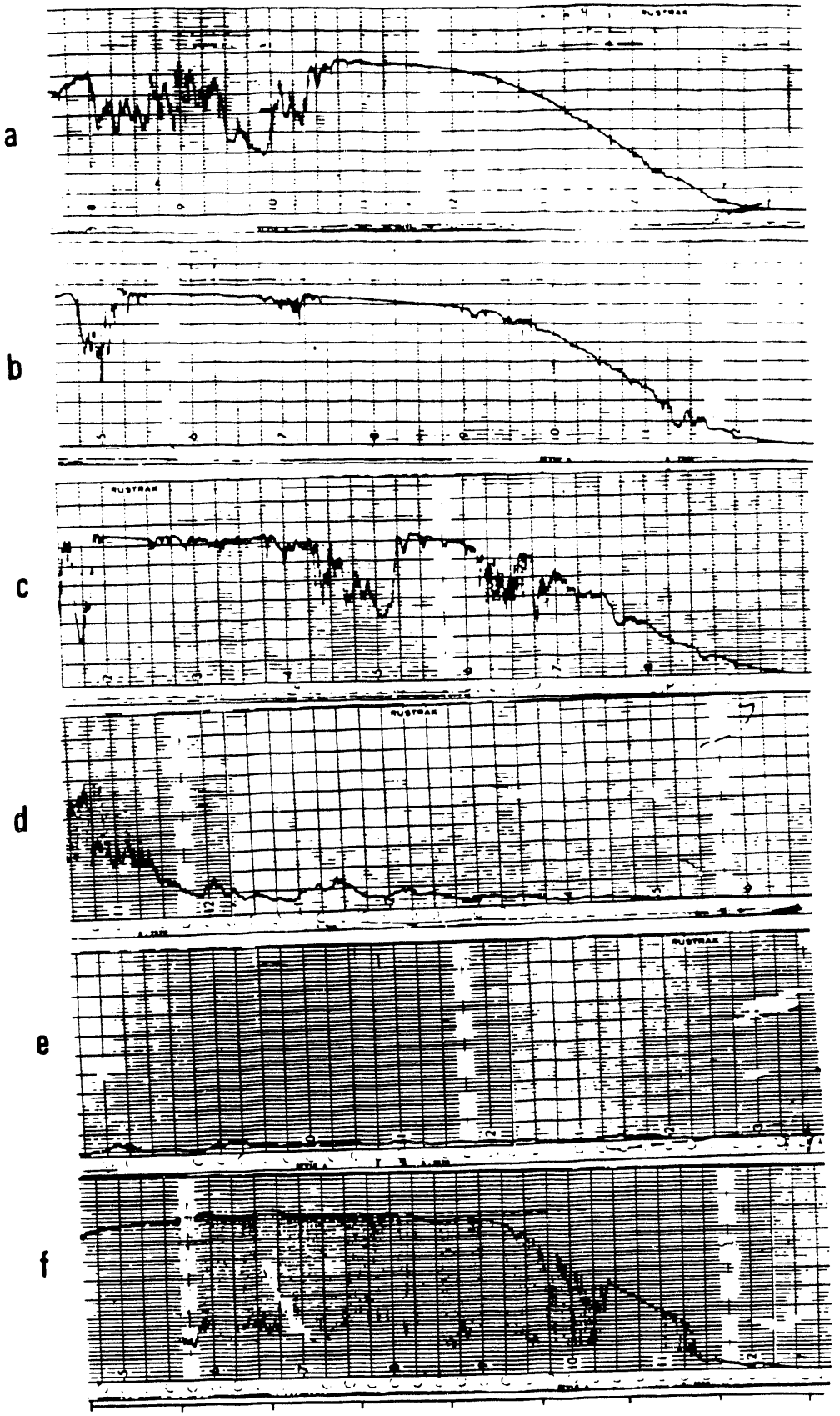

Figure 2.

concentrator, and the target cannot be isolated. Imaging and non-imaging optical systems will provide similar concentrations at target distances within the capabilities of imaging systems. Peak achievable concentrations in air are computed using eqn. 2.4 in Bassett et al. (1989), the fundamental theorem in non-imaging optics, which is given above. Concentrations for a paraboloidal reflector are computed from Winston (1991) and are computed only for target illumination angles up to 45° off axis, which give the highest concentration. Both are given in the Table 1.

Table 1. Concentration Ratios for Various Reflectors

f number	C_{max} (ratio in air)	$C_{max}/C_{max}(f=0)$	Paraboloidal
0.00	44000.	1.00	not feasible
0.25	35200	0.80	" "
0.50	22000	0.50	" "
0.71	14667	0.33	11000
0.75	13539	0.31	10864
1.00	8800	0.20	8250
1.8*	3152	0.072	3133
2.0	2588	0.059	2578

(*NREL primary concentrator value)

The peak value, 44000, is equal to the square of the ratio of the earth-to-sun distance to the radius of the sun. The average earth-to-sun distance is 146.9 x 10^6 km, and the radius of the sun is approximately 0.7 x 10^6 km. The maximum concentration, C_{max}, gives the limit to the ratio of concentrated-to-unconcentrated sunlight determined by geometric optics or, equivalently, by combined application of the first and second laws of thermodynamics. The peak intensity in kW/cm^2 depends on the local insolation, which varies with air mass, humidity, etc.

In some cases, a primary dish concentrator designed for f=0.75 or f=1 may provide higher useful flux on target than a primary/secondary combination designed for a large object distance. This is in spite of the fact that a standard parabolic reflector has sufficient optical distortion (coma) that low f numbers do not achieve the theoretical concentration. Longer focal lengths have the additional advantage of making axial placement of the target less sensitive.

3.2.1.2 Maximum Concentrations in Dielectric Materials

The sizes of images formed inside a dielectric material are reduced in each dimension by n, the index of refraction of the material. This reduction may be viewed as a result of the reduction in wavelength, which occurs inside a dielectric, and may be derived using the conservation of radiance (Bassett et al. 1989).

Thus, C_{max} is higher within a dielectric by a factor of n^2 on a surface, and n on a line than it is in air. This increase is not specific to non-imaging systems. Concentrations achieved inside a dielectric cannot propagate outside and exceed the theoretical maximum in air because of the variation of the critical angle for total internal reflection with the index of refraction of the dielectric; the required fraction of the flux is internally reflected at the

boundary. Similarly, a dielectric black-body cavity cannot be heated to a super-solar temperature because its energy density is higher by n^3 than an empty cavity at the same temperature.

Indeed, concentrated solar energy coupled to a dielectric material can reach the highest possible concentration only if the concentrator has the same dielectric constant and is coupled directly to the object.

3.2.1.3 Collection Efficiency

The methods of non-imaging optics provide design principles that build in efficient collection of solar radiation. Nonetheless, imaging systems, including refractive or reflective systems, are able to collect incoming radiation with the same types of efficiencies, limited by the reflection at surfaces or absorption losses in materials.

The requirement for a significant concentrator-to-object distance appears to limit the peak working solar flux to values in the 2000 to 5000 sun range for primary concentrators, and to the 10,000 sun range for combined primary/secondary systems.

3.2.2 Capabilities of the NREL Solar Furnace

3.2.2.1 Concentration Parameters

The NREL Solar Furnace consists of a tracking heliostat of 38 m^2 that fills a primary concentrator of 12 m^2. The NREL primary concentrator was designed with a relatively high f number of 1.8 for a theoretical maximum concentration ratio of 3133 in order to minimize optical aberration of the off-axis paraboloidal design. Because values of 2300 suns have been measured, the primary concentration is achieving 73% of the theoretical level, which is consistent with reflectivity losses. This efficiency value assumes that the 2300 value quoted by A. Lewandowski of NREL is a concentration ratio rather than a total flux value based on a nominal insolation of 1 kW/m^2. Much of the UV in the solar spectrum is preserved because of the use of front-surface aluminum mirrors. The primary provides a Gaussian-profile beam of 9 kW total power, with about 6 kW centered in an area of 88 cm^2. The wavelength distribution between 300 and 2500 nm is shown in Fig. 1.

A secondary concentrator available at the NREL Solar Furnace was designed specifically to match the primary. Its input aperture is 6 cm and the output is 1.4 cm, for a reduction in area of about 18. The target location is in the output aperture plane. It has achieved an enhancement of the flux from the primary of about a factor of 10, reaching 21,000 suns. This value is 48% of the maximum theoretical value in air.

Table 2. NREL Solar Furnace Specifications

Heliostat	38 m^2, planar front-surface aluminum mirrors
Primary	12 m^2, front-surface aluminum mirrors, off-axis paraboloid constructed from segments
Secondary	Ag-coated, water-cooled Cu-Te alloy with an output aperture of 1.4 cm
Fluxes achieved	
Primary alone	Gaussian beam, 9 kW total power 2300 suns peak power, 8 kW in 88 cm^2
Primary and Secondary	21,000 suns, hemispherical illumination of a 1.4-cm. diameter area.

3.2.2.2 Heating with the NREL Solar Furnace

The temperatures achievable with a given energy flux depend on the absorptivity and emissivity of the target, and their match to the incoming spectrum. For a target that is a small opening in an ideal black-body cavity, Table 3 gives equivalent temperatures at different flux levels.

Table 3. Equivalent Temperature at Different Flux Levels

Concentration	Flux, kW/cm^2	Equivalent Blackbody T,K
100	0.01	1153
500	0.05	1724
1000	0.1	2050
2000	0.2	2440
5000	0.5	3065
10000	1.0	3645
15000	1.5	4034
20000	2.0	4334

3.2.2.3 Heating Rates

Radiation provides surface heating that must propagate inward by conduction or be carried away by radiation, evaporation, or pyrolysis. Solar radiation at the 1000-sun level provides a heat flux of 100 W/cm^2, which can in principle provide heating rates in the 10^6 °C/sec. range for small particles. In discussing the heating rate and its effects on the chemical or physical transformation of condensed phase media, it is important to specify what fraction of the total volume of the workpiece is undergoing rapid heating and to determine whether or not spatial or temporal variations in the temperature field within the sample are exerting significant effects on reactivity or other desired behavior (e.g., annealing). Hajaligol et al. (1988, 1991) discuss quantitative approaches in this regard, with particular reference to effects on the global kinetics of the rapid pyrolysis of solids such as coal and cellulose, and identify several other studies pertinent to this topic.

In particular, Hajaligol et al. (1988) noted that time and spatial temperature gradients within pyrolyzing coal particles can exert strong effects on devolatilization behavior including apparent pyrolysis kinetics. In response, they mathematically modeled transient and spatial nonisothermalities within a single, spherical coal particle undergoing pyrolysis, with temperature-invariant thermal and physical properties. Analyses were performed for two surface heating conditions of practical interest, a constant rate of increase in surface temperature, and a constant surface heat flux density. The treatment provides three distinct time-dependent indices of heat-transfer effects by quantitatively predicting the extent of agreement between (a) center-line and surface temperature (i.e., the classical index based on spatial gradients in temperature alone), and between (b) volume-averaged pyrolysis rate [or (c) volume-averaged pyrolysis weight loss], and the corresponding quantity calculated by using the particle surface temperature for the entire particle volume. Regimes of particle size, surface heating rate or surface heat flux density, and reaction time, where particle "isothermality" according to each criterion (a-c) is met to within prescribed extents, were computed for conditions of interest in entrained gasification and pulverized-coal combustion, including pyrolysis under nonthermally neutral conditions. The concept of distinct, "non-isothermality" indices for temperature, for rate, and for conversion can in principle be extended and applied to any condensed phase system of interest for processing in solar furnaces. The rate and conversion indices were intentionally formulated to take account of the effects of spatial and temporal variations in sample temperature on conversion rates and conversion itself. Thus, they may prove more useful in evaluating how sample temperature variations can be expected to impact reactor sizing, process control and operability, and practically attainable yields of desired products.

Applications of this analysis to interpretation of the global kinetics of pyrolysis of cellulose sheets of different thickness led Hajaligol et al. (1991) to some further conclusions especially relevant to understanding effects of the ultrahigh (surface) heating rates attainable with solar concentrators. Their study predicted, for rates of change of surface temperature on the order of $10^5 \sim 10^6$ ^{o}C/sec (by endothermic reaction of the substrate, or by high external insolation under thermo-neutral conditions), the existence of a second domain of sample non-isothermality where heat transfer into the sample and near-surface chemical reaction become essentialy decoupled, at least temporarily. Under these conditions, the chemical reaction is confined to a surface layer too thin to support significant temperature non-uniformities and pyrolysis (or other reactions) occur virtually free of heat transfer limitations. In practice such conditions might well arise in some applications of solar concentrators, e.g., during pyrolysis of very reactive, low thermal conductivity materials and in so-called ablative pyrolysis of solids.

The above analyses of Hajaligol et al. (1988, 1991) are a useful starting point for estimating solar-concentrator-derived values of heat flux densities for which significant effects on sample non-isothermality can be expected.

3.3 Costs and Characteristics of Radiative Sources

Radiative sources for rapid heating, materials processing, and chemical production include arc lamps, pulsed excimer, pulsed and c.w. CO_2 and YAG lasers, as well as the solar furnace. For comparison with the commodity chemical costs in appendix A, we sought to obtain estimates of the costs associated with various radiation sources. We find that the cost of solar photons is quite competitive with that for arc lamps for batch applications, based on the analysis of Kolb (1990), and with CO_2 laser sources, and is lower than the cost of laser-generated UV photons in the solar wavelength regime.

3.3.1 Cost of Solar Photons

In order to compare solar concentrator costs with costs from other sources on a common basis, a levelized approach was used. The methodology is consistent with Kolb's (1990) economic analysis of a 100-kW arc lamp system. Total direct capital costs are scaled using a constant factor to estimate indirect costs associated with installation. Annualized costs are then estimated using an annual fixed charge rate multiplied by total direct and indirect costs. Annual operating costs are then added to obtain total annual cost. Levelized costs are then determined by dividing these annualized costs by the useful energy delivered to the target during one year of operation. The final result can be expressed in dollars per kilowatt-hour thermal, dollars per gigajoule(GJ), dollars per mole of photons, or some other equivalent unit.

A wide range of levelized costs for solar photons have been reported. The stated values range over a factor of 200. We discuss three recent estimates below. For comparison with other energy sources, and with previous economic analyses, we examine both the cost per energy unit and the cost per mole of photons. The energy content of radiation is given by

$$E_{N0} = N_0 h\nu = N_0 hc/\lambda = (119624/\lambda\,(\text{nm}))\ \text{kJ/mole}$$
$$= (33.229/\lambda\,(\text{nm}))\ \text{kWht/mole}$$

At the approximate peak of the AM1 solar distribution near 550 nm, this formula gives 217.5 kJ/mole.

Approximately 30% of the solar photons in the AM1 spectrum (see Fig. 1) in terms of number density are between 300 and 700 nm. This number is a lower limit to the fraction of the solar energy appearing in that range because the remaining energy is in the infrared (IR). We thus estimate 50% to be a reasonable energy fraction for the 300-to-700-nm range, with the remaining energy in the IR.

At the November 7-8, 1990, NAS/NRC meeting, E. Bilgen gave the lowest recent cost values, estimating the cost of high-temperature solar heat at \$1 to \$3/GJ from dish systems and \$5 to \$10 /GJ for central receiver systems (Hammache and Bilgen 1988).

Based on those references, the cost in \$/mole of solar radiation between 300 and 700 nm is approximately, for dish collectors, 0.0002175 x (\$1 to \$3) / 0.5 = \$0.000435 to \$0.001305/mole, and for central receivers, \$0.002175 to \$0.00435/mole. If we assume that the average wavelength of the IR available in the other half of the spectral energy is about 1100 nm, then the costs of IR are about half of the values given above per mole of photons.

The data in M. Carasso's letter of September 1990 give an installed cost of \$400 to \$500 /kWt (kilowatt thermal) of high-temperature solar heat at the 1000 sun-level. To this figure must be added an estimate of the system lifetime, maintenance costs, and duty factor. Lifetimes in the 10-to-20-year range, with maintenance costs about 10% of the installed cost per year, give values near \$10/GJ. A comparison of the economics of solar furnaces and arc lamps in the 1000-to-5000-sun range (Kolb 1990) gives higher figures. In particular, his lower bound on the installed cost of a 48-kW (target energy) furnace is \$6312/kW, and a levelized energy cost is quoted of approximately \$0.75/kWht (kilowatt-hour thermal) for 4 hours operation per day (typical electrical costs are \$0.10/kWh). This corresponds to \$208/GJ of energy delivered on target, or \$0.042/mole of photons for a nominal wavelength of 600 nm. If only a portion of the total solar spectrum is actually

utilized in a process, then the cost for that portion is correspondingly higher. For example, levelized costs are estimated as:

- $0.091/mole in the 300-to-700-nm band (center 550 nm)
- $0.045/mole in the 700- IR band (center 1100 nm)

The available estimates of the cost of solar photons vary by a factor of 200, from high to low.

3.3.2 Cost of Arc Lamp Photons

The source closest in character to the solar spectrum is the Vortek arc. It is an electrically driven, compact, high-intensity source that attains temperatures in the arc itself of more than 10,000 K, hotter than the sun's surface. It has been used for the pumping of high-power YAG lasers, and a variety of materials processing applications.

G. Kolb of Sandia National Laboratory has presented an economic analysis (Kolb 1990), which indicates that a dedicated solar furnace for batch processing applications is approximately equal in levelized energy cost to the Vortek arc for processes requiring 1000-sun fluences and 4-hours-per-day operation. For fluences at the 5000-sun level, the economics more strongly favors the solar furnace. Assuming an average emission frequency of 500 nm (0.06646 kWh/mole) the costs are:

- at 1000 suns -- $1.3/kWht or $0.086/mole
- at 5000 suns -- $2.2/kWht or $0.146/mole

A primary system alone at a solar furnace is capable of providing levelized power at the 1000-sun level. Levelized power at 5000 suns requires a secondary concentrator. A secondary concentrator can be designed with a useful concentrator-workpiece distance and still achieve enough excess power to operate at a constant 5000 suns.

Disadvantages of the solar furnace discussed by Kolb include the need to modify or redesign existing buildings to couple the solar power to the processing line. The primary advantages of this energy source include little or no need for external electrical sources, no need for cooling water, lower operating and maintenance costs, and higher concentrator-to-target distances.

3.3.3 Cost of Laser Photons

Woodin et al. (1990), give $10 to $70/mole of 193-nm photons from an excimer laser (incorrectly identified as a KrF laser rather than an ArF laser). They give two conflicting values for the cost of CO_2 photons. A direct cost of $0.10 to $0.50 /mole for CO_2 photons is given, but they also quote a value of $11.40 /kWht for CO_2 photons, corresponding to $0.038/mole. The presentation by W. Short dated November, 16, 1989, on a comparison of solar furnace costs versus c.w. CO_2 lasers, gives a a levelized cost of about $5/kWht for CO_2 laser energy, a still lower cost.

Although the Woodin et al. values for UV photon costs may be somewhat high, earlier versions of Fig. 3 showed unrealistically low costs for excimer lasers as primary sources, perhaps supplied by a laser salesman of that era. It is now recognized by workers in the field that excimer lasers are more expensive than other primary laser sources, and are at

least comparable to costs of Nd-YAG-pumped or flash-lamp-pumped dye lasers (secondary sources).

3.3.4 Cost of Product Processed by Photons

The cost estimate from Woodin et al. (1990) of $10 to $70/mole of UV photons is considerably more expensive than the cost of solar photons given above, even considering the 2.85 ratio between the energy of ArF photons at 193 nm and the solar peak at about 550 nm. Table 4 and Figure 3 compare the costs of photon energy from various sources, normalized to a common basis of dollars per gigajoules energy delivered.

As Woodin et al.(1990) note, quantum yield is the key parameter in translating the $0.091/mole quoted above for solar photons into dollars per pound of processed material. For example, assuming a quantum yield of 1 and a molecular weight of product of 100, the cost of solar photon energy per pound of product is

$$\$0.091/\text{mole} \times 1/100\ \text{mole/g} \times 453.6\ \text{g/lb} = \mathbf{\$0.41/lb.}$$

Industrial processes involving chain reactions or catalytic effects would reduce this cost by the ratio of the quantum yield.

Table 4. Photons -- Their Energy and Cost

	E_0 (kJ/mole)	Cost ($/mole)	Cost ($/GJ)
Broadband sources			
Solar furnace 1000 - 5000 suns (600 nm center wavelength)	200	0.042	208
Vortek arc 1000 suns	239	0.086	360
5000 suns	239	0.146	610
CO_2	.12	0.03	2,500
Nd:YAG (1064 nm)	112	3.94	35,000
Alexandrite (720-800 nm)	158	4.05	40,000
Frequency-doubled-YAG (532 nm)	225	15.75	70,000
Pulsed dye (600 nm, YAG-pump)	200	46.00	230,000
Argon ion	250	13.75	55,000
ArF excimer	620	40.00	64,500
Solar-Pumped Lasers			
Nd:YAG	112	1.80	16,000
Dye (600 nm)[a]	200	2.20	11,000
Cr:Nd:GSGG[a]	112	1.12	10,000

[a] Under development by R. Winston, University of Chicago. We thank Prof. R. Winston for providing these data.

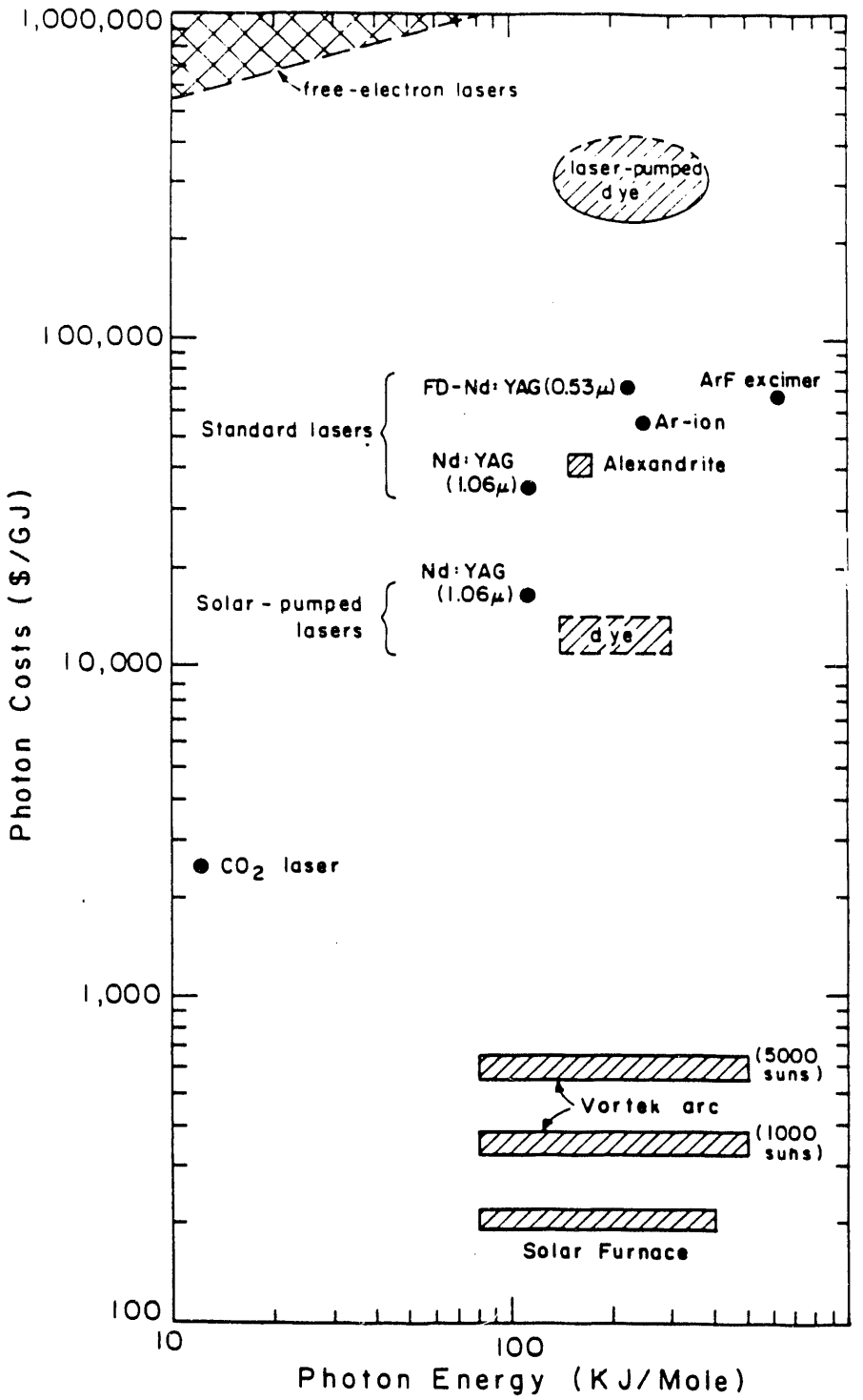

Figure 3. Relative costs of photon energy from various sources.
Adapted from a figure by Dr. J. Yardley (Allied Signal Corporation), which originally appeared in J.I. Steinfeld et al., Laser Photochemistry and Diagnostics: Recent Advances and Future Prospects: Report on an NSF/DOE Seminar for Government Agency Representatives (June 1979).

SECTION 4

EVALUATION AND DECISION CRITERIA

We developed two complementary sets of criteria for screening potential innovative processes for beneficial utilization of concentrated solar energy. We identified those processes showing the greatest promise, and specified the research required for understanding the basic mechanisms involved in the process and for possible eventual demonstration of technical feasibility. These criteria are grouped as *scientific and technical feasibility*, and *economic and practical considerations.*

4.1 Scientific and Technical Feasibility

In attempting to assess the technical feasibility of suggested applications of concentrated solar energy, we first considered whether an existing, identified application for photon energy could be done *better* with concentrated solar energy than with alternative sources, such as conventional process heat, laser sources, or arc lamps. By "better", in this context, we mean one or more of the following:

- increased efficiency gained by using the solar source;
- higher throughput;
- decreased side products and/or undesired effects; and
- reduced fossil energy consumption per unit of product.

In Section 3 we summarized comparisons that have been made among concentrated solar energy and arc lamps (such as the Vortek arc) and laser sources for thermal processing, specifically, the CO_2 laser. Several general conclusions can be drawn from these comparisons. First, even though the solar source will always consume less fuel than lasers and arc lamps for a given amount of energy delivered to the source, the economic cost of that energy is by far the smallest component of the overall process cost. As discussed in Section 4.2, the capital cost of the solar concentrator is the determining component for any process.

The second general conclusion is that any gain in throughput or efficiency resulting from the bandwidth and/or light flux advantages of the solar source must be prorated over the limited availability of the source resulting from diurnal cycles and atmospheric fluctuations. This is discussed further in Section 4.2.

A more exciting set of possibilities, which are a major focus of this report, would exploit the *unique* features of concentrated solar energy for *new applications* or *new process chemistry.* These features include

- availability of combined thermal (infrared heating) and photon (visible and near-UV) energy from the same source;
- high flux in the near-infrared region of the spectrum;
- rapid heating of irradiated materials to ca. 4000 K;

- large bandwidth of simultaneously available photon energies; and
- lack of coherence, as contrasted with laser sources.

In Section 5 we describe a number of possible processes in a variety of application areas that may benefit from these unique features of the solar source. In doing so, we have tried to make some assessment of the risk of failure and chance of success for a particular process to prove feasible, and to assess the required level of development effort that may be necessary for proof-of-concept at a commercially relevant scale. Such judgments are difficult and subjective at best, however, and can rarely be projected with success before the research is actually carried out.

4.2. Economic and Practical Considerations

Detailed costing and economic evaluations of concentrated solar furnaces and/or their process applications are outside the scope of the present study. However, these analyses would need to be made at some point in the development cycle of technically encouraging processes, and ample written (e.g., Perry et al. 1984, Peters and Timmerhaus 1980) and software resources (Aspen Tech 1990; SRI 1990) are available for quantitative process cost estimating. There is value here in discussing qualitatively, how economic and related constraints may be expected to impact the selection and development of different options for viable commercial applications of concentrated solar photons.

4.2.1 Qualitative Cost Considerations

Simplified economic evaluations divide total process cost into capital charges (the cost to borrow and pay back over a prescribed period, the money needed to purchase major items of equipment, real-estate, buildings, etc.), operating charges (the costs to actually run the process, e.g., labor, maintenance, expendable supplies, feedstocks), and process utilities, e.g., energy to run the process. Compared to alternative technologies such as lasers or arc lamps, solar furnaces offer economic advantages in the energy component of their operating costs since the input energy is free. For lasers and arc lamps one must consider the cost of electricity C_E and the efficiency with which the device converts electrical energy to photons (η_{EP}) to obtain the comparable energy component of the cost of photolytic energy C_p:

$$C_p = C_E / \eta_{EP}$$

Of course, the other operating costs of each device must also be accounted for, i.e., labor, maintenance, etc. Solar furnaces may also offer economic advantages in these categories under certain circumstances, e.g. when the competing candidate hardware is unusually sensitive to environmental and other operating factors and thus very costly to maintain and operate continuously.

Capital costs offer special challenges for solar concentrators because diurnal variations, and shorter term fluctuations arising from clouds, storms, etc. change the available solar flux density, as shown in Fig. 2. Near maximum daily solar insolation is typically available for only 2 to 3 hours before and after 12:00 noon, i.e., for about 4 to 6 hours per day. If a furnace and process are sized to utilize essentially 100% of this near-peak intensity, steady operation will thus be limited to about one-fourth to one-sixth of each day. Capital amortization charges accrue to manufactured product cost as a quotient of the plant capacity factor -- simply stated the higher the daily output per unit of capital invested, the lower the

impact of capital charges (essentially interest) on the cost of the product and hence on the marketplace competitiveness of the process of interest. Because of these lower capacity factors, capital charges per daily unit of output from the solar concentrator must be multiplied by factors of 4 to 6, or the capital cost of the plant must be amortized over periods four to six times shorter than those of other processes. Particular attention must be given to processes where the solar concentrator accounts for a relatively small fraction of the total capital cost. In this case, the relatively short duty cycle of the concentrator is holding captive the rest of the process capital. These considerations will not necessarily render solar-furnace-based processes economically non-competitive, but they must be carefully accounted for even at relatively early stages of examining the benefits and trade-offs of each process option.

An additional cost-related factor is that the maximum solar insolation S is inherently limited to about 1 kW/m^2 at the earth's surface. This means that per unit area of primary collector there is a maximum energy available for useful applications. This energy collection capacity of the collector will in turn set an upper bound on the capacity per collector area of the intended process application. If the solar energy required to manufacture a pound of product from the process is E_S, the process capacity C per unit collector area is given by

$$C = S/E_S$$

in units of for example, pounds per square meter of collector area. Because the quantity S is fixed, the "unit capacity" (pounds per unit area of collector) of solar furnace processes will depend on E_S. Products requiring significant added energy for manufacture (high E_S values) will be attainable in lower unit capacity. However, some of these products (e.g., fine ceramic powders) are of high commercial value and may command selling prices that will offset capital and operating costs of the solar furnace. As discussed below, high value added products require much smaller markets to break even. Thus, trade-offs in process capacity due to available solar furnace capacity, market requirements, and product selling price must be carefully evaluated in reaching decisions on the potential viability of a process based on use of a solar concentrator.

4.2.2 Related Operational Issues

The duty cycle variations of solar furnaces may also impact strategies for the design, operation, and control of solar concentrator processes. Systems must be designed to detect and respond to short-term variability in delivered photon fluxes, e.g. by adjusting optics, process feed rates, or workpiece dimensions or exposure time. Effects of both underpowering and overpowering on process dynamics must be understood, in turn requiring knowledge of the rates of key chemical reactions and of heat transmission to and within workpieces. For example, excessive attenuation of incoming solar flux may slow process rates or even terminate operability. Excessive heating may produce undesired effects including workpiece degradation by ablation, or by generation of unwanted side products. These effects may become especially critical in processing small workpieces with insufficient thermal inertia to dampen fluctuations in incoming solar power. Small workpieces generally have short thermal response times and hence will require process control systems capable of detecting and correcting for modifications in delivered photon flux densities in times that are shorter than the thermal response time of the workpiece.

4.2.3 Analysis Tools

There are many commercially available software "tools" to help analyze the technical and economic merits of proposed new processes. The most important type of software program is a process flow sheet simulator. ASPEN PLUS (Aspen Tech 1990), marketed and maintained by Aspen Technology, Inc. of Cambridge, Massachusetts, is one such simulator that is widely used by industry and academia in the United States and abroad. The original development of ASPEN PLUS was carried out by the MIT Energy Laboratory's ASPEN Project from 1975-1981 under sponsorship from the U.S. Department of Energy (DOE) and industry.

A simplistic view of a generic chemical process is shown in Figure 4. At its heart is a chemical reaction, which in the present context would involve the solar furnace. The reaction products usually need to be separated and/or purified before they are sold. Further, the process should be integrated to use energy and materials efficiently, for example, by designing and operating heat exchanger networks for efficient heat recovery. Finally, process utilities are required to provide heat, power, cooling, etc., to the appropriate process operations (e.g. distillation). A process simulator helps a user model this entire complex system, and to easily compare different process options (e.g. equipment configurations and operating conditions) and by these means to select a final design that is both technically and economically sound.

Figure 5 shows that at the core of a flow sheet simulator is a set of mathematical models that are used to solve the problem specified by the user. The user must input pertinent information about the process such as defining the unit operations and unit processes to be modeled, describing how these unit operations and processes are connected together, and specifying the process inputs. For example, in ASPEN PLUS, this may all be done graphically and through pop-up forms. The results generated by the simulator include heat and material balances, equipment performance parameters, and, if desired, an economic evaluation of the process. By running case studies and sensitivity analyses, the user can select the best design from among several prescribed alternatives, and begin to optimize that design. ASPEN PLUS also gives the user flexibility to add new models to the system, such as a solar furnace model.

While a flow sheet simulator is good at modeling and improving an existing flow sheet, it relies on the user to synthesize the original design. New tools are now becoming available to assist in synthesis of the process itself. One such tool is ADVENT (also marketed and maintained by Aspen Technology), which is based on a technique called "pinch technology" (see Karp et. al, 1990 for a detailed discussion). Pinch technology allows the design engineer to set process energy targets a priori and then guides the engineer in designing a flow sheet to meet these targets. Used in conjunction with a process simulator, pinch technology helps a design engineer to synthesize a process that optimally balances capital and energy costs.

4.2.4 Responsiveness to National Needs

Concentrated solar photons offer potential to make significant contributions in several areas of current national concern. Concerns in these areas may increase in the national consciousness over the next decade and well into the twenty-first century. Among these areas of concern are: (1) environmental issues, e.g., emissions from fossil fuel combustion of gases associated with greenhouse effects on global climate change, emissions of pollutants that contribute to adverse environmental health effects and/or acid rain (e.g. SO_x, NO_x, particulates and polycyclic matter), and the production of solid or

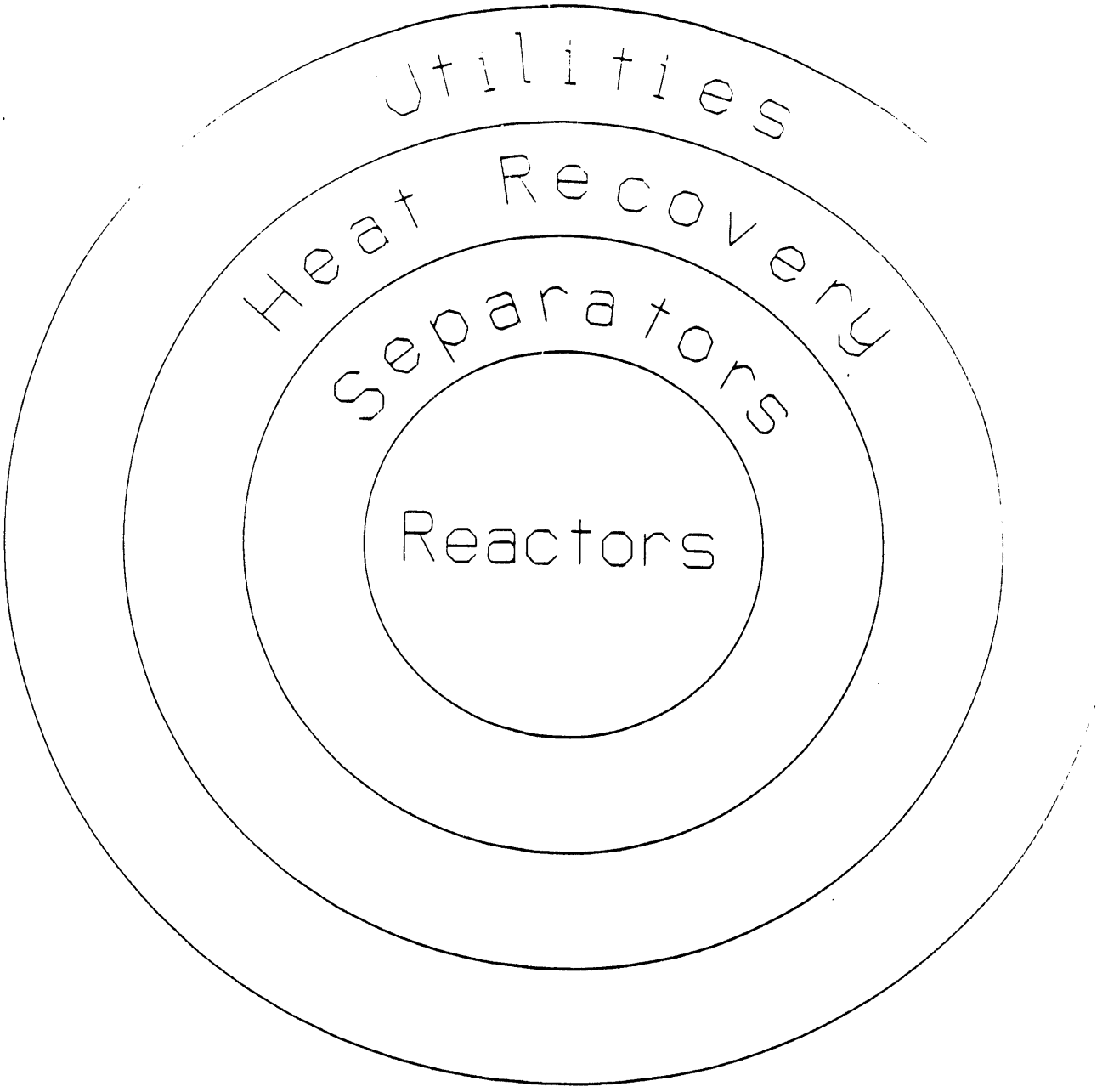

Figure 4. A generic chemical process flow sheet.

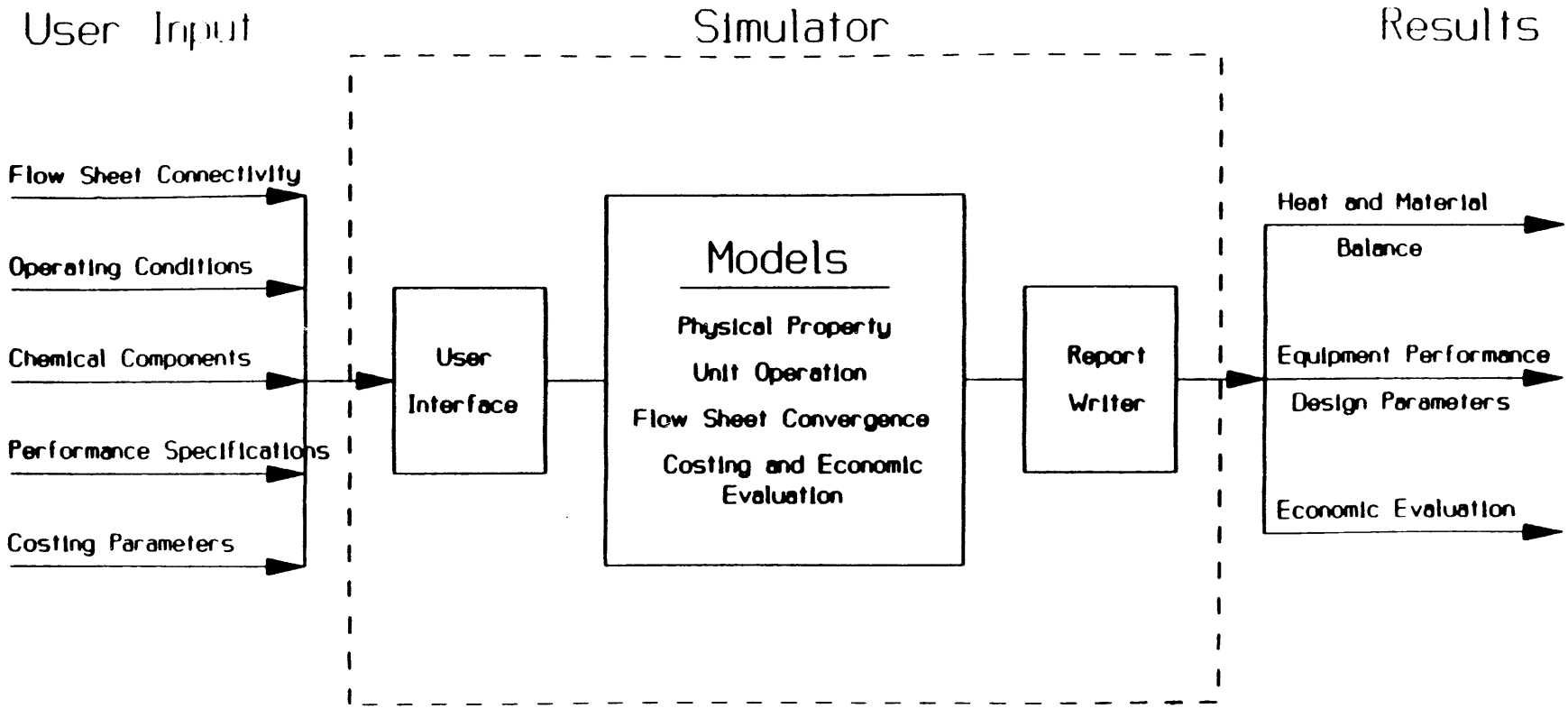

Figure 5. Typical inputs and models used in chemical process simulations.

hazardous wastes; (2) reduction of national dependence on imported energy, especially energy supplies subject to political instability or cartel- rather than market-driven prices; (3) the need to enhance global competitiveness of U.S. technology and to expand markets for U.S. manufacturing industries; and (4) the desire for sound national, continental, and global stewardship of energy and all resources.

Regarding environmental issues, aside from relatively minor amounts of electricity for lighting and instrumentation, solar furnaces use renewable solar energy as their main energy input. There is potential for significant displacement of fossil or nuclear Btu's in high-intensity process applications especially when recognizing the energy losses associated with the different efficiencies of energy conversion processes. Thus, to compute the fossil Btu's displaced (E_{FD}) by deriving high-grade process energy from a solar furnace one must account for the efficiency of converting fossil fuels to electricity (η_{FE}) and of converting electricity to photon energy, E_P, in candidate competing photon sources such as lasers or arc lamps (η_{EP}), giving

$$E_{FD} = E_P/(\eta_{FE}\ \eta_{EP})$$

At present, a typical value for η_{FE} is about 0.37 for a good pulverized coal plant using current technology and pollution controls to limit both SO_x and NO_x emissions (EPRI 1990). Currently available first-generation integrated coal gasification-combined cycle technology has achieved η_{FE} values of 0.42. There are projections that with molten carbonate fuel cells fired by gas from advanced coal gasification technologies η_{FE} could approach 0.6 by the year 2020 (EPRI 1990). Even with this high value for η_{FE}, the previous equation shows that, given the small value of η_{EP} for lasers and arc lamps (see Section 3.3), solar furnaces offer substantantial opportunity for displacing fossil-based energy in certain applications.

This displacement impacts all of items (1) through (4) above. It eliminates the corresponding emissions of CO_2, NO_x, SO_x, particulates, and polycyclics associated with the fossil source, and for coal-fired electric generation stations it eliminates substantial quantities of solid waste. For example, conventional pulverized coal-fired utility boilers equipped with flue gas desulfurization equipment produce about 360 lb. of solid waste for each 1000 kWh of electricity generated (EPRI 1990). Future coal-based electricity generation technology is expected to include advanced molten carbonate fuel cell systems fueled by state-of-the-art coal gasifiers. However, even these systems, which are projected to be in commercial operation by the year 2020, are estimated to produce solid wastes exceeding 100 lb. per 1000 kWh of electricity generated. Solar furnaces have no solid wastes. This could lead to major benefits in terms of societal acceptance and reduced operating charges, especially given that solid waste management costs are expected to increase rapidly as additional landfills are permanently closed and as federal, state and local regulations of solid wastes become more restrictive. For example, legislation continues to be proposed in Congress to prohibit interstate transport of hazardous wastes.

Regarding energy dependence, augmented use of solar energy contributes to reduced need for energy from nondomestic sources and thus to greater security and stability of energy supplies. Clearly, such security is desirable in light of uncertainties regarding the possible future behavior of some major holders of fossil minerals and of expected persistence of significant volatility in petroleum prices. Solar furnaces offer potentially significant advantages when the energy to be displaced is of high quality, e.g., high-temperature process heat that would otherwise be derived from electrically driven thermal plasmas or

from photolytic or photothermal energy that would otherwise be obtained from lasers or arc lamps. The reason is that significant losses in energy in converting fossil fuels to electricity and electricity to photons (see previous equation) means that several-fold more Btu's of raw fossil fuel energy would be required to remit the equivalent amount of prime value energy.

Regarding competitiveness, successful development of economically competitive processes using solar concentrators could open up new domestic and international markets for U.S. technology and thereby contribute to job growth, exports, and a better balance of payments position. As a final point, concentrated solar technologies may open up special opportunities for industrial applications in less developed countries poor in fossil or other mineral energy, but rich in solar resources. This could afford these nations the opportunity to enter new markets and achieve improved living standards, assisted in part by U.S. developed technologies. Further, U.S. national, regional, and global stewardship of fuel minerals and other natural resources could also be enhanced by the reduced pollution, solid waste, and fossil fuel consumption achievable with successful applications of solar furnaces.

Quantitative evaluation of economic and national security benefits of success in arenas (1) - (4) is difficult at this time. Indeed, an active research area for economists is learning how to measure the true cost of environmental impacts from different technologies and thus the cost of benefits potentially realizable from alternative technologies that mitigate or eliminate adverse environmental or other societal effects. In this regard, global climate change and the cost and benefits of current and alternative energy technologies have attracted particular attention. Results of these economic studies are expected to provide over the next few years data and modeling methodologies that will be of great value in evaluating the costs and benefits to the global environment of solar concentrators, and of other alternative energy scenarios.

4.2.5. Global Cost Comparison Methods

Figure 3 shows the cost of photon energy from several sources, e.g. arc lamps, various lasers, and concentrated solar furnaces. Figure A.1 in appendix A shows, as would be expected, that higher value added products generally are demanded in lower quantities. These figures can be used together to identify potentially economically acceptable nitches for use of solar furnaces in the manufacture of very high value added products. More detailed process definition and costing using the methodologies and considerations discussed above can then be used to examine further cumulative economic attractiveness of solar furnace options that show initial promise.

SECTION 5

SPECIFIC PROCESSES SHOWING POTENTIAL PROMISE FOR CONCENTRATED SOLAR ENERGY APPLICATIONS

In this section, we identify a number of photochemical, materials-processing, and other types of processes that emerged from our discussions and literature survey as having at least potential promise as an application of concentrated solar energy. For each such process, we have attempted to assess the current state of knowledge (including identified centers of expertise in each area) and the research needed to advance potential commercial viability. In order to make a more quantitative assessment of the estimated potential for technical demonstration, and on what time scale this is likely to occur, we recommend the use of the quantitative process modeling tools described in the preceding section.

5.1 Basic Photochemistry

From a scientific point of view, the most interesting potential applications of concentrated solar energy are those in which the solar optical photons directly produce an excited state, with the ensuing photochemistry leading to useful products. For the purpose of discussion we have divided this wide-ranging topic into two parts. For many processes, the underlying photochemical mechanisms and rate coefficients are not well enough determined to even begin to assess its potential usefulness. These cases are discussed in this section. In other cases, the mechanisms and kinetic parameters are known, and process modeling is appropriate to determine potential commercial viability. Applications of known photochemical processes of this sort will be discussed in Section 5.3.

5.1.1 Evaluation of Multiphoton Processes

A fundamental question that needs to be addressed at the outset is whether concentrated solar radiation could induce multiphoton processes in molecular systems, or whether the systems' response is strictly linear. Nonlinear or multiphoton processes, such as two-photon absorption, frequency multiplication, and sub-Doppler spectroscopy, depend on the sequential absorption of two photons within a time defined by one of the relaxation times of the system (Lin et al. 1984; Lin 1986). Some examples follow:

- In sub-Doppler spectroscopy and in two-photon absorption with a near-resonant intermediate state, collisional relaxation can depopulate the initially populated levels before another photon can be absorbed.

- In two-photon absorption with a remote intermediate state, the time delay between absorption of successive photons is given by the uncertainty principle to be

$$\delta t = h/(E_2 - E_1),$$

  so that large detunings of the intermediate state require extremely high peak powers.

- In the case of frequency doubling, internal crystal relaxation times affect the minimum powers required and help determine the nonlinear coefficients of the material.

Solar radiation, even at the highest levels achievable by concentrators, is too broad banded and not sufficiently intense to drive nonlinear or multiphoton processes. The cross sections for strongly allowed molecular absorptions are typically on the order of 10^{-17} or 10^{-16} cm^2. The total solar flux at the 10,000-sun level is about 3.5×10^{21} photons/sec/cm^2. If 1% of the solar radiation is absorbed (for a solid or liquid absorber), then on the order of 1000 photons may be absorbed per second, requiring millisecond lifetimes. However, solid or liquid relaxation times are generally in the range of 10^{-12} seconds. In gas samples, a much smaller fraction of the solar spectrum is absorbed, although relaxation rates may be longer, in the 10^{-6} second range. Solar fluxes are thus too weak for multiphoton absorption processes. Frequency doubling crystals generally require powers in the range of 1 MW/cm^2, compared to the flux at the surface of the sun of 6.3 kW/cm^2. This understanding has propelled the development of solar-pumped lasers (see Section 5.6) with an eye to the development of intracavity frequency doubling or mode-locked designs, which can provide narrow bandwidths and high peak powers.

Although direct multiphoton excitation is not possible with solar sources, the temperature associated with concentrated solar radiation, ranging up to 3000 K, corresponds to Boltzmann excitation of many vibrational overtone and combination levels to about 2100 cm^{-1} and beyond. Because isolated molecules do not reradiate as black-bodies, some vibrational ladders may be somewhat hotter than the bulk temperature. This level of vibrational excitation may enhance the reactivity of species by extending "hot-band" absorption of UV bands out to longer wavelengths, where the solar source is richer. Another mechanism for enhanced reactivity is sequential absorption via metastable states or reactive intermediates, which may be populated at the high temperatures in the solar field. High-temperature photochemistry studies by T. Milne at SERI have shown that high light levels may enhance reactivity beyond the level provided by heat alone. This type of reactivity enhancement has received little attention, at least as compared with the current rage in chemical physics for studying supersonically cooled molecules and clusters. A research emphasis on high-temperature high-intensity photochemistry is strongly recommended. Such research could lead to significant new applications of concentrated solar energy.

5.1.2. Example of New Photochemistry Possibilities

An example of a new photochemistry that could have intriguing implications for concentrated solar energy applications is the C_{60} cluster molecule (Pool 1990; Mackay 1990; Curl and Smalley 1991). This new form of pure carbon was identified in laser vaporization/supersonic beam experiments (Kroto et al. 1985) and given the cognomen "buckminsterfullerene" because of its geodesic truncated icosahedral structure. It had not been possible to isolate significant quantities of this material, however, until late in 1990 when Kratschmer et al. (1990) devised a preparative method that employs evaporation from an electrically heated graphite in an inert-gas atmosphere, followed by solvent extraction of the C_{60} product. This provided enough material for measurements to be carried out on the substance, including spectroscopic and photophysical properties. It was found, for example, that C_{60} possesses strong absorbance in the near-UV and visible regions [absorption coefficient > 10^4 cm^{-1} for solid material below 500 nm, with a tail extending out past 700 nm (Kratschmer 1990)] and that excitation in these bands generates large amounts of singlet oxygen via a triplet photosensitization process (Arbogast et al. 1991). Recently Howard et al. (1991) described production of significant quantities of C_{60} and C_{70} fullerenes in flames.

The preparation and photosensitized reactions of this material might fit very well with the properties of concentrated solar sources. The electrode vaporization may be simply a thermal process that could be driven by absorption of light in the graphite. C_{60} itself may be a good

chromophore for solar wavelengths, particularly for singlet oxygen generation, which is a reactive species for many photochemical and biochemical transformations. The current price for commercially produced C_{60} is $1000 per gram of pure material ($400,000/lb) (Howard 1991) which is well above the current cost threshhold for photon processing While C_{60} is itself an intriguing substance, we are not necessarily suggesting a major research effort on this specific system. Rather, this example is an illustration of how new research opportunities in this area may arise rapidly and unexpectedly. If the solar concentrator were set up as a user facility, such opportunities could be investigated and exploited in an efficient, productive, and timely manner. The establishment of such a user facility is one of the principal recommendations of this report.

5.2 Photothermal Conversion

A number of heat-pump-like cycles have been suggested for capture, storage, transmission, and recovery of solar energy. A schematic of a generic cycle incorporating these operations with a solar concentrator is shown in Figure 6. The figure depicts energy capture by concentration of solar insolation Q_s onto a working medium that may absorb energy by an increase in its sensible enthalpy and/or by enthalpy uptake by endothermic phase changes or chemical reactions. The energy release step frees up stored energy Q_R, equal to Q_s less energy lost during the collection and release processes, Q_{LC} and Q_{LR}, respectively (i.e., $Q_R = Q_s - Q_{LC} - Q_{LR}$). The net energy released, Q_R, can then be used for the desired application, for example in production of electricity as shown in Figure 6. Typically associated with cycles of this type are losses of the working medium during energy collection and recovery (M_{LC} and M_{LR}, respectively), and additional, so-called parasitic energy losses, E_P, reflecting partial utilization of the raw energy output of the cycle to operate plant utilities such as pumps.

Ignoring the material losses, the overall efficiency of the energy cycle of Figure 6, can be analyzed in terms of four contributing components:

- Energy capture efficiency: $\eta_C = (Q_s - Q_{LC})/Q_s$
- Energy release efficiency: $\eta_R = Q_R/(Q_R + Q_{LR})$
- Gross cycle efficiency: $\eta_g = E_g/Q_R$
- Net cycle efficiency: $\eta_n = E_n/E_g$

where E_g and E_n are, respectively, the gross and net amount of electrical energy generated by the cycle per unit of solar energy input, i.e., the amount of electrical energy available before and after debiting for electrical energy utilized for parasitic purposes (Figure 6). The quantity η ($= E_n/Q_s$) is then equal to the product of these four efficiencies.

Thus, attractive cycles should provide, for each of the above four efficiencies, values as high as possible, consistent with constraints on capital and operating costs for the process. Two orientation calculations are helpful in illustrating possible limitations in cycle performance as well as opportunities for improved technology. Capture and release efficiencies are process dependent, but 80% can be taken as a nominal optimistic value for each. Typical efficiencies for conversion of heat to electricity in steam Rankine cycles are 30% to 35%, although values as high as 40% can be obtained in modern plants if major pollution control equipment does not have to be operated (EPRI 1990). More importantly in the current context, these efficiencies depend on the steam temperature and pressure, and hence on plant materials and on the

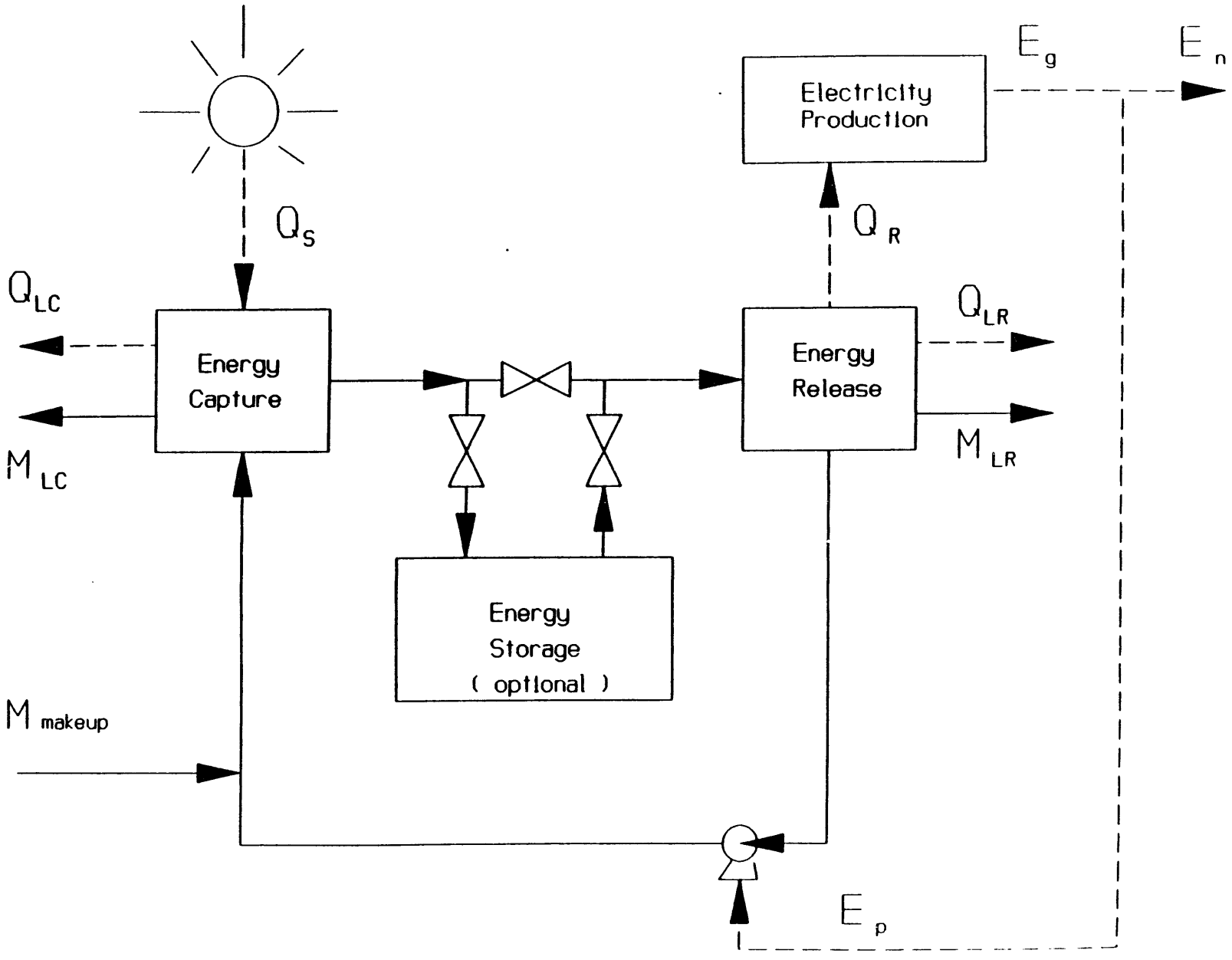

Figure 6. Generic cycle flow chart.

temperature at which Q_R is made available. For example, at 250°C, typical steam Rankine cycle conversion efficiencies are about 14% to 20%(Armstead and Tester 1987), whereas the 40% value would require supercritical steam at a temperature approaching 600°C (EPRI 1990). Assuming for the parasitic efficiency the quite reasonable value of 95%, a net cycle efficiency of 24% (0.8 x 0.8 x 0.4 x 0.95) is calculated for the very high efficiency Rankine cycle. However, if the Rankine cycle efficiency drops to 25% the net cycle efficiency would be 15% (0.8 x 0.8 x 0.25 x 0.95).

If electricity is the desired product of the cycle, then these efficiencies should be compared with other solar-based options. For example 15% is comparable to the upper end of the efficiency range for commercially available silicon photovoltaic cells (Glasstone 1982). However, the solar thermal cycle of Figure 6 may be more complex to operate and maintain and would probably have higher capital costs. On the other hand, an efficiency of 24%, if economically competitive, could give the solar thermal cycle an advantage over photovoltaics. Furthermore, the cycle of Figure 6 offers the very important advantage of optional storage of solar thermal energy for use in electric power generation or other applications as desired. Photovoltaics would require battery or other means of storing electrical energy and may not be able to match the efficiencies of storing heat or chemicals capable of heat release by exothermic reactions.

The above discussion also shows that when using Rankine cycles there can be a significant efficiency penalty with declining temperatures for release of Q_R. A second observation is that there may be cases where solar furnace cycles of the type shown in Figure 6 may prove to be more valuable in applications requiring direct heat energy, including the option for energy storage, rather than electricity generation. Thirdly, a more detailed analysis would account for effects of loss of working medium (M_{LC} and M_{LR}), and the need for a makeup materials stream.

The take-home lesson of this discussion is the importance of carrying out further process simulation, economic, and marketing analyses to define preferred application opportunities for such cycles under a range of conditions.

5.3 Photochemical Applications

In light of the overall constraints on applications of photochemistry to chemical synthesis and processing, as detailed in appendix A, we have focused our attention on those processes that exploit the properties of concentrated solar photons to the greatest advantage. The primary property in this context, is the high overall photon flux over a range of wavelengths between 300 and 2000 nm. The absence of hard-UV (below 300 nm) radiation significantly limits the types of primary photochemical reactions that can be exploited, but several processes have emerged as candidates for further exploration and possible application.

5.3.1. High-Intensity Laser-Jet Photochemistry.

R.M. Wilson and co-workers at the University of Cincinnati have been investigating novel photochemical processes that can be made to take place in a flowing solvent jet under high-intensity laser irradiation. The technique involves sequential excitation of transient photochemical intermediates, in which photochemically generated transient species with suitable absorption properties are excited further and produce relatively large amounts of photoproducts that are not observed under low intensity conditions (Wilson et al. 1990). The jet acts as a light trap, increasing the effective photon flux on the reactants to the order of a few Einsteins $sec^{-1}cm^{-2}$. While the 1 KW/cm^{-2} available from the solar concentrator corresponds to only 0.01 Einsteins $sec^{-1}cm^{-2}$, the large available bandwidth may compensate for the lower

flux. One process in particular, the conversion of methylbenzophenone to anthrone, requires simultaneous irradiation by two ion lasers at wavelengths in the 334 to 364 nm and 458 to 514 nm bands. Replacement of two expensive, energy-inefficient lasers by a single solar source appears to be a particularly attractive possibility in this case. The solvent-jet apparatus might be particularly compatible with the dielectric concentrator described in Section 3.2.1. A similar jet technique has also been used on photodeposition applications (see Section 5.5.2).

5.3.2 Photoelectrochemistry at High Intensities.

We have distinguished three generic types of applications for photon-driven electron transport processes: direct photovoltaic electricity generation (not considered in this study), charge-transfer and electron-transfer processes in solution, and photochemical processes at electrode surfaces.

A principal desired application for photoelectrochemistry is the "water-splitting" reaction producing hydrogen gas as a storable, transportable fuel. Despite extensive prior work in this area, a practical system for accomplishing this has not yet been identified and the applicability of concentrated solar energy to the present generation of systems appears to be limited (Glandt and Myers 1976), although Nozik and co-workers at SERI have suggested that quantum-well devices might permit more efficient utilization of high-intensity solar radiation (Parsons et al. 1990). Langhoff (1990) has suggested, in this connection, a role for broadband absorbers such as the diatomic halogens, which produce reactive free radicals by photodissociation. Attack of Cl or Br (from Cl_2 or Br_2, respectively) on water to produce O_2 and HX, for example, might be studied as part of a solar-driven water-splitting cycle, with the acid HX decomposed by solar-energy-based electrolysis or metal surface reaction. This reaction system might be a prototype for setting up a solar-driven gas-phase reaction facility. Another set of compounds having possible applications in water-splitting reactions has been identified by H.B. Gray and co-workers at Cal Tech. Use of $IrX_6^{-3}(aq)$, for example, in reduction of $X^-(aq)$ to halogen dimer may be particularly promising, particularly when combined with the radical attack of $X\cdot$ on water for production of HX, as mentioned above. The C_{60}-catalyzed photogeneration of oxygen mentioned in Section 5.1.2 could also have potential for water splitting, but much more needs to be known about this process before a realistic assessment could be made.

There are additional areas in which heterogeneous photoelectrochemistry could find applications; one of these is in deposition or etching of thin films on surfaces, which is discussed in Sections 5.5.2 and 5.5.3.

5.3.3 Photomedicine and Photobiology

Much of the current research on the biological effects of light focuses on understanding the molecular biology of what happens when plant or animal tissues absorb light. Examples include:

- effects of low-intensity UV radiation on the immune system;
- effects of short-duration light pulses on human vision;
- mechanisms of selective action of phototherapeutic drugs, such as hematoporphyrin derivatives;
- effects of visible light on human physiology and psychology.

Most of these studies utilize continuous light sources such as CW lasers or spectrographically dispersed arc lamps (Watanabe et al. 1982).

Most biological and biomimetic processes do not function well at irradiation levels greater than 1 sun; indeed, many organisms' metabolic processes are photoinhibited at higher brightnesses (Brown 1990). Work at the Weizmann Institute on the carotene-producing algae *Dunaliella* suggests that a few organisms, such as this, may benefit from a fractionally higher flux level of solar radiation, but concentrations greater than a few suns would generate temperatures in excess of 100°C, which would of course be fatal to any form of life with which we are familiar.

5.4 Materials Processing and Surface Photochemistry

Materials processing encompasses the production and modification of materials. Many different techniques are used to process materials, ranging from presses for compressing pellets of materials together, vacuum chambers for layer-by-layer growth of materials, lasers for ablating materials, and grinders for removing unwanted edges. The most pertinent set of techniques that relate to possible applications for a solar concentrator are those utilizing lasers and other light sources.

There are several advantages of using light over traditional means. Lasers provide precise control for the localization of reactions. The light comes from a remote source so samples can be easily moved or replaced, and it can be coupled into any environment, from liquids to toxic gases. Also, because of the localization, the amount of precursor used can be reduced by injecting directly into the interaction area. This is very important when either expensive or hazardous chemicals are used.

In the literature search procedure described in Section 2.4 and appendix B, we retrieved a large number of published references about photon-driven surface chemistry and materials processing. These were sorted by the identity of the material and the nature of the process into the categories listed in Table 5.

Table 5. Photon-driven surface chemistry materials and processes

Materials	Processes
carbon (and diamond)	ablation
ceramics (incl. powders)	alloying
II-VI (CdTe, HgCdTe,...)	annealing
III-V (GaAs, InP,...)	cladding
metals	deposition
metal-oxides	desorption, vaporization
polymer	doping
silicon (also SiC, etc.)	drilling
silicon nitride	etching
silicon oxide	hardening
steel (and iron)	melting
superconductors	plasma (ionization, charge carrier generation)
	recrystallization
	surface treatment (general, unspecified)

From this extensive list, we sought to identify those materials and processes that would potentially benefit from the use of concentrated solar energy. We excluded processes that required light at wavelengths below 300 nm or that exploited the spatial coherence of a laser to produce micro-scale features, as in direct writing of semiconductor devices.

The solar concentrator could replace light sources that drive thermal reactions where the light is used to heat a substrate. Traditionally, these reactions are done with CW lasers with power densities up to 100 KW/cm^2. A major advantage of the solar source is the ability to produce large speckle-free beam profiles caused by the incoherent nature of the light source (for example neglecting losses, flux densities of 10 KW over a 10 cm^2 area would be obtained by a 10,000-fold concentration of the natural solar energy received by a 10 m^2 primary collector). This will produce even heating from the beam profile and allow faster scan rates and increased total energy delivery to the material.

Among the areas of materials processing identified as benefiting from concentrated solar light are surface treatment of metals, thin-film deposition and etching, production of fine ceramic powders, and materials testing and evaluation for high-temperature conditions. A great deal of research is still needed on many of these topics before process development can take place, because in many cases the basic mechanisms and kinetic parameters have not been well established.

5.4.1. Surface Treatment

A number of photon-induced processes have been used to produce increased hardness, corrosion resistance, or friction reduction in the processing of metals, alloys, and machined parts, such as cladding, alloying, melting and transformation hardening. The present technology for these processes uses CW CO_2 lasers or more traditional thermal methods. Much of the technological development in this area has taken place in Korea and Europe (U.K., Germany, and the Swiss Federal Institute of Technology in Lausanne).

Cladding and alloying are processes in which the outer surface (up to several mm) of a workpiece is chemically changed. Cladding bonds an outer layer that is pre-deposited on the surface, either by electrodeposition (Cr, Ni), thermal spray (Cr, Mo, carbides) or vapor deposition (Zn, W) (Dekumbis 1987) to the base material. Alloying actually melts the base material and allows the mixing of the pre-deposited layer with the base material. High CO_2 laser powers, on the order of 10^4 W/cm^2 are required for this process.

In transformation hardening, the surface of a material is heated to just below the melting point, then rapidly cooled. The effect of the thermal cycle on iron and steel is the conversion from an austenite structure to a hard martensite structure. A surface graphite layer can be sprayed onto the workpiece to increase absorption. Lower CO_2 laser powers, on the order of 10^3 W/cm^2, are required for these applications.

The feasibility of using a concentrated solar source for alloying and cladding operations is marginal, because of the high intensities required, but may be more favorable for transformation hardening. The CO_2 laser produces a wavelength of 10.6 μm, at which the absorption of metals is around 3%. In the solar spectral region , the absorptivity of metals increases, up to a value of 50% to 70%, at the shorter wavelengths, as shown in Fig. 7. In addition, several processes require the addition of a deposited layer to the workpiece that will undergo the processes, which can further increase the absorption of the solar radiation.

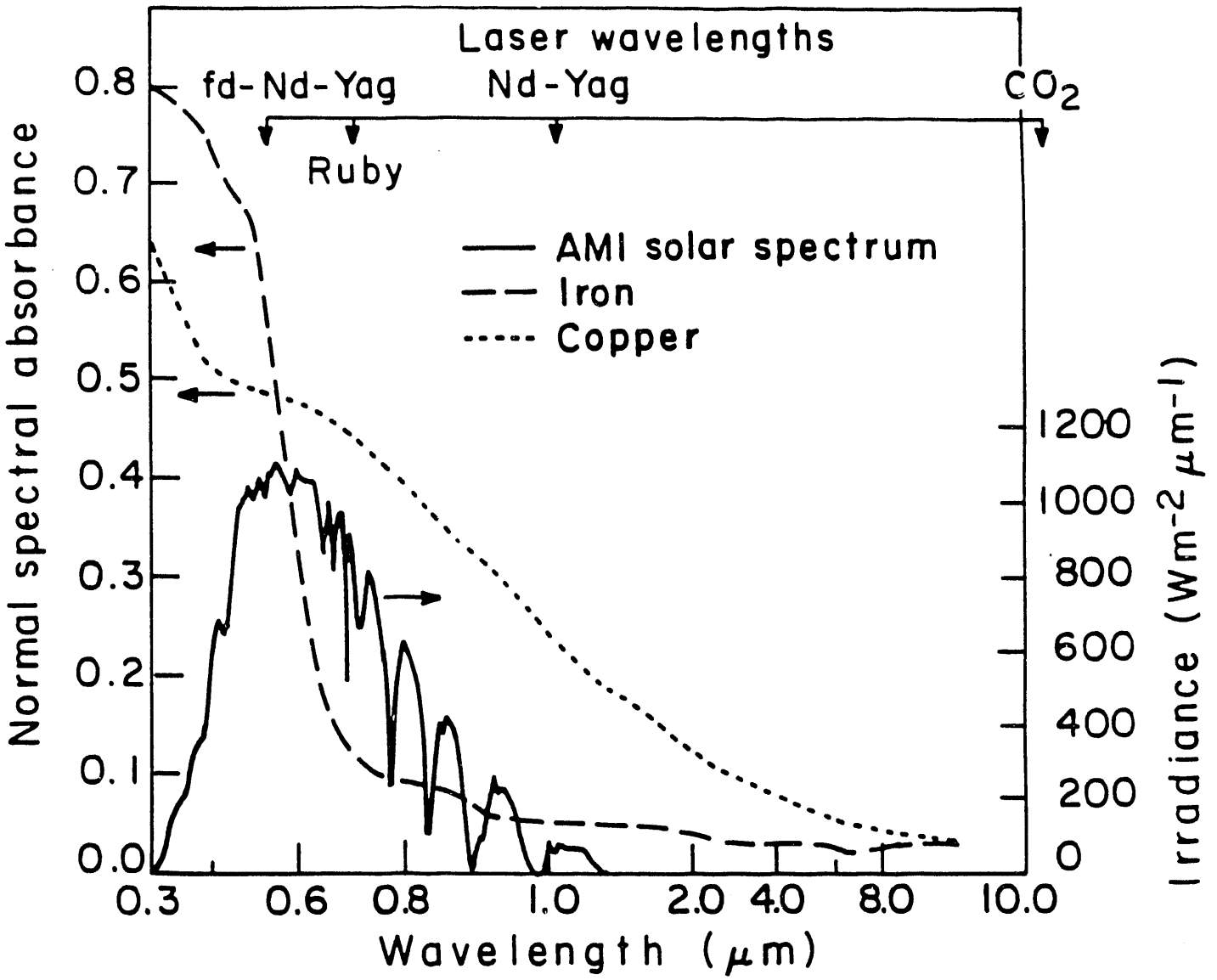

Figure 7. Comparison of AM1 solar spectrum with metal absorptives (from Pitts *et al.*, 1990).

As a first step to assessing the viability of concentrated solar energy for these applications, detailed calculations should be carried out on energy coupling to the surface for a variety of conditions of interest. In doing so, the restrictions on proximity of the workpiece to source optics discussed in Section 3.2.1 must be taken into account. Preliminary estimates suggest that the required intensities may be available from the solar concentrator. Additional benefits may accrue from the large irradiation area of the solar source. This could provide a broader, more uniform working zone, and could raise throughput by allowing faster scan rates and fewer passes over the workpiece.

5.4.2 Deposition

The deposition of materials is an area of industrial importance. Using light as a source of energy to drive deposition reactions has been studied for many years (Herman 1989; Haigh and Aylett 1988). The outcome of these studies has indicated that there are three typical routes for the deposition to occur. These are thermal, photochemical, and reactions involving both.

The deposition route taken is controlled generally by the type of light source used. Typically for photochemical deposition, high-power, pulsed UV and IR lasers are used. This allows several photons to be absorbed by the precursor molecule, thus producing a well fragmented, sometimes atomic, reactive species to interact with both gas phase species and the deposition substrate. Photothermal reactions use both pulsed and CW lasers in the whole wavelength range from the UV to the IR to heat a substrate and cause the incident precursors to adsorb dissociatively. This is directly analogous to thermal chemical vapor deposition (CVD) in which the substrate is electrically heated. The mixed photochemical/photothermal route will typically occur when the laser beam interacts simultaneously with the substrate and the gas-phase precursor.

The solar concentrator can be used for deposition in most cases where CW laser heating has been used. Two advantages of the concentrator are the ability to provide uniform speckle- free illumination over broad areas because of its noncoherent nature and a large total energy delivery to the substrate so faster scan rates can be used. The concentrator would have many of the existing advantages of laser processing, such as the ability to limit gas loads, which is important when working with hazardous precursors, and use of a room temperature apparatus for high-temperature depositions and easier sample handling. The disadvantage of the concentrator is the inability to produce narrow features in the sub-micron range.

Photodeposition can be done in both the gas and liquid phases. Gas-phase deposition is used most often in the electronics industry when sample purity is of primary importance, e.g., in crystal growth. An advantage of gas-phase deposition is that no solvents are needed and the precursors can be obtained at very high purity levels. Liquid-phase deposition is typically used for lower purity, large area film growth. However, some examples are known of high-purity deposition from liquids.

5.4.2.1 Gas-Phase Deposition Systems

Metals. The deposition of metals from the gas phase, onto substrates using concentrated solar light will be primarily driven via thermal pathways. Most precursors are optically transparent in the gas phase in the solar spectral region. However, photon absorption by precursors adsorbed on substrates is possible due to the broadening of optical transitions to lower energies (Ehrlich and Osgood 1981). This enhanced absorption may help facilitate thin-film deposition at slightly lower temperatures than at which purely thermal deposition would occur.

There are three typical precursor types that are used for thermal CVD and should be good for solar-assisted CVD. These are metal carbonyls, metal halides, and metal organics.

Metal carbonyls have been studied the most and can be used to deposit Fe (Allen and Tringubo 1983; Jackman et al. 1986, Xu and Steinfeld 1990), Ni (Allen et al. 1985, Petzoldt et al. 1984), and the refractory metals W, Cr, and Mo (Singmaster et al. 1989; Allen and Tringubo 1983). Pure films can be formed by simply flowing the gaseous metal carbonyl evenly over a heated substrate. The solar concentrator can be used to either heat the substrate directly, if it absorbs in the solar spectrum, or to photo-initiate the reaction on a transparent substrate, then heat the newly formed film. The photolytic reaction alone, at the intensities and wavelengths available from the concentrator, is not sufficient to produce high-purity thin films.

Tungsten can also be deposited from its fluoride (WF_6) in a similar thermal deposition scheme (Zhang et al. 1987; Gottsleben and Stuke 1988). In one case, a mixture of WF_6 and SiH_4 is used with a 150°C substrate to initiate the very exothermic reaction that leads to pure tungsten thin-film deposition (Black et al. 1990). Also because of the low-temperature, high-scan rates can be used to cover large areas with a smooth film. This is the best source for photo-assisted deposition of tungsten. Another halide that can be used is $TiCl_4$ to produce pure titanium films (Tsao et al. 1983).

To complement the metals from the carbonyl and halide deposition (Fe, Ni, W, Cr, Mo, Ti), metal films of Au, Cu, Pt, Pd, Ir, Al, Cd, and Ga can be deposited with metal organics. Again, photothermal techniques are used to obtain films of >95% purity. The first class of these is the acetylacetonates (AcAc).

Acetylacetonates readily decompose at temperatures around 200°C, so relatively low-temperature depositions can be done. In addition to the low-temperature decomposition, these precursors absorb in the near UV so the deposition can be photochemically assisted. The low temperature and the possibility of a photochemically assisted mechanism could allow high scan rates for large area, smooth film deposition, as seen earlier with the WF_6/SiH_4 system. This should be a very good system to use with the solar concentrator, taking advantage of its broadband frequency nature to provide a synergistic effect tying both photochemical and photothermal processes together with the speckle-free imaging of noncoherent light to deposit very pure films both evenly and speedily. The metals that can be deposited in this way include Au, Cu, Pt, Pd, and Ir.

The second major type of metal organics is trimethyl and triethyl complexes. These are frequently used in thermal and photothermal CVD to deposit Al and Ga, but have also been used for Cd deposition. Typically, these precursors are used for the metal component in complex semiconductors, GaAs or AlGaAs. A hybrid of these metal-organic-type precursors is trimethylamine aluminum hydride. This hybrid has been used to photothermally deposit Al films of >97% purity levels.

The best systems for using concentrated solar light to deposit pure metal films from the gas phase are the halides for W and Ti, the AcAc's for Au, Cu, Pt, Pd, and Ir, and the trimethyl compounds for Al and Ga. In all these systems, the main driving force for deposition is thermal.

Elemental Semiconductors. The deposition of elemental semiconductor films can be done with a photothermal scheme very similar to metal deposition mentioned earlier. Both silicon and germanium are deposited by using their methane analog, SiH_4 and GeH_4, respectively. Substrate temperatures of at least 350°C are required for silicon deposition, whereas germanium can be grown at 300°C. Ge-Si alloys can also be deposited by simply mixing the

two precursors in the correct ratios. Photochemical deposition would not be possible with the solar concentrator because of the lack of absorption of the hydrides at solar wavelengths and low power densities.

III-V Semiconductors. Compound semiconductor deposition is "very complex and poorly understood" (Herman 1989). As with the elemental semiconductors, photo-induced thermal deposition can be used to produce GaAs, and GaP semiconductors as well as the ternary III-V semiconductors: GaAsP, AlGaAs, and InGaAs. An alternative to the purely thermal deposition is photo-assisted atomic layer epitaxy (ALE). ALE uses alternating precursor gas pulses to deliver a layer of molecules to a substrate and visible and UV light to assist the dissociation by photochemical means. Trimethyl gallium and arsine are used for both the thermal deposition method and the ALE method. The other precursors for the ternary III-V semiconductors are trimethyl aluminium, triethyl indium and phosphine. Dimethyl zinc can be added to the precursor gases to incorporate Zn as a dopant.

II-VI Semiconductors. The deposition of II-VI semiconductors must be done at low temperatures to prevent atomic diffusion. It is therefore not feasible to deposit these material using the solar concentrator source, because of excessive substrate heating.

Insulators. Insulator deposition is feasible using the solar concentrator. Again, the reactions are photothermal and all the general considerations mentioned in the metal and semiconductor section pertain to this area. The insulators that can be deposited are silicon dioxide (Szikora et al. 1984) and silicon nitride (Sugimura et al. 1987) from SiH_4 with N_2O and NH_3, respectively; titanium dioxide from a $TiCl_4/H_2/CO_2$ mixture; aluminum oxide or sapphire from trimethylaluminium and N_2O (Minakota and Furukawa 1986); zinc oxide from dimethyl zinc and NO_2 or N_2O (Solanki and Collins 1983); tantalum oxide from pentamethoxy-tantalum and N_2 (Yamagishi and Tarui 1986); phosphorous nitride from PH_3 and NH_3 (Hirota and Mikami 1985); and chromium oxide thin films and crystals from CrO_2Cl_2 (Arnone et al. 1986). Tin oxide has also been grown from $SnCl_4$ and residual oxygen on GaAs (Tokuda et al. 1988).

Polymers. The deposition of polymer thin films using light has been accomplished by photolyzing precursors in the gas phase above a substrate with pulsed lasers. An example of this is the photolysis of 1-methyl-1-silacyclobutane to form an organosilicon polymer (Pola et al. 1988). The addition of SF_6 to the precursor gas was used as an "energy conveyer" to assist the energy transfer from the 10.6-μm IR photons to the precursor. In this context, it would be useful to identify some inert absorbers that could act as photosensitizers in the solar spectrum.

Superconductors. The deposition of superconducting thin films is a field of intense research. It has been determined that one of the best current methods for depositing these materials is by "laser sputtering", which requires short, high-intensity light pulses (Bauerle 1989). Because such ablative transfer works best under short-pulse conditions, its use of concentrated solar light for the deposition of superconducting thin films would require significant innovations in the solar concentrator hardware for control of light intensity and exposure time of workpieces.

5.4.2.2 Liquid Phase Deposition Systems

Deposition of materials on substrates from solutions using light is also possible. There are trade-offs with using the liquid medium for depositing materials, however. A major advantage is the simplicity of the apparatus; all that is needed is a container that can hold a liquid and support a substrate below the liquid surface. In the simplest case there is no gas handling, except for vapor removal. The disadvantage is that the deposited films have more impurities than the gas-phase analogs.

The main constraint of depositing from liquids is that the reactions must occur at the substrate surface. If the solution absorbs the light, thermal pluming will occur and nonuniform layers will be formed. Using solar light would be advantageous, because solution absorption wavelengths could be removed from the light source while still leaving sufficient intensity to drive the deposition.

A possible use for the liquid deposition would be to precoat workpieces that are going to undergo surface treatment. This could be an ideal case for a multistep solar-assisted materials processing plant.

Metal films can be deposited from solutions, either by thermal reactions on a substrate or photoelectrochemically on semiconductors. Both methods can be done with the solar concentrator.

Dibenzene complexes of chromium and molybdenum have been used to deposit Cr and Mo with carbon contamination levels below 10% (Yokoyama et al. 1984). Gold and copper can be deposited from commercially available plating solutions. A technique has been developed that uses a jet (cf. Section 5.3) to deliver plating solution to the laser spot on a substrate giving good quality films and high deposition rates (von Gutfeld and Vigliotti 1985). This type of technique could be adapted to utilize fully the broadband nature of the solar spectrum. Some portions of the spectrum could be absorbed by the solution, facilitating the dissociation of the precursor in the solution, while the rest of the spectral intensity heats the substrate to ensure maximum adhesion of the partially dissociated precursor to the growing film.

Palladium has been deposited from a solution of acetonitrile, methanol and $Pd(NCMe)_6(PF_3)_2$ using a 325-nm source to photothermally heat a substrate (Montgomery and Mantei 1986). An aqueous solution of chloroplatinic acid solution has been used for platinum deposition (Karlicek et al. 1982).

Photoelectrochemical deposition has been demonstrated on p-type silicon and p- and n-type GaAs. Both palladium/cyanide and gold/cyanide plating solutions were shown to deposit the metal, either Pd or Au, on illuminated p-type Si and GaAs, while depositing on dark areas of n-type GaAs when illuminated through a mask (Micheels et al. 1981). Similar results were seen using a copper, zinc and cadmium plating solution; Zn and Cd were efficiently deposited on illuminated p-type silicon and the Cu was not (Rose et al. 1983).

A variety of other materials, including semiconductors, insulators, and photovoltaic materials, can be deposited by photoreaction in liquids. In fact, the only example of solar-assisted deposition found in the literature is the work carried out in Mexico on deposition of highly photosensitive CdS thin films (Nair and Nair 1987). The deposition process uses an extremely simple technique: microscope slides are placed vertically into 50-mL beakers that are filled with an aqueous mixture of thiourea, cadmium acetate, triethanol-amine, and ammonia. Then the apparatus is covered with a larger inverted beaker and placed in the noonday sun for 1 to 2 hours.

The films formed by this technique have optoelectric qualities that surpass films deposited by other techniques and the film growth and quality is highly reproducible. Film thicknesses of 0.5 μm are obtained with photoconductivity of 0.5 ohm^{-1} cm^{-1} and photo/dark conductivity ratios of ~10^7 for AM1.

These results demonstrate a purely solar-driven reaction in which no electrical energy was used. No real explanation of the deposition mechanism is given in the report on this work, and

it is possible that the solar radiation is used simply to heat the solution, rather than to initiate a specific photochemical reaction.

5.4.3 Etching

Etching is the converse of deposition, in that material is removed from, rather than added to, a surface. Numerous instances of photoetching, using pulsed or CW lasers, have been reported in the literature. There is potential for using a solar source for these applications, particularly for broad area etching in either the gas or liquid phase. As mentioned in the preceding section, an advantage of using a noncoherent source is the ability to obtain uniform, speckle-free beam profiles, and thus uniform surface exposure. The corresponding disadvantage, of course, is the inability to focus the light for direct etching of narrow features.

5.4.3.1 Gas-Phase Systems

The gas-phase etching of silicon by Cl_2 (Okano et al. 1984) has been done using a Hg-Xe arc lamp. Similar etching results are seen with GaAs (Ashby 1985) and $GaAs_{1-x}P_x$ alloys with x=0.2 and 0.37 (Ashby 1986), using HCl as the etchant.

These reactions are believed to be photoelectrically driven, making it possible to carry out the process at lower substrate temperatures. Solar radiation could be applicable to chlorine etching processes, because Cl_2 absorbs to the red of 300 nm.

5.4.3.2 Liquid phase Systems

Photoenhanced etching in the liquid phase has been studied more extensively than in the gas phase. The materials that have been etched are Si (Bunkin et al 1985), GaAs (Podlesnik et al. 1984), InP (Bowers et al 1985), GaP (Johnson and Tisone 1984), CdS (Tenne and Hodes 1983).

As in the gas-phase work, the majority of the etching reactions in the liquid phase are photoelectrically driven, giving up to a hundred times enhancement over the dark reaction (Bowers et al. 1985). A solar source could be a direct replacement for currently used light sources in such applications if the economic and source availability factors discussed in Section 4.2 can be satisfactorily addressed.

5.4.4. Materials Testing

Solar furnaces allow condensed phase samples to be heated to very high temperatures (> 4000 K), in the presence of inert, reducing, or oxidizing reagents, and under elevated pressures (100 atm or more, depending on availability of windows). Further, this can be accomplished while maintaining cold walls in the confinement chamber and cold supports for the workpiece; the sample, if thick enough and heated from one side, becomes its own support. The solar furnace can also provide controlled temperature-time histories, including rapid heating of shallow surface regions of a specimen, and thus can be used to interrogate melting and solidification phenomena in complex refractory materials. These features make solar furnaces well suited for measuring thermochemical and thermophysical properties of refractory and other specialized materials under the high severity conditions of temperature, pressure, and reactive atmosphere, often of current scientific and practical interest. One example is determination of phase diagrams for ultrahigh melting point refractories. Further, a solar furnace offers these capabilities while avoiding certain disadvantages of competing techniques. Electron beam heating requires a vacuum and may result in unwanted ionization of the specimen or of volatiles

evolved during heating of the sample. Radio frequency heating requires that the workpiece be, or contain, an electrical conductor.

Research needs on high-temperature ceramics for energy applications have been reviewed by Bowen (1980). Some of the potential benefits of the solar furnace approach are rather well illustrated by the work of Foex (1965), who determined the melting point of calcium oxide in a solar furnace using a calibrated pyrometer. His result (3223 K) was significantly higher than the previously reported value of 2887 K. Foex's method is believed to have been little affected by sample contamination arising from high-temperature reactions of the specimen with its support (JANAF 1974). Foex also reasoned that a previous measurement technique in which the CaO was held on tungsten supports at high temperature was probably flawed caused by the reaction of CaO and the metallic tungsten to form $WO_3 \cdot 3CaO$, with the $WO_3 \cdot 3CaO$ depressing the observed melting point of the CaO. This could account for the lower melting point value that had apparently been accepted for many years prior to Foex's work (JANAF 1974).

5.4.5 Synthesis of Ceramic Powders *

Haggerty and co-workers at MIT have developed processes for producing fine, sinterable ceramic powders by CO_2-laser-driven gas-phase reactions (Haggerty and Cannon 1981). As a part of the present study, we attempted to identify areas of opportunity for producing such materials from gaseous precursors using the concentrated solar spectrum to effect the reaction. Only a very select group from the wide range of ceramic materials used as powders are practical candidates for a solar-heated powder synthesis process. Bases for selection include cost, purity, diameter, size uniformity, shape, agglomeration, and process chemistry. Essentially, all of the criteria must satisfy critical targets before a material and process will find usage in the marketplace.

Cost alone will eliminate powders of traditional ceramic materials from consideration. Typical of the materials eliminated on this basis include standard grades of alumina ($0.40-$0.60/kg), clays ($0.02-$0.20/kg), magnesia ($0.60/kg), silica ($0.025-$0.22/kg) and titania ($1.58/kg). It is only the so-called "advanced ceramics" that have costs that can justify premium synthesis processes.

Advanced ceramic materials used as powders include special grades of alumina, aluminum nitride, aluminum titanate, barium titanate, beryllium oxide, boron nitride, lead titanate, molybdenum disilicide, sialon, silicon carbide, silicon nitride, zirconia, etc. Others could include several of the rare earth phosphors, and the formation of diamond powder in the CO_2-laser-induced gas-phase decomposition of ethylene has recently been reported (Buerki and Leutwyler 1991). The sales prices of these powders are extremely variable, depending on specifications. Although many sell at prices as much as $200/kg, there is considerable pressure for achieving significant price reductions so that finished components can compete with alternative lower cost, frequently well-established materials. An example of this is silicon nitride exhaust valves for automotive engines for which the cost of the constituent Si_3N_4 powders approximately equals the cost of a finished metal valve. Unless powder costs are reduced significantly, ceramic valves cannot be manufactured at a price at which they can be sold.

The second generalization is that the application must require powders with diameters less than approximately 2 to 3 μm. If larger particle sizes are acceptable, it will probably be less

---

* This section was prepared by Dr. J.S. Haggerty.

expensive to synthesize the material in a bulk form and to reduce powders to their final particle size by comminution processes.

Figure 8 summarizes 1982-1983 sales prices of Acheson SiC in 5000-kg lots as a function of particle size (solid circles). The sales price is essentially constant for particle sizes greater than 100 μm. Below 100 μm, the cost of these powders increases rapidly with decreasing particle size. A 1/d extrapolation was used to project prices into the submicron range needed for consolidation by sintering mechanisms at practical temperature levels.

The cost of small diameter powders increases rapidly because of factors contributing to the process energy per kilogram of material. This parameter is also shown on Figure 8. The specific energy increases with smaller powders because the specific surface area of the powders becomes increasingly significant and because the comminution process becomes progressively less efficient. Combined, these effects generally give between a 1/d and a $1/d^2$ relationship between cost and diameter. The correlation between cost and process energy curves is evident.

Figure 8 also shows current selling prices of nominally 1 μm diameter SiC powders as a circular cross-hatched region. These prices, ~$20/kg, are approximately an order of magnitude less than projections based on the extrapolated curve. The difference results from a combination of improved processing, increased competition for a growing market for high-quality structural ceramics, and prices that are closer to manufacturing costs. To relate these prices to the inherent comminution costs, dashed lines have been drawn with slopes corresponding to 1/d and $1/d^2$ dependencies through the extremes of the price range until they intercept the horizontal curve corresponding to the minimum cost. The region defined by the dashed lines probably represents nearly the minimum price of SiC powders made by comminution. By this analysis, powder prices begin to rise rapidly for diameters smaller than ~8 μm rather than ~100 μm.

The horizontal shaded region on this figure summarizes a range of projected manufacturing costs for SiC powders made from CO_2 laser-heated SiH_4-based reactant gases. Although absolute costs are subject to specific cost assumptions, the solar-heated powder synthesis process should exhibit many of the same characteristics. Unlike a comminution process, a powder synthesis process need not exhibit a cost dependence on particle size. Provided the process is capable of making agglomerate-free, small diameter powders, direct synthesis processes can enjoy an important cost advantage for very small diameter powders. Gas-phase synthesis represents one of the lowest cost options for the 0.2-to-0.3-μm diameter powders currently used for state-of-the-art structural ceramics. Additionally, these synthesis processes yield powders with narrower size distributions and with higher purities than are characteristic of ceramic powders made by comminution processes.

Figure 9 illustrates an important criterion for selecting viable particle formation and growth mechanisms for making cost-competitive, small diameter powders. To yield a high-value powder, the exposure time, the particle number density,and the growth mechanism must be selected to avoid formation of agglomerated powders in the finished product. Interparticle collision times, defined by number density, size,and temperature, are critical in this regard. Growth by CVD mechanisms requires low number densities to avoid interparticle collisions during relatively long exposures to slow growth rate conditions (low supersaturation) that are needed to suppress sustained nucleation of new particles. Decreasing particle number density and increasing growth time both proportionally reduce a reactor's specific production rate (kg/liter-h of reactor volume). In contrast, growth by collision-coalescence mechanisms depend on high collision rates between high number density particles. Reported operating conditions for high-quality, uniform size Si powders are indicated by the "collision -

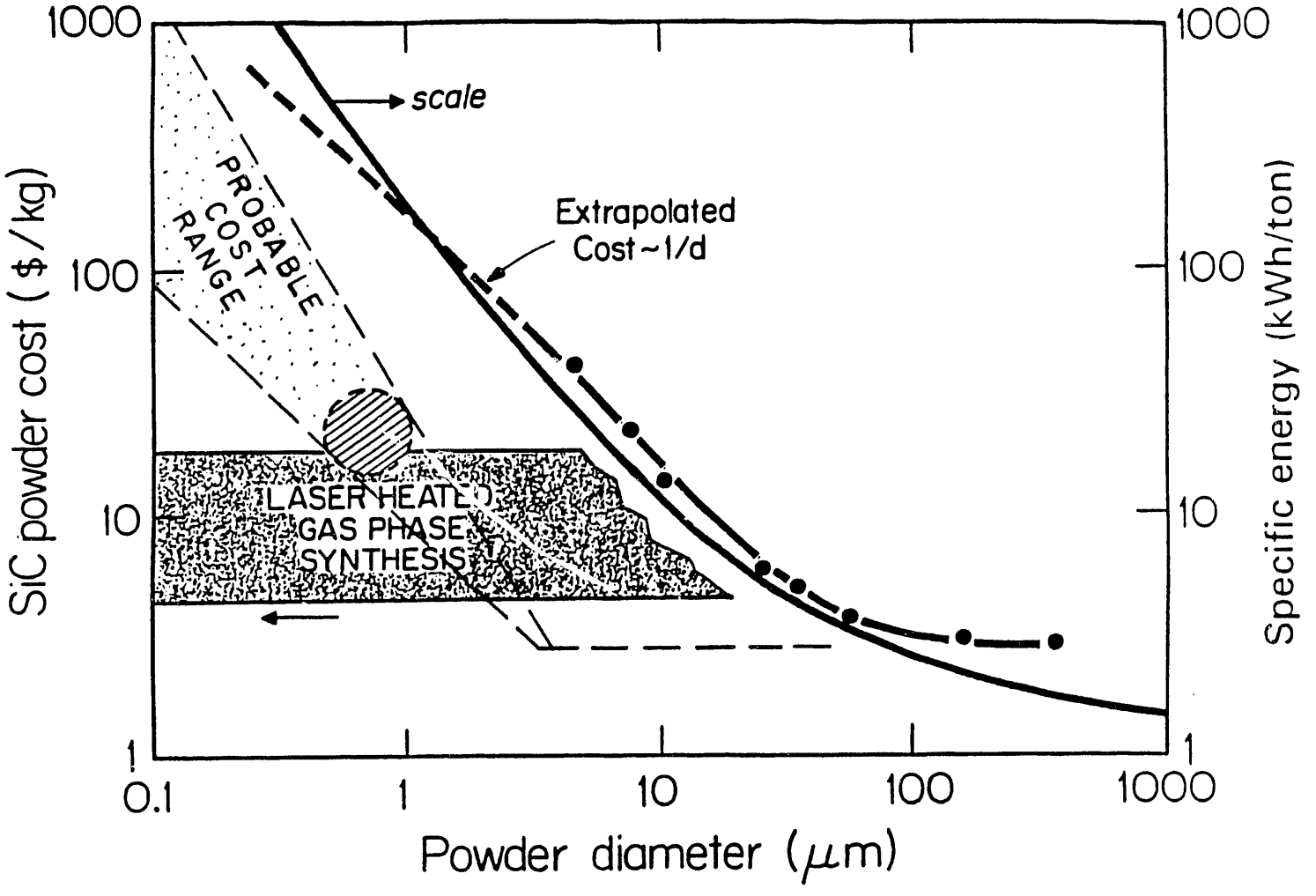

Figure 8. Cost estimates for SiC powders as a function of particle size, d. Comminution processes typically exhibit 1/d to $1/d^2$ dependencies. Gas-phase synthesis processes do not exhibit this size dependence, and thus can have a significant cost advantage for the submicron size powders needed for state-of-the-art ceramic parts.

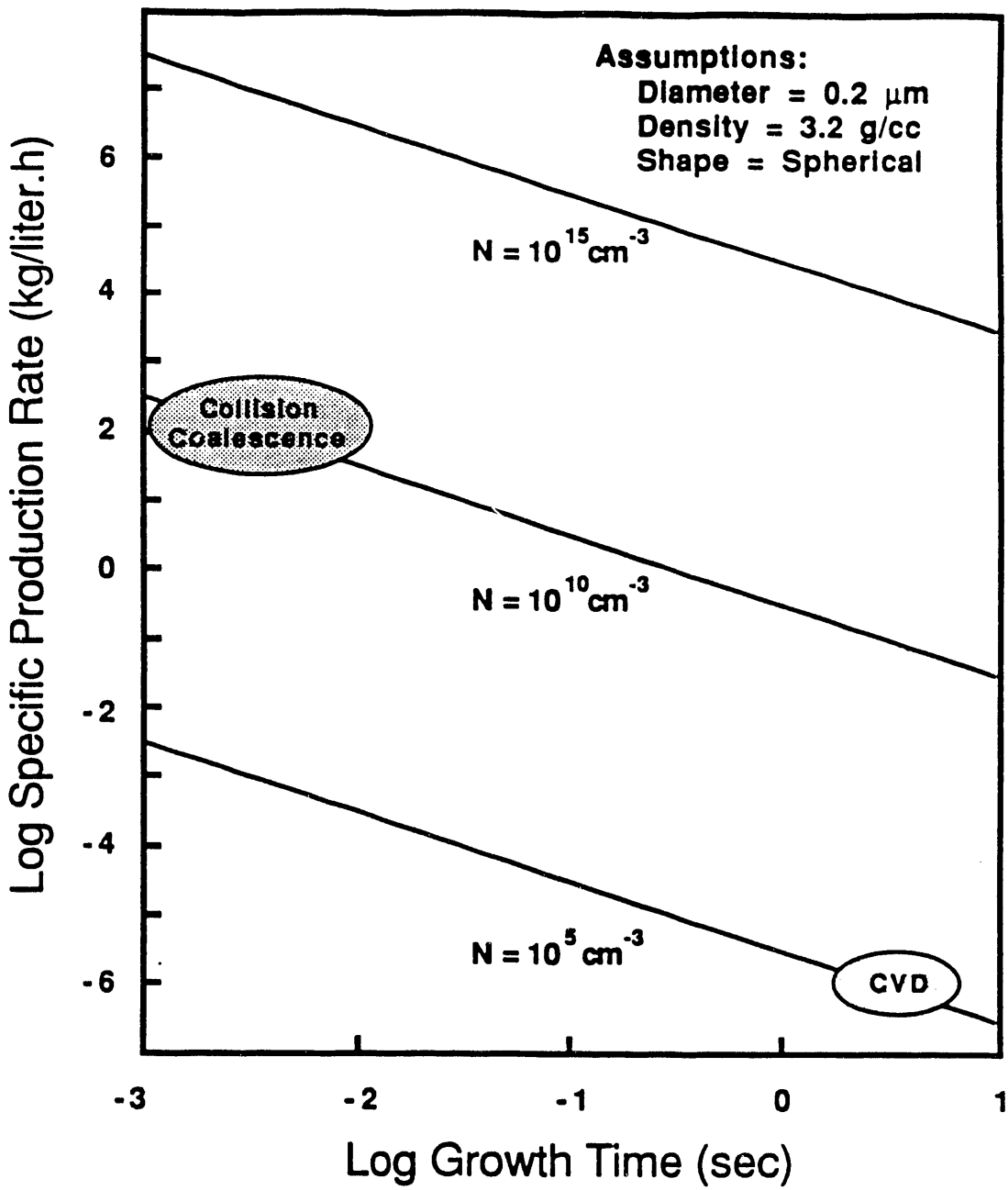

Figure 9. Hourly mass flow rates per unit volume as a function of residence (growth) time for 0.2 μm diameter spherical powders. The collision-coalescence domain is typified by number densities on the order of 10^{10} cm^{-3} and growth times between 1 and 10 ms. The CVD domain requires much lower number densities (~10^5 cm^{-3}) to avoid interparticle collisions during the long growth times (~5 s) required under low supersaturation conditions.

coalescence" and the "CVD" areas in Figure 9. The difference between the specific production rates of the two types of processes is in excess of 10^8. The CVD process produces ~10 grams for each liter of reaction volume in a year, whereas the collision-coalescence process produces ~2,000 tons. Even with displacements that could result from process improvements or changes in assumptions, it is obvious that the difference between the specific production rates will have important cost ramifications that favor synthesis by collision-coalescence mechanisms. This conclusion means that the synthesis chemistry and the reaction sequence must permit formation of liquid particles so that coalescence can keep up with high rates of collision during growth of particles greater than ~ 100Å in diameter.

Reaction enthalpies provide another important criterion for determining whether solar-heated processes will be able to produce cost-competitive products. Amortization costs for capital expenses of sophisticated, controlled-atmosphere powder synthesis equipment demand high mass flow rates and essentially continuous duty cycle production processes. Many of the reactions based on the lower cost candidate reactants are highly endothermic. Because it is unlikely that solar sources will ever practically deliver industrial levels of process power (hundreds of kilowatts), solar-heated reactors will be forced either to use typically more expensive exothermic chemistries or to operate at a significant cost disadvantage because of low throughput if endothermic chemistries are used.

The selection process for identifying suitable ceramic powders presents a formidable challenge in terms of identifying chemistries that will give reasonable prognosis of satisfying production cost targets defined by highly competitive alternative materials and processes. Potential applications, existing and candidate materials, and existing and alternative processes must be evaluated critically. Both commodity and high-value niche markets must be studied. If likely candidates are identified, engineering design criteria have been developed that will permit the solar-heated synthesis processes to be designed and developed with a high level of confidence.

5.5 Solar-Pumped Lasers

Although the prospects for solar-pumped laser development are not a primary focus of this study (a more complete evaluation is being done in a parallel study at SRI), we want to discuss briefly the current research directions, and the future promise, of this use of concentrated solar energy.

The purpose of developing solar-pumped lasers is the development of solar-powered sources capable of driving nonlinear processes (e.g., harmonic generation), and providing sources for applications requiring narrow-band radiation, (e.g., isotope separation). There are two types of solar-pumped laser systems being developed: lasers pumped by direct solar irradiation and lasers driven indirectly by black-body radiation in a cavity heated by solar irradiation.

5.5.1 Direct Solar Pumping

Direct solar pumping has been used successfully to side-pump Nd-YAG in a CPC concentrator at the Weizmann Institute in Israel. Prototypes have been developed at the University of Chicago for Nd-YAG end-pumped by a dielectric non-imaging concentrator, and for a Rhodamine dye laser side-pumped inside a specially designed non-imaging concentrator; however, they have not yet operated successfully (Winston 1990).

The important design requirements in both cases include efficient collection and coupling of the solar radiation to the lasing medium, minimizing losses in the laser cavity and cooling of the lasing medium. Calculations for the most promising solid state lasers operating in the near-IR and visible regions and for dye lasers indicate that lasing thresholds can be reached, and overall

efficiencies of 2% to 3% achieved (1.2% actual in the Weizmann laser). Limitations on efficiency include the incomplete absorption of the solar spectrum and the incomplete conversion of absorbed energy to lasing levels.

An important barrier to scale-up of solid state lasers is the heat load because of energy absorbed by levels not involved in lasing. Removal of excess heat from the laser rod will have associated costs in terms of energy and equipment. The variability of solar flux will also be a major problem at high output levels. Lasing rods used in commercial solid state lasers must be designed for specific operating temperatures and pump levels to prevent thermal lensing effects and thermal damage.

Dye lasers are susceptible to the same thermal load problems as solid state lasers because the dye solution must be cooled and the thermal instabilites in the dye flow affect lasing. It is believed by Prof. Winston of the University of Chicago that these problems may be more manageable in the case of dye lasers. Dr. Janes, an affiliate of the MIT Spectroscopy Laboratory, feels that thermal instabilities will also provide limits to dye laser scale-up, similar to those for solid state systems.

Solar pumping of both solid state and dye lasers is a field at a very early stage of development. Considerable research needs to be done on cavity designs and heat load/scale-up requirements. A user facility with a large aperture, high-flux solar source will make it much easier to design and test prototypes at a variety of scales.

5.5.2 Black Body Pumping

One of the problems of direct pumping of lasing media by concentrated solar energy is the incomplete absorption of the solar spectrum. Pumping by a black-body cavity overcomes this limitation because energy that is not absorbed by the lasing medium is absorbed and reradiated by the cavity itself. Thermal problems caused by incomplete conversion of absorbed energy to lasing levels still limit the efficiency of the laser and require a considerable investment in cooling.

Gas or liquid lasing media may be circulated through the black-body cavity, and then into a heat exchanger or radiator. Solid state lasers require a flow of cooling liquid or gas in an envelope around the rod, which must then be cooled. For Nd-YAG, optimum efficiency of absorption into 1.06-μm lasing bands occurs at temperatures above 2500 K (Christiansen 1990). At that temperature, 30% of the energy is expected to be absorbed by the 1.06-μm levels, leaving 70% of the absorbed energy to be dissipated as waste heat. Frequency-selective coatings on the lasing rods may reduce the excess heat.

5.6 Special Applications

Unusual manufacturing requirements or constraints, or special geographical situations, may provide opportunities for new or unconventional utilization of solar concentrators. In remote locations, solar concentrators may prove useful as the heat source for Stirling or Rankine engines (Langhoff 1990). These would provide shaft power to operate electrical generators and water storage pumps to counteract the effects of diurnal variations in solar energy availability. There is a need to carry out cycle efficiency analyses for this application and to compare it with other renewables- and nonrenewables-based options for generating shaft power (and electricity) in remote locations. Technical areas in need of further research include materials problems associated with sodium heat pipes for transferring concentrated solar energy to the free piston expansion chamber of the Stirling engine (Langhoff 1990).

While displacement of an imported joule or Btu of energy by a domestically available and renewable amount is of interest, the quality of that displaced energy, i.e., the temperature at which it must be delivered to be effective in the process of interest, is also important. In this regard, the solar concentrator is capable of generating thermal energy at very high temperatures and thus may offer special advantages as a renewable source of high-temperature process heat, especially above 300°C. Alternative sources of high process temperatures include combustion of fossil and other fuels, and electricity-driven thermal plasmas. The solar furnace provides high-temperature process heat from a renewable, domestically secure source. Further, the solar furnace does not contribute to net increases in atmospheric carbon dioxide concentrations. For these reasons, carbon taxes or other regulatory factors, or national security considerations, may enable solar furnaces to be viewed as more competitive with some of the above alternatives for certain applications.

Applications of solar concentrators to destruction of hazardous wastes was not within the scope of the present study, although this application now commands significant interest as a potential practical use for solar concentrators. In the present study, it is instructive to examine another potential application of solar concentrators in the waste management area, namely waste recycling rather than waste destruction. The rationale is as follows. Toxic or otherwise hazardous or unwanted coproducts from chemical processes and other industries are often so dilute, so contaminated, or so refractory, that they must be permanently disposed of, for example, by incineration or biodegradation. In contrast, some hazardous industrial residues are also amenable to thermal recovery of valuable chemicals or their precursors. For example, pyrolysis has been used to recover HCl or other monomers from waste samples of thermoplastics such as polyvinylchloride, teflon, polystyrene, and polymethyl-methacrylate (Hong 1987). However, there remains opportunity to optimize for hazardous and other industrial process residues, thermal or partially thermal, recovery/recycling technologies, including approaches based on solar concentrators. Successful development of such technologies would allow industry to recycle at least some of their toxic residues to valuable chemicals, thereby reducing the volumes of process wastes requiring expensive treatment, storage, and disposal. Candidate wastes for solar thermal processing include solid halogenated organic residues from polymer manufacturing processes.

The literature on polymer pyrolysis is supportive of this proposed application. Table 6 shows data from Fong (1986) and Fong et al. (1986) on effects of temperature and treatment time on the major products from pyrolysis of a rather complex thermoplastic natural polymer (an eastern U.S. bituminous coal). External hydrogen was not employed in these experiments. Here "extractables" were recovered by rapidly quenching the partially reacted material, and then extracting the residue with pyridine at roughly its boiling point (115.5°C). Extractables are a potentially valuable product, precursor, or recycle feed. Other data from Fong (1986) and Fong et al. (1986) show an optimum treatment "severity" (temperature and time) for recovering large extract yields (up to about 70 wt.% of the starting material). Inadequate treatment provides too little conversion, while excess severity causes molecular weight growth and further conversion of the extracts to a carbonaceous residue (char or coke).

The parent chemical structure and thermal decomposition chemistry of coal are sufficiently complicated that extractables are generally complex mixtures of hundreds of aromatic, hetero-aromatic, and aliphatic compounds. Literature data (Cullis and Hirschler 1981; Boonstra and van Amerongen 1949; Shafizadeh and Fu 1973) show that controlled pyrolysis of simpler starting materials, including cellulose, rubber, and several synthetic polymers such as polymethylmethacrylate, poly (p-chlorostyrene), and poly(alpha-methylstyrene) remits high yields of the corresponding parent monomer (80 to >90 wt %). Pyrolysis of other simple polymers (e.g., polyethylene, polyvinylchloride) gives low yields of monomers (Cullis and Hirschler 1981), although improvements may be possible if a suspected rapid repolymerization of reactive intermediates can be prevented.

Solar concentrators could provide the means to subject process wastes and residues to properly chosen heating and cooling cycles, allowing at least partial reprocessing of those wastes to monomers or other valuable products. Research is needed to establish technically and economically viable treatment conditions. These are expected to depend on the thermal degradation chemistry and on the composition, phase, morphology, and overall heterogeneity of the waste. Research should focus on identifying treatment conditions optimizing recycle product yields *and* quality (measured in terms of recovery of separable quantities of specific monomers or other premium value feedstocks, intermediates, or by-products). Even those recycling conditions providing high yields of desired products can be expected to generate some "secondary" residues that may be hazardous. The composition, toxicity, and gasification/oxidation reactivity of secondary residues should be determined to index their potential hazard and assess possible remediation options.

A related opportunity is to learn how to optimally use the thermal and photochemical effects of concentrated solar photons, with or without added heterogeneous catalysts, to achieve desired yields and quality of recycled products. The potential of solar furnaces to drive combined thermal, photochemical, and catalytic processes may offer special advantages in recycling mixed wastes, e.g., by tuning certain wavelength bands to chromophores unique to one waste component or by use of recoverable photosensitizers. Success here would address one of the very challenging current problems for waste recycling technologies, namely the desire to reprocess mixed wastes to useful products without first separating the mixture into individual components.

Potential benefits to industry of recycling process wastes would include recovery of valuable feedstocks, intermediates, or by-product chemicals, and reductions in the amounts of hazardous process residues that would require expensive treatment, storage, and disposal.

TABLE 6. Yield of Coal Extractables from Controlled Heating without External Hydrogen or Donor Solvents[a,b,c]

Heatup Rate, °C/s	Final Temp., °C	Total Thermal Soak Time, s	Quench Rate, °C/s	Extractables Yield, wt% DAF[d]
3300	635	0.5	4500	60
450	582	2	e	69
470	540	4	1100	71

[a]Data of Fong (1986); Fong et al. (1986).
[b]Total pressure 1 atm of helium.
[c]Coal: Pittsburgh No. 8 bituminous.
[d]Extractables yield determined as described in text.
[e]Not known.

SECTION 6

FINDINGS AND RECOMMENDATIONS

In this report, we reviewed numerous suggested possibilities for applications of photochemistry to chemical and materials processing, with particular attention to concentrated solar energy. The purpose of the thorough review of previous work in these areas was to ensure that "that which has been done" is not simply duplicated, unless there is a strong prospect that by doing so new, useful information and/or new potential processes may be discovered.

Our overall conclusion is that there may be a number of processes which, if not entirely novel, represent essentially new applications for concentrated solar energy. Furthermore, they appear to be feasible with present or anticipated near-term technology, and therefore merit further investigation. In addition, it is our view that ongoing developments in many diverse areas of science and technology will open new, unforeseen opportunities in applications of concentrated solar energy relevant to national needs.

At present our consensus is that the most economically defensible applications for solar concentrators will most probably be found in the manufacture or processing of high value added materials, in specialized situations where solar resources are readily available and other energy sources are in short supply, or in central user facilities for research and testing applications. During the next one to two decades it is possible that changes in national or international policies or priorities, advances by economists in learning how to measure costs and benefits of environmental factors, national security issues, or advances in technology may produce situations where additional applications become economically interesting.

In order to respond to this diversity of potential applications, our principal recommendation is to establish a National Solar Concentrator Research Facility at the NREL Solar Furnace site in Golden, Colorado. This would promote testing and evaluation of a wide range of proposed processes. The Department of Energy has had extensive and, for the most part, rewarding experience with specialized user facilities, such as the synchrotron radiation sources at Brookhaven and Wisconsin and the new electron-beam metal processing consortium at Sandia (Dagani 1990). A National Solar Concentrator Research Facility would provide a unique resource for the country and would promote applications of solar concentrator technology by drawing on the considerable expertise available in academic, industrial, and national laboratories.

Among the many possibilities which might be explored in depth at such a facility are the new C_{60} chemistry and "laser-jet" photochemistry, discussed in Sections 5.1 and 5.3; applications to materials processing and synthesis of fine ceramic powders, discussed in Section 5.5; and special applications such as solar-powered waste recycling, discussed in Section 5.7. A further suggestion which arose during our discussions was that effective use could be made of the high near-infrared flux in the solar source by installing a near-IR Fourier-Transform spectrometer at such a facility. This instrument could find extensive use in measurement of the optical properties of compounds and materials in this wavelength range. Such information, which is needed for solar process design and optimization, is frequently not available.

The intermittency and limited duty cycle of the solar source could potentially be a problem in scheduling user time; however, when compared with the extended downtimes frequently encountered in large central user facilities, such as particle accelerators, the overall duty cycle of a Solar Concentrator Research Facility may be quite favorable.

Our recommendations now follow.

1. Establish a National Solar Concentrator Research Facility with an extramural support program. Such a user facility, which would be located at the current NREL site in Colorado, can be modeled after the synchrotron light source facilities at Brookhaven and Wisconsin or the recently established Sandia Electron-Beam Facility for Specialty Metals Processing. The extramural support program would provide an incentive for users to come to the facility, and would enable them to carry out the necessary preliminary work and apparatus construction in their own laboratories. In such a facility, a variety of concentrator designs may be appropriate for applications requiring a range of solar flux:

- a paraboloidal trough (100 suns, no tracking) for relatively low-flux applications;
- the existing primary concentrator for applications requiring 1000 to 5000 suns; and
- a secondary (dielectric) concentrator capable of exceeding 20,000 suns, for solar-pumped laser research and applications such as laser-jet photochemistry.

A corollary of this recommendation is that no large-scale demonstration facility is recommended at this time, pending further research and analysis.

2. Among the most promising near-term potential applications identified are those in the areas of materials processing and materials testing. Of particular interest are certain types of surface treatment of metals and alloys, deposition of selected thin-film materials, synthesis of fine ceramic powders, and testing of materials for high severity environments, such as solar thermal reactors and space and nattonal defense applications.

3. A research emphasis on high-temperature, high-intensity photochemistry is strongly recommended. Such research could lead to significant new applications of concentrated solar energy.

4. Several additional specialized "niche" applications for concentrated solar energy have been identified in Section 5.7, such as driving Stirling engines or on-site waste recycling. Such applications may have export potential to and be suitable for situations in which conventional energy sources are unavailable or especially expensive.

5. Methodologies should be established for systematic continuing evaluation of identified and other potential applications for concentrated solar energy, based on the criteria developed during this study. These criteria include the scientific and technical aspects discussed in Section 4.1, the practical and economic aspects discussed in Section 4.2, and context externalities such as environmental impact and energy security.

6. Detailed economic analysis of a few candidate processes should be carried out using the quantitative process modeling tools described in Section 4. The objective of such analysis would be to define the energy price breakeven point at which a process may become economically viable with respect to alternatives. The "carbon cost" (for energy derived from fossil fuels), "radwaste cost" (for nuclear energy), and other costs associated with downstream environmental and health burdens, should be accounted for in such comparisons.

7. A high priority should be placed on involving industry in solar energy applications development. During the course of this study, several sites of potential interest in industry were identified. These included Cummins (Stirling Engine), Inrad (photochlorination), and Coors (ceramic powders). Given the limited time available, however, it was not possible to pursue these contacts at greater length to establish the nature and level of industrial interests. Mechanisms to facilitate collaborative interactions between the public and private sectors, such as the recently enacted CRADA Program, are expected to be valuable in matching industrial needs and interests with solar concentrator capabilities.

8. There is a need for increased public awareness about solar energy programs and about possible funding for solar energy applications. In the study team's discussions with other scientists, a frequently encountered response was lack of information about current programs, and pleasant surprise on learning of efforts under way to utilize solar energy in the United States. One possible mechanism for accomplishing this would be to hold a symposium on solar concentrator optics and applications at a venue such as a Society of Photo-Optical Instrumentation Engineers (SPIE) Conference or the Intersociety Energy Conversion Engineering Conference.

SECTION 7

REFERENCES

Albach, G., 1991, "New Roles for Lamps in Materials Processing," Photonics Spectra, January, 1991, p. 149.

Allen, S.D. and A.B. Tringubo, 1983, J. Appl. Phys. **54,** 1641.

Allen, S.D., R.Y. Jan, S.M. Mazuk and S.D. Vernon, 1985, J. Appl. Phys. **58,** 327.

Arbogast, J.W., A.P. Darmanyan, C.S. Foote, Y. Rubin, F.N. Diederich, M.M. Alvarez, S.J. Anz and R.L. Whetten, 1991, J. Phys. Chem., **95,** 11.

Armstead, H.C.H. and J.W. Tester, 1987, Heat Mining, E.& F.N. Spon, New York, p. 403.

Arnone, C., M. Rothschild, J.G. Black and D.J. Ehrlich, 1986, Appl. Phys. Lett. **48,** 1018.

Ashby, C.I., 1985, Appl. Phys. Lett. **46**, 752.

Ashby, C.I., 1986, J. Vac. Sci. Technol. **A4**, 666.

AspenTech, 1990: Aspen Technology, Inc. of Cambridge, Mass. supports and maintains the ASPEN PLUS process simulator, which includes an integrated preliminary grade cost estimation system. The software is available commercially.

Avron, M., 1990, The Biotechnology of Cultivating *Dunaliella* Rich in Beta-Carotene: from Basic Research to Industrial Production, presented at SERI NRC/NAS Workshop on the Use of Concentrated Solar Energy, Golden, Colorado.

Bassett, I.M., W.T. Welford and R. Winston, 1989, "Non-imaging Optics for Flux Concentration," in Progress in Optics XXVII, (E. Wolf, ed.), Elsevier, Amsterdam (NL).

Bauerle, D., 1989, Appl. Phys. A **48**, 527.

Bilgen, E., 1990, Thermal, Thermochemical and Hybrid Solar Hydrogen Production, SERI NRC/NAS Workshop on the Use of Concentrated Solar Energy, Golden, Colorado.

Black, J.G., S.P. Doran, M. Rothschild and D.J. Ehrlich, 1990, Appl. Phys. Lett. **56**, 1072.

Boonstra, B.B.S.T. and G.J. van Amerongen, 1949, "Pyrolytic Decomposition of Rubber into Isoprene," Ind. and Eng. Chem., **41**, 161.

Bowen, H.K., 1980, "Basic Research Needs on High Temperature Ceramics for Energy Applications," Mat. Sci. and Eng. **44,** 1-56.

Bowers J.E., B.R. Hemenway and D.P. Wilt, 1985, Appl. Phys. Lett. **46**, 453.

Brown, L.M., 1990, Production Potential of Biochemicals from Algae Under Increased Solar Irradiance and Other Biotechnological Innovations Enabled by Higher Solar Concentration, presented at SERI NRC/NAS Workshop on the Use of Concentrated Solar Energy, Golden, Colorado.

Buerki, P.R. and S. Leutwyler, 1991, J. Appl. Phys. **69**, 3739.

Buhl, M.L., R.E. Bird, R.U. Bilchak, J.S. Connolly and J.R. Bolton, 1984, Solar Energy **32**, 75.

Bunkin F.V., B.S. Luk'yanchuk, G.A. Kozlova, A.I. Portniagin, A.A. Yerymenko and P. Mogyorosi, 1985, Appl. Phys. A **37**, 117.

Carasso, M. and A. Lewandowski, 1990, private communication.

Chemical Marketing Reporter, 1991, various issues. Source of many of the data on costs and yearly production volume of chemicals in Figure A.1.

Christiansen, W.H., 1990, SERI NRC/NAS Workshop on the Use of Concentrated Solar Energy, Golden, Colo.

Cullis, C.F. and M.M. Hirshcler, 1981, The Combustion of Organic Polymers, Oxford University Press, New York, p. 119,

Curl, R.F. and Smalley, R.E., 1991, Scientific American **265** (4), 54.

Dagani, R., 1990, "DOE Technology To Be Shared with Industry," Chem. and Eng. News **68**, 31, pp. 20-21.

Dekumbis, R., 1987, Chem. Eng. Prog. **83**, 23.

Ehrlich, D.J. and R.M. Osgood, Jr., 1981, Chem. Phys. Lett. **79**,381.

EPRI, 1990, "Breaking Through Performance Limits Beyond Steam," EPRI Journal **15**, 8, pp. 4-11.

Foex, M., 1965, Solar Energy **9**, 61.

Fong, W.S., 1986, "Plasticity and Agglomeration of Coal Pyrolysis," Sc.D. Thesis, Dept. of Chemical Engineering, MIT, Cambridge, Mass.

Fong, W.S., Y.F. Khalil, W.A. Peters and J.B. Howard, 1986, "Plastic Behavior of Coal Under Rapid-Heating High-Temperature Conditions," Fuel **65**, 195-201.

Glandt, E.D. and A.L. Myers, 1976, Ind. Eng. Chem. Process Des. Dev. **15**, 100.

Glasstone, S., 1982, Energy Deskbook, sponsored by the USDOE, available as DE82013966 (DOE/IR/05114-1), National Technical Information Service, U.S. Department of Commerce, Springfield, Va., p. 350.

Gleckman, P., J. O'Gallagher and R. Winston, 1989, "Concentration of Sunlight to Solar-Surface Levels Using Non-imaging Optics," Nature **339**, 198-200.

Gottsleben, O. and M. Stuke, 1988, Appl. Phys. Lett. **52**, 2230.

Haggerty, J.S. and W.R. Cannon, 1981, "Sinterable Powders from Laser-driven Reactions" in Laser-induced Chemical Processes, (J.I. Steinfeld, ed.), Plenum Press, New York, p. 165.

Haigh, J. and M.R. Aylett, 1988, Prog. Quant. Electr. **12,** 1.

Hajaligol, M.R., W.A. Peters and J.B. Howard, 1988, "Intraparticle Nonisothermalities in Coal Pyrolysis," Energy & Fuels, **2**, 430-437.

Hajaligol, M.R., W.A. Peters and J.B. Howard, 1991, "Effects of Transient Heat Transfer on Kinetics Parameters for Cellulose Pyrolysis," Combustion and Flame (submitted).

Hammache, A. and E. Bilgen, 1988, Intl. J. Hydrogen Energy **13**, 539.

Herman, I.P., 1989, Chem. Rev. **89,** 1323.

Hirota, Y. and O. Mikami, 1985, Electr. Letts. **21,** 77.

Hong, K.C.C., 1987, "Plastic Waste and the Environment," Term paper in Subject 10.72J/TPP52J, MIT, Cambridge, Mass.

Howard, J.B., 1991, private communication.

Howard, J.B., J.T. McKinnon, Y. Makarovsky, A.L. Lafleur and M. E. Johnson, 1991, "Fullerenes C_{60} and C_{70} in Flames," Nature **352,** 139-141.

JANAF, 1974, JANAF Thermochemical Tables, 1974 Supplement, entry "Calcium Oxide (CaO) (crystal)."

Jackman, R.B., J.S. Foord, A.E. Adams and M.L. Lloyd, 1986, J. Appl. Phys. **59,** 2031.

Johnson A.W. and G.C. Tisone, 1984, Mat. Res. Soc. Symp. Proc. **29**, 145.

Karlicek, R.F., V.M. Donnelly and G.J. Collins, 1982, J. Appl. Phys. **53,** 1084.

Karp, A., R. Smith and S. Ahmod, 1990, Pinch Technology: A Primer, Report by Linnhoff March, Inc. to the Electric Power Research Institute, Palo Alto, CA. EPRI Report No. CU-6775.

Kolb, G., 1990, Solar Furnaces vs Arc Lamps -- A Comparison of the Economics of Energy Delivery, SERI NRC/NAS Workshop on the Use of Concentrated Solar Energy, Golden, Colorado.

Kratschmer, W., L.D. Lamb, K. Fostiropoulos and D.R. Huffman 1990, Nature **347,** 354.

Kroto, H.W., J.R. Heath, S.C. O'Brien, R.F. Curl and R.E. Smalley 1985, Nature **318,** 162.

Langhoff, P.W., 1990, private communication.

Lin, S.H., Y. Fujimura, H.J. Neusser and E.W. Schlag, 1984, Multiphoton Spectroscopy of Molecules, Academic Press, New York.

Lin, S.H., 1986, Advances in Multiphoton Processes and Spectroscopy, Vol. 2, World Scientific Publishing Pte Ltd, Singapore.

Mackay, A.L., 1990, Nature **347**, 336.

Micheels, R.H., A.D. Darrow and R.D. Rauh, 1981, Appl. Phys. Lett. **39**, 418.

Minakota, M. and Y. Furukawa, 1986, J. Electr. Mater. **15**, 159.

Montgomery, R.K. and T.D. Mantei, 1986, Appl. Phys. Lett. **48**, 493.

Nair, P.K. and M.T.S. Nair, 1987, Solar Energy Materials **15**, 431.

Neugebauer, G., and E.E. Becklin, 1973, "The Brightest Infrared Sources," Sci. Am. **228**, 28.

Noyes, R.W., 1976, "New Developments in Solar Research," in Frontiers in Astrophysics, (E.H. Avrett, ed.), Harvard Univ. Press, Cambridge, Mass.

Okano, H., Y. Horiike and M. Sekine, 1985, Japanese J. Appl. Phys. **24**, 68.

Parsons, C.A., B.R. Thacker, D.M. Szmyd, M.W. Peterson, W.E. McMahon and A.J. Nozik, 1990, J. Chem. Phys. **93**, 7706.

Perry, R.H., D.W. Green and J.O. Maloney, 1984, Perry's Chemical Engineers' Handbook, Sixth Edition, especially F.A. Holland, "Process Economics," Chapter 25, McGraw-Hill, New York.

Peters, M.S. and K.D. Timmerhaus, 1980, Plant Design and Economics for Chemical Engineers, Third Edition, McGraw-Hill, New York.

Petzoldt, F., K. Piglmayer, W. Krauter and D. Bauerle, 1984, Appl. Phys. A. **35**, 155.

Pitts, J.R., J.T. Stanley, E. Tracy, Y. Shacton and C.L. Fidd, 1990, Materials Processing with Concentrated Solar Radiation, presented at SERI NRC/NAS Workshop on the Use of Concentrated Solar Energy, Golden, Colorado.

Podlesnik D.V., H.H. Gilgen and R.M. Osgood, 1984, Appl. Phys. Lett. **45**, 563.

Pola J., V. Chvalovsky, E.A. Volnina and L.E. Guselnikov, 1988, J. Organometallic Chem. **341**, C13.

Pool, R., 1990, Science **250**, 209.

Richtmyer, F.K., E.H. Kennard and T. Lauritsen, 1955, Introduction to Modern Physics, McGraw-Hill Book Co., New York, pp. 110-113.

Rose, L.T., D.H. Longendorfer and R.D. Rauh, 1983, Appl. Phys. Lett. **42**, 193.

Ross, P.R., 1990, "A Million Watts of Light," Sci. Amer. **263** (11), p. 138.

Shafizadeh, F. and Y.L. Fu, 1973, "Pyrolysis of Cellulose," Carbohy. Res. **29**, 113.

Singmaster, K.A., F.A. Houle and R.J. Wilson, 1990, J. Phys. Chem. **94**, 6864.

Smoluchowski, R., 1983, The Solar System, Sci. Am. Books, New York.

Solanki, R. and G.J. Collins, 1983, Appl. Phys. Lett. **42**, 662.

SRI, 1990, The Stanford Research Institute Process Engineering Program (PEP) is available to subscribers for a fee. Programs are used to perform in-depth economic evaluations of chemical processes.

Sugimura, A, Y. Fukuda and M. Hanabusa, 1987, J. Appl. Phys. **62**, 3222.

Szikora, S., W. Krauter and D. Bauerle, 1984, Mater. Lett. **2**, 263.

Tenne, R. and G. Hodes, 1983, Surf. Sci. **135**, 453.

Thekaekara, M.P., 1974, Appl. Opt. **13**, 518-522.

Tokuda, J., M. Takai, K. Gamo and S. Namba, 1988, Mater. Res. Soc. Symp. Proc. **101**, 261.

Tsao, J.Y., R.A. Becker, D.J. Ehrlich and F.J. Leonberger, 1983, Appl. Phys. Lett. **42**, 559.

von Gutfeld, R.J. and D.R. Vigliotti, 1985, Appl. Phys. Lett. **46**, 1003.

Watanabe, M., M. Furuya, Y. Miyoshi, Y. Inoue., I. Iwahashi and K. Matsumoto, 1982, Photochem. Photobiol. **36**, 491.

Welford, W.T. and R. Winston, 1989, High Collection Non-imaging Optics, Academic Press, San Diego.

Wilson, R.M., K.A. Schnapp, K. Hannemann, D.M. Ho, H.R. Memarian, A. Azadnia, A.R. Pinhas and T.M. Figley, 1990, Spectrochim. Acta **46A**, 551.

Winston, R., 1990, private communication.

Winston, R., 1991, Sci. Am., **264**, 76.

Woodin, R.L., D.S. Bomse and G.W. Rice, 1990, Chem. and Eng. News **68**, 51, p. 20.

Xu Xin and J.I. Steinfeld, 1990, Appl. Surf. Sci. **45**, 281.

Yamagashi, K. and Y. Tarui, 1986, Jap. J. Appl. Phys. **25**, L306.

Yokoyama, H., S. Kishida and K. Washio, 1984, Appl. Phys. Lett. **44**, 755.

Zhang, G.Q., T. Szorenyi and D.J. Bauerle, 1987, Appl. Phys. **62**, 673.

APPENDIX A.
GENERAL PRINCIPLES OF PHOTON-DRIVEN CHEMISTRY

A.1 Fundamental Principles

Ever since the laser became generally available as a source of intense, tunable, coherent radiation, many chemists, physicists, and materials scientists have sought to make use of these devices in chemical processing. Numerous studies and reviews (Cantrell et al. 1979; Kaldor and Woodin 1982; Lyman 1987; Steinfeld and Wrighton 1976; Steinfeld et al. 1979; Steinfeld 1981; Woodin et al. 1990) have suggested possibilities, and also delineated the constraints that must be taken into account in evaluating these possibilities. Because many of these considerations apply equally well to solar-driven as to laser-driven processes, we summarize here some of the principal findings in these studies.

Several mechanisms exist by which chemical reactions may be induced or accelerated by absorption of optical radiation. If the absorbed energy is rapidly dissipated in the material, the resulting bulk temperature increase may simply induce a *photothermal* acceleration of the reaction rate. If absorbed infrared energy is retained in the vibrational degrees of freedom of an isolated molecule. in which thermalization is not possible, decomposition or isomerization caused by *vibrational* photochemistry may ensue. Because the energies of infrared photons corresponding to vibrational fundamental absorptions (3000 to 500 cm^{-1}) are, in general, considerably less than the activation barriers for such reactions, absorption of several infrared photons is required to reach the reaction threshhold. This infra-red multi-photon excitation (IRMPE) process has been widely studied using pulsed CO_2 lasers (Ambartzumian and Letokhov 1977; Francisco and Steinfeld 1986). However, as has been shown in Section 5.1, the spectral brightness of even the highest attainable concentrated solar flux is many orders of magnitude less than that which would be required for IRMPE. Excitation through vibrational overtone absorptions in the near-infrared part of the spectrum can, in principle, deposit sufficient energy in a single molecule for a reaction to occur. The limitation on this process is that cross sections for overtone absorption are much smaller than for fundamental absorption; the decrease is about a factor of 10 for each increment in vibrational quantum number change. A further mechanism for photochemical excitation is via *electronic* states, which typically lie in the ultraviolet part of the spectrum.

Opportunities for solar-driven photochemistry are somewhat restricted by these fundamental constraints. Because the solar spectrum does not extend below 300 nm, only low-lying (<30,000 cm^{-1}) electronic states can be accessed directly. In favorable situations, vibrational overtone excitation may be possible with the near-infrared flux from highly concentrated sources. In most instances, the simple photothermal process will be dominant. This may be advantageously combined with photoexcitation of vibrationally "hot" species and/or chemical intermediates, as considered in Section 5.

A.2 Economic Constraints on Applications

Despite extensive efforts in academic, industrial, and national research laboratories, relatively few applications of laser-driven chemistry have emerged to date. A primary reason for this is the high cost of photons as chemical reagents, compared with the selling price of typical commercial and commodity chemicals. This comparison, which has been made by Kaldor and Woodin (1982) and Woodin et al. (1990), among others, is shown in Figure A1. It is clear that high-volume commodity chemicals, which appear in the lower right-hand part of the figure, must have a low selling price to be economically viable. This places them below the cost threshhold associated with photon-driven chemistry. Only small-volume specialty chemicals, in the upper left-hand part of the figure, can be sold at prices high enough to

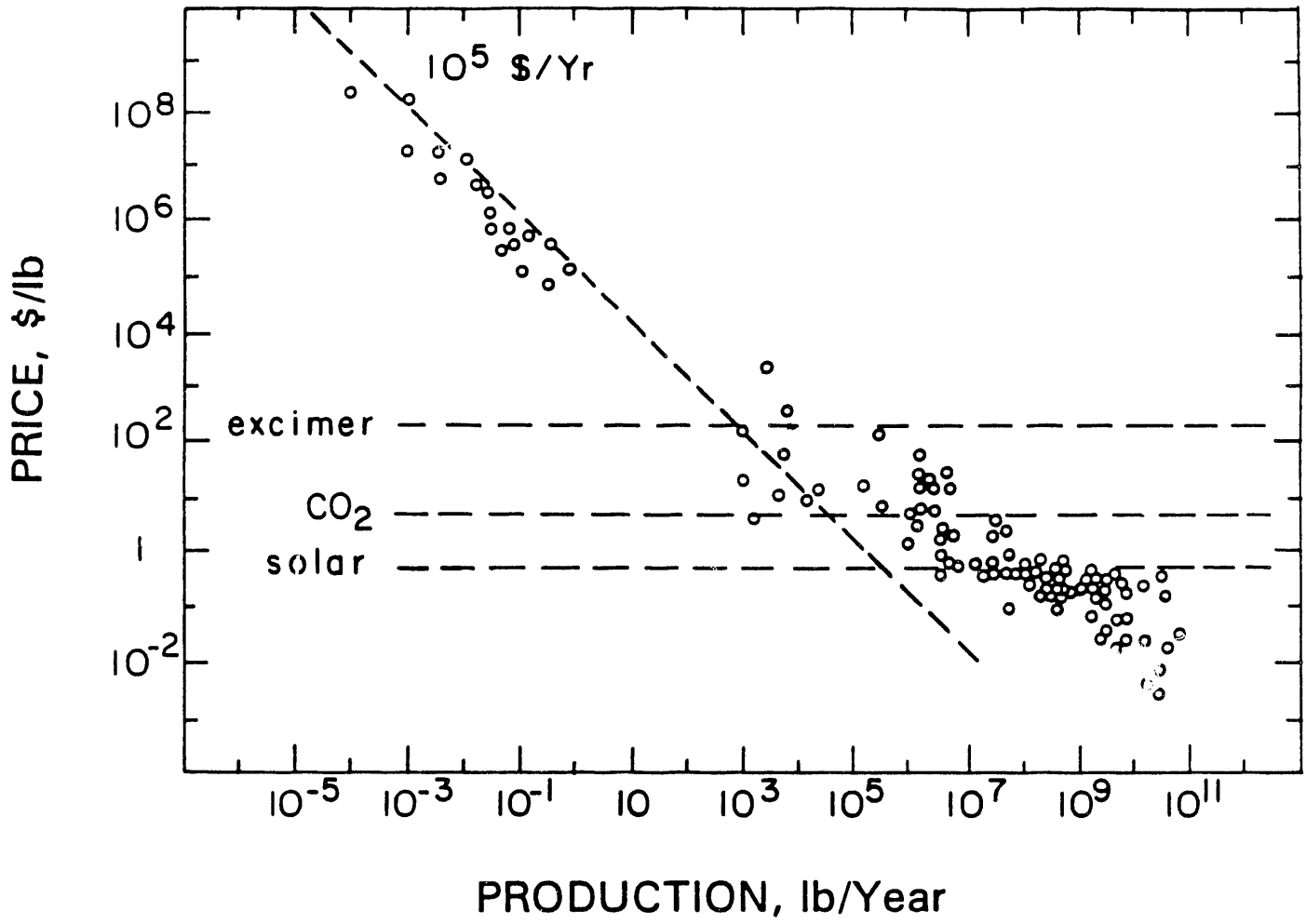

Figure A1. Price production volume correlation for industrial chemicals: The excimer, CO_2, and solar cost lines are those estimated for processing a nominal "1 lb" of material, using photon energy cost estimates from Section 3: adapted from Kaldor and Woodin (1982) and Yardley (1990).

recover the photon energy costs. Examples of such specialty products might be pharmaceuticals, biological materials, and isotopically enriched compounds.

In summary, while the costs associated with concentrated solar photon processing are slightly more favorable than for laser processing, its applicability is still largely limited to high-value-added materials in which the photon energy cost is only a small part of overall processing costs. Examples of such high-value-added materials and processes include surface treatment of microelectronic devices and complex biological (possibly genetically engineered) compounds in which additional high-cost processing steps are required. This limitation can be relaxed somewhat if the photons are used non-stoichiometrically, e.g., to initiate a chain reaction with a long chain length or to activate a catalyst with a large turnover number. This may be realized in a photoinitiated exothermic reaction in which the reaction is maintained by energy released following an initial activation step. Fine powder synthesis (Section 5.5.3) may be an example of such a process. Finally, there may be special situations in which solar energy is available in the absence of other energy sources, such as those described briefly in Section 5.7.

References

Ambartzumian, R.V. and V.S. Letokhov, 1977, "Multiple Photon Infrared Laser Photochemistry," in Chemical and Biochemical Applications of Lasers, Vol. 3 (C.B. Moore, ed.), Academic Press, New York, pp. 167-314.

Cantrell, C.D., S.M. Freund and J.L. Lyman, 1979, "Laser-Induced Chemical Reactions and Isotope Separation," in Laser Handbook, Vol. 3 (M. Stitch, ed.), North-Holland Publishing Co., Amsterdam, pp. 485-576.

Chemical Marketing Reporter, 1991, various issues. Source of many of the data in Figure A.1 on costs and yearly production volume of chemicals

Francisco, J.S. and J.I. Steinfeld, 1986, "Photochemistry, Photophysics, and Spectroscopy of Molecular Infrared Multiple Photon Excitation," in Advances in Multiphoton Processes and Spectroscopy, Vol. 2 (S.H. Lin, ed.), World Scientific Publishing, Singapore, pp. 79-173.

Kaldor, A. and Woodin, R.L., 1982, Proc. I.E.E.E. **70,** 565.

Lyman, J.L., 1987, "Laser-Induced Molecular Dissociation: Applications in Isotope Separation and Related Processes," in Laser Spectroscopy and Its Applications (L.J. Radziemski, R.W. Solarz, and J.A. Paisner), M. Dekker Inc., New York, pp. 417-505.

Steinfeld, J.I. and M.S. Wrighton, 1976, "The Laser Revolution in Energy-Related Chemistry," National Science Foundation Workshop Report, Washington, D.C.

Steinfeld, J.I. et al., 1979, Laser Photochemistry and Diagnostics: Recent Advances and Future Prospects, Report on a NSF/DOE Seminar for Government Agency Representatives,Washington, D.C.

Steinfeld, J.I. (ed.), 1981, Laser-Induced Chemical Processes, Plenum Press, New York.

Woodin, R.L., D.S. Bomse and G.W. Rice, 1990, "Lasers in Chemical Processing", Chem. and Eng. News **68,** (51), pp. 20-31.

Yardley, J.T., 1990, Potential Industrial Applications of Photons, presented at SERI Workshop on Potential Applications of Solar Photons.

APPENDIX B
A Guide to the Data bases

The following 16 data bases within Pro-Cite were created:

Name	No. of Citations+	General Content	Search Criteria§
photoele	1334	photoelectrochemistry	(electr* AND photo*)OR photoelectr*
matpho	1136	light and materials	(photo* OR lase*) AND deposit* OR (photo* OR lase*) AND etch* OR (photo* OR lase*) AND anneal* OR photo* AND chem* AND surface OR lase* AND surface
phosyn	460	light induced synthesis	photo* AND synth*
photocat	167	photocatalysis	photocat*
photoox	153	photooxidation	photoox*
photobio	94	photobiology	photobio*
phochsyn	93	photochemical synthesis	synth* AND (photochem* OR (photo* AND chem*))
solchem	66	solar chemistry	solar* AND chem*
solarlas	33	solar lasers	solar* AND lase*
photocon	32	photoconversions	photoconv*
photomed	20	photomedicine	photomed*
photochl	14	photochlorination	photochl*
solsynth	6	solar synthesis	solar* AND synth*
photohal	2	photohalogenation	photohal*
photodmb++	466	photodegradation of wastes	
miscdmb¶	200	photodegradation of wastes	

\+ The value for the number of citations is intended only as a rough estimate.

++ The complete data bases as obtained from Dr. D. M. Blake of NREL. Many of the citations can also be found in other data bases in which they are relevant.

¶ A data base consisting of those citations that were not relevant to any of the other data bases and appear only here; subset of photodmb.

§ The "*" is the usual DOS filename extender.

The search criteria listed were used to search the SCI but in no way define a limit to those citations that may be found in each data base (i.e., citations discovered and entered individually may have titles that do not satisfy the criteria but nevertheless belong).

In accord with the scope and guidelines of our literature search, a group of irrelevant subjects was devised and incorporated into every search. The intent of this was to eliminate those citations that satisfied the various data base criteria but dealt with an area irrelevant to our purposes. The following areas comprised our list of irrelevant subjects: photolithography, electronics, nuclear reactions, photography, photoemissions, and reactions dealing with photoaffinity.

For convenience, the two data bases containing more than 1000 citations (photoele and matpho) were partitioned into more manageable subsets. These subsets can be selected out of the whole data base using a preformulated search procedure that utilizes the ability to search using

authority lists saved within Pro-Cite. These preformulated searches are in no way perfect--they merely return citations whose titles match their criterion. Indeed, in eyes of their creators, these searches yield a workable, coherent group of references that can be useful given the volume of material, and may serve as starting points for other individualized searches.

Instructions telling how to select the subsets are provided in this Appendix as well as in the Pro-Cite manual starting on page 8-44. The following authority lists with their individual criteria have been created to subdivide the two large data bases, photoele and matpho.

Photoele Authority List

Name	Citations	General Content
phelech	430	pure photoelectrochemistry
eletrans	361	electrons and charge transfer (donating and accepting)
phovolt	29	photovoltaics

Matpho Authority List

Name	Citations	General Content
metal+	413	pure metals
silicon	151	silicon
III-V	81	III-V type semiconductors
supercon	58	superconductors
steel	48	steel and cast iron
metaloxi	45	metal oxides
siloxide	35	silicon oxides
carbon	16	carbon
II-VI	16	II-VI type semiconductors
silnitr	10	silicon nitride
titannit	4	titanium nitride

+ Because of the excessive size of a search dealing with metals, a few citations that clearly belong are not selected with this preformulated criterion. For a more complete search of metals, search for the metal name in the title.

Quick instructions for selecting subsets

1. OPEN one of the two large files.
2. Choose the SELECT option.
3. Choose the SEARCH option
4. In the search box, type "#4=" (This code corresponds to a title search in Pro-Cite.)
5. Press F4 to see listing of authority lists, and choose the authority list corresponding to the search you wish to implement. This can be done by moving the cursor with the "up" and "down" keys and hitting RETURN at the desired list name.
6. What you see before you is the actual preformulated criterion for your search. Copy this into the search window by hitting RETURN next to the first line of criteria.

7. Repeat steps 5 and 6 until all lines of criteria are copied into the search window.

8. Hit RETURN to prompt the search. The desired subset will be those citations that are now called "selected."

Of course, one is not limited to those searches that have been preformulated. Any title search may be created simply by following steps 1-4 and entering the desired words in accord with the guidlines detailed in chapter 8 of the Pro-Cite manual.

A note about the disks

Data bases are divided among the three disks as follows:

Disk 1	**Disk 2**
photobio	matpho
photocat	phosyn
photoele	solchem
solsynth	photoox
phochsyn	photochl
	photohal
	photomed
	photocon
	solarlas

Disk 3
photodmb
miscdmb

The following authority lists are all on Disk 3:

eletrans	silnitr
phovolt	siloxide
phelech	steel
metaloxi	supercon
metal	titannit
carbon	II-VI
silicon	III-V

APPENDIX C.
INITIAL LIST OF POTENTIAL PROCESSES FOR UTILIZATION OF CONCENTRATED SOLAR ENERGY

The following is a list of possible areas for research, investigation, and possible development that emerged from the initial discussions of the study panel. No attempt was made at that stage to apply screening criteria or to prioritize. The order and numbering of topics in this list is essentially arbitrary. An initial version of this list was delivered to SERI on November 30, 1990 (subcontract task 2). This slightly revised version is being included with the Final Report in order to preserve all of the suggestions that arose during our discussions, even though they have not all been analyzed in detail.

---

1. High-temperature photochemistry, including

   - synthesis of complex aromatic molecules from simple precursors;
   - photothermal conversion of methane and other carbon-based feedstocks to acetylene and benzene;
   - second-order photochemistry, i.e., absorption of high-intensity radiation by chemical intermediates. A related issue concerns avoiding photodecomposition of desired products in photochemical synthesis;
   - identification of factors favoring absorption of radiation at visible and near-IR wavelengths, such as adsorption on surfaces (see below), valence unsaturation, hot bands at high temperatures;
   - flash vaporization (dielectric concentration in liquid droplets).

2. Photosensitized reactions, including

   - 1,3-cycloaddition in presence of o-naphthoquinones;
   - photolytic activation of crown ethers.

3. Identification of an efficient photolytic H or OH source for 500- 1500-nm irradiation.

4. Large-scale production of C_{60} (and perhaps related cluster materials) from carbon by photothermal processing under inert-gas atmosphere.
   (Emphasis on this as case-in-point for user research facility; also new findings re singlet oxygen generation [see 9])
   Related possibility: regeneration of activated charcoal sorbents

5. Solar furnaces for solid waste recycling (plastics, metals, glass).

6. Photoconversion, e.g., water splitting in quantum structures ("quantum dots," microclusters, micelles) or stacked photoelectric membranes (R. Gordon).

6a. Possible new energy storage cycles (see 18).

7. Photoconversion in homogeneous media using transition-metal complexes or halogen (chlorine, bromine) redox systems.

8. Two-stage, in-situ photosplitting of water.

9. Reactions using photogenerated metastable singlet oxygen.

10. Photomedicine and photobiology, including

    - research on effects of wavelength, bandwidth, and modest increases in insolation on plant and animal growth;
    - photo-production of carotene in saline-water organisms (as currently practiced at Weizmann Institute of Science, Israel);
    - photosensitization of drugs, including toxicity, therapeutic potency, and possible photo-induced toxic effects such as photocarcinogenicity;
    - research on beneficial or toxic synergistic effects of solar radiation with environmental pollutants, personal care products, foodstuffs, and human physiology -- examples might include photo-induced relaxation of blood vessels, photo-induced release of endorphins (Seasonal Affective Disorder).

11. Kinetic measurements using concentrated solar photons, including

    - in vitro experiments to explore kinetics of biological photoprocesses, e.g., of deep-sea organisms;
    - studies of plant growth such as "action spectra" of metabolic processes;
    - laboratory measurements of atmospheric photochemical processes, especially of long-wavelength absorbers such as organic peroxides.

12. Adaptation of solar concentrator as source for rapid, high-brightness near-infrared Fourier transform spectroscopy

13. Materials processing applications, including

    - production of diamondlike carbon materials and films from heated hydrocarbons;
    - production of ceramics or composites;
    - coating of fibers;
    - cutting, scribing, and annealing of devices and components;
    - photochemistry (photodissociation and photoreaction) of molecular species adsorbed on surfaces;
    - production of metastable phases or alloys;
    - precious metal (Au, Pt, Rare Earths) metallurgy under controlled atmospheres;
    - spallation drilling for mining and construction applications;
    - comminution applications;

- cellulose delignification;
- crude-oil reforming (contained porphyrins as chromophores);
- solar thermal sources for primary metallurgy, coking, and calcining in energy-poor (e.g., third-world) regions.

14. Materials research and testing at high temperatures and heating rates, including
    - space and high-altitude aircraft materials, e.g., solar thrusters;
    - window and heat-pipe materials for solar furnaces and solar thermal engines (the optical properties of many materials at these high temperatures are not well known);
    - measurement of phase diagrams for refractory materials under a wide range of practically important atmospheres;
    - test conditions in which simulation of high-intensity thermal radiation fields (e.g., simulating nuclear blast effects) is essential;
    - accelerated testing of solar panels, aerospace components, and consumer products.
15. Alternative to electron-beam methods for heating, ablation, or evaporation of refractory materials.
16. Solar propulsion schemes: specifically, how is solar energy efficiently transferred to a rapidly flowing gas at high temperatures?
17. Solar-driven Stirling engines, e.g., for third-world use in water pumping and storage: transfer of solar energy to working fluid, use of heat pipes, etc.
18. Methane $\longleftrightarrow$ "synthesis gas" (CO, H_2) cycle; under development at Weizmann Institute of Science, Israel.
19. Solar-pumped laser (solid-state or dye solution); being pursued by R. Winston at the University of Chicago, and by others. Investigation of alternative materials (e.g., bulk diamond, cubic zirconia) for dielectric concentrator is suggested.

Document Control Page	1. NREL Report No. NREL/TP-253-4422	2. NTIS Accession No. DE92001246	3. Recipient's Accession No.

4. Title and Subtitle

High-Flux Solar Photon Processes: Opportunities for Applications

5. Publication Date
June 1992

6.

7. Author(s)
J.I. Steinfeld, S.L. Coy, H.Herzog, J.A. Shorter, M. Schlamp, J.W. Tester, W.A. Peters

8. Performing Organization Rept. No.

9. Performing Organization Name and Address

Departments of Chemistry and Chemical Engineering
Massachusetts Institute of Technology
Cambridge, Mass. 02139

10. Project/Task/Work Unit No.
SI21.1010

11. Contract (C) or Grant (G) No.

(C) XM-0-10135-1

(G)

12. Sponsoring Organization Name and Address

National Renewable Energy Laboratory
1617 Cole Blvd.
Golden, CO 80401

13. Type of Report & Period Covered
Subcontract Report

14.

15. Supplementary Notes
NREL Technical Monitor: Meir Carasso (303) 231-1353

16. Abstract (Limit: 200 words)

The overall goal of this study was to identify new high-flux solar photon (HFSP) processes that show promise of being feasible and in the national interest. Electric power generation and hazardous waste destruction were excluded from this study at sponsor request. Our overall conclusion is that there is promise for new applications of concentrated solar photons, especially in certain aspects of materials processing and premium materials synthesis. Evaluation of the full potential of these and other possible applications, including opportunities for commercialization, requires further research and testing.

17. Document Analysis
a. Descriptors
high solar flux applications; high flux concentrators; potential high flux applications
b. Identifiers/Open-Ended Terms

c. UC Categories
233

18. Availability Statement
National Technical Information Service
U.S. Department of Commerce
5285 Port Royal Road
Springfield, VA 22161

19. No. of Pages
78

20. Price
A05

Form No. 0069E (6-30-87)

DATE
FILMED
7/22/92